Pedro Filipe Lima Marques

Modeling Complex Contact Mechanics in Railway Vehicles for Dynamic Reliability Analysis and Design

UMinho | 2020

Universidade do Minho
Escola de Engenharia

Pedro Filipe Lima Marques

Modeling Complex Contact Mechanics in Railway Vehicles for Dynamic Reliability Analysis and Design

setembro de 2020


REPÚBLICA PORTUGUESA
CIÊNCIA, TECNOLOGIA E ENSINO SUPERIOR
FCT
Fundação para a Ciência e a Tecnologia
NORTE2020
CENTRO 2020
ALENTEJO 2020
POCH
PORTUGAL 2020
UNIÃO EUROPEIA
Fundo Social Europeu

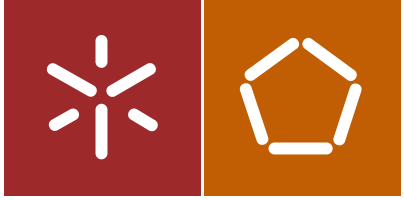

Universidade do Minho
Escola de Engenharia

Pedro Filipe Lima Marques

Modeling Complex Contact Mechanics in Railway Vehicles for Dynamic Reliability Analysis and Design

Tese de Doutoramento
Programa Doutoral em Líderes para Indústrias Tecnológicas

Trabalho realizado sob a orientação de
Professor Doutor João Paulo Flores Fernandes
Professor Doutor Jorge Alberto Cadete Ambrósio

setembro de 2020

DIREITOS DE AUTOR E CONDIÇÕES DE UTILIZAÇÃO DO TRABALHO POR TERCEIROS

Este é um trabalho académico que pode ser utilizado por terceiros desde que respeitadas as regras e boas práticas internacionalmente aceites, no que concerne aos direitos de autor e direitos conexos.

Assim, o presente trabalho pode ser utilizado nos termos previstos na licença abaixo indicada.

Caso o utilizador necessite de permissão para poder fazer um uso do trabalho em condições não previstas no licenciamento indicado, deverá contactar o autor, através do RepositóriUM da Universidade do Minho.

Licença concedida aos utilizadores deste trabalho

Atribuição-NãoComercial
CC BY-NC

https://creativecommons.org/licenses/by-nc/4.0/

ACKNOWLEDGMENTS

The accomplishment of this work involved a significant amount of work, commitment and dedication from myself during the past years. However, these efforts would be vainly applied, if several individuals and institutions were not on my side, supporting me in all possible ways. With their help, I have surpassed difficulties, have learnt, have grown professional and personally and, ultimately, I had been able to perform this thesis. To all of them, I would like to express my deepest gratitude.

To my supervisor, Professor Paulo Flores, I thank his belief in my potential always pushing me further, which made me exceed what I thought my capacities were. His knowledge, carefulness and friendship were essential for the achievement of this work and I am truly grateful.

To my co-supervisor, Professor Jorge Ambrósio, I am grateful for his wise and friendly advices, together with all lessons learnt from him. Despite some physical distance, he was always committed to that I could develop a good job.

I am deeply thankful to *Fundação para a Ciência e a Tecnologia* (FCT) for funding this work through the PhD grant PD/BD/114154/2016, in the context of MIT Portugal Program.

During this project, I had the opportunity to visit the *Politécnico di Milano* during six months under the supervision of Professor Stefano Bruni, to whom I want to thank for his contribution to the scientific merit of this work with its guidance and recognized knowledge in railway field. I want to extend this acknowledgement to Doctor Binbin Liu which also helped me during my stay in Milan.

I want to give a special thanks to my colleague and friend Doctor Hugo Magalhães, who had an exceptional importance in the development of this work, for sharing his expertise in railway field, programming and much more. From University of Lisbon, I also want to thank Pedro Antunes, João Costa and Paula Jorge for always receiving me well.

To the scientific community, I am grateful for all the stimulating conversations and knowledge shared, in particular, to all the brilliant researchers that I have been the pleasure to meet during these years. At this point, I have to highlight Doctor João Pombo, for all the help in this work, Professor Hamid Lankarani, for his friendship and expertise, Professor Jerzy Piotrowski, for sharing his thoughts on the use of contact tables, and Doctor Yu Sun, for sharing his knowledge on the evaluation of contact pressure.

I would like to show my gratitude to the Department of Mechanical Engineering of the University of Minho for all institutional support and providing me the opportunity to serve as assistant lecturer. Several Professors from University of Minho had supported me along this academic path, therefore, I would like to acknowledge Professors Alexandre F. Silva, José C. Teixeira, José Gomes, Nuno Dourado and, specially, Professor Pimenta Claro, who introduced me to this field in my first year.

To all my colleagues that had been in the Department of Mechanical Engineering, I want to express my gratitude for their unceasing encouragement and support, namely Javier Sanchez, João Silva, José Pereira, Manuel Araújo, Rita Ferreira and Sara Cortez. Special thanks to Flavia Barbosa and Vítor Lopes for their authentic friendship and unwearying enthusiasm.

My girlfriend, Adriana Costa, deserves a huge acknowledgement for her patience, understanding and support during the past years. Her help was certainly important.

To my sister, Inês, an (almost) Engineer, I would like to thank for her complicity and trust.

Finally, I want to give the most important acknowledgement to my parents, to whom I dedicate this work, for their belief in my capacities and, most of all, for the tools they gave me through life that made this day possible.

Muito obrigado a todos!

STATEMENT OF INTEGRITY

I hereby declare having conducted this academic work with integrity. I confirm that I have not used plagiarism or any form of undue use of information or falsification of results along the process leading to its elaboration.

I further declare that I have fully acknowledged the Code of Ethical Conduct of the University of Minho.

RESUMO

Modelação da mecânica do contacto complexa em veículos ferroviários para projeto e análise dinâmica fiáveis

O uso de metodologias computacionais para estudar o comportamento dinâmico de veículos ferroviários é cada vez mais comum, pois permite analisar o desempenho do veículo numa dada via, ajudar a projetar sistemas de suspensão, travagem ou tração, estudar o dano dos componentes, entre outros. Neste tipo de ferramentas, a modelação da interação do veículo com a via, traduzindo-se no contacto entre as rodas e os carris, tem particular importância. Posto isto, o presente trabalho visa desenvolver métodos computacionais que permitam uma análise mais detalhada do contacto propondo avanços relativos aos métodos existentes na literatura. Para a deteção de contacto entre a roda e o carril, foi desenvolvida uma abordagem tridimensional para identificação dos pontos de maior interferência, na qual as geometrias da roda e do carril são definidas como superfícies paramétricas. Este método tira partido do facto de a roda ser um corpo de revolução e o carril uma superfície de arrastamento, permitindo identificar o contacto entre perfis gerais, sem a necessidade recorrer a simplificações que evitem a existência de uma zona côncava na roda, isto é, permite a abordagem de contacto entre superfícies conformes. Nas abordagens atuais ao problema do contacto roda-carril, assume-se que a área de contacto é plana, contudo, essa hipótese deixa de ser válida para contactos onde exista alguma conformidade. Nesse sentido, foi desenvolvida uma metodologia para a determinação de uma zona de contacto curva em que a direção normal à superfície de contacto varia ao longo da mesma. Este método permite evitar descontinuidades no cálculo das forças de contacto normais como é aqui demonstrado em diversos casos de teste para o contacto estático entre rodas e carris. A avaliação das forças de contacto tangencial é determinante na interação roda-carril, sendo aqui proposta a utilização de tabelas de pesquisa para o cálculo dessas forças para permitir a diminuição do tempo de cálculo. Neste caso, uma tabela de procura com cinco varáveis de entrada, que considera uma região de contacto definida por uma dupla elipse, é utilizada para estudar o erro de interpolação devido à sua discretização. Com a metodologia proposta é possível estudar a exatidão da tabela de pesquisa sendo, neste processo, apresentadas duas versões melhoradas desta tabela, com minimização de erro ou com minimização da sua dimensão. O modelo multicorpo de uma carruagem do Metro de Lisboa é utilizado para demonstrar as metodologias desenvolvidas neste trabalho através da realização de análises dinâmicas em condições de operação. A cinemática do veículo, a localização dos pontos de contacto, as forças de contacto e as variáveis de entrada da tabela de procura são analisados em detalhe. Os resultados mostram que a utilização de perfis de rodas realistas em detrimento de perfis simplificados tem um impacto significativo na dinâmica do veículo e no tipo e número de contactos desenvolvidos. Da mesma forma, o uso de modelos não-Hertzianos para o cálculo das forças de contacto também tem uma influência considerável no comportamento dos veículos ferroviários relativamente às abordagens correntes.

Palavras-chave: Contacto conforme; Contacto roda-carril; Deteção de contacto; Dinâmica ferroviária; Tabelas de pesquisa de forças de contacto.

ABSTRACT

Modeling complex contact mechanics in railway vehicles for dynamic reliability analysis and design

The use of computational tools to study the dynamic behavior of railway vehicles has been increasing due to its wide range of applications, namely to assess the performance of a vehicle in given track, design suspension, traction or braking systems, analyze the damage of components, among others. In this context, the vehicle-track interaction, which consists of the contact between wheels and rails, plays an important role. Thus, the present work aims to develop computational methodologies which allow a more detailed contact modeling presenting advances over the models available on the literature. In what concerns the contact detection between wheel and rail, a three-dimensional approach to identify the main contact points between wheel and rail was established. This methodology treats both geometries as parametric surfaces and takes advantage of the fact that the wheel is a revolution body and the rail is a sweep surface. Moreover, this allows to determine the contact between general surfaces, without using a simplified wheel profile which avoids the concave region, i.e., it treats the contact between conformal surfaces. In the current approaches to deal with wheel-rail contact, a planar contact region is assumed, however, this hypothesis is violated in the presence of conformality. Hence, it was developed a methodology to evaluate a curved contact patch in which the normal direction to the contact surface varies over the contact area. This method avoids discontinuities on the normal contact force evaluation, as demonstrated here through some wheel-rail static cases. The evaluation of tangential contact forces is fundamental in the context of wheel-rail interaction and, in this work, the utilization of lookup tables for the calculation of these forces is proposed for sake of the reduction of calculation time. Thus, a lookup table with five input variables, in which the contact patch is regularized to a simple double-elliptical contact region, is utilized to study the interpolation error due to its discretization. According to the presented methodology, it is possible to study the accuracy of a given lookup table and, in this process, two enhanced versions of this table are presented, one with minimization of the interpolation error and other with minimization of its size. The dynamic analyses of a multibody model of a trailer vehicle from Lisbon subway system in operation conditions are utilized to validate the methodologies developed in this work. The kinematics of the vehicle, the location of the contact points, the contact forces and input variables of the lookup table are analyzed in detail. The results demonstrate that the use of realistic wheel profiles has a significant influence in the dynamic response of the vehicle and in the type of identified contacts. Similarly, it is shown that the utilization of non-Hertzian contact models for the evaluation of both normal and creep forces also influences the dynamics of railway vehicles when compared with current approaches.

Keywords: Conformal contact; Contact detection; Lookup tables for contact forces; Railway dynamics; Wheel-rail contact.

TABLE OF CONTENTS

LIST OF FIGURES

LIST OF TABLES

List of Abbreviations

BEM	Boundary Element Method
CAE	Computational Aided Engineering
DAE	Differential Algebraic Equations
EDAM	Engineering Design and Advanced Manufacturing
EU	European Union
FEM	Finite Element Method
KBTNH	Kalker Book of Tables for Non-Hertzian
LHS	Latin Hypercube Sampling
LTI	Leaders for Technical Industries
LuT	Lookup Table
MBS	Multibody Systems
RCF	Rolling Contact Fatigue
SDEC	Simple Double-Elliptical Contact

This page is intentionally left blank.

Chapter 2

Latin Symbols

Symbol	Unit (SI)	Description
a	m	Longitudinal semi-axis of contact ellipse
b	m	Lateral semi-axis of contact ellipse
$c_{11}, c_{22}, c_{23}, c_{33}$	-	Kalker creepage coefficients
$\mathbf{D}$	-	Jacobean matrix of the constraint equations
e_0, e_1, e_2, e_3	-	Euler parameters
$\mathbf{f}$	N	Vector of external forces acting on a body
f	N	Resultant tangential contact force caused by the longitudinal and lateral creepages in Polach's method
f_{L}	N	Resultant creep force magnitude computed with linear theory
f_{n}	N	Normal contact force magnitude
$f_{x\mathrm{L}}$, $f_{y\mathrm{L}}$	N	Longitudinal and lateral creep forces computed with linear theory
f_x	N	Longitudinal creep force magnitude
f_y	N	Lateral creep force magnitude
$f_{y\mathrm{S}}$	N	Lateral tangential force due to the influence of spin creepage in Polach's method
G	Pa	Shear modulus of rigidity
$\mathbf{g}$	N, N·m	Vector of generalized external forces and gyroscopic moments
$\mathbf{g}^{\mathrm{c}}$	N, N·m	Vector of reaction forces and moments on the kinematic joints
$\mathbf{J}$	kg·m^2	Inertia tensor
K	N/m$^{1.5}$	Generalized contact stiffness
k_{NL}	-	Correction factor for the creep forces computed with the linear theory
$\mathbf{M}$	kg, kg·m^2	Global mass matrix

m_z	N·m	Spin moment
N	-	Number of bodies
$\mathbf{n}$	-	Normal vector to the surface in the contact point
$\mathbf{n}$	N·m	Vector of external moments acting on a body
n	-	Hertz contact force exponent
$\mathbf{p}$	-	Euler parameters vector
p	Pa	Contact pressure
p_0	Pa	Maximum contact pressure
$\mathbf{q}$	-	Vector of generalized coordinates
$\mathbf{r}$	m	Position vector
s_r	m	Rail longitudinal coordinate
s_w	rad	Wheel angular coordinate
$\mathbf{t}_s$	-	Tangential vector to the surface in the longitudinal direction
$\mathbf{t}_u$	-	Tangential vector to the surface in the lateral direction
t	s	Time
$\mathbf{u}_e$	-	Unit vector to define Euler parameters
u_r	m	Rail lateral coordinate
u_w	m	Wheel lateral coordinate
V	m/s	Forward velocity of the wheelset
$\mathbf{v}$	m/s, rad/s	Generalized velocities vector
$\mathbf{v}_{rel}$	m/s	Relative linear velocity between wheel and rail contact points

Greek Symbols

Symbol	Unit (SI)	Description
α	-	Baumgarte stabilization coefficient
β	-	Baumgarte stabilization coefficient
$\boldsymbol{\gamma}$	-	Right-hand side vector of accelerations constraint equations
δ	m	Penetration depth
$\boldsymbol{\lambda}$	-	Vector of Lagrange multipliers
μ	-	Coefficient of friction

$\boldsymbol{\tau}$	Pa	Tangential tractions
$\boldsymbol{\upsilon}$	-	Right-hand side vector of velocities constraint equations
υ_{C}	-	Modified translational creepage
υ_x	-	Longitudinal creepage
υ_y	-	Lateral creepage
$\boldsymbol{\Phi}$	-	Vector of kinematic constraints
φ	1/m	Spin creepage
ϕ	rad	Angle to define Euler parameters
$\boldsymbol{\omega}$	rad/s	Angular velocity vector

Chapter 3

Latin Symbols

Symbol	Unit (SI)	Description
$\mathbf{A}_{\mathrm{r}}$	-	Rail transformation matrix
$\mathbf{A}_{\mathrm{w}}$	-	Wheel transformation matrix aligned with rail frame
$\mathbf{A}_{\mathrm{ws}}$	-	Wheelset transformation matrix
$\mathbf{A}_{\mathrm{w,s}}$	-	Transformation matrix for rotation about wheel's axis
$\mathbf{a}_{\mathrm{w}}$	-	Axial vector of the wheel coordinate system
$\mathbf{a}_{\mathrm{ws}}$	-	Axial vector of the wheelset coordinate system
$\mathbf{b}_{\mathrm{r}}$	-	Binormal vector of the rail coordinate system
$\mathbf{b}_{\mathrm{w}}$	-	Binormal vector of the wheel coordinate system
$\mathbf{b}_{\mathrm{ws}}$	-	Binormal vector of the wheelset coordinate system
$\mathbf{d}$	m	Distance vector between wheel and rail contact points
$\mathbf{d}_{\mathrm{rw}}$	m	Distance vector between wheel and rail profiles
$\mathbf{f}_{\mathrm{nl}}$	-	Vector of residual from contact nonlinear equations
f_{r}	m	Ordinate of the rail profile
f_{w}	m	Ordinate of the wheel profile
H	m	Distance between left and right wheel profiles
$\mathbf{h}_{\mathrm{w}}$	m	Local position vector of the wheel coordinate system

N_{r}	-	Number of rail nodal points
$\mathbf{n}_{\mathrm{r}}$	-	Normal vector of the rail coordinate system
$\mathbf{n}_{\mathrm{r},P}$	-	Normal vector to the rail surface on point P in global coordinates
$\mathbf{n}_{\mathrm{r},P,\mathrm{r}}$	-	Normal vector to the rail surface on point P in local coordinates
$\mathbf{n}_{\mathrm{w},Q}$	-	Normal vector to the wheel surface on point Q in global coordinates
$\mathbf{n}_{\mathrm{w},Q,\mathrm{w}}$	-	Normal vector to the wheel surface on point Q in local coordinates
$\mathbf{n}_{\mathrm{w}}$	-	Normal vector of the wheel coordinate system
$\mathbf{n}_{\mathrm{ws}}$	-	Normal vector of the wheelset coordinate system
$\mathbf{R}_{\alpha}$	-	Rotation matrix of yaw angle
$\mathbf{R}_{\varphi}$	-	Rotation matrix of roll angle
$R^{\mathrm{s}}_{\mathrm{r},P}$	m	Radius of rail surface on point P in the longitudinal direction
$R^{\mathrm{u}}_{\mathrm{r},P}$	m	Radius of rail surface on point P in the lateral direction
$R^{\mathrm{s}}_{\mathrm{w},Q}$	m	Radius of wheel surface on point Q in the longitudinal direction
$R^{\mathrm{u}}_{\mathrm{w},Q}$	m	Radius of wheel surface on point Q in the lateral direction
$\mathbf{r}_{P}$	m	Position vector of point P in the rail in global coordinates
$\mathbf{r}_{Q}$	m	Position vector of point Q in the wheel in global coordinates
$\mathbf{r}_{\mathrm{r}}$	m	Position vector of the origin of the rail profile
$\mathbf{r}_{\mathrm{r},P}$	m	Distance vector from rail origin to point P in global coordinates
$\mathbf{r}_{\mathrm{r},P,\mathrm{r}}$	m	Position vector of point P in rail's local coordinates
$\mathbf{r}_{\mathrm{w},Q}$	m	Distance vector from wheel origin to point Q in global coordinates
$\mathbf{r}_{\mathrm{w},Q,\mathrm{w}}$	m	Position vector of point Q in wheel's local coordinates
$\mathbf{r}_{\mathrm{ws}}$	m	Position vector of wheelset center of mass
s_{r}	m	Rail longitudinal coordinate
s_{w}	rad	Wheel angular coordinate
$\mathbf{t}_{\mathrm{r}}$	-	Tangent vector of the rail coordinate system
$\mathbf{t}_{\mathrm{r,s},P}$	-	Tangent vector to the rail surface on point P in longitudinal direction in global coordinates
$\mathbf{t}_{\mathrm{r,u},P}$	-	Tangent vector to the rail surface on point P in lateral direction in global coordinates
$\mathbf{t}_{\mathrm{r,u},P,\mathrm{r}}$	-	Tangent vector to the rail surface on point P in lateral direction in local coordinates
$\mathbf{t}_{\mathrm{w,s},Q}$	-	Tangent vector to the wheel surface on point Q in longitudinal direction in global coordinates

$\mathbf{t}_{\mathrm{w,u},Q}$	-	Tangent vector to the wheel surface on point Q in lateral direction in global coordinates
$\mathbf{t}_{\mathrm{w,u},Q,\mathrm{w}}$	-	Tangent vector to the wheel surface on point Q in lateral direction in local coordinates
u_{r}	m	Rail lateral coordinate
$u_{\mathrm{r,lower}}$	m	Lower bound of rail lateral coordinate in the interpenetration zone
$u_{\mathrm{r,upper}}$	m	Upper bound of rail lateral coordinate in the interpenetration zone
u_{w}	m	Wheel lateral coordinate
$u_{\mathrm{w,lower}}$	m	Lower bound of wheel lateral coordinate in the interpenetration zone
$u_{\mathrm{w,upper}}$	m	Upper bound of wheel lateral coordinate in the interpenetration zone
x, y, z	m	Cartesian coordinates

Greek Symbols

Symbol	Unit (SI)	Description
α	rad	Yaw angle
β	rad	Rotation angle between wheel and wheelset coordinate systems
$\gamma_{\mathrm{r},P}$	-	Rail contact angle on point P
$\gamma_{\mathrm{w},Q}$	-	Wheel contact angle on point Q
Δx	m	Increment of the contact point location in the rail longitudinal direction
δ	m	Penetration depth
$\kappa^{\mathrm{s}}_{\mathrm{r},P}$	1/m	Curvature of rail surface on point P in the longitudinal direction
$\kappa^{\mathrm{u}}_{\mathrm{r},P}$	1/m	Curvature of rail surface on point P in the lateral direction
$\kappa^{\mathrm{s}}_{\mathrm{w},Q}$	1/m	Curvature of wheel surface on point Q in the longitudinal direction
$\kappa^{\mathrm{u}}_{\mathrm{w},Q}$	1/m	Curvature of wheel surface on point Q in the lateral direction
ξ, η, ζ	-	Body fixed coordinate system
φ	rad	Roll angle

Subscripts and Superscripts

Symbol	Description
L	Left side
P	Point P

Q	Point Q
R	Right side
r	Rail
s	Longitudinal direction
side	Both left and right sides
u	Lateral direction
w	Wheel
ws	Wheelset

Chapter 4

Latin Symbols

Symbol	Unit (SI)	Description
$\mathbf{A}_{\mathrm{cp}}$	-	Contact patch transformation matrix
$\mathbf{A}_{\mathrm{r}}$	-	Rail transformation matrix
$\mathbf{A}_{\mathrm{w}}$	-	Wheel transformation matrix aligned with rail frame
$\mathbf{A}_{\mathrm{w,s}}$	-	Transformation matrix for rotation about wheel's axis
$\mathbf{A}_{\mathrm{w,s},i}$	-	Transformation matrix for rotation about wheel's axis of strip i
$\mathbf{A}_{\mathrm{w,s},Q}$	-	Transformation matrix for rotation about wheel's axis on point Q
A	1/m	Average contact curvature in longitudinal direction
a	m	Longitudinal semi-axis of contact ellipse
$\mathbf{B}_{\mathrm{r}}$	-	Transformation matrix from rail to contact patch reference system
$\mathbf{B}_{\mathrm{w}}$	-	Transformation matrix from wheel to contact patch reference system
B	1/m	Average contact curvature in lateral direction
b	m	Lateral semi-axis of contact ellipse
C	-	Contact region
C_{δ}	-	Hertz contact parameter
c_{d}	-	Damping factor
c_{e}	-	Coefficient of restitution
$\mathbf{c}_{\mathrm{r}}$	m	Constant term of rail contact point

$\mathbf{c}_{\mathrm{w}}$	m	Constant term of wheel contact point
d	m	Distance between deformed wheel and rail surfaces
d_{r}	m	Position of deformed rail surface
d_{w}	m	Position of deformed wheel surface
E	Pa	Young's modulus
f	m	Undeformed distance function
$\mathbf{f}_{\mathrm{n}}$	N	Normal contact force vector
f_{n}	N	Normal contact force magnitude
$f_{\mathrm{n},i}$	N	Normal contact force magnitude of strip i
f_{r}	m	Ordinate of the rail profile
$f_{\mathrm{r},i}$	m	Ordinate of the rail profile of strip i
$f_{\mathrm{r},P}$	m	Ordinate of the rail profile on point P
f_{w}	m	Ordinate of the wheel profile
$f_{\mathrm{w},i}$	m	Ordinate of the wheel profile of strip i
$f_{\mathrm{w},Q}$	m	Ordinate of the wheel profile on point Q
G	Pa	Shear modulus of rigidity
H	m	Distance between left and right wheel profiles
$h_{k(k+1)}$	m	Penetration minimum between maxima k and k+1
h_{r}	1/Pa	Rail material parameter
h_{w}	1/Pa	Wheel material parameter
$\mathbf{h}_{\mathrm{w}}$	m	Local position vector of the wheel coordinate system
K	N/m$^{1.5}$	Generalized contact stiffness
L_{r}	m	Arc length of rail profile in the interpenetration region
$L_{\mathrm{r},i}$	m	Arc length of rail profile at strip i
L_{w}	m	Arc length of wheel profile in the interpenetration region
$L_{\mathrm{w},i}$	m	Arc length of wheel profile at strip i
N_{m}	-	Number of maxima of penetration function
N_{s}	-	Number of strips in the interpenetration region
m	-	Parameter proportional to the longitudinal semi-axis of contact ellipse
n	-	Parameter proportional to the lateral semi-axis of contact ellipse

n	-	Hertz contact force exponent
$n_{\mathrm{r},i}$	m	Distance in normal direction from contact patch to rail profile at strip i in the curved contact
$\mathbf{n}_{\mathrm{r},P}$	-	Normal vector to the rail surface on point P in global coordinates
$\mathbf{n}_{\mathrm{s},i}$	-	Normal vector at strip i in the reference system of curved contact
$n_{\mathrm{w},i}$	m	Distance in normal direction from contact patch to wheel profile at strip i in the curved contact
p	Pa	Contact pressure
p_0	Pa	Maximum contact pressure
$\mathbf{R}_{\alpha}$	-	Rotation matrix of yaw angle
$\mathbf{R}_{\varphi}$	-	Rotation matrix of roll angle
$R_{\mathrm{r}}^{\mathrm{s}}$	m	Radius of rail surface in the longitudinal direction
$R_{\mathrm{r}}^{\mathrm{u}}$	m	Radius of rail surface in the lateral direction
$R_{\mathrm{w}}^{\mathrm{s}}$	m	Radius of wheel surface in the longitudinal direction
$R_{\mathrm{w}}^{\mathrm{u}}$	m	Radius of wheel surface in the lateral direction
R_0	m	Nominal wheel radius
$\mathbf{r}$	m	Position vector
r	-	Ratio of penetration velocity for smoothing
$\mathbf{r}_{\mathrm{cp,r},i}$	m	Distance vector from contact patch origin to strip i in the rail in global coordinates
$\mathbf{r}_{\mathrm{cp,w},i}$	m	Distance vector from contact patch origin to strip i in the wheel in global coordinates
$\mathbf{r}_P$	m	Position vector of point P in the rail in global coordinates
$\mathbf{r}_Q$	m	Position vector of point Q in the wheel in global coordinates
$\mathbf{r}_{\mathrm{r}}$	m	Position vector of the origin of the rail profile
$\mathbf{r}_{\mathrm{r,p}}$	m	Position vector of rail contact point projected in the rail coordinate system
$\mathbf{r}_{\mathrm{r},P}$	m	Distance vector from rail origin to point P in global coordinates
$\mathbf{r}_{\mathrm{r},P,\mathrm{r}}$	m	Position vector of point P in rail's local coordinates
$\mathbf{r}_{\mathrm{r},y_i}$	m	Distance vector from rail origin to strip i in the rail in global coordinates
$\mathbf{r}_{\mathrm{s},i}$	-	Position vector of strip i in the reference system of curved contact
$\mathbf{r}_{\mathrm{w,p}}$	m	Position vector of wheel contact point projected in the rail coordinate system
$\mathbf{r}_{\mathrm{w},Q}$	m	Distance vector from wheel origin to point Q in global coordinates

$\mathbf{r}_{\mathrm{w},Q,\mathrm{w}}$	m	Position vector of point Q in wheel's local coordinates
$\mathbf{r}_{\mathrm{w},y_i}$	m	Distance vector from wheel origin to strip i in the wheel in global coordinates
$\mathbf{r}_{\mathrm{ws}}$	m	Position vector of wheelset center of mass
$\mathbf{r}_{y_i\mathrm{r}}$	m	Position vector of strip i in the rail in global coordinates
$\mathbf{r}_{y_i\mathrm{w}}$	m	Position vector of strip i in the wheel in global coordinates
s	m	Curved axis of curved contact patch
s_{ci}	m	Lateral position of the i^{th} penetration maximum in the curved contact patch reference system
s_{ei}	m	Lateral position of the ending limit of the i^{th} curved contact patch
s_i	m	Lateral position of strip i in curved contact
s_{si}	m	Lateral position of the starting limit of the i^{th} curved contact patch
s_{w}	rad	Wheel angular coordinate
$\mathbf{t}_{\mathrm{s},i}$	-	Tangent vector at strip i in the reference system of curved contact
$\mathbf{t}_{\mathrm{w,s},Q}$	-	Tangent vector to the wheel surface on point Q in longitudinal direction in global coordinates
$\mathbf{t}_{\mathrm{w,u},Q}$	-	Tangent vector to the wheel surface on point Q in lateral direction in global coordinates
u_{r}	m	Rail lateral coordinate
$u_{\mathrm{r},i}$	m	Rail lateral coordinate of strip i
$u_{\mathrm{r},P}$	m	Rail lateral coordinate on point P
$u_{\mathrm{r,lower}}$	m	Lower bound of rail lateral coordinate in the interpenetration zone
$u_{\mathrm{r,upper}}$	m	Upper bound of rail lateral coordinate in the interpenetration zone
u_{w}	m	Wheel lateral coordinate
$u_{\mathrm{w},i}$	m	Wheel lateral coordinate of strip i
$u_{\mathrm{w},Q}$	m	Wheel lateral coordinate on point Q
$u_{\mathrm{w,lower}}$	m	Lower bound of wheel lateral coordinate in the interpenetration zone
$u_{\mathrm{w,upper}}$	m	Upper bound of wheel lateral coordinate in the interpenetration zone
v_0	m/s	Penetration velocity tolerance
w_{r}	m	Displacement of rail surface
w_{w}	m	Displacement of wheel surface
w_{wr}	m	Displacement of combined wheel and rail surfaces
x, y, z	-	Cartesian coordinates

x_{cp}, y_{cp}, z_{cp}	-	Contact patch coordinate system
$x_{cp,i}$	m	Longitudinal position of strip *i* in the contact patch reference system
x_L	m	Leading edge of contact patch
x_s, y_s	-	Planar coordinate system for curved contact
$x_{s,i}, y_{s,i}$	-	Position of strip *i* in the reference system of curved contact
y_c	m	Lateral position of the main contact point in the contact patch reference system
y_{ci}	m	Lateral position of the i^{th} penetration maximum in the contact patch reference system
$y_{cp,i}$	m	Lateral position of strip *i* in the contact patch reference system
y_{ei}	m	Lateral position of the ending limit of the i^{th} contact patch
$y_{h_{k(k+1)}}$	m	Lateral position of penetration minimum between maxima *k* and *k*+1
y_{si}	m	Lateral position of the starting limit of the i^{th} contact patch
$z_{cp,r,i}$	m	Normal position of strip *i* in the rail in the contact patch reference system
$z_{cp,w,i}$	m	Normal position of strip *i* in the wheel in the contact patch reference system
z_p	m	Distance between undeformed wheel and rail penetrated surfaces
z_{wr}	m	Undeformed distance between wheel and rail surfaces

Greek Symbols

Symbol	Unit (SI)	Description
α	rad	Yaw angle
ΔL_r	m	Arc length of rail profile for each strip
ΔL_w	m	Arc length of wheel profile for each strip
Δs	m	Width of contact strip
Δs_0	m	Specified width of contact strip
Δx_i	m	Increment of the location of the contact point in the rail longitudinal direction of strip *i*
Δx_P	m	Increment of the location of the contact point in the rail longitudinal direction on point *P*
Δy	m	Wheelset lateral displacement
$\Delta\gamma$	rad	Contact angle variation
δ	m	Maximum penetration depth

δ_{cp}	m	Penetration depth over the contact patch
δ_i	m	i^{th} maximum of penetration depth
ε	-	Penetration correction factor
θ	-	Angle for determining the axes of contact ellipse
θ_i	rad	Angle of strip i in the curved contact patch
$\kappa^{\mathrm{s}}_{\mathrm{r},P}$	1/m	Curvature of rail surface on point P in the longitudinal direction
$\kappa^{\mathrm{u}}_{\mathrm{r},P}$	1/m	Curvature of rail surface on point P in the lateral direction
$\kappa^{\mathrm{s}}_{\mathrm{w},Q}$	1/m	Curvature of wheel surface on point Q in the longitudinal direction
$\kappa^{\mathrm{u}}_{\mathrm{w},Q}$	1/m	Curvature of wheel surface on point Q in the lateral direction
ξ, η, ζ	-	Body fixed coordinate system
σ	-	Poisson's ratio
φ	rad	Roll angle
$\boldsymbol{\omega}$	rad/s	Angular velocity vector

Subscripts and Superscripts

Symbol	Description
c	Penetration maximum
cp	Contact patch
e	End
H	Hertzian
KP	Kik-Piotrowski
NH	Non-Hertzian
n	Normal
P	Point P
Q	Point Q
r	Rail
s	Start
SZG	Sun, Zhai and Guo
w	Wheel
ws	Wheelset

Chapter 5

Latin Symbols

Symbol	Unit (SI)	Description
A_{cp}	m^2	Area of contact patch
a	m	Longitudinal semi-axis of contact ellipse
b	m	Lateral semi-axis of contact ellipse
c	m	Equivalent radius of the SDEC region
E	Pa	Young's modulus
F_x	N	Longitudinal creep force magnitude
F_y	N	Lateral creep force magnitude
$\mathbf{f}$	-	Vector of output variables
f	m	Undeformed distance function
f_j	-	j^{th} output variable
f_{n}	N	Normal contact force magnitude
f_x	-	Normalized longitudinal creep force
f_y	-	Normalized lateral creep force
g	-	Semi-axes ratio
k_0, k_1, k_2, k_3	-	Polynomial coefficients for calculating the characteristic length
M_z	N·m	Spin moment
m	-	Number of output variables of the lookup table
m_z	-	Normalized spin moment
N_{c}	-	Number of cells of the lookup table
N_{e}	-	Number of edges of the lookup table
N_{p}	-	Number of points of the lookup table
n	-	Number of input variables of the lookup table
$n_{\mathrm{a}}, n_{\mathrm{b}}$	-	Coefficients for calculating the characteristic length
n_{c}	-	Index of a given cell of the lookup table
n_i	-	Number of points of i^{th} input variable of the lookup table
R	m	Rolling radius for obtaining the SDEC patch

R_1, R_2	m	Radii of the undeformed distance function for SDEC patch
w_i^1	-	Weighting coefficient for the lower value of the i^{th} input variable
w_i^2	-	Weighting coefficient for the upper value of the i^{th} input variable
W_1, W_2, W_3	m	Dimensions of non-Hertzian contact patch
x, y, z	-	Cartesian coordinates
$\mathbf{x}$	-	Vector of input variables
x_i	-	i^{th} input variable
x_i^1	-	Lower value of the i^{th} input variable for interpolation
x_i^2	-	Upper value of the i^{th} input variable for interpolation
y_0	m	Distance from the origin to the center of SDEC patch

Greek Symbols

Symbol	Unit (SI)	Description
α	rad	Creepage angle
δ	m	Maximum penetration depth
δ_0	m	Corrected penetration depth
η	-	Parametrized lateral creepage
θ	-	Maximum semi-axes ratio
μ	-	Coefficient of friction
ν	-	Creepage modulus
ξ	-	Parametrized longitudinal creepage
ρ	-	Characteristic length of the elliptical contact patch
σ	-	Poisson's ratio
υ_x	-	Longitudinal creepage
υ_y	-	Lateral creepage
φ	1/m	Spin creepage
χ	-	Parametrized spin creepage
ψ	-	Shape number

Subscripts and Superscripts

Symbol	Description
c	Cell
e	Edge
int	Interpolation
p	Point
r	Rail
w	Wheel

Chapter 6

Latin Symbols

Symbol	Unit (SI)	Description
A_{cp}	m^2	Area of contact patch
a	m	Longitudinal semi-axis of contact ellipse
b	m	Lateral semi-axis of contact ellipse
c	N·s/m	Damping coefficient
c_e	-	Coefficient of restitution
E	Pa	Young's modulus
f_n	N	Normal contact force magnitude
f_r	m	Ordinate of the rail profile
f_w	m	Ordinate of the wheel profile
f_x	N	Longitudinal creep force magnitude
f_y	N	Lateral creep force magnitude
g	-	Semi-axes ratio
H	m	Distance between left and right wheel profiles
I	$kg·m^2$	Moment of inertia
k	N/m	Stiffness coefficient
R_0	m	Nominal wheel radius

s_r	m	Rail longitudinal coordinate
s_w	rad	Wheel angular coordinate
t	s	Time
u_r	m	Rail lateral coordinate
u_w	m	Wheel lateral coordinate
W_1, W_2	m	Dimensions of non-Hertzian contact patch
x, y, z	m	Cartesian coordinates

Greek Symbols

Symbol	Unit (SI)	Description
α	rad	Creepage angle
Δs_0	m	Specified width of contact strip
ε	-	Penetration correction factor
μ	-	Coefficient of friction
ν	-	Creepage modulus
ξ, η, ζ	-	Body fixed coordinate system
σ	-	Poisson's ratio
χ	-	Parametrized spin creepage
ψ	-	Shape number

Subscripts and Superscripts

Symbol	Description
r	Rail
w	Wheel

This page is intentionally left blank.

"*Nothing can be loved or hated unless it is first understood.*"
Leonardo da Vinci

1. INTRODUCTION

The high demand for the optimization of processes and products pursuing the minimization of the employed resources, namely time, costs or manpower, together with the growth of computational power led to the tremendous development of computer aided engineering tools during recent decades. Hence, the utilization of computational means to enhance and accelerate different stages of the design and development of mechanical systems has been gaining an irreplaceable importance either in detriment of experimental methods or trial and error approaches or to complement them. More recently, computational methodologies evolved from the successive studies of specific disciplines to the simultaneous simulations with several fields of knowledge to enhance the performance of the design object trough multidisciplinary approaches. The utilization of these tools is cross-cutting to all areas of engineering, especially those with the greatest economic impact. This is the case of railway dynamics, in which CAE tools play a crucial role into the development of new technologies, maintenance procedures and in their enhancement. The vehicle-track interaction, which takes a preponderant role on the vehicle performance, safety, comfort or structural health of components is a crucial element in the evaluation of the impact of railway systems, being the focus of this research work. Thus, the contact mechanics of the wheel and rail interaction is studied, and strategies to develop accurate and reliable models are proposed here.

1.1. Motivation

In a worldwide context, the increase of traffic demand, with its implications on congestion, safety of energy supply, and climate change, is one of the major issues that society faces. Thus, one of the main goals is to make the transportation of people and goods safer, more efficient and environmentally more friendly, while promoting the economic developments. There is a need to have a competitive and efficient transportation network to fulfil the population and industrial needs. At this stage, despite of the railway

vehicles presenting several advantages, they have a strong competition from other surface, waterway and airway vehicles. It has been demonstrated that implementation of high-speed railway lines is responsible by shifting passengers from other means of transportation to railway (ERA, 2020). Figure 1.1 shows the changes in passenger traffic of some air routes in Europe and Asia after the implementation of high-speed railway lines. For instance, in 2007, it was launched a new high-speed rail between Paris and Strasbourg which produced a reduction of more than 80% of the air passengers for this route in 2014 when compared with 2006, before the construction of high-speed line. Moreover, the European Commission has the ambition that the railway sector takes on a larger share of the transport demand, and some of their main goals are to triple the length of the existing high-speed rail network by 2030, to connect all core network airports to the rail network by 2050, to shift 30% of road freight over 300 km to other modes such as rail or waterborne transport by 2030, and more than 50% by 2050, among others (Shift2Rail, 2018). Bearing that in mind, it is mandatory to improve the trains quality, i.e., make them quieter, more comfortable and more reliable, to enhance the rail network infrastructure in order to have lower life-cycle cost and capability of following the growing passenger and freight mobility demand.

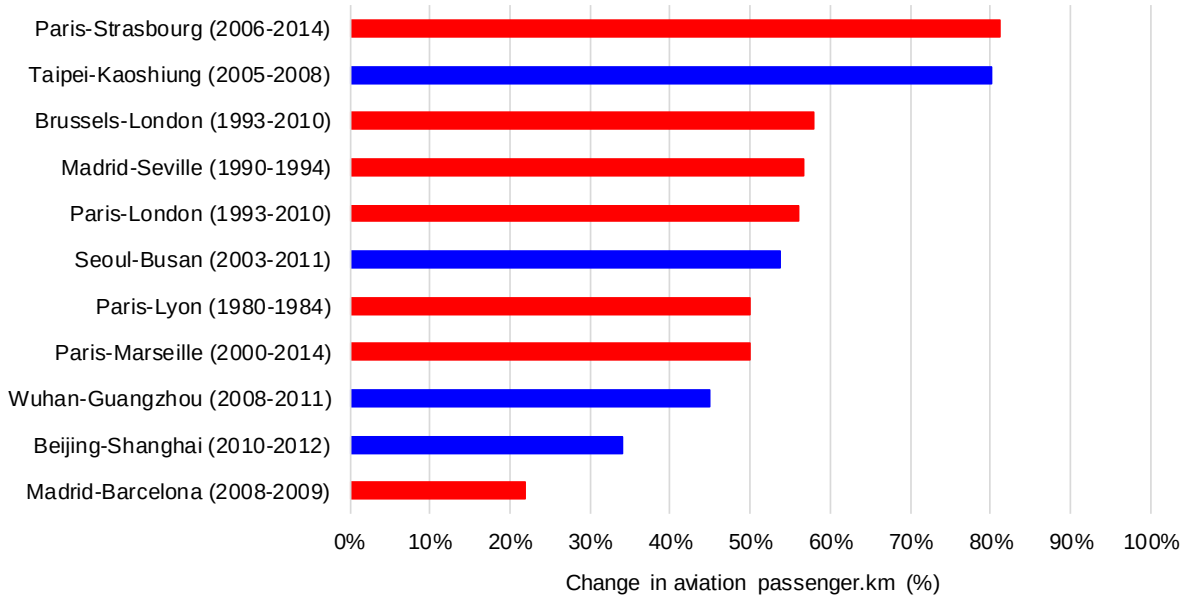

Figure 1.1 – Average percentage change in passenger activity on selected air routes after high-speed rail implementation in Europe (red) and Asia (blue) - (adapted from ERA (2020)).

Currently, there are around 275 vehicles and 3000 km of track in the Portuguese railway system. In 2017, more than 122 million passengers used railway vehicles in Portugal (+6.3% than 2016), and around 9 million tonnes of freight had been transported (UIC, 2018). This increasing tendency on railway usage has been verified for the last years, and shows that, for short and medium distance travels, the

railway vehicles are preferred. However, it is required to invest in the development of such vehicles and corresponding infrastructures to maintain their competitiveness. For instance, in terms of railroad quality, Portugal is below the EU average (Schwab, 2018), as shown in Figure 1.2. The low quality of railway infrastructures demonstrates the importance of enhancement of the railway service and, hence, improving consumer's satisfaction which is below many European countries, as depicted in Figure 1.3. In short, the comfort and safety in railway transport need to be improved, and the cost must be reduced, in order to attract more passengers. This priority is becoming more effective since one of the main investment fields of Portugal2030 Program is Mobility and Transports (PNI2030, 2019).

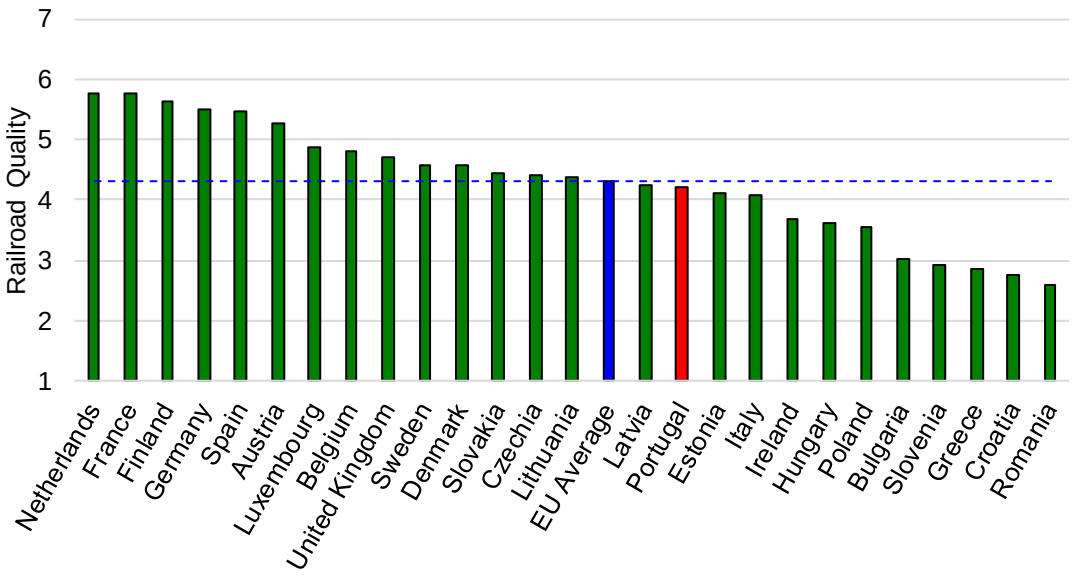

Figure 1.2 – Railroad Quality (2016-2017). Rating based on a survey by the World Economic Forum, using a scale from 1 (extremely underdeveloped) to 7 (extensive and efficient).

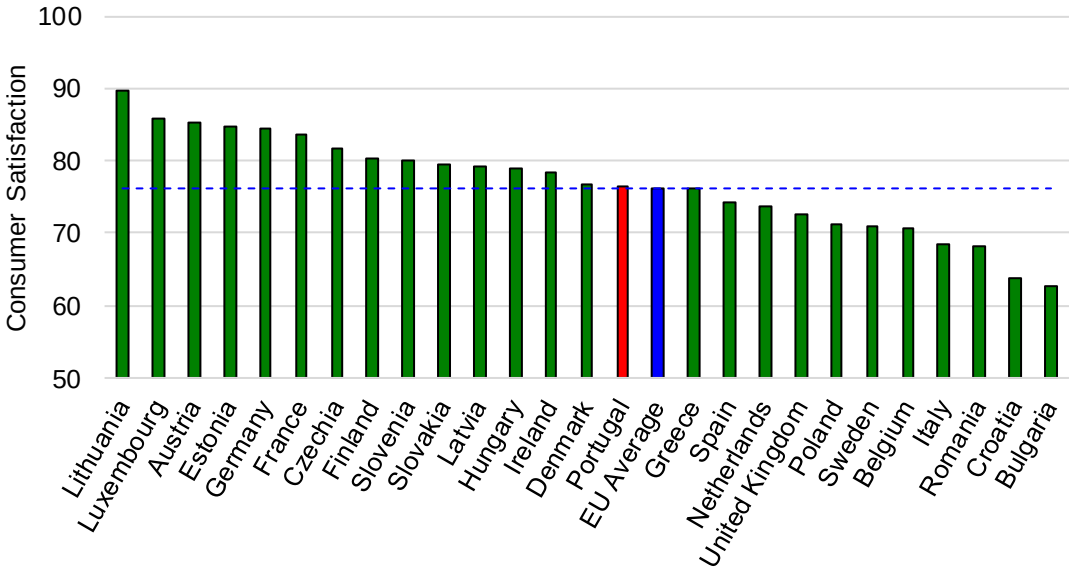

Figure 1.3 – Consumer satisfaction with rail transport (2015). This ranking is based on the 'Market Performance Indicator' which is calculated considering: comparability, trust, problems & detriment, expectations and choice.

The comfort in a railway vehicle is strongly related to the level of noise and vibration that the passengers are subjected to, which is expected to be as low as possible. The main sources of these disturbances are associated with the dynamical performance of the vehicle and the interaction between the vehicle and the track. The former depends on the vehicle aerodynamics, on the materials used on its construction, and on its suspension systems, while the latter consists of the contact interaction between wheel and rail. Therefore, the general motivation of this research deals with the development of advanced computational methodologies that allow for realistic and meaningful dynamic analysis of railway vehicles, which, ultimately, allow for the improvement of their performance, both in terms of safety and comfort. Although the computational tools are expected to be comprehensive, including the vehicle modelling (Bruni et al., 2007) or track modelling (Antunes et al., 2019), the main focus of the current work is on the contact between the wheel and rail surfaces which ultimately drives the complete vehicle dynamics (Meymand et al., 2016). It is accepted that a reliable and efficient methodology to model the railway vehicle dynamics is of paramount interest for the virtual homologation of railway vehicles (Magalhães et al., 2016a). Furthermore, the design of suspension, traction or braking systems (Bruni et al., 2011), the study of vehicle stability on tracks with irregularities (Pombo and Ambrósio, 2012), among others, are object of specialized analysis with the goal of improving vehicle performance.

The interaction between the wheel and the rail does not only affect the motion of the vehicle, but also the deterioration of the mechanical components themselves. The wheel-rail contact is responsible for many local damaging phenomena resulting from the existence of both cyclic and occasional large normal and tangential forces. Therefore, knowing them with accuracy is the steppingstone into handling their effect in the vehicle behavior. In the subsequent paragraphs, the main damaging phenomena produced by wheel-rail interaction are characterized, being their most relevant causes identified which can be mitigated based the detailed study of its contact mechanics during design stage.

The presence of massive slip, as in the case of the wheels being blocked, can lead to a huge increase of contact temperature, as depicted in Figure 1.4(a), that induces the appearance of severe defects, namely wheel flats (Figure 1.4(b)) and rail burns (Figure 1.4(c)). This rise of contact temperature tends to modify the tribological properties of the contact interaction, namely in what concerns the relations between stresses and strains. Clearly, any operational or system design procedure requires a good understanding of the wheel-rail contact phenomena if the mitigation of their aspects are to be tackled.

(a) (b) (c)

Figure 1.4 – (a) Scenario of contact temperature increase due to extreme slip; (b) wheel flat; and (c) rail burn.

The corrugation of both wheel and rail surfaces is also a very common defect on railway systems, which consists in the development of quasi-sinusoidal irregularities with short wavelength (Nielsen and Johansson, 2000; Grassie, 2009, El Beshbichi at al., 2020), as pictured in Figure 1.5. The corrugation phenomenon can occur from multiple reasons, namely due track resonance vibration, affected by the elements' stiffness and distance between sleepers, due to running close to the traction limit, which produces changes between roll and slip states, or due to excessive heavy haul (Grassie, 2009). There are mainly three damaging mechanisms associated with corrugation, that is, wear, plastic bending and plastic flow. Moreover, there is a similar out-of-round wheel defect which called polygonization (Bogacz and Frischmuth, 2016) which is characterized by a small number of minima and maxima of the radius. Wheel polygonization is typically caused by stick-slip effects and oscillations from vehicle/track resonances, and mostly affects high-speed trains. The basis to mitigate any of the problems to the vehicle performance listed here is to better understand the impact of the wheel-rail contact in the development of any of these damaging phenomena.

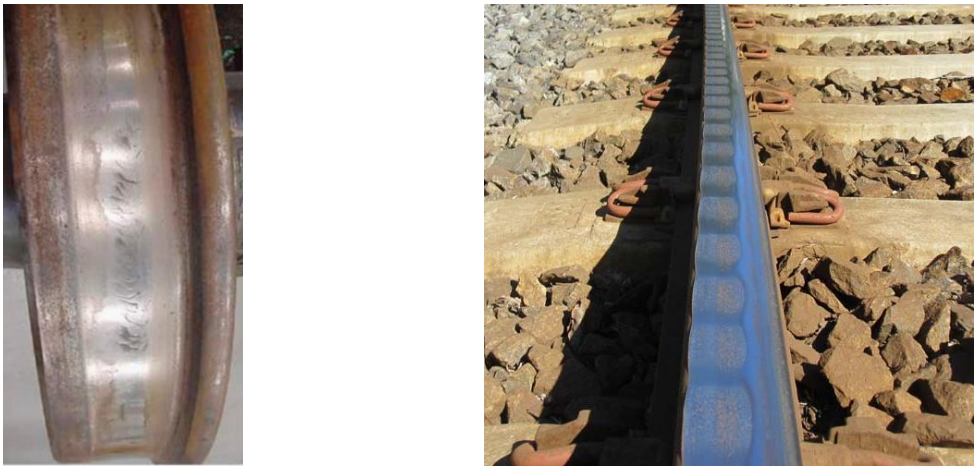

(a) (b)

Figure 1.5 – Corrugation of (a) wheel and (b) rail elements

Rolling contact fatigue (RCF) is one of the major causes of damage on the wheel and rail elements due to the cyclic high contact stresses resulting from their interaction, which leads to the appearance of cracks both on the surface or some millimeters to centimeters below it (Turnia et al., 2007; Ekberg et al., 2014). The subsurface RCF is mainly initiated by the presence of local material defects, while the surface RCF is typically associated with the ratcheting phenomenon which results in damage growth. It must be noted that the RCF effects are magnified by the presence of corrugation. The defects that appear on the rail surface can assume the form of head checks (Figure 1.6(a)) or squats (Figure 1.6(b)), while, in the wheel surface, the defects are known as pitting or fish scales (Figure 1.6(c)).

(a) (b) (c)

Figure 1.6 – Defects resulting from the rolling contact fatigue, namely (a) head checks, (b) squats and (c) wheel pitting.

The wear of both profiles represents one of the most significant issues affecting the railway maintenance costs and vehicle dynamic performance (Braghin et al., 2009; Enblom, 2009). Generally, the wear of profiles is associated to any loss or removal of material which leads to the modification of the original contact surfaces. This phenomenon can occur due to adhesive wear, abrasive wear, plastic deformation or phase transformation. Due to the high degree of complexity associated with the wheel-rail interaction, there is a non-uniform distribution of the normal and tangential stresses through the contacting surfaces which leads to the existence of different levels and mechanisms of wear at different points of the profiles. Therefore, the wear of both elements is highly dependent of the contact conditions, namely loading, slip or lubrication. In that sense, traction, braking and curve negotiation are the running condition in which high wear is prone to occur (Braghin et al., 2009). In many situations, the wear of both wheel and rail lead to noticeable changes of the rail and wheel profiles, as clearly demonstrated by the highly worn profiles, wheel in Figure 1.7(a), and rail in Figure 1.7(b). These worn profiles have an influence

on the riding safety and dynamical performance of the vehicle, since the wheel-rail geometry is responsible by restraining the vehicle motion (Bruni and Braghin, 2009). Typically, the curve negotiation leads to the wear development, in the sense that the contacting surfaces tend to be more conformal, as schematized in Figure 1.7(c). In terms of maintenance actions, the cost of reshaping, or replacing, a worn rail profile is tremendous due to the comprehensive length of the railway tracks. Regarding the wheel, when the modifications introduced by the wear exceeds a defined threshold, the wheel is grinded to its original profile, although its nominal radius is being reduced. This procedure, besides requiring the removal of the train from active service, produces a reduction of the height of the rim which diminishes the wheel's mechanical resistance. Therefore, the number of re-profiling operations is limited.

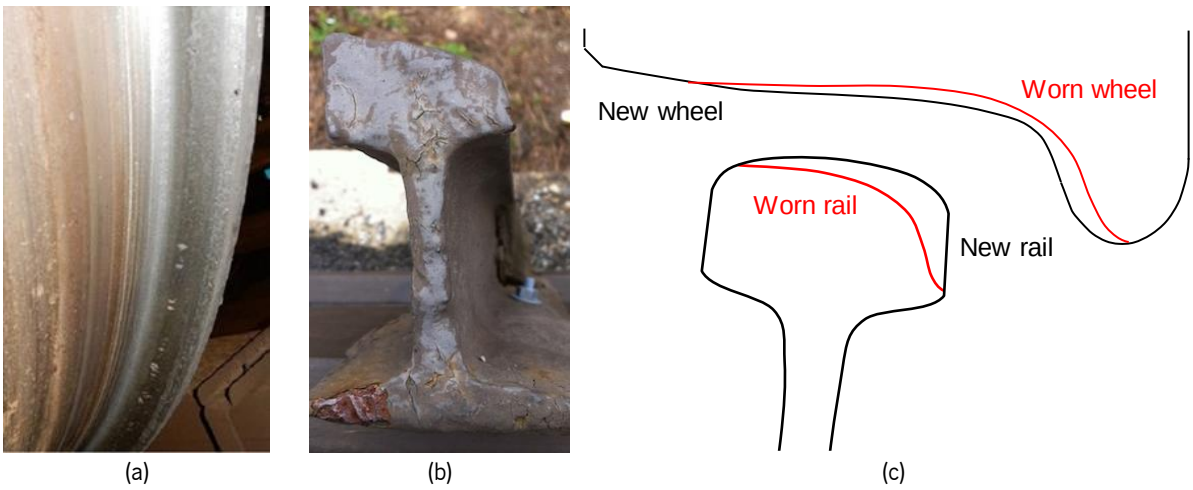

Figure 1.7 – Highly worn profiles: (a) wheel; and (b) rail. (c) Schematic representation of the comparison between new and worn profiles.

Since most of the vehicle and track maintenance costs result from the wheel and rail damage, the accurate modelling of their interaction allows to identify approaches to reduce the damaging phenomena and, consequently, mitigating the corresponding costs. In the same direction, the prediction of the crack growth or profile wear evolution supports the advanced knowledge of when maintenance is required, eventually leading to the avoidance of unnecessary inspections of the elements (Bevan et al., 2013; Tao et al., 2016; Shebani and Iwnicki, 2018; Tsujie et al., 2019). A reliable computational tool for contact modeling can be employed in the enhancement of vehicle properties to reduce wear or RCF, namely through the optimization of the wheel profiles and vehicle suspension systems (Ignesti et al., 2013; Ye et al., 2020), or even through the control of the vehicle motion for improved operation conditions. A reliable computational study of the vehicle operation can also be adopted to improve the track performance in terms of damage control, that is, optimizing the track geometry, e.g. track curvature or cant. It must be emphasized that the study of damaging phenomena through numerical modeling

involves performing long time simulations, since the wear or crack evolution are slow processes, hence, it demands the development of computationally efficient methodologies that support their efficient use in operation design strategies.

1.2. Scope and Objectives

This work has been developed under the Leaders for Technical Industries (LTI) doctoral program within the Engineering Design and Advanced Manufacturing (EDAM) focus area of the MIT Portugal Program. The EDAM focus area was established in 2006, and its vision includes three main lines, i.e., integrated learning education, promotion of intellectual challenges and leadership. Bearing this mind, the LTI PhD program targets to develop projects in which innovation and entrepreneurship take a preponderant role, focusing on product and/or process development and taking into account economics, managements and social aspects. This program is recognized by generating new scientific knowledge and new engineering solutions to capture value in highly competitive industrial areas. Moreover, the program aims to graduate leaders for multidisciplinary teams which can face new and complex technological challenges and conduct research programs in industry environments.

Taking this into consideration, the main goal of this work is to develop a computational tool in which the contact between the wheel and rail is modeled in a realistic manner to study the dynamics of railway vehicles. Hence, it is expected that the developed methodologies are used to perform reliable simulations of railway vehicles that ultimately result in a reduction of time and costs during design and maintenance phases. The vehicle/track validation, design of components, assessment of vehicle performance and prediction of maintenance cycles are some of the potential applications of such computational tool.

In order to achieve the main purpose of this thesis, it is of paramount importance to divide it into specific objectives which establish the different steps to be followed. Thus, the subsequent goals have been outlined:

- to develop a computer code for efficient dynamic analyses of multibody systems, in particular railway vehicles;
- to define realistic wheel and rail contacting geometries;

- to develop an efficient and accurate strategy for the contact detection between realistic wheel and rail surfaces;
- to determine the contact patches resulting from the wheel-rail interaction for any given configuration;
- to calculate the normal pressure distribution in a conformal contact region without discontinuities;
- to establish Lookup Table methodologies to improve the efficiency of railway dynamic simulations.

The accomplishment of the defined objectives is demonstrated throughout this document. It must be highlighted that most of these achievements are associated to contributions to the state of the art of wheel-rail contact modeling.

1.3. State of the Art

The research and design of railway vehicles and infrastructures is a multidisciplinary field which involves very distinct areas as structural mechanics, vibrations, tribology, control theory, fluid mechanics or dynamics of mechanical systems. In that sense, the study of different phenomena associated with the track and the vehicle is often carried out independently, although, due to the development of more advanced computational models, cross-disciplinary investigations are increasingly required.

The use of computational methodologies is experiencing an increasing popularity in the railway field as they allow to save time and resources when compared to empirical tests, while allowing to obtain optimized performances since it is possible to investigate different designs or parameter changes with minor efforts. Simulation enables to inspect a wider range of input conditions, which would be impracticable to test in real scenarios, and to obtain data from the vehicle performance that are unattainable with the available measurement systems, namely contact forces magnitude and location (Urda et al., 2020a; Urda et al., 2020b), creepages, among others (Evans and Berg, 2009). It is observed that the areas with the most prominent development are the design of traction and braking systems, pantograph-catenary interaction (Bruni et al., 2018), noise and vibration, analysis of vehicle stability, development of active or passive suspension elements, vehicle aerodynamics, design of track geometry, and analysis of wheel-rail contact interaction. Most of these research areas, which have a strong

interdependence on the wheel-rail interaction, i.e., affect the nature of the contact forces and are influenced by the way of modeling those forces, are briefly discussed hereafter.

The study of train longitudinal dynamics is mostly concerning the motion of the train along the track direction which involves the interaction of different vehicles within the same train and traction and braking operations (Wu et al., 2016a; Cole et al., 2017). The longitudinal motion of the train highly influences the comfort and safety of the passengers, and it is affected by the control of the traction system in the locomotive, the braking control in all carriages, track characteristics, rolling stock attributes and connection between vehicles. Regarding the wagon connection systems, it is usually realized through draw gears or buffers (Wu et al., 2015; Wu et al., 2016b), which are responsible for transmitting tractive and braking forces. The control of the longitudinal velocity of vehicles assumes a crucial role on its stability and requires a reliable modeling of the traction and braking technologies, but it is also necessary to take into account the wheel-rail contact properties which limits the ability to generate those forces (Oprea et al., 2013). Once again, the aspects associated to the contact mechanics between the different mechanical elements condition the overall behavior of the interacting systems.

The modeling of suspensions components takes a preponderant role on the reliability of railway dynamics simulations, since these elements are responsible for the stability and vibration suppression of the vehicle during service (Facchinetti et al., 2010). Generally, a passengers' railway vehicle has a double-stage suspension system, in which the primary suspension connects the wheelsets to the bogie frame, being mostly responsible for its stability, and the secondary suspension, which links the bogie frame to the carbody, is responsible to suppress the high frequency oscillations. The suspensions are composed by a wide variety of elements with a different mechanical behavior, namely coil springs, leaf springs, rubber springs, air springs, hydraulic dampers, traction links, anti-roll bars and bump stops (Bruni et al., 2020). Although these components can be modeled in detail with a full description of material properties and physical phenomena, it may be computationally expensive to include such a detailed model in the dynamic analysis of the whole vehicle (Bruni et al., 2011). Therefore, more simplified models are usually adopted, which offer a similar response to the realistic ones. The number of trains with active and semi-active suspensions has been increasing over the last decades, since it represents an alternative to improve the riding comfort (Fu et al., 2020). This issue has a significant role on the control of tilting trains (Persson et al., 2009). The modeling approaches utilized to described the different mechanical components have a preponderant role on the contact mechanics between the wheel and rail, since they affect the magnitude and variations of those contact forces.

The investigation of the aerodynamics of railway vehicles have been gaining more attention last decades due to its importance on the vehicle performance with the increase of vehicles maximum speed. The development of high-speed trains increased the awareness to the growth of energy losses associated with drag forces, noise and vibrations and, hence, the enhancement of their aerodynamic performance allow a considerable improvement of efficiency and the corresponding reduction of fuel consumption. This decrease of aerodynamic drag forces can be achieved through modifications on the cross-sectional area, train length, shape of the train's vehicles, external surface roughness of the vehicle body and geographical aspects of the surrounding environment (Raghunathan et al., 2002). The aerodynamics performance in the presence of strong crosswinds is also relevant for the vehicle running safety (Carrarini, 2007), this issue improves the risk of overturning specially for long-span bridges, high-rise bridges and embankments. Moreover, the aerodynamic effects of two trains crossing each other, the wind induced by the train in the platforms and pressure variations in tunnels are other aspects to which has been given some attention. Besides the numerical simulation of the air flow field through computational fluid dynamics methods, the design of railway vehicles envisaging the aerodynamic performance is also conducted using scale models in wind tunnel experiments (Cheli et al., 2010). The phenomena of ballast projections, associated to the vehicle aerodynamics, due to air flow in high-speed trains, is a damaging phenomenon that can impair the operation of railway vehicles (Premoli et al., 2015). It must be noted that the aerodynamic forces developed affect in a great manner the contact loads generated in the vehicle-track interaction.

The railway track is responsible to guide the trains smoothly as possible, support the dynamic loads resulting from the wheel-rail interaction and transmit such loads to its foundation, which can be a subgrade, a bridge deck or a tunnel floor (Zhai, 2019). The traditional ballasted tracks are constituted by rails, rail pads, fasteners, sleepers, ballast and subgrade, while the ballastless or slab tracks, which are widely employed in modern high-speed lines and urban railways, use concrete slabs to replace the sleepers and ballast. Nowadays, the slab tracks have been replacing ballasted tracks, mainly when better performance is needed, since they show better stiffness uniformity, higher running stability, and lower maintenance costs (Bezan et al., 2010). In what concerns the numerical modeling of the track structure, the most simplified procedure is to consider it fully rigid. However, there are several different approaches to take into account its flexibility, i.e., lumped-mass model, finite element method, boundary element method, discrete element method, continuous beam method, among others (Zhai et al., 2009; Costa et

al., 2020a). Only the accurate modelling of track dynamic behavior allows to assess reliably the vehicle's running safety and ride comfort, therefore, those aspects must be considered into the track design stage.

The wheel-rail contact interaction plays a fundamental role on the railway vehicles dynamics, since the contact forces generated are responsible to guide the vehicle, i.e., balance the centrifugal force during curve negotiation and to promote traction and braking forces. The contact is normally observed between steel rails and steel wheels, which makes it very stiff yielding small contact patches, around 1 cm^2, varying according the contact location and normal load magnitude. Thus, the accurate modeling of the wheel-rail contact is fundamental to analyze the dynamic response of the vehicle for any running conditions, requiring to take into account several complex phenomena that occur during contact, namely the local surfaces' deformation, the variation of profile curvature, the shape of contact region, the surfaces' adhesion or the relative motion between wheel and rail in the contact zone (Kalker, 1990; Meymand et al., 2016). Besides the effects on the vehicle performance, the wheel-rail contact forces also contribute for several tribological phenomena that affects the deterioration of both contacting surfaces, as wear, plastic deformation or rolling contact fatigue. The wear leads to loss of material due to the sliding between both surfaces, and these modifications on the contact profiles produce new types of contact patches and pressure distribution configuration since they result in different relative positions (Enblom, 2009). Although the changes on the profiles may enhance or decrease the train dynamic performance, they normally yield more conformal contacts and higher wear rates which demand maintenance operations. The wheel-rail contact produces high loads in small contact areas, which contributes to the presence of high normal contact pressures, emphasized when the gauge corner of the rail contacts the wheel flange resulting in an even smaller contact area, higher pressure eventually surpassing the material yield strength. This tends to occur during curve negotiation and its cyclic repetition leads to the plastic deformation of the rail surface and, consequently, modification of the wheel-rail contact geometry. Due to the cyclic loading, rolling contact fatigue cracks tend to develop on both rail and wheel surfaces. A proper contact modeling technique is required to predict the appearance and growth of the crack (Ekberg et al., 2014; Zhao et al., 2020) and to mitigate its damaging effects.

In a dynamic simulation of railway vehicles, in the time domain, the numerical modelling of the contact between wheel and rail is usually the bottleneck in terms of computational efficiency. Solving the contact problem involves several numerical procedures that are time consuming, on one hand, while the high stiffness of the contact forces tends to reduce the time step adopted in the integration process, which slows the computational procedure, in the other hand. To solve the contact problem between a wheel

and a rail, three main steps are always required, videlicet, the contact detection procedure, the calculation of normal contact force and identification of contact area, and the calculation of tangential forces due to contact creepages. First, the search for the contact points' location requires a pre-processing of the geometry of the wheel and rail profiles, which is commonly simplified to promote computational efficiency of this procedure. This is achieved by avoiding the wheel transition fillet or consider only the planar profiles instead of three-dimensional surfaces. Generally, the contact detection can be performed considering an elastic or constraint approach in which the bodies can locally deform or be fully rigid. The constraint approach also involves the pre-processing of the contact location for several wheel-rail relative positions, which are stored in lookup tables. In what the normal contact force is concerned, the complexity of the contact model is normally associated with the determination of the contact patch shape. The most simplified and fastest approach, known as Hertzian approach, is to consider that all contact patches assume an elliptical shape, being the size of the ellipse calculated based only on the curvatures of the contact point previously identified. The normal force magnitude may depend on the surfaces' penetration, for the elastic approach, or on the reaction forces obtained from the equations of motion, for the constraint approach. More advanced models that take into account the neighborhood of the main contact point can be also employed, avoiding some numerical discontinuities and providing more realistic results in terms of contact area, although they are generally more time-consuming. Regarding the evaluation of the tangential tractions, there is a strong dependence on the contact creepages, i.e., the relative velocities between the wheel and rail surfaces on the contact points. These creepages are given by three non-dimensional quantities, namely the longitudinal, lateral and spin creepages. The longitudinal and lateral creepages represent the tangential relative slip between surfaces in the rolling and lateral directions, respectively. The spin creepage expresses the angular slip velocity around the normal vector on the contact point, which is normally not null due to the typical conicity of the wheel surface which makes that the wheel contact angle, i.e., the angle between the wheel axis and the plane where the contact patch lies, is also not null. This creepage has a significant impact on the generation of lateral creep forces and tends to assume higher values when the contact point moves towards the wheel flange, where the contact angle is higher. Thus, the contact creepages produce longitudinal and lateral creep forces, which are fundamental for the vehicle guidance and overall wheel-rail contact phenomena, and a spin moment which has, in most cases, small magnitude and it is often neglected. To compute the creep forces, there are several approaches that approximate the contact patch by an ellipse, which complies with Hertzian theory. The Kalker linear theory allows to calculate the exact values of creep forces for an infinite

coefficient of friction, which would enforce adhesion in the whole patch. However, due to the friction limit, the contact patch cannot be fully adhesive, unless creepages are null. Therefore, for small creepages, the contact patch is partially adhesive, near to the leading edge, and partially sliding, near the trailing edge. For high creepage values, the contact area might be in full slip state. Bearing this in mind, there are several simplified models that allow to consider the saturation of the frictional force. More demanding methodologies can be employed to solve the tangential problem as the finite element method or boundary element method (Kalker, 1990), although they are not suitable to be employed in dynamic simulations.

The advances of computational capacity promote the development of more sophisticated analyses in the context of railway dynamics. The multibody models are now more complex with the elimination of several simplifications implemented in the past to ensure their feasibility. Among these elements of increased complexity, the contacting geometries, the use of linear force elements, the suppression of some components with minor influence are highlighted. The railway dynamics involves a wide range of areas of knowledge, therefore, there is a trend and, simultaneously, a challenge, to establish multi-physics simulations. This normally involves a co-simulation procedure, which couples the multibody simulation of the vehicle with different solvers, that allows a multidisciplinary study as, for instance, control of the wheels' rotation (Perez et al., 2013), optimization of vehicle properties (Mousavi-Bideleh and Berbyuk, 2016), evolution of profiles' wear (Bosso and Zampieri, 2020), flexibility of railway track (Olivier et al., 2020), pantograph-catenary interaction (Antunes et al., 2020), control of active suspensions (Kozek et al., 2011) or aerodynamic effects (Li et al., 2013).

The recognized reliability and efficiency of modern multibody simulation software makes them fundamental design and analysis tools for vehicles manufacturers, infrastructures companies, consultants, operators and research entities. The main goals associated to the use of these computational models consist in improving the design process and reducing the physical testing activities, which still represent a significant cost in the design process. Due to the potential knowledge of multibody simulation of railway vehicles, most of the recently developed standards and guidelines envisage their application as part of the vehicle authorization process (Polach and Evans, 2013). The degree of confidence on the virtual homologation of vehicle varies according to each standard or design guidelines. For instance, the European standard EN 14363:2016 allows the use of computational simulations for the vehicle acceptance in four situations, namely the extension of the range of test conditions, approval of a vehicle subsequent to a modification, approval of a new vehicle through the comparison with an already approved similar vehicle and investigation of the dynamic behavior in the event of components' failure (Polach et

al., 2015). One of the main concerns associated with the use of multibody simulations in the acceptance of railway vehicles deals with the model validation, that is, the assessment of the accuracy of the computational model to represent the physical prototype regarding the intended purpose. The model validation is done by comparing the model simulations with the physical prototype on-track test results. However, there is an absence of quantitative criteria to perform an objective assessment of the model accuracy, which requires an evaluation from an independent reviewer to attest its validation. Some works have been recently developed in the sense of providing general methodologies to assess the validity of computational models of railway vehicles (Polach and Böttcher, 2014; Polach et al., 2015; Götz and Polach, 2018) and some dedicated European projects have been strongly funded for the same purpose (PantoTRAIN, AeroTRAIN and DynoTRAIN).

The real performance assessment of railway vehicles and tracks is of paramount importance for their design being the validation of their computational models an important part of the assessment. Bearing that in mind, the testing and monitoring of railway vehicles, or their components, can be done recurring to diverse techniques, that is, laboratory tests, wayside measuring systems and on-board measuring systems. The components characterization, conducted on the laboratory with small or medium test rigs, identifies the components response to several working condition. This is typically applied to the suspension elements (Jin et al., 2020). The structural testing of the vehicle components is also performed in the laboratory recurring to strength, fatigue and crashworthiness tests. After the assembly of the vehicle, this is tested statically or quasi-statically to find parasitic or secondary effects of the suspension components that appear from the combination of several individual components. The on-track measurements of the vehicle dynamic behavior have two distinct purposes: the validation of computational models, and the acceptance of a new vehicle design. In terms of model validation, the field testing required is linked with the purpose of using the model (Polach et al., 2015). In the case of vehicle acceptance, the tests must be in agreement with the standards imposed by a given country or company, and the vehicle needs to meet all the specified criteria in terms of ride comfort or running safety. Moreover, it is also necessary to realize the measurement of the track geometry (Andani et al., 2016), and the wheel and rail profiles. These measurements allow, on the one hand, to monitor the deterioration of these components and, on the other hand, to accurately characterize the irregularities on the track and the wear on the profiles not only to plan maintenance actions but also to increase the reliability of computer simulations. In what concerns to the railway vehicles testing, the use of roller rigs is of central importance, since they allow to test vehicles in running conditions without requiring line tests (Jaschinski et al., 1999;

Zhang et al., 2002; Allotta et al., 2010). Some of their advantages consist in not being affected by weather conditions, allowing to study an individual phenomenon and its variations being their experiments reproducible. All these experimental measurement techniques are also important to collect data that is used in the development of numerical modeling methodologies, which improves the reliability of such methodologies.

1.4. Organization of the Thesis

This thesis focuses on the development and implementation of numerical methodologies for the accurate and efficient evaluation of the wheel and rail contact interaction. It includes the detection of contact points between wheels and rail, the evaluation of normal pressure, the calculation of creep forces and the performance of dynamic analysis. With those general objectives, this document is divided into seven chapters.

The first chapter provides the motivation and background to develop this research work and, in that context, the state-of-art of railways dynamics field is introduced here. Also, the main objectives of this work are listed, and the novel contributions are highlighted.

In Chapter Two, a literature review of the main methodologies associated with the modeling of wheel-rail contact in the context of dynamic analysis is presented. The multibody dynamics formulation applied in this work is revisited, as well as the existing approaches for modeling railway vehicles and tracks. The methodologies to deal with the geometric description of the contact surface and the detection of their contact points are also identified. An overview of the evolution of contact models for the assessment of both normal and creep forces is provided. Then, the application of Lookup Tables approaches in the context of the wheel-rail contact in railway dynamics is discussed.

Chapter Three focuses on the main geometric aspects of the wheel-rail interaction with particular emphasis on the contact detection strategies. The wheel and rail are mathematically described as parametrized surfaces, namely the wheel is treated as a solid of revolution of a planar profile with an angular and a lateral parameter while the rail is considered as an extruded surface of another planar profile with a longitudinal and a lateral parameter, being their parametrization presented in detail. Simplifications of the wheel profile to avoid the transition zone and computational difficulties, which considers a fully convex surface are discussed. The minimum distance method is described and its

limitations to the contact detection of real wheel and rail profiles are demonstrated. Then, a novel alternative approach to search the contact between general wheel and rail profiles is proposed.

Chapter Four focuses on the contact mechanics of wheel-rail interaction, namely on the identification of the contact patch and on the identification of its associated normal pressure distribution. A simple Hertzian-based contact model is considered, as well as the semi-Hertzian contact models proposed by Kik and Piotrowski (1996) and Sun et al. (2018). The conformal contact is also addressed through the use of a curved surface to contain the contact patch, instead of the commonly used planar contact patches. Finally, several static wheel-rail interaction scenarios are utilized to discuss the advantages and limitations of the current and novel approaches presented in this work.

In Chapter Five, the use of Lookup Tables, in the context of wheel-rail interaction, is studied. A LuT for the evaluation of creep forces and moment is revisited and further improved. Then, a methodology for the assessment of LuT accuracy is presented, which consist of an analysis of the variation of the input parameters and the evaluation of the interpolation error in the cells and edges of the LuT. Resorting to the outcomes of this methodology, novel configurations for the LuT are proposed, either with lower size or with higher accuracy.

Chapter Six includes the multibody dynamic simulations of railway vehicles in order to assess the performance of the methodologies presented in this work. The multibody model of ML95 trailer vehicle is used as illustrative application case, and several running scenarios are applied to demonstrate the effectiveness of the contact detection and force evaluation methodologies proposed in this work. These dynamic analyses allow to compare the application of real and simplified wheel profiles, and the implementation of the curved contact patch approach to better describe the contact mechanics between wheel and rail. Moreover, the LuT for evaluation of creep forces are also employed and discussed in face of using other methods for the contact forces evaluation. The results are analyzed through the dynamic response of the vehicle, as well as in terms of the computational efficiency.

Finally, in Chapter Seven, the most relevant conclusions of the present work are outlined. Selected lines of research are proposed for future investigation on the field of contact mechanics for wheel-rail interaction.

1.5. Novel Contributions of the Thesis

This PhD thesis provides a general methodology to model wheel-rail contact in the context of railway vehicle dynamic simulations. Several aspects of the contact modeling are investigated, namely the geometries definition, the contact detection, the contact patch determination and the normal and tangential forces calculation. In addition, some of these tasks substantiate contributions to the state of the art in the railway field.

In what concerns the detection of contact resulting from the wheel-rail interaction, a general three-dimensional procedure to deal with general wheel and rail profiles is provided. This technique allows to determine the contact points for any relative configuration of the wheel with respect to the rail, without any simplification of the contacting geometries. This methodology shows that the simplification of the wheel's profile affects the dynamic response of the vehicle.

The modeling of conformal contact is tackled in this work, and a methodology to identify the normal contact patch and its corresponding pressure distribution is proposed. This model does not assume a planar contact region, as current models, in turn, the contact patch lies on a curved surface obtained from the wheel and rail geometries on the interference region. Therefore, there is a variation of contact angle along the contact patch which is a novel understanding of the contact phenomena. This approach allows to avoid the presence of unrealistic discontinuities on the evaluation of the normal contact forces that arise from the use of planar contact patches.

A technique to assess the accuracy of a given LuT with multiple inputs is provided. This includes the analysis of variation of input variables and calculation of the interpolation error at the center of the cells and at the middle of the edges. This analysis allows to identify the major sources of the interpolation error and mitigate them by rearranging the LuT domain. This strategy is applied to a LuT that computes the creep forces and creep moment based on CONTACT software. These developments support the use of more accurate LuT for the wheel-rail contact while maintaining its computational cost, or alternatively, to maintain their current accuracy while decreasing significantly their computational costs. The novel developments in the generation of wheel-rail contact LuT are significant advances to the current state-of-art in railway dynamics simulations.

"*If you can't explain it to a six year old, you don't understand it yourself.*"
Albert Einstein

2. LITERATURE REVIEW

In the context of railway dynamics, the wheel and rail contact problem is a fundamental part of the study of the whole system (Meymand et al., 2016). The computational simulation of the dynamic behavior of a railway vehicle requires the development and solution of a mathematical model suitable to describe the system. During the early age of railway vehicles, the problems of interaction between the vehicle and track were addressed using empirical approaches. The collapse of Stephenson's bridge, across the River Dee at Chester, in 1847 led to the development of the first analytical model of a vehicle interacting with a flexible track (Iwnicki, 2006). Although this model was based in a substantial number of assumptions, it marked the beginning of the mathematical analysis of railway dynamics which has continued and developed to this day. This chapter presents an overview of the existing literature for several issues related with vehicle-track interaction, its dynamic analysis and methods used for the purpose.

2.1. Multibody Dynamics

Multibody dynamic methodologies are the most powerful and common approaches to handle the general railway dynamics problems. A general multibody mechanical system, as depicted in Figure 2.1, can be seen as collection of bodies, constrained by kinematic pairs and acted by generalized forces, that can describe large relative translations and rotations (Nikravesh, 1988; Haug, 1989; Schielen, 1997). The simplest element on a MBS is the free particle for which the laws of motion derived by Newton (1686) describe its dynamical behavior. Later, Euler (1776) extended this description to include the rotational motion enabling the analysis of the dynamics of a free body. A system with constrained rigid bodies was first considered by D'Alembert (1743) to present the concept of dynamic equilibrium derived from the principle of virtual work. Then, Lagrange (1788) used a formulation based on energy balance to derive the system equilibrium equations in the form of the Lagrange's equations of first and second kind. The equations of first kind represent a set of differential algebraic equations (DAE) which treats the constraints explicitly,

while the equations of second kind express a set of ordinary differential equations (ODE). At that point, the study of MBS dynamics was only possible for very simple systems or resorting from significant simplifications. The available computational power just allowed to consider the study of more complex systems a few decades ago. Thus, the field of multibody dynamics evolved ever since computer power became more available enabling the development of more efficient methodologies, while decreasing the simulation time and allowing the inclusion of more complex phenomena to make the analyses more realistic.

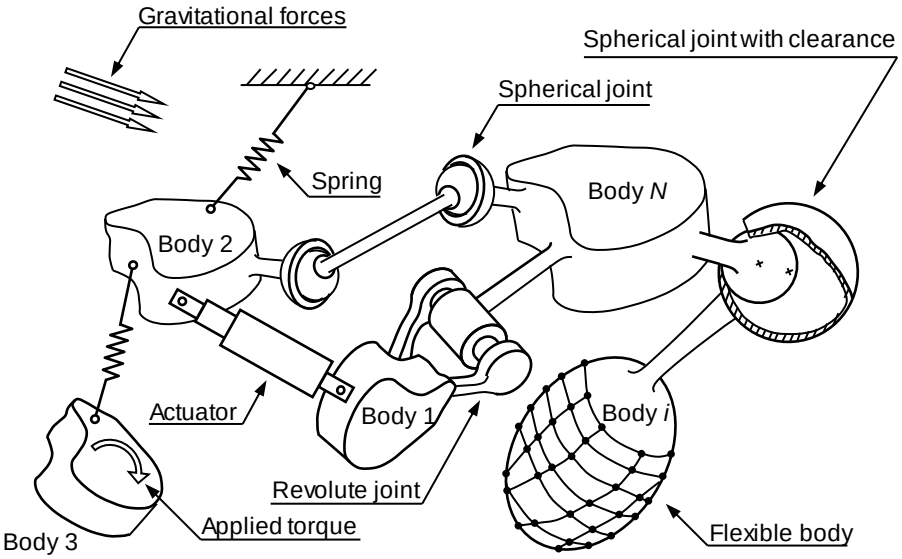

Figure 2.1 – Schematic abstract representation of a general multibody system with the most representative elements, namely bodies, joints and forces.

The evolution of the field of multibody dynamics led to the development of several formulations mostly associated to the type of coordinates used (Eberhard and Schielen, 2006; Flores, 2015; Nikravesh, 2019). In this work, it is considered a body-coordinate formulation, or absolute coordinates, in which each body is represented by six coordinates made of three translations and three rotations, which are known as Cartesian coordinates. Although this formulation requires the construction of a large system of equations since an equilibrium equation is necessary for each coordinate, being the system augmented with the existing constraint equations, it involves a very straightforward and systematic implementation in computer codes. Alternatively to this formulation, another type of Cartesian coordinates known as point-coordinate formulation or several types of joint-coordinate formulations can also be employed. The point-coordinate formulation, also known as natural coordinates, treats the system as a collection of interconnected points, being the major difference from the body coordinates the absence of any rotational coordinates. In the point-coordinate formulation, the total number of equations is similar to the body-coordinate formulation, however, most of the constraints arise naturally from the definition of the bodies rather than from the kinematic joints.

The joint-coordinate formulation, or relative coordinates in short, can be used to produce a smaller set of equations that is generally associated to the number of degrees of freedom of the mechanical system, but at the cost of an higher nonlinearity of the system and of a more complex implementation. Hence, this formulation becomes more efficient from the computational point of view in open-chain systems, but presents shortcomings for closed-loop systems.

The bodies that comprise the multibody system represent the mechanical components and can be considered either rigid or flexible. In a rigid body, the degrees of freedom are only associated to its translation and rotation, while, in a flexible body, additional degrees of freedom are considered associated to its deformation. Since the modeling of flexible bodies significantly increase the computational cost of a dynamic simulation, it must be considered only if their deformations have impact on the response of the system. In most applications, the assumption of rigid bodies is a reasonable modeling choice. The angular position of a rigid body can be defined by three successive rotations using, for instance, Euler angles or Bryant angles. However, the description of a rigid body orientation by three coordinates produces singularities for some configurations of the bodies which lead to computational difficulties. In order to avoid singularities, in the context of this work, the angular orientation of a rigid body is defined using Euler parameters (Nikravesh, 1988). This formulation allows the angular representation based on Euler's theorem on finite rotation, which expresses that any rotation in the three-dimensional space can be described by a rotation over a given axis of a certain angle. Thus, the vector of generalized coordinates for a given body i can be expressed by seven coordinates as

$$\mathbf{q}_i = \left\{ \mathbf{r}_i \;\; \mathbf{p}_i \right\}^{\mathrm{T}} \tag{2.1}$$

in which $\mathbf{r}_i$ represents the vector of the translational coordinates of body i in global coordinates, given by

$$\mathbf{r}_i = \left\{ x_i \;\; y_i \;\; z_i \right\}^{\mathrm{T}} \tag{2.2}$$

and $\mathbf{p}_i$ denotes the vector of Euler parameters for body i and can be written in the following form

$$\mathbf{p}_i = \left\{ e_0 \;\; e_1 \;\; e_2 \;\; e_3 \right\}^{\mathrm{T}} = \left\{ \cos\frac{\phi}{2} \;\; \mathbf{u}_{\mathrm{e}} \cos\frac{\phi}{2} \right\}^{\mathrm{T}} \tag{2.3}$$

where ϕ is the angle that the body must be rotated about the unique axis represented by the unit vector $\mathbf{u}_{\mathrm{e}}$ so that its reference frame would be parallel to the global reference frame. Although the utilization of Euler parameters involves four coordinates to describe the orientation of the body, the number of independent coordinates remains three since the constraint that $\mathbf{p}_i$ is a unit vector must be imposed.

In what concerns to the generalized velocities and accelerations, the problem of singular positions does not exist, therefore, the concept of angular velocity can be employed. Thus, the generalized velocities vector of a rigid body can be written as

$$\mathbf{v}_i = \left\{ \dot{\mathbf{r}}_i \;\; \boldsymbol{\omega}_i \right\}^{\mathrm{T}} \tag{2.4}$$

in which $\boldsymbol{\omega}_i$ denotes the vector of angular velocities of body *i*. Hence, the generalized accelerations vector is defined as the time derivative of Eq. (2.4).

The joints of a mechanical system are generally responsible to connect the different bodies by constraining their relative motion. The joints assume different functions due to their topology, thus, they can be spherical, revolute or prismatic among many other types. Depending on the degree of accuracy required, the constraints can be modeled as ideal joints or imperfect joints. The former simply treat the joints as kinematic relations between the connecting bodies, while the latter may reproduce realistic phenomena of the joint which can include local deformations, wear, clearance, friction, lubrication, just to mention a few (Tian et al., 2018).

The ideal joints are mathematically described by a set of kinematic constraint equations in which the number of independent equations expresses the number of constrained degrees of freedom. The kinematic constraints can be classified as holonomic or nonholonomic, whether or not they can be integrable into a form involving only coordinates, respectively, constraints are also classified as rheonomic or scleronomic, whether or not they are explicitly a function of time, respectively. Thus, in a constrained multibody system, the set of holonomic constraint equations can be written as follows

$$\boldsymbol{\Phi} \equiv \boldsymbol{\Phi}(\mathbf{q}, t) = \mathbf{0} \tag{2.5}$$

in which $\mathbf{q}$ denotes the vector of the generalized coordinates of the system and t is the time variable. Then, Eq. (2.5) can be differentiated with respect to time producing the velocities constraint equations as

$$\dot{\boldsymbol{\Phi}} \equiv \mathbf{D}\mathbf{v} - \boldsymbol{\upsilon} = \mathbf{0} \tag{2.6}$$

where $\mathbf{D}$ is the Jacobean matrix of the constraint equations, $\mathbf{v}$ denotes the vector of the generalized velocities of the system and $\boldsymbol{\upsilon}$ represents the right-hand side of the velocities constraint equations which is null for the scleronomic constraints, since it holds the partial derivatives with respect to time. Differentiating Eq. (2.5) twice with respect to time, the constraint equations at acceleration level are obtained as

$$\ddot{\boldsymbol{\Phi}} \equiv \mathbf{D}\dot{\mathbf{v}} - \boldsymbol{\gamma} = \mathbf{0} \tag{2.7}$$

in which $\dot{\mathbf{v}}$ is the vector of generalized accelerations of the system and $\boldsymbol{\gamma}$ is right-hand side vector of the acceleration constraint equations which contains the quadratic velocity terms and the terms that are solely function of velocity, position and time.

The equations of motion of a multibody system can be derived according to three main methodologies, namely the Newton-Euler's method, Lagrange's method, and Kane's method. Since the three approaches are equivalent, the Newton-Euler equations were adopted for this work due to its straightforwardness in terms of implementation and assemblage of the equations of motion for a general multibody system. The Newton-Euler equations relate the motion of the center of mass of the rigid bodies with the forces and moments acting upon them, and can be written as

$$\mathbf{M}\dot{\mathbf{v}} = \mathbf{g} + \mathbf{g}^{\mathbf{c}} \tag{2.8}$$

where $\mathbf{M}$ represents the mass matrix of the global system which results from the concatenation of the mass matrix of each body as

$$\mathbf{M} = \begin{bmatrix} m_1\mathbf{I}_{3\times3} & \mathbf{0} & & & & & & \\ \mathbf{0} & \mathbf{J}_1 & & & & & & \\ & & \ddots & & & & & \\ & & & m_i\mathbf{I}_{3\times3} & \mathbf{0} & & & \\ & & & \mathbf{0} & \mathbf{J}_i & & & \\ & & & & & \ddots & & \\ & & & & & & m_N\mathbf{I}_{3\times3} & \mathbf{0} \\ & & & & & & \mathbf{0} & \mathbf{J}_N \end{bmatrix} \tag{2.9}$$

in which m denotes the mass of the body and $\mathbf{J}$ is the respective inertia tensor. In Eq. (2.8), $\mathbf{g}$ is the vector of external generalized forces and gyroscopic moments, given as

$$\mathbf{g} = \begin{Bmatrix} \mathbf{f}_1 \\ \mathbf{n}_1 - \tilde{\boldsymbol{\omega}}_1\mathbf{J}_1\boldsymbol{\omega}_1 \\ \vdots \\ \mathbf{f}_i \\ \mathbf{n}_i - \tilde{\boldsymbol{\omega}}_i\mathbf{J}_i\boldsymbol{\omega}_i \\ \vdots \\ \mathbf{f}_N \\ \mathbf{n}_N - \tilde{\boldsymbol{\omega}}_N\mathbf{J}_N\boldsymbol{\omega}_N \end{Bmatrix} \tag{2.10}$$

where $\mathbf{f}$ expresses the sum of the external forces acting on the origin of the body fixed frame, $\mathbf{n}$ is the sum of the external moments acting on a body, and $\tilde{\boldsymbol{\omega}}\mathbf{J}\boldsymbol{\omega}$ is the term that represents the gyroscopic

moments. Vector $\mathbf{g}^{\mathrm{c}}$ denotes the reaction forces and moments on the kinematic joints in the global coordinate system. In an unconstrained multibody system, $\mathbf{g}^{\mathrm{c}}$ is null. Using the Lagrange multipliers technique, the vector of reaction forces is expressed as a function of the Jacobian matrix of the constraint equations and the vector of Lagrange multipliers in the form

$$\mathbf{g}^{\mathrm{c}} = -\mathbf{D}^{\mathrm{T}}\boldsymbol{\lambda} \tag{2.11}$$

where $\boldsymbol{\lambda}$ denotes the vector of the Lagrange multipliers, being its size equal to the number of holonomic constraints, since each element is associated to the reaction force/moment imposed by each kinematic constraint.

The dynamic equations of a constrained multibody system can be obtained by introducing Eq. (2.11) into Eq. (2.8), which can be gathered with acceleration constraint equations given by Eq. (2.7) as

$$\begin{bmatrix} \mathbf{M} & \mathbf{D}^{\mathrm{T}} \\ \mathbf{D} & \mathbf{0} \end{bmatrix} \begin{Bmatrix} \dot{\mathbf{v}} \\ \boldsymbol{\lambda} \end{Bmatrix} = \begin{Bmatrix} \mathbf{g} \\ \boldsymbol{\gamma} \end{Bmatrix} \tag{2.12}$$

This system of DAE of index-1 represents the system's equations of motion and it can be solved for the generalized accelerations vector and the Lagrange multipliers vector (Eich-Soellner and Führer, 1998; Ilchmann and Reis, 2017; Pappalardo and Guida, 2018; Pappalardo et al., 2020). Then, the motion of the multibody system can be achieved through the time integration of the velocities and accelerations observed in each time step to obtain the new positions and velocities, respectively.

In what concerns to the wheel-rail interaction, the contact forces can be included into the equations of motion in different manners depending whether a constraint approach or an elastic approach is employed. In the former, the contact between the wheel and rail is expressed in terms of kinematic constraints and the normal contact forces are obtained as reaction forces, while, in the latter, the contact forces are included in the vector of external loads acting upon the wheelsets. More details on these modeling approaches are given in the following sections of this work.

The solution of Eq. (2.12) allows to determine the accelerations of the system in each time step, but it does not ensure that the positions and velocities constraints are satisfied, since they are not explicitly included into the equations of motion. Thus, the error introduced by the numerical integration procedure leads to the violation of both positions and velocities constraint equations (Bauchau and Laulusa, 2008; Marques et al., 2017). There are several methods to handle the problem of constraints violation which fall into three main categories, namely the constraint stabilization approaches, the coordinate partitioning methods and the direct correct formulations. The constraint stabilization approaches do not fully eliminate

the violations but allow to keep their values under control (Baumgarte, 1972; Park and Chiou, 1988). These approaches are very straightforward in terms of formulation and implementation which make them very popular, as long as their stabilization parameters are suitably chosen (Flores et al., 2011). Regarding the coordinate partitioning methods, they require that the system's coordinates to be divided into independent and dependent ones (Wehage and Haug, 1982; Nikravesh and Haug, 1983; Neto and Ambrósio, 2003). Thus, the integration process can be performed only on the set of independent coordinates and the dependent ones can be then accurately calculated using the constraints equations. However, these methods can present some numerical inefficiency when, for particular system's configurations, it is necessary to change the independent coordinate set during the dynamic simulation. Finally, the direct correct formulations are employed to correct a set of coordinates obtained after the integration process, hence, they adjust the values of the state variables so they can satisfy the constraint equations (Bayo et al.,1988; Blajer, 2002; Marques et al., 2017). Their drawback is that the several corrections introduced are perceived by the integrator as high frequency perturbations leading to an adjustment of the time step of the integrator.

In the context of this work, the Baumgarte stabilization technique is employed to keep the violation of the constraints under acceptable values (Baumgarte, 1972). In this constraint stabilization approach, the acceleration constraint equations are modified in order to include two additional terms for the feedback control of positions and velocities constraints violation. Thus, Eq. (2.12) can be rewritten as

$$\begin{bmatrix} \mathbf{M} & \mathbf{D}^{\mathrm{T}} \\ \mathbf{D} & \mathbf{0} \end{bmatrix} \begin{Bmatrix} \dot{\mathbf{v}} \\ \boldsymbol{\lambda} \end{Bmatrix} = \begin{Bmatrix} \mathbf{g} \\ \boldsymbol{\gamma} - 2\alpha\dot{\boldsymbol{\Phi}} - \beta^2\boldsymbol{\Phi} \end{Bmatrix} \tag{2.13}$$

where α and β are positive values that represent the feedback control parameters for the velocity and position constraint violations, respectively.

The numerical aspects of the resolution of the equations of motion must be taken into consideration. Thus, the choice of the integration algorithm plays an important role in the efficiency of dynamic simulations, especially when dealing with stiff systems, i.e., systems for which the dynamic response exhibit high and low frequency contents. The use of time integrators with variable time step is the most common and suitable choice for problems with contact-impact events, since the accurate determination of the starting and ending instant of the contact is of paramount importance. Among these, those dealing with stiff equations are preferred to handle the fast dynamics of the contact problem.

2.2. Vehicle and Track Modeling

In order to perform multibody dynamics simulations of a railway vehicles, it is necessary to characterize the vehicle and track models. Initially, due to computational limitations, the research tools were devoted to the understanding of simple phenomena of vehicle dynamics, namely stability, curving behavior or ride quality (Evans and Berg, 2009). For this purpose, the vehicles were modeled resorting to coarse simplifications which were, sometimes, unable to represent the real vehicle performance. The major advances on this research field led to the application of railway vehicle simulations in specialized design tools for the assessment and optimization of their performance in an early stage of the design process. Hence, the multibody simulations have been used as a complement of the experimental testing, allowing the assessment of the train performance for selected operation conditions. This approach, already used in the framework of virtual homologation, evaluates the running safety and riding comfort of the vehicles (Wilson et al., 2011). This requires the utilization of computational models with high reliability to faithfully reproduce the actual behavior of the components.

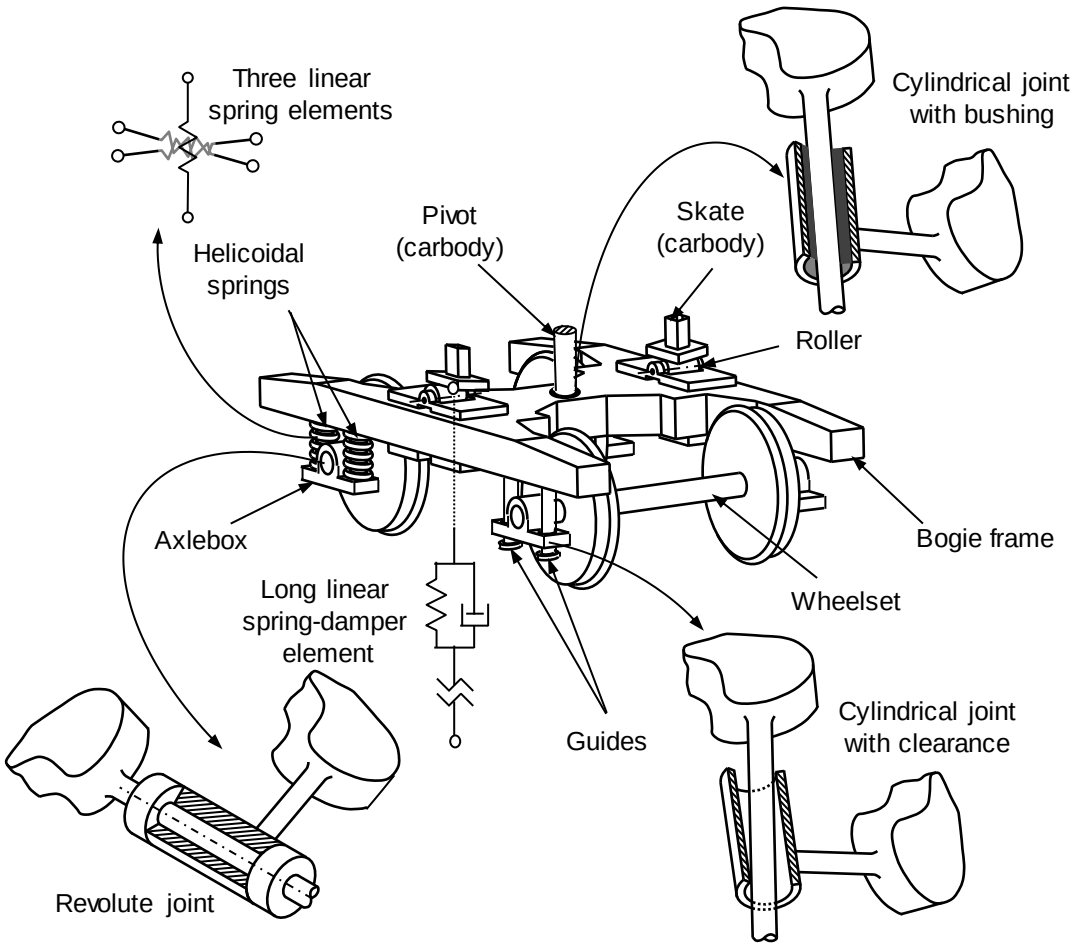

Figure 2.2 – Schematic representation of a train bogie (Magalhães et al., 2016b).

A generic train carriage consists of the carbody, where the passengers and cargo are transported, the bogies frames, which are connected to the carbody by several mechanical elements forming the secondary suspension, and the wheelsets, which are coupled to the bogie frame through the primary suspension, as schematized in Figure 2.2. A good part of the accuracy of the vehicle dynamic model is associated with the wheel-rail contact model, which is discussed in detail in this work, and to the suspensions' model (Bruni et al., 2011). In most cases, the remaining components of the train are considered to be rigid bodies and, holding most of the mass of the vehicle, namely the carbody, bogie frames and wheelsets. Thus, such mechanical components are defined through their mass, inertia tensor and center of mass location. Moreover, either for passenger train or freight train, it is important to consider not only their structural inertia but also the mass and inertia of the interior cargo, since it affects significantly the vehicle dynamics (Iwnicki, 2006). Nevertheless, when studying the behavior of a railway vehicle subjected to interaction that excite its high frequencies, the flexibility of these components is required, namely for the carbody (Sun et al., 2016) or for the wheelsets (Fang and Bruni, 2019). Note that it has been demonstrated that considering a flexible wheelset, through a 3D finite element model, affects the predicted hunting motion of the vehicle (Kaiser and Popp, 2006; Kaiser, 2012).

Mechanical components of a system are connected by coupling elements whose mathematical models can range from simple linear springs to very complex and sophisticated models (Eickhoff et al., 1995; Bruni et al., 2011). The degree of complexity of the modeling techniques for the coupler between different subsystems, such as two adjacent cars and for both primary and secondary suspensions, highly affects the reliability of the simulation results. The selection of appropriate values for the stiffness and damping coefficients of these elements, as well as the location of their attachment points, is fundamental for obtaining a valid model which leads to a correct dynamic response of the vehicle. It has been shown that the lateral stability of the vehicle is significantly influenced by the suspension parameters (Lee and Cheng, 2005; Wilson et al., 2010). Moreover, the modeling of components, such as air-springs, yaw dampers, rubber bushings, antiroll bars, among others (Facchinetti et al., 2010; Bruni et al., 2011; Magalhães et al., 2016b), require the understanding of the physical behavior of these parts and knowledge in different areas of solid mechanics, fluid mechanics and tribology. Three simple nonlinear models of coupling components of a railway vehicle suspension are exemplified in Figure 2.3 (Ling et al., 2014). Due to the large impact of suspension characteristics on the vehicle dynamic response, Magalhães et al. (2016a) and Cheng and Hu (2015) developed numerical techniques for the optimization of the suspension parameters to improve the vehicle dynamic performance, actually showing that even simple

coupling models can be used with advantage to achieve better designs or improved operation characteristics.

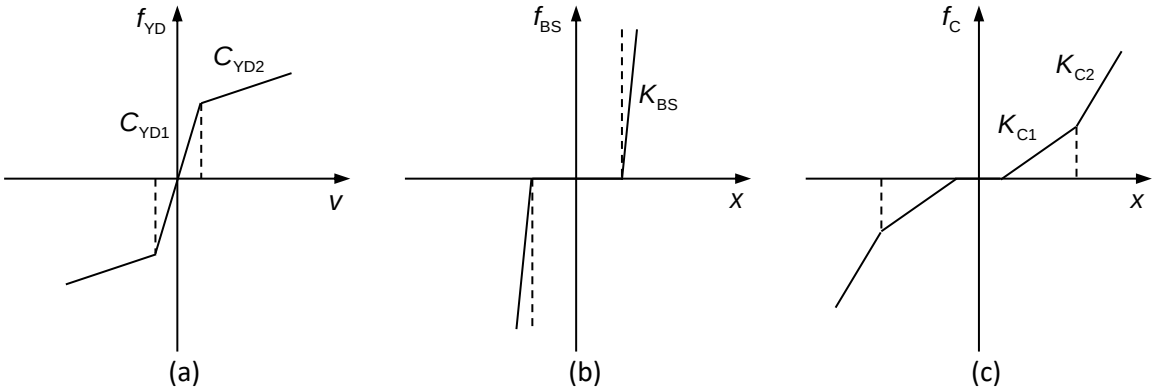

Figure 2.3 – Example of nonlinear models for train components: (a) Yaw damper, (b) Bump-stop, and (c) Coupler.

Nowadays, tools based on control theory are increasingly important for the modelling of railway vehicles, since most trains include actuator elements which are utilized to improve the vehicle performance (Bruni et al., 2007; Goodall, 2011). The use of active suspension systems presents several advantages as to promote higher speed by improving ride quality and reducing vehicle-track interaction hazards (Hedrick, 1981; Goodall et al., 2014). Moreover, the tilting trains consists of a paradigmatic example of employment of control theory on railway technology. In these trains, the roll motion is actively controlled to allow the vehicle to negotiate curves at higher velocity, for that the roll angle of the carbody is increased inwards relatively to the curve which reduces the lateral acceleration felt by the passengers (Zolotas et al., 2007; Persson et al., 2007). Finally, the longitudinal velocity can be controlled by acting on the traction and braking systems with different purposes, such as improving traveling time or decreasing energy consumption (Miyatake and Ko, 2010).

The track modeling approach selected to study particular cases of railway vehicle operation also have the potential to influence the dynamic behavior of the railway vehicle. Berzeri et al. (2000) propose a methodology for the analytical definition of the track, in which, firstly, a 2D curve representing the track centerline projected onto the horizontal plane is considered, then, the elevation angle and, lastly, the superelevation, which allows to obtain the cant angle. Later, Pombo and Ambrósio (2003) presented an approach to describe the geometry of the track through a set of nodal points, in which the location and cant angle were defined. In this method, the nodal points are parametrized by cubic polynomial piecewise functions (splines), describing the path of track's centerline and of each of the rails center and cross-section orientation.

Taking into consideration the track irregularities in railway dynamics makes the dynamic simulations more realistic, since they introduce physically based perturbations on the smooth behavior of an ideal designed track. Although these irregularities result from the lateral and vertical displacements of each rail, they are characterized by four parameters, i.e., the alignment, the longitudinal level, the cant variation and the gauge variation (Pombo, 2004). The alignment refers to the lateral displacement of each rail with respect to its design. The longitudinal level represents the vertical displacement of each rail along the track comparatively with the desired configuration. The cant variation is the difference between the real and projected cant height. Finally, the gauge variation, which gives the distance between the rails' profiles, is also used to measure the track irregularities and is related with the alignment. Among the techniques that can be employed to assess the track irregularities, the most utilized approaches consist in adopting metrology cars or optical measurement systems (Andani et al., 2016). However, some researchers developed methodologies to estimate the track irregularities though the measurements of vehicle dynamics (Weston et al., 2007a; Weston et al., 2007b; De Rosa et al., 2019). More recently, Costa et al. (2020b) proposed a methodology for the generation of synthetic irregularities, thus allowing to include such perturbations in railway tracks even when they are not measured experimentally.

Pombo and Ambrósio (2012) proposed a methodology to include the track irregularities by utilizing the data collected by the railway companies during track inspection. The authors utilized real data from a route between two metro stations and compared the numerical and experimental values. They concluded that the presence of track irregularities increases the forces generated on the wheel-rail contact, and decreases the ride comfort. Naeimi et al. (2015) studied the influence of track irregularities associated to the longitudinal level on the wheel-rail contact forces. They compared the contact forces on a trailer vehicle for three segments of tangent track measured from real railway lines and three segments of tangent track with artificial V-shaped defects, and demonstrated that higher contact forces are obtained when compared with the smooth design scenario while showing that the size of the irregularities tends to increase the amplitude of contact forces. Nokhbatolfoghahai et al. (2018) analyzed the dynamic response of tank trains considering liquid sloshing and track irregularities and showed that the increase in the vehicle speed tends to increase the vehicle accelerations and generally the higher the liquid in the tank the lower the accelerations. Moreover, Sadeghi et al. (2019) investigated the effects of track irregularities on slab tracks on the ride comfort with a 2D dynamic model. They concluded that irregularities with short wavelength have significant effect on decreasing the ride comfort and that their amplitude has negligible influence on the critical speed of the train.

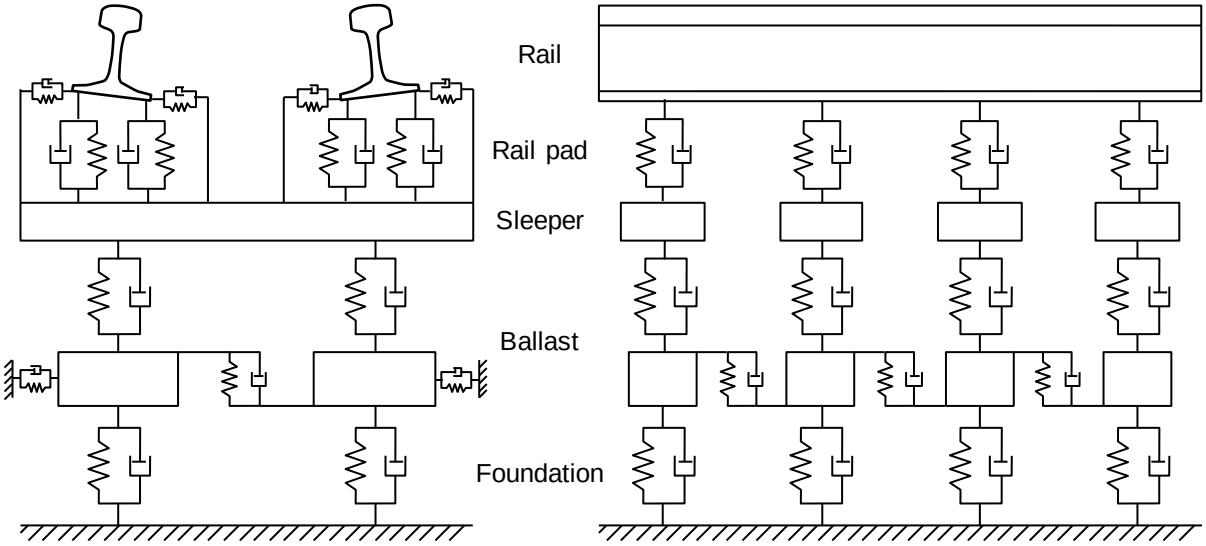

Figure 2.4 – Typical three-dimensional model to represent a flexible ballasted track structure (cross-section view and lateral view).

For the study of the railway vehicle dynamics, it is usual to consider a fully rigid track, however, some researchers have studied the influence of its flexibility on the dynamic behavior of the system (Zhai et al., 2009; Di Gialleonardo et al., 2012; Pombo et al., 2013; Costa et al., 2020a). Furthermore, the track flexibility is also a topic of interest for high frequency (Martínez-Casas at al., 2017) and geomaterials studies (Paixão et al., 2016). In fact, the railway track can be treated as an elastic structure with damping, which transmits vibration from and to the vehicle through the wheel-rail contact forces. A typical ballasted track model must consider the damping and stiffness of all its structural components, as exemplified in Figure 2.4. In this case, the rails are generally represented as Bernoulli-Euler beams which are supported by mass, spring and damper elements that represent the rail pad, sleepers, ballast and foundation. It must be noted that this structure is slightly different when modelling a slab-track (Aggestam et al., 2018; Yang et al., 2020). In order to simulate simultaneously the track and vehicle dynamics and take into account the coupling effects, it is often required to adopt a co-simulation procedure since the both vehicle and track are solved with different numerical techniques, namely multibody systems methodology and finite element method (Wu et al., 2018; Antunes et al., 2019). Chamorro et al. (2011) proposed an approach for modeling track flexibility using the floating frame of reference formulation and showed that that the flexibility can affect significantly the contact forces. Di Gialleonardo et al. (2012) found that considering the deformation of the rails makes the critical speed of the vehicle decrease about 10%, however, it considerably increases the computational effort. Antunes et al. (2019) also studied the coupling effects between the railway vehicle dynamics and the railway track geometry and flexibility, and demonstrated significant differences on the vehicle kinematics mainly during curve negotiation. The

authors showed that higher lateral forces are achieved when using a co-simulation approach to consider track flexibility, although this approach requires a computational time around 57 times higher.

Due to the increasing interest on the railway vehicle simulation, several commercial software offer packages dedicated to the dynamics of railway vehicles, namely SIMPACK, VAMPIRE, VI-grade, GENSYS or NUCARS (Shu et al., 2006). Iwnicki (1998) presented a detailed benchmark for the various software tools, in which representative vehicles and track are used to compare different modeling strategies, but also the various software. Later, Shackleton and Iwnicki (2008) focused the benchmark on the contact problem and proposed two different test cases, one using a single wheel to examine the contact specifics, and other using a simplified railway vehicle to compare the differences in terms of vehicle dynamics. Marquis and Pascal (2008) also proposed benchmark of a single unsuspended wheelset loaded with a constant vertical force to compare different methodologies for modeling the normal force in the interaction. These benchmarks are used today by the most varied researchers to demonstrate new methods or modeling issues.

2.3. Wheel and Rail Geometric Definition

The wheels and rails existing nowadays evolved from early systems in which vehicles ran on plateways. Initially, the wheels had cylindrical treads and no flanges, and ran on horizontal plates with vertical guiding edges. Similarly, the mathematical representation of wheel and rail geometries had also evolved during the past century, both in terms of complexity and reliability. The simplest way to describe the wheel geometry is considering it as being purely conical (Carter, 1916). Although this is only considered a good approximation in the early life of the wheel, without wear, and when the contact between the wheel flange and rail does not occur. In what concerns to the rail, the most basic shape is to consider it as a cylinder, which involves assuming a constant radius (Iwnicki, 2006). Figure 2.5(a) represents the combination of these two simple representations, that is, a pure conical wheels and cylindrical rails. Since the coned wheels assumption is only valid for new wheels, Wickens (1965) considered wheels with concave surface in transversal direction to support the analytical derivation of the equations of motion for profiled wheels. In his formulation, both wheel and rail are treated as circular arcs, as depicted in Figure 2.5(b). This assumption allows to study the influence of selected parameters on the stability of the bogies and wheelsets (Bhaskar et al., 1997a; Bhaskar et al., 1997b). However, this assumption is only valid for small wheelset lateral displacements, since existing wheel and rail profiles have continuous varying radii.

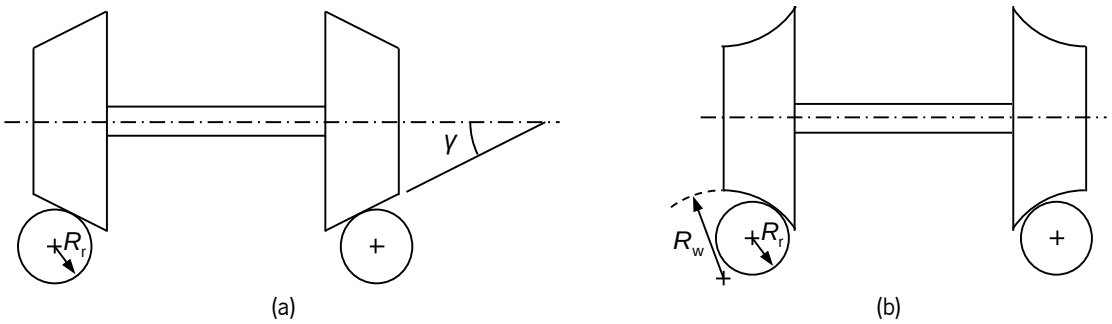

Figure 2.5 – Representation of cylindrical rail interacting with (a) conical and (b) circle wheels

Another simple approach consists in considering a conical wheelset on a knife edge rail as schematized in Figure 2.6 (Elkins, 1992). This simplification consists of using a geometric constraint, which is very unrealistic, mainly when there is flange contact. According to Elkins (1992), the methods for determination of geometric constraints for real wheel and rail profiles involve always four steps: (i) specify the wheel and rail profiles in a numerical form for the default position and orientation; (ii) represent the profiles as series of mathematical functions; (iii) determine the location of the contact points for a given number of relative positions of the wheelset with respect to the rails; (iv) use the contact point locations to determine the required contact characteristics as rolling radii, contact angles, etc. Several authors also utilized the constraints approach for contact detection, although with more complex geometry description (De Pater, 1988; Fisette and Samin, 1994; Shabana and Sany, 2001; Shabana et al., 2005; Sugiyama and Suda, 2009; Recuero and Shabana, 2014).

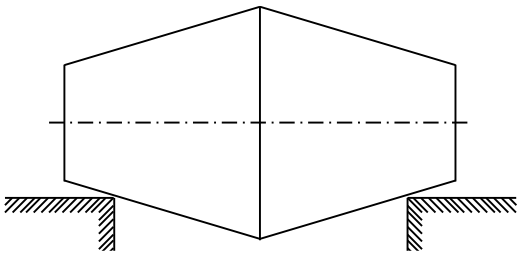

Figure 2.6 – Conical wheelset on knife edge rails

Although simple geometries were initially used to describe the wheel and rail profiles, the real profiles hold significantly more complex shapes. Nevertheless, the geometric simplifications described enable analytical studies of the vehicle and track dynamics in an epoch in which the computational calculation was very limited. Thus, in order to model accurately the real profiles, a more detailed geometric description must be defined, to represent the several wheel profile zones and the different radii in the rail head. Figure 2.7 schematizes a new wheel profile and specifies different zones with geometries described in the standards (UIC, 2004). In an analogous manner, a representation of a rail profile with its characteristic dimensions is shown in Figure 2.8 (BS, 2011).

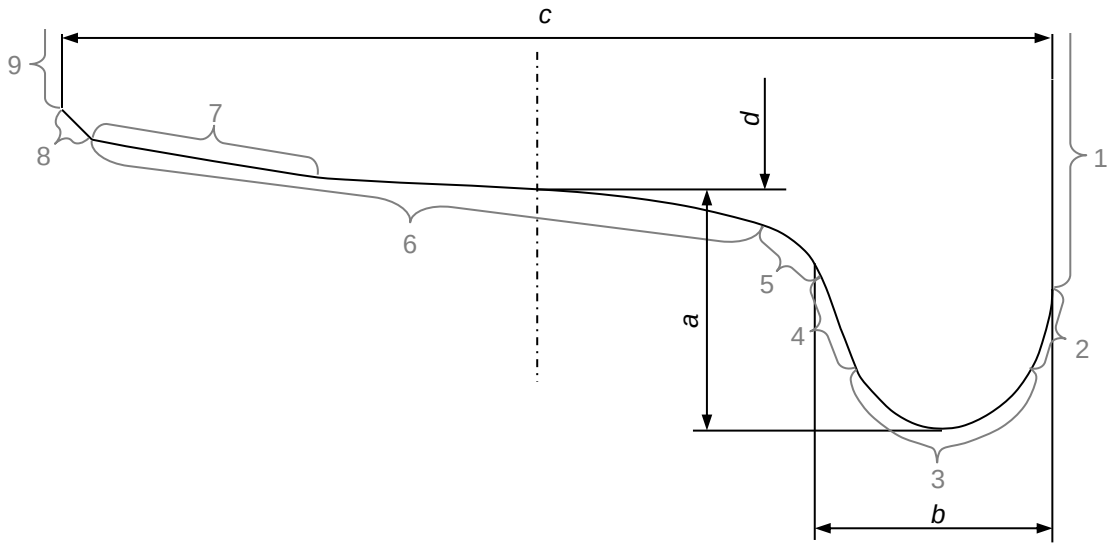

Figure 2.7 – Description of the wheel profile: 1 - Internal surface of wheel; 2 - Internal surface of flange; 3 - Flange top; 4 - External surface of flange; 5 - Flange fillet; 6 - Running surface; 7 - Slope of external section of the running surface; 8 - External bevel of running profile; 9 - External surface of wheel; a - Flange height; b - Flange thickness; c - Wheel width; d - Running tread diameter. (UIC 510-2, 2004)

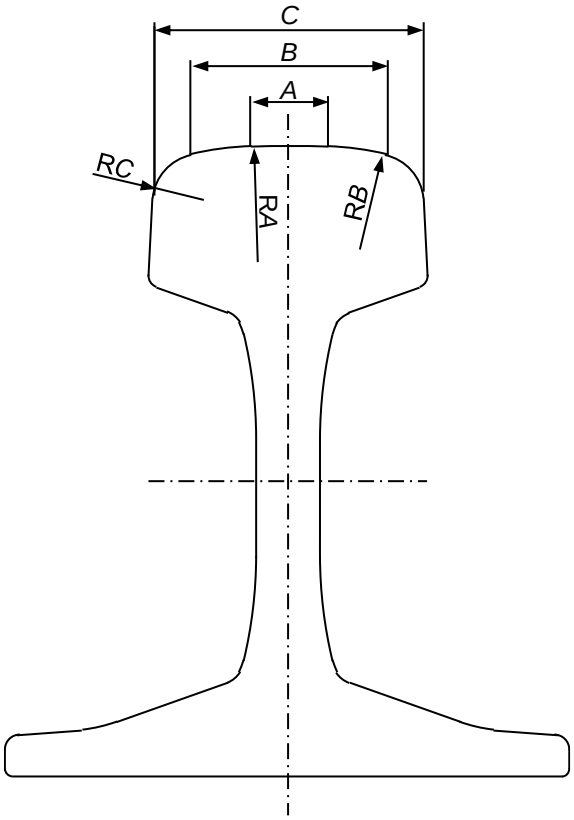

Figure 2.8 – Schematic representation of rail profile 60E1 according to BS EN 13674-1 (2011)

One of the most popular methods to describe the wheel and rail geometry is by polynomial interpolation of a given number of points identified on its surface, particularly by polynomial splines (Persson and Iwnicki, 2004; Braghin et al., 2006; Pombo et al., 2007). This type of procedures has the

advantage of exhibiting local geometrical control, i.e., the variation of the position of a control point only affects the neighborhood of that point without changing the rest of the curve (De Boor, 1978) and easily including variations of their nominal geometry in their geometrical description.

The mathematical description of the wheel and rail profiles consists of a two-dimensional representation which can be extended to the three-dimensional space by defining their external surfaces. A bi-dimensional approach for the description of the wheel and rail has the advantage of allowing fast and straightforward numerical models, but poses significant limitations regarding an accurate representation of the contact scenarios, as, for instance, in the presence of angular misalignments. Typically, the wheel and rail are represented by two parametric surfaces (Pombo and Ambrósio, 2005; Shabana et al., 2005; Sugiyama and Suda, 2009; Sugiyama et al., 2009), as depicted in Figure 2.9. The surface of each rail is obtained through the sweep of its cross-section along a certain path, in turn, the wheel surface is described as a revolution of its cross-section about its own axis. Since both cross-sections are defined as function of their lateral coordinate, each of these of surfaces is characterized by two parameters, i.e., any point on the rail surface is defined by the lateral (u_{r}) and longitudinal (s_{r}) coordinates, and a point located on the wheel surface is given by the lateral (u_{w}) and angular (s_{w}) coordinates.

During the resolution of a typical contact problem, subsequently to the geometrical definition of the contacting entities, the search for potential contact points is performed. The contact detection phase can be a very straightforward task and solved analytically if the contacting bodies have simple geometries. However, in the most general case, the contacting surfaces can have an arbitrary shape, and the search for the potential contact points is a demanding and complex task. Regarding the wheel-rail contact, it is common that the contacting surfaces have a non-conformal geometry, namely when the area of contact of the rail exists either with the wheel flange or with the wheel tread, which simplifies considerably the search for contact points. However, when the contact occurs on the running fillet, shown in Figure 2.7, the surfaces tend to become conformal and the contact cannot be reduced to a single point. Some authors neglect this transition zone for sake of simplicity and represent the wheel profile as two independent curves (Pombo et al., 2007; Marquis and Pascal, 2008; Sugiyama et al., 2009). Although this simplification avoids some numerical problems and improves the numerical efficiency (Recuero and Shabana, 2014; Marques et al., 2019a; Marques et al., 2020), it does not allow the study of local phenomena, such as wear or rolling contact fatigue.

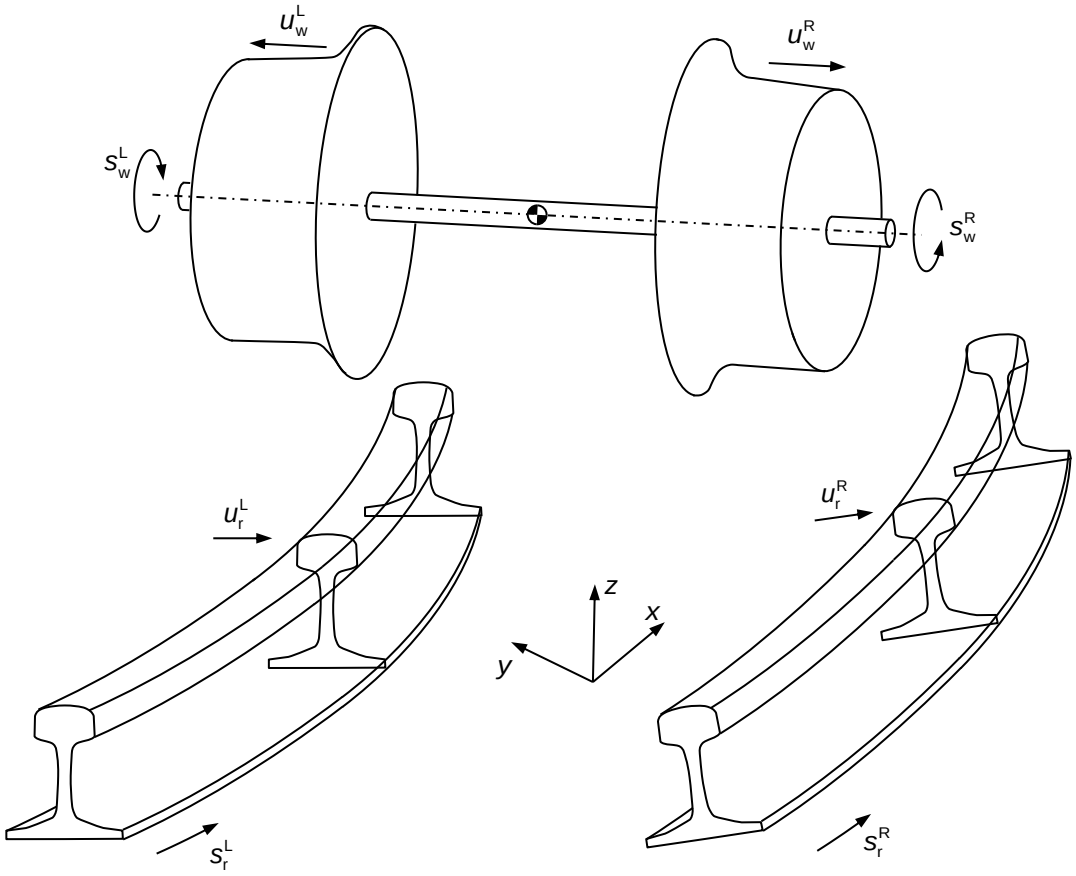

Figure 2.9 – Representation of wheel and rail parametrized surfaces

The strategy utilized for the contact detection is intimately linked with the geometric description of the potential contacting surfaces. Thus, algebraic approaches can be employed (Falomi et al., 2011; Magalhães et al., 2020) in which the contact points are sought in a continuous manner through constraints imposed to the normal and tangential vectors. Alternatively, in the nodal search method, the profiles are described by a set of nodal points which are used to perform a discrete evaluation of the penetration between both profiles (Bozzone et al., 2011a; Sugiyama et al., 2012). This approach has typically higher computational cost. Moreover, the contact detection procedure strongly affects the efficiency and accuracy of the overall contact modelling. In a broad sense, the contact search approach can be performed online or offline. In the former, the location of the contact points is determined online using iterative procedures at every time step of the dynamic simulation (Pombo et al., 2007; Malvezzi et al., 2008; Marques et al., 2020). In the offline approach, the location of the contact points is precomputed by performing a contact geometry analysis for selected relative positions of wheel and rail cross-sections, and this information is stored in a lookup table which is invoked in each time step of the integration process (Sugiyama and Suda, 2009;.Bozzone et al., 2011b; Escalona and Aceituno, 2019; Aceituno et al., 2020).

2.4. Contact Force Models for Wheel-Rail Contact

The wheel-rail interaction stands as a particular case of contact modeling using multibody systems formulations, in which one of the contacting bodies is rolling over the other. The resolution of contact problems is quite frequent in the context of a multibody system dynamics, and it comprises three fundamental steps. First, the geometry of the interacting bodies must be defined, that is, the mathematical description of the contacting surfaces, either by continuous functions or discrete set of points. Secondly, the contact detection between both bodies has to be performed to find the potential contact points. The degree of complexity of this task is intimately associated with the shape of the contacting surfaces. Simplifying the contacting geometries is a common approach to mitigate the complexity of the contact problem and expedite its resolution. Finally, a proper contact model is used to evaluate the contact forces, both on the normal and tangential directions with the respect to the surfaces. The most common methodologies to evaluate the contact forces in the context of wheel-rail interaction are discussed in this section.

In different epochs, several authors attempted to provide surveys on the existing methods to model the wheel-rail contact (Kalker, 1979; Elkins, 1992; Pascal and Sauvage, 1993; Piotrowski and Chollet, 2005; Meymand et al., 2016), some of them focusing only on the normal (Sichani et al., 2014a) or tangential contact force models (Shen et al., 1983; Vollebregt et al., 2012).

Hertz (1881) was a precursor on the study of contact mechanics. Under the assumptions that: the contacting bodies can be approximated by half-spaces; they are constituted of linear elastic, isotropic and homogenous materials; the contact is frictionless; and the curvature is constant over the contact; the elastic Hertzian contact theory was developed. This implies that the bodies are locally flexible. The normal force is given as a function of the pseudo-penetration between the contacting bodies as

$$f_{\mathrm{n}}^{\mathrm{H}} = K\delta^{n} \tag{2.14}$$

where K denotes the contact stiffness which depends on the material and geometric properties of the contact points, n is the exponent that defines the nonlinearity of the contact, and δ expresses the pseudo-penetration or indentation of the contacting bodies that represents their local elastic deformation. The Hertzian approach defines an elliptical contact patch only based on the curvature of the main contact point, with the pressure distribution given by

$$p(x,y) = p_0\sqrt{1-\left(\frac{x}{a}\right)^2-\left(\frac{y}{b}\right)^2} \tag{2.15}$$

where p_0 is the maximum pressure located at the center of the contact patch, and a and b denote the semi-axes of the contact ellipse which is schematically represented in Figure 2.10.

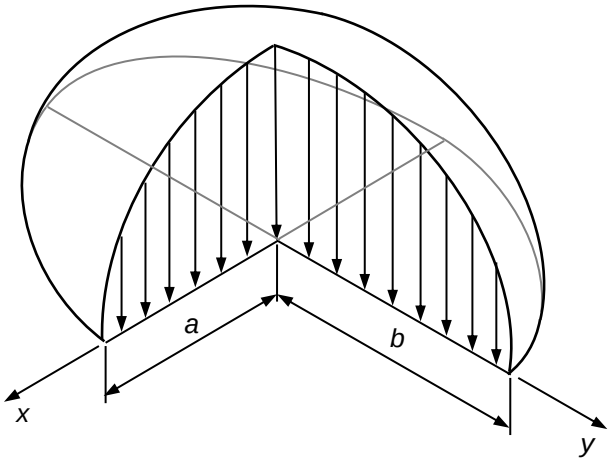

Figure 2.10 – Representation of elliptical pressure distribution of Hertzian contact patch.

Based on Hertzian theory, Carter (1926) used a two-dimensional approach to demonstrate that, in normal operation conditions, tangential traction in rolling direction is below the friction limit. In the front of the patch, the surfaces stick together, and the surface strain is constant, while, in the rear of the patch, the pressure between surfaces is insufficient to support the strain and, hence, the surfaces slip. This results in a traction profile similar to the one represented in Figure 2.11, in which the tangential tractions are below the friction limit in the adhesion area, and assume its value in the sliding zone. This limit is expressed by

$$\left\|\boldsymbol{\tau}(x,y)\right\| \leq \mu p(x,y) \tag{2.16}$$

in which $\boldsymbol{\tau}$ is the vector of tangential tractions at any point of the contact patch and μ is the sliding coefficient of friction. It must be emphasized that Eq. (2.16) must be verified in the whole patch.

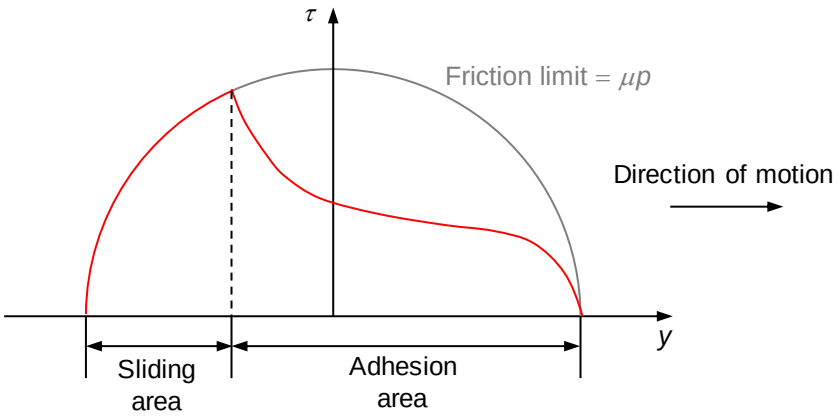

Figure 2.11 – Schematic representation of the traction bound for a Hertzian contact patch.

The tangential forces acting on the contact are defined through the integration of the tangential tractions over the contact area in the rolling and lateral directions. These forces, generally referred to as creep forces, are the longitudinal and lateral creep forces, respectively. The creep forces are generated from the relative motion of the contacting surfaces which exists when two elastic bodies are pressed against and roll over each other. Sliding between surfaces occurs when the relative linear velocity of the wheel with respect to the rail at the contact point is not null. In the case that the angular velocity of the wheel is not perpendicular to the normal vector to the surface in the contact point, spin occurs. If the wheel is rolling without sliding and spin, the motion is characterized as being pure rolling.

For high levels of sliding, the tangential tractions reach the friction limit in the whole contact area being the contact patch in fully sliding mode. However, for small levels of sliding, the contact patch is in an hybrid state, as described in Figure 2.11, for which there is an adhesion part and a sliding part. In order to quantify the relative motion in the contact zone, the concept of creepage is introduced, being the longitudinal, lateral and spin creepages computed, respectively, as

$$\upsilon_x = \frac{\mathbf{v}_{\text{rel}}{}^{\text{T}}\mathbf{t}_{\text{s}}}{V} \tag{2.17}$$

$$\upsilon_y = \frac{\mathbf{v}_{\text{rel}}{}^{\text{T}}\mathbf{t}_{\text{u}}}{V} \tag{2.18}$$

$$\varphi = \frac{\boldsymbol{\omega}^{\text{T}}\mathbf{n}}{V} \tag{2.19}$$

where $\mathbf{v}_{\text{rel}}$ denotes the relative linear velocity of the surfaces on the vicinity of the contact point, $\boldsymbol{\omega}$ represents the angular velocity of the wheel, V is the magnitude of the forward velocity of the wheelset, $\mathbf{n}$ defines the normal vector to the surface in the contact point, and $\mathbf{t}_{\text{s}}$ and $\mathbf{t}_{\text{u}}$ are the tangential vectors on longitudinal and lateral directions, as shown in Figure 2.12.

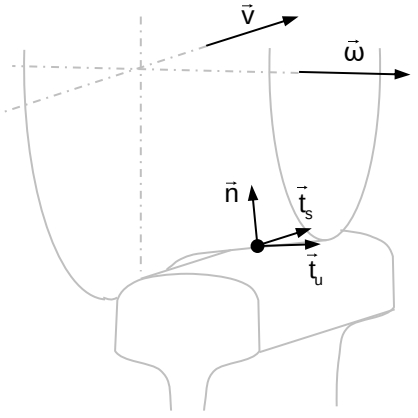

Figure 2.12 – Representation of the wheel linear and angular velocities, and the normal and tangential vectors on the contact point.

Generalizing the Carter's theory to a three-dimensional analysis, Johnson (1958a) established a relationship between creepages and creep forces for spherical elastic bodies, neglecting the spin creepage. Later, Vermeulen and Johnson (1964) extended the study for non-spherical bodies. Johnson (1958b) also studied the case of spherical rolling bodies with very small pure spin, i.e., without lateral and longitudinal creepages. Kalker (1967) proposed the linear theory for rolling contact, in which the spin creepage is considered. This theory assumes a linear growth of traction inside the contact patch. Although this assumption leads to the violation of Eq. (2.16) near the trailing edge, it results in a linear relationship between creepages and creep forces given as

$$\begin{Bmatrix} f_x \\ f_y \\ m_z \end{Bmatrix} = -Gab \begin{bmatrix} c_{11} & 0 & 0 \\ 0 & c_{22} & \sqrt{ab}c_{23} \\ 0 & -\sqrt{ab}c_{23} & abc_{33} \end{bmatrix} \begin{Bmatrix} \upsilon_x \\ \upsilon_y \\ \varphi \end{Bmatrix} \tag{2.20}$$

in which f_x and f_y denote the longitudinal and lateral creep forces, respectively, m_z represents the spin moment, G is the equivalent shear modulus of rigidity of the pair of materials, and c_{11}, c_{22}, c_{23} and c_{33} are the creepage coefficients tabulated by Kalker (1990) being obtained as a function of the Poisson's ratio and the ratio of semi-axes of contact ellipse, a/b. This method does not consider the friction limit, since it allows the creep forces to increase indefinitely with the increase of the contact creepages. Although commonly used in a wide number of works, the linear theory can only be applied for small creepage values or assuming infinite friction.

Shen et al. (1983) improved this work by proposing a heuristic nonlinear model which performs the saturation of creep forces obtained with Eq. (2.20). Hence, the creep forces are calculated as

$$\begin{Bmatrix} f_x \\ f_y \end{Bmatrix} = k_{\mathrm{NL}} \begin{Bmatrix} f_{x\mathrm{L}} \\ f_{y\mathrm{L}} \end{Bmatrix} \tag{2.21}$$

where k_{NL} is the correction factor for the creep forces computed with the linear theory, namely $f_{x\mathrm{L}}$ and $f_{y\mathrm{L}}$, being defined by

$$k_{\mathrm{NL}} = \begin{cases} \dfrac{\mu f_{\mathrm{n}}}{f_{\mathrm{L}}} \left[\left(\dfrac{f_{\mathrm{L}}}{\mu f_{\mathrm{n}}} \right) - \dfrac{1}{3} \left(\dfrac{f_{\mathrm{L}}}{\mu f_{\mathrm{n}}} \right)^2 + \dfrac{1}{27} \left(\dfrac{f_{\mathrm{L}}}{\mu f_{\mathrm{n}}} \right)^3 \right] & f_{\mathrm{L}} \le 3\mu f_{\mathrm{n}} \\ \dfrac{\mu f_{\mathrm{n}}}{f_{\mathrm{L}}} & f_{\mathrm{L}} > 3\mu f_{\mathrm{n}} \end{cases} \tag{2.22}$$

in which f_{L} is the resultant linear creep force given as

$$f_{\mathrm{L}} = \sqrt{{f_{x\mathrm{L}}}^2 + {f_{y\mathrm{L}}}^2} \tag{2.23}$$

It must be noted that this method is only valid for small values of spin creepage. Therefore, it is not suitable for flange contact, since the large values of contact angle produce high spin.

Kalker (1990) continued his research into the complete rolling contact theory which resulted in the development of DUVOROL, a FORTRAN program in which the contact patch is discretized using the boundary element method. This program handles all possible rolling contact problems for bodies with identical elastic constants using the Hertzian theory. The DUVOROL was used by the British Railway to study the vehicle motion, but since it uses the BEM and the complete theory, it makes the program not sufficiently efficient for vehicle simulation. The computational efficiency of the program for the rail-wheel interaction was obtained by British Railway which constructed a book of tables for the tangential forces with 4 inputs, namely longitudinal, lateral and spin creepages and semi-axis ratio of the contact ellipse. This approach implies a pre-processing step, which can be computationally expensive, i.e., to generate the tables. Then, during simulation, the creep forces are quickly obtained through linear interpolation of the pre-calculated data. The use of LuT is a common approach when using rather inefficient models and always requires a trade-off between size and accuracy. Therefore, the selection of LuT discretization has a high impact on its accuracy and efficiency of the analysis (Marques et al., 2019b).

In order to overcome the difficulties of the original program, Kalker (1982a) developed another computer program named CONTACT, which came to be the DUVOROL's successor and, still today, the reference on wheel-rail contact calculation. Although CONTACT also uses BEM, it is generalized for non-Hertzian contact patches, which largely extends the scope of application and its accuracy. The main drawback of this program concerns its computation time, which limits its use in dynamic analyses. In spite of that, CONTACT is commonly employed for validation of other more expedite methods that have been developed to handle the wheel-rail contact.

Bearing the computational efficiency in mind, Kalker (1982b) proposed another computer code called FASTSIM, which is based on the simplified rolling contact theory. This theory considers a Hertzian contact patch and relies on the assumption that the contact can be locally represented by three springs that are independent of what happens in the neighborhood of the contact patch. The main advantage of this theory concerns its computational efficiency, which is the major reason for being employed. For Hertzian contact patches, it was shown that FASTSIM has an error lower than 15% when compared with CONTACT. Then, FASTSIM was extended to be utilized for the calculation of creep forces in non-Hertzian contact (Kalker, 1983), but it presented less satisfactory results. Regardless of the suitability of FASTSIM

for some applications, it may not be appropriate to be employed in complex multibody systems, being alternative methods developed and demonstrated in this work.

Since the CONTACT algorithm is too slow to be used online in dynamic simulations, Kalker (1996) proposed a LuT based on CONTACT in which only Hertzian contact is considered to allow its parametrization. This routine was called USETAB and had the same genesis of the LuT used by the British Railway based on DUVOROL.

Polach (1999) proposed an alternative algorithm to evaluate the tangential forces. This is an analytical model that calculates the creep forces and moment based on the contact geometry and creepages. This method considers an elliptical contact patch with Hertzian pressure distribution. Its main advantage lies on its computational efficiency, when compared with FASTSIM, and, mainly, with CONTACT. The Polach's method can be written similarly to Eq. (2.20) as

$$\begin{Bmatrix} f_x \\ f_y \\ m_z \end{Bmatrix} = \begin{bmatrix} f/\upsilon_{\mathrm{C}} & 0 & 0 \\ 0 & f/\upsilon_{\mathrm{C}} & f_{y\mathrm{S}}/\upsilon_{\mathrm{C}} \\ 0 & 0 & 0 \end{bmatrix} \begin{Bmatrix} \upsilon_x \\ \upsilon_y \\ \varphi \end{Bmatrix} \tag{2.24}$$

where υ_{C} defines the modified translational creepage, f is the resultant tangential contact force caused by the longitudinal and lateral creepages, and $f_{y\mathrm{S}}$ denotes lateral tangential force due to the influence of spin creepage. More details on the computation of these variables can be found in (Polach, 1999). Since the matrix coefficients depend on the contact creepages, this model does not show a linear behavior.

Knothe and Le-The (1985) considered a non-Hertzian contact patch by dividing it into strips along the rolling direction. They modified the Kalker's simplified theory by performing the integration of the tangential tractions in each strip separately. Piotrowski (1982) examined for the first time the hypothesis of having two distinct contact points between wheel and rail at the same time, i.e., the rail interacting with the wheel tread and wheel flange separately. Later, Piotrowski and Kalker (1988) verified that the cross-influence between these two contact patches can be neglected without introducing significant error, if they are located far apart from each other.

One of better accepted methodologies to deal with the existence of one or more non-elliptical contact patches is the multi-Hertzian contact technique, which assumes that the contact zones can be replaced by a set of elliptical contact patches. This method is graphically represented in Figure 2.13 where two distinct ellipses are used to approximate the actual non-Hertzian contact area. Pascal and Sauvage (1992) proposed a methodology which considers that, when several points of contact can be

identified close to each other, their contact patches can be reduced to an equivalent elliptical contact patch. This technique of replacing the multi-Hertzian contact model by one equivalent ellipse has been tested recurring to CONTACT for the case of S1002 and UIC60 (Pascal, 1993), and the conclusion is that it is not a suitable alternative since it presents unsatisfactory results for the contact forces.

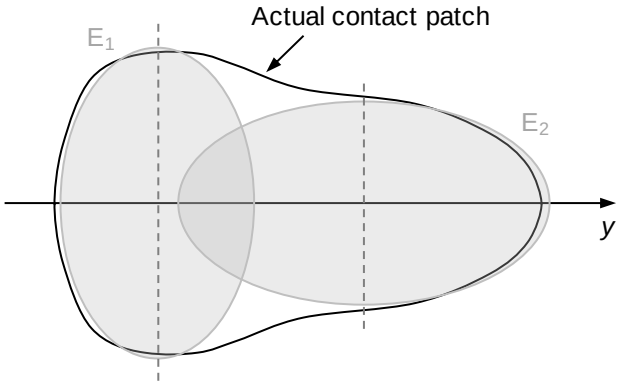

Figure 2.13 – Representation of Multi-Hertzian contact model.

Kik and Piotrowski (1996) proposed a fast and approximate methodology to evaluate the normal load for non-elliptical contact patch. This method considers quadratic contacting surfaces in the rolling direction, which results in an elliptical pressure distribution in that direction. This assumption is also called semi-Hertzian contact. In the lateral direction, the contact patch is divided into strips, as represented in Figure 2.14, being their size determined based on the undeformed distance function defined between the wheel and rail profiles (Piotrowski and Kik, 2008). This method takes advantage of the half-space approach and computes the normal pressure distribution based on the penetration and location of the main contact point, which represents the origin of the contact patch local reference system, depicted in Figure 2.14.

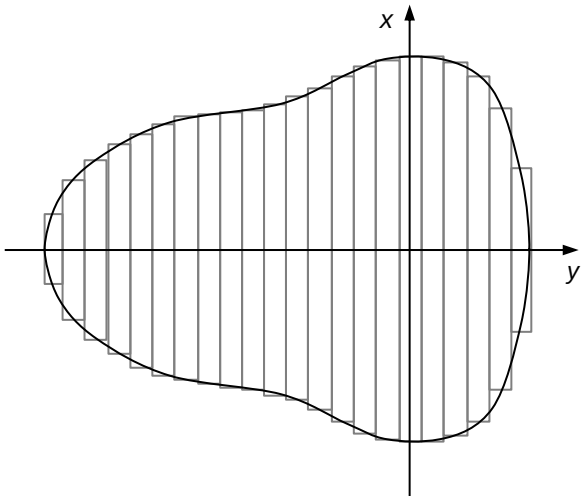

Figure 2.14 – Representation of the discretization of the contact patch into strips with semi-Hertzian approach.

The different theories for the rolling contact of wheels and rails, overviewed so far, are based on the elastic approach, which allows the relative interpenetration between the two contacting surfaces. Alternatively, a constraint approach is also used to model wheel-rail contact, which involves the definition of nonlinear kinematic constraints limiting the number of relative degrees of freedom of the wheel with respect to the rail to five, by constraining their normal interference. De Pater (1988) proposed a methodology to evaluate the wheel-rail contact forces based on such position constraints for a wheelset running on a tangent track. Later, Fisette and Samin (1994) presented a constraint approach in which the left and right wheels are treated independently, i.e., the wheelset is not rigid. The constraint approach has the advantage that the normal contact force and the location of the contact points are determined during the resolution of the system's equations of motion; i.e., they are represented by the Lagrange multipliers that appear in Eq. (2.11), associated to the reaction forces.

Shabana et al. (2001) further developed the constraint approach recurring to the augmented Lagrangian formulation (Shabana and Sany, 2001). In this approach, the wheel and rail surfaces are both described by two parameters each. These parameters are used to define the contact conditions between the wheel and the rail, which are based on the tangent and normal vectors and form a set of five kinematic constraint equations. Since the four non-generalized surface parameters are unknowns to be identified, the constraint equations only eliminate one relative degree of freedom between the wheelset and the rails. In this methodology, the creep forces are calculated recurring to USETAB using the location of the contact points and normal forces from the previous time step, i.e., their calculation is out of synch with the normal force evaluation. This procedure is adopted because the normal contact forces, required to evaluate the creep forces, are calculated during the resolution of the equations of motion while the creep forces themselves are already required to form the equations of motion.

Due to the increase of the available computational capacity, techniques that are more computer demanding, such as the Finite Element Method, were adopted to treat the wheel-rail interaction. Telliskivi and Olofsson (2001) utilized FEM to study wheel-rail contact and compared the contact patches and normal pressure obtained with the analytical Hertzian approach with CONTACT based on the Boundary Element Method. This study was carried with the FEM program ANSYS for several static test cases and showed that the main differences between the shape of contact patches and pressure distribution occur in curves with small radius. The FEM is also extremely inefficient from the computational point of view, although it does not impose the half-space assumption or the elastic materials assumption. Later, Liu et al. (2006) studied fatigue crack initiation in train wheels recurring to FEM to evaluate the stress

distribution in the contact, thus generating results that reinforce the conclusions of previous works in what wheel-rail contact is concerned.

Shabana et al. (2004) also proposed an elastic force model in which the normal force is calculated recurring to a Hertzian based approach and, the creep forces are determined using USETAB. Later, Shabana et al. (2005) compared both elastic and constraint approaches and concluded that they are in good agreement.

Alonso and Giménez (2005) present an alternative method to evaluate the normal pressure and the shape of the contact patch, in which the Hertzian theory is modified through the discretization of the contact area and the application of a shape distortion. Subsequently, they proposed an alternative method for the calculation of tangential forces with a modified FASTSIM for non-elliptical contact patches (Alonso and Giménez, 2007). This approach focuses on the calculation of the flexibility parameters and the approximation of the contact patch by two different semi-ellipses.

A compensation for the local curvatures, assuming semi-Hertzian conditions, is proposed by Ayasse and Chollet (2005) for the identification of the contact patch divided into strips, being this compared with multi-Hertzian strategies. Quost et al. (2006) used FASTSIM algorithm but adapted to the strips discretization in order to assess the tangential forces. It shows a good agreement with CONTACT for non-Hertzian contact patches. More recently, Sebés et al. (2014) presented a multi-Hertzian method which is an extension of semi-Hertzian model by Ayasse and Chollet (2005), although it considers the plasticity effects. Computationally, this method is about five times faster than that presented by Ayasse and Chollet (2005) since the interpenetration between wheel and rail is checked for a smaller number of points. Although, the inclusion of plasticity does not affect the dynamic behavior of the vehicle, the authors claim that it is of interest to consider it when studying other phenomena such as rolling contact fatigue.

Pombo et al. (2007) suggested an approach to model wheel-rail contact considering an elliptical contact patch. In that sense, the normal force is evaluated with a Hertzian contact model accounting for energy dissipation and, for the creep forces, three different theories were compared, namely Kalker linear theory (1967), Heuristic nonlinear model (Shen et al. 1983) and Polach nonlinear model (1999). Later, Magalhães et al. (2020) compared this modeling approach with another using a non-Hertzian model (Kik and Piotrowski, 1996) in the context of dynamic simulations and identified differences on the dynamic response of the systems.

Piotrowski (2010) presented an extension of FASTSIM which models the coefficient of friction as a function of the slip velocity and takes into account friction anisotropy. Vollebregt and Wilders (2011) also focused on the FASTSIM algorithm by improving the integration in space. These authors proposed a second-order integration algorithm called FASTSIM2, which has faster convergence and consequently, requires a coarser discretization for the same accuracy. More recently, Vollebregt (2014) suggested an enhancement for CONTACT algorithm based on experimental data. These changes focus on dependence of creep forces on the slip velocity, namely the reduction initial slope of traction curve, which reduces the tangential stiffness due to roughness and contamination, and the decrease of traction for high creepages i.e., the drop of friction after attaining its maximum value.

Bozzone et al. (2011a; 2011b) presented a wheel-rail contact model in which the contact detection is performed recurring to a LuT, and the contact is treated separately in the wheel flange and wheel tread. The normal force is found using a Hertzian approach, although, in the flange contact, besides the local contact flexibility also the flange bending is considered, i.e., it is treated as a cantilever beam. The heuristic nonlinear model, which performs the saturation of Kalker linear theory, is employed for the computation of the tangential forces.

Meli et al. (2011) proposed an elastic model that solves the Navier's elasticity equation for the wheel-rail contact. This model consists of finite element approach integrated in a multibody simulation. The authors focus the on the efficiency of the numerical strategies to solve this problem. More recently, this research group developed a new methodology to model the adhesion effects in the wheel-rail interaction (Allotta et al., 2014; Meli and Ridolfi, 2015).

Sichani et al. (2014b) delivered a new methodology for the evaluation of the normal pressure and estimation of the contact patch area, named ANALYN. This method, as other simplified methods, is based on the virtual penetration concept and considers the discretization of the contact patch into longitudinal strips, but not neglecting the surface deformations. Thus, ANALYN shows a good agreement with CONTACT for the selected static cases, and its computational speed is about 300 times faster. Relatively to the tangential contact problem, Sichani et al. (2016) proposed a modification to FASTSIM algorithm in order to be compliant with the strip theory, which is called FaStrip. This new method has a better performance than FASTSIM when using CONTACT as reference.

Liu et al. (2016) also studied the normal contact problem and developed a new methodology based on Kik-Piotrowski strips method (1996) that takes into account effects of yaw angle, corrections of

the predicted contact width and length, and enhancement of pressure distribution. The results demonstrated that this methodology presents significantly better results than the classical Kik-Piotrowski model when the yaw angle is significant, namely, when negotiating small radius curves.

Yang et al. (2016) used FEM to study the dynamics of the transition from single-point, i.e., tread contact, to two-point contact, which involves tread and flange contact. Thus, it was possible to verify the impact of this transition on the local stresses and slip between surfaces. An increase of the wave propagation of micro-slip, which ultimately contributes to the appearance of defects, such as corrugation or fretting, was observed.

The use of Kik-Piotrowski model produces discontinuities in the normal force magnitude, since it depends on the location of the maximum penetration point which might change instantaneously under particular conditions. Bearing that in mind, Sun et al. (2018) proposed a modification to this contact model in which this dependency does not occur and, therefore, the shifts on the location of main contact point are smooth resulting in smooth variations of the contact force. This program is designated by MKP, which means Modified Kik-Piotrowski. More recently, Sun et al. (2020) improved their model by introducing a modification that takes into account the effect of yaw angle on the evaluation of the contact, being named MKP-YAW. This model demonstrated a great agreement with CONTACT in terms of normal force magnitude, however, it exhibited some discrepancies in what concerns to the normal pressure distribution and shape of the contact patch.

Most of the wheel-rail contact force models available in the literature are limited to their application in non-conformal contact cases, as represented in Figure 2.15(a). Although this condition covers most of the possible interaction scenarios, in which the rail interacts directly with the tread or flange, when negotiating sharp curves or due to worn profiles, the conformal contact tends to occur in the running profile fillet zone. The conformity of wheel-rail contact was studied for the first time by Paul and Hashemi (1981). They proposed a methodology to calculate the pressure distribution and contact patch shape for closely conforming elastic surfaces. In this type of contact, the assumption of a planar contact region is not valid, therefore, the patch curvature must be considered, as depicted in Figure 2.15(b), and the normal direction varies along the contact. Paul and Hashemi (1981) compared the pressure distribution and contact shape in a static case for a conformal and non-conformal approach, and significant differences were found. Later, Bhaskar et al. (1997a; 1997b) also studied the conformal contact, in which the spin creepage has special focus since the curvature of the contact patches implies that the spin creepage varies with the variation of the contact angle. Recuero and Shabana (2014)

identified the problem of contact detection in a conformal zone using the contact search methods that rely on nonconformal contact conditions. The common methods of contact search fail in finding a unique solution in a conformal case, implying that when using a constraint approach the solution of the equations of motion fail due to a singular Jacobian matrix. The authors propose to eliminate as many equations as the degree of singularity to overcome such singularity. More recently, Marques et al. (2020) also verified this problem and proposed an alternative method to search the main contact point. Vollebregt and Segal (2014) highlighted the importance of accurately model the conformal contact, recurring to FEM to determine the geometric influence functions utilized in CONTACT, demonstrating, in the process, the differences between the proposed conformal model and a the Hertzian approach. Afterwards, Vollebregt (2018) presented some corrections and further results. Independently, Blanco-Lorenzo et al. (2016) used finite element models in ABAQUS to study the effects of the degree of conformity on surface traction, subsurface stresses and frictional work distributions. Pascal and Soua (2016) showed that the multi-Hertzian techniques can also be applied with success to conformal contact cases. Later, Pascal and Sany (2020) verified the dynamic behavior of an unsuspended wheelset using the multi-Hertzian technique, the results for conformal profiles were compared against the nonconformal profiles and significant differences were found.

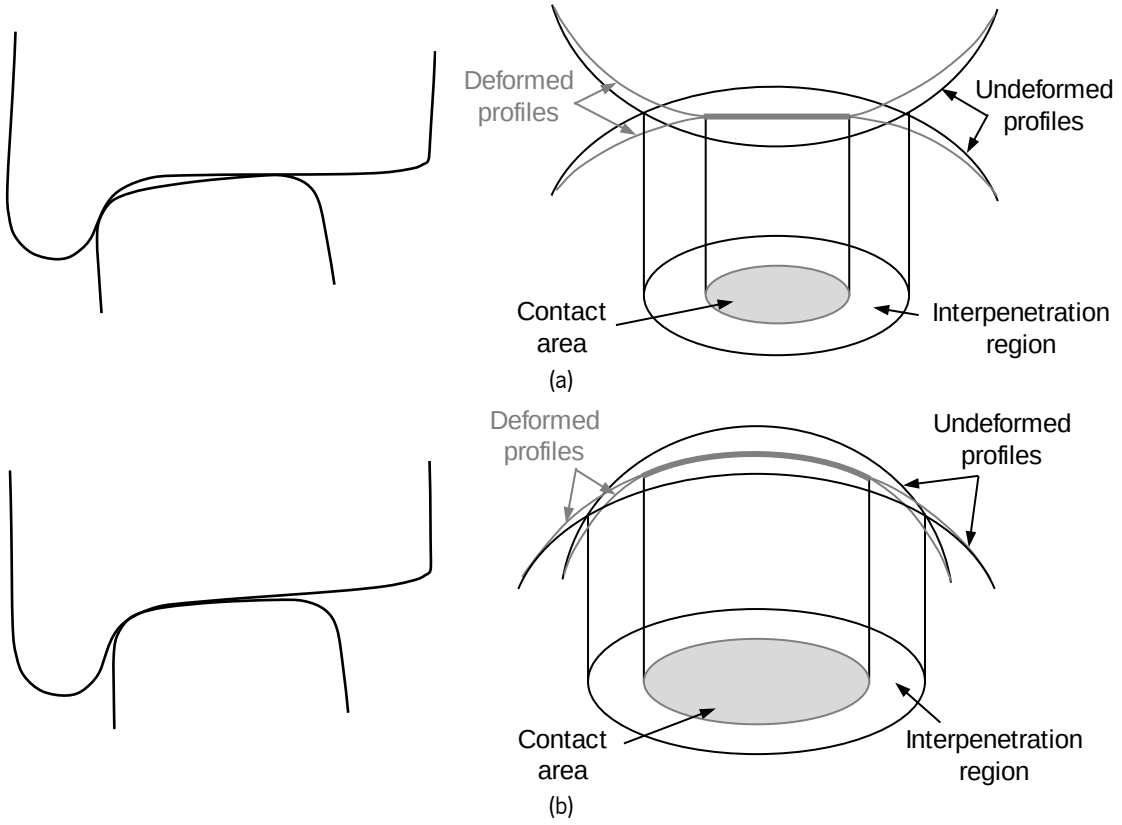

Figure 2.15 – Schematic representation of the contact region for (a) a non-conformal case (planar contact patch) and (b) conformal case (curved contact patch)

Several wheel-rail contact force models presented in this section are not applied in the context of vehicle dynamic simulations, since forward dynamics time integration requires computational efficiency and numerical smoothness that these approaches do not possess. Moreover, to investigate detailed contact phenomena, such as wear or rolling contact fatigue, more accurate models, which can be applied in dynamic studies, are usually required. Therefore, only selected methods for the wheel-rail contact can be used in the context of dynamic analysis of railway vehicles. Such methods are identified and used in the course of this work.

2.5. Lookup Tables for Wheel-Rail Contact

A Lookup Table (LuT) consists of computational surrogate of the online computation of a given function by searching in an array containing pre-calculated values that do not suffer modifications during the execution of the program. This approach is widely used because it can provide significant savings in terms of computation time, since collecting values from the memory tends to be faster than evaluating burdensome functions, while maintaining a good accuracy. The use of tables to gather values of function in a given domain precedes the development of computer science. Throughout history many tables were developed to represent trigonometric and logarithmic functions, for instance (Campbell-Kelly et al., 2007). As a matter of fact, the evaluation of trigonometric and logarithmic functions is a widespread application of LuT in computer programs, since their exact calculation can considerably slow computations. Thus, these functions are generally assessed through the interpolation of the data previously stored in a LuT.

Although the usage of LuT can be a suitable alternative to decrease the computational burden, it comprehends several shortcomings and limitations which may preclude its application. Firstly, the amount of memory required to store the table must be available, which is closely related with the number of entries of the LuT and, consequently, with the accuracy of the interpolated values. This issue is even more preponderant when dealing with LuT with multiple inputs and outputs, since the number of entries increases exponentially with the number of input and output variables. Secondly, the time required to compute the table can be an obstacle to employ this methodology. Although it only needs to be evaluated once, if the LuT generation is too time-consuming, it is not feasible to consider this option. Finally, the use of LuT to replace an exact function involves considering a limited domain, that is, the values of lower and upper bound of each input variables must be defined, and the LuT does not allow to evaluate values outside such domain.

In a similar manner, the use of LuT in the wheel-rail contact modeling requires the generation of a pre-calculated table which stores the values of the function, such as the normal and creep forces, in a set of points that constitute the domain of the table. Then, during a simulation, for a given input, such as the relative position and orientation between rail and wheel, the output parameters required for the dynamic analysis are computed through the interpolation of the LuT. Therefore, the online calculation of a cumbersome function, which is generally slow but accurate, can be promptly approximated through a linear interpolation of tabulated data.

LuT approaches are employed in a wide variety of fields in which the computational efficiency plays a key role (Palermo et al., 2013; Li et al., 2014; Machado et al., 2014). Bearing in mind that the dynamic simulations of railway vehicles usually involve high computational costs, the contact detection procedure (Bozzone et al., 2011a; Escalona and Aceituno, 2019) and the contact forces evaluation (Kalker, 1996; Piotrowski el al., 2017) are frequently performed resorting to using LuT. Regarding wheel-rail contact forces, the first LuT was developed by the British Rail (Rose, 1984) for a parametrized elliptical contact patch where Kalker's DUVOROL program is used to calculate the creep forces (Kalker, 1982a). Since the LuT was limited to Hertzian contact patches, the elliptical regularization of the non-elliptical contact patches was required. This table had four input parameters and a relatively small size with a total of 3220 entries since, at the time, the pre-calculation time and the computer storage had major limitations. Later, Kalker (1982a) created a larger LuT called USETAB, also based on elliptical regularization of the contact patch. The table had 115 000 entries in which the stored creep forces were determined with the CONTACT software (Kalker, 1990). This LuT was enhanced by Vollebregt (2009) resulting in a table of 100 000 entries called USETAB 1.2. This improved version is currently used in commercial codes, namely NUCARS and VAMPIRE. More recently, a new Kalker Book of Tables for Non-Hertzian contact (KBTNH), where a non-elliptical contact patch regularization has been suggested using five input parameters, was introduced by Piotrowski et al. (2017; 2019). This regularization assumes that the contact patch can be approximated by a single double elliptical contact shape, which allows to capture the longitudinal creep force generated by the spin creepage.

Vollebregt et al. (2012) demonstrated that the USETAB provides significantly better results than other simplified approaches (Shen et al., 1983; Polach, O., 1999; Vollebregt and Wilders, 2011) when compared with the complete rolling contact theory (Kalker, 1990). It must be noted that the accuracy of the interpolated values must be controlled, since the function to be replaced is already an approximation of the reality. Thus, the design of the LuT domain is of paramount importance because it influences the

error of the approximations. Although the increase of the number of points of the LuT tends to improve its accuracy, it also increases the size of the table, and the effort required to generate it, while increasing the computation time needed to search it and interpolating a given point during the dynamic analysis. Therefore, accuracy and efficiency aspects make the selection of the number of LuT points and their location in the complete domain of extreme importance. Typically, the selection is made empirically, due to lack of systematic techniques either to evaluate the LuT accuracy or to generate it. Most of the existing methods are limited to single input and output LuT (Aus and Korn, 1969; Deng et al., 2009; Wilcox et al., 2011) and cannot be extended to multiple inputs and outputs LuT (Magalhães et al., 2018). This work explores aspects of the construction of LuT that balance accuracy and efficiency in a novel way, based on the control of the interpolation errors in each cell of the LuT.

"*Nothing in life is to be feared, it is only to be understood.*
Now is the time to understand more, so that we may fear less."
Marie Curie

3. GEOMETRY OF THE WHEEL-RAIL SYSTEM

In the dynamic analysis of railway vehicles, the numerical definition of the geometry of the contacting bodies for the vehicle-track interaction assumes a preponderant role. Therefore, the methodology selected for describing the wheel and rail surfaces is directly associated with the degree of accuracy with which the results are obtained, since it allows to describe the real geometries of these components with a variable level of precision. The contacting surfaces can be described either by polygonal models, as a polygonal soup, or non-polygonal models, as in the case of parametric or implicit surfaces (Lin and Gottschalk, 1998). In order to take advantage of the shape of the contacting bodies, the wheel and rail are defined through parametric surfaces thus allowing for a continuous description of the surfaces when searching for the contact points. Hence, the parametric description enables to formulate algebraic contact conditions for which the location of the contact point also varies continuously. The selection of the contact detection procedure has a significant impact on the efficiency and accuracy of the dynamic analysis of multibody systems, and its relevance increases with the increasing complexity of the geometry of the contacting surfaces, such as in the case of wheel-rail interaction. In this chapter, the parametrization of the surfaces is presented, and two different contact detection methodologies are discussed. First, the minimum distance method, which has been widely utilized for searching the potential contact points between convex surfaces (Pombo et. al., 2007; Machado et al., 2014; Magalhães et al., 2020), is described. Afterwards, an alternative approach applicable to real wheel profiles that comprise non-convex regions is proposed for the wheel-rail contact.

3.1. Wheel and Rail Geometric Parametrization

Since the geometry of the contacting surfaces constrains the possible contact scenarios, it is crucial to have an accurate and complete description of the wheel and rail geometries. Hence, in this work, wheels and rails are mathematically represented by parametrized surfaces, i.e., the location of any

point on each of surface can be defined by two parameters (Pombo et. al., 2007; Magalhães et al., 2020), as it is schematized in Figure 3.1 for the wheels and the rails.

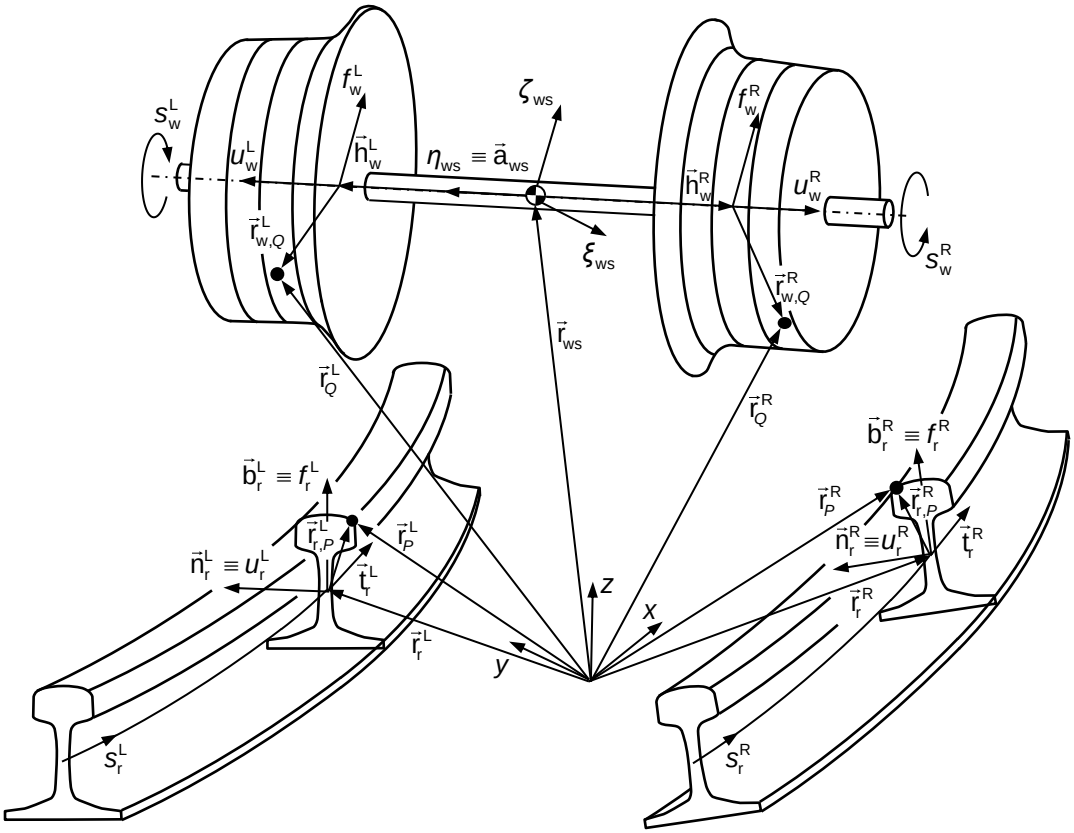

Figure 3.1 – Parametrization of wheel and rail surfaces.

The surface of each rail is obtained through the sweep of its cross-section along a given path, which is represented by a set of nodal points and interpolated with a suitable spline. These nodal points define the position and orientation of the rail as function its arc length, s_r^{side}, as depicted in Figure 3.2. Note that the superscript *side* can be defined as "L" or "R", whether it refers to the left or right rails, respectively. The position of the origin of the rail profile is defined by $\mathbf{r}_r^{side}$ vector, and its orientation is given by a set of vectors $\mathbf{t}_r^{side}$, $\mathbf{n}_r^{side}$ and $\mathbf{b}_r^{side}$, which represent the tangent, normal and binormal vectors, respectively. For each rail, a database is constructed resorting to a pre-processor tool that uses the nominal track design geometry, namely, its curvature and cant angle, and the track irregularities to generate the current track geometry used in the railway dynamic analyses (Pombo and Ambrósio, 2012; Ambrósio et al., 2015). The structure of each database is represented in Figure 3.3, in which N_r is the total number of nodal points, and it contains the values of the vectors $\mathbf{r}_r^{side}$, $\mathbf{t}_r^{side}$, $\mathbf{n}_r^{side}$ and $\mathbf{b}_r^{side}$ in all of them. In order to obtain the rail data for a given location, i.e. s_r^{side}, the database is interpolated using cubic polynomials, which guarantees second order continuity. Then, the rail profile is represented by a

two-dimensional function, in which u_{r}^{side} is the surface parameter that defines the lateral rail coordinate and f_{r}^{side} denotes the dependent vertical coordinate, as it is displayed in Figure 3.4(a). It must be noted that the directions of u_{r}^{side} and f_{r}^{side} coincide with the normal and binormal vectors of the rail, as represented in Figure 3.1.

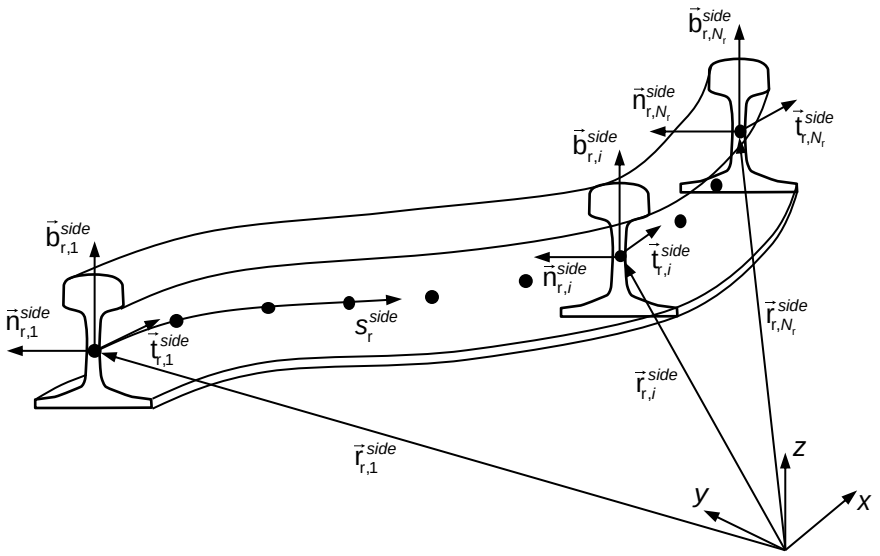

Figure 3.2 – Graphical representation of the rail database.

In turn, since the wheelset is a body of revolution, the wheel surface can be defined by the rotation of its cross-section about its own axis. Thus, any point in the wheel surface is characterized by the angular position s_{w}^{side}, and the lateral coordinate u_{w}^{side}. In a similar manner, the wheel profile is represented by a two-dimensional function, in which f_{w}^{side} denotes the dependent wheel profile coordinate, as depicted in Figure 3.4(b).

s_{r}^{side}	$\mathbf{r}_{\mathrm{r}}^{side}$			$\mathbf{t}_{\mathrm{r}}^{side}$			$\mathbf{n}_{\mathrm{r}}^{side}$			$\mathbf{b}_{\mathrm{r}}^{side}$		
$s_{\mathrm{r},1}^{side}$	$r_{\mathrm{r},1,x}^{side}$	$r_{\mathrm{r},1,y}^{side}$	$r_{\mathrm{r},1,z}^{side}$	$t_{\mathrm{r},1,x}^{side}$	$t_{\mathrm{r},1,y}^{side}$	$t_{\mathrm{r},1,z}^{side}$	$n_{\mathrm{r},1,x}^{side}$	$n_{\mathrm{r},1,y}^{side}$	$n_{\mathrm{r},1,z}^{side}$	$b_{\mathrm{r},1,x}^{side}$	$b_{\mathrm{r},1,y}^{side}$	$b_{\mathrm{r},1,z}^{side}$
⋮	⋮	⋮	⋮	⋮	⋮	⋮	⋮	⋮	⋮	⋮	⋮	⋮
$s_{\mathrm{r},i}^{side}$	$r_{\mathrm{r},i,x}^{side}$	$r_{\mathrm{r},i,y}^{side}$	$r_{\mathrm{r},i,z}^{side}$	$t_{\mathrm{r},i,x}^{side}$	$t_{\mathrm{r},i,y}^{side}$	$t_{\mathrm{r},i,z}^{side}$	$n_{\mathrm{r},i,x}^{side}$	$n_{\mathrm{r},i,y}^{side}$	$n_{\mathrm{r},i,z}^{side}$	$b_{\mathrm{r},i,x}^{side}$	$b_{\mathrm{r},i,y}^{side}$	$b_{\mathrm{r},i,z}^{side}$
⋮	⋮	⋮	⋮	⋮	⋮	⋮	⋮	⋮	⋮	⋮	⋮	⋮
$s_{\mathrm{r},N_{\mathrm{r}}}^{side}$	$r_{\mathrm{r},N_{\mathrm{r}},x}^{side}$	$r_{\mathrm{r},N_{\mathrm{r}},y}^{side}$	$r_{\mathrm{r},N_{\mathrm{r}},z}^{side}$	$t_{\mathrm{r},N_{\mathrm{r}},x}^{side}$	$t_{\mathrm{r},N_{\mathrm{r}},y}^{side}$	$t_{\mathrm{r},N_{\mathrm{r}},z}^{side}$	$n_{\mathrm{r},N_{\mathrm{r}},x}^{side}$	$n_{\mathrm{r},N_{\mathrm{r}},y}^{side}$	$n_{\mathrm{r},N_{\mathrm{r}},z}^{side}$	$b_{\mathrm{r},N_{\mathrm{r}},x}^{side}$	$b_{\mathrm{r},N_{\mathrm{r}},y}^{side}$	$b_{\mathrm{r},N_{\mathrm{r}},z}^{side}$

Figure 3.3 – Representation of rail database with position and orientation in the nodal points as function of arc length.

The definition of both wheel and rail cross sections, represented in Figure 3.4, can be performed through an analytical function or with a set of nodal points, in which the continuous evaluation of both profiles is commonly performed by cubic spline interpolation of the nodal points. In this work, the wheel and

rail profiles are defined analytically according standards (UIC, 2004; BS, 2011). However, the use of nodal points to describe the profiles might be an interesting approach when the shape of the profile changes during the analysis, as in the case of wear studies, or when it is obtained from experimental measurements.

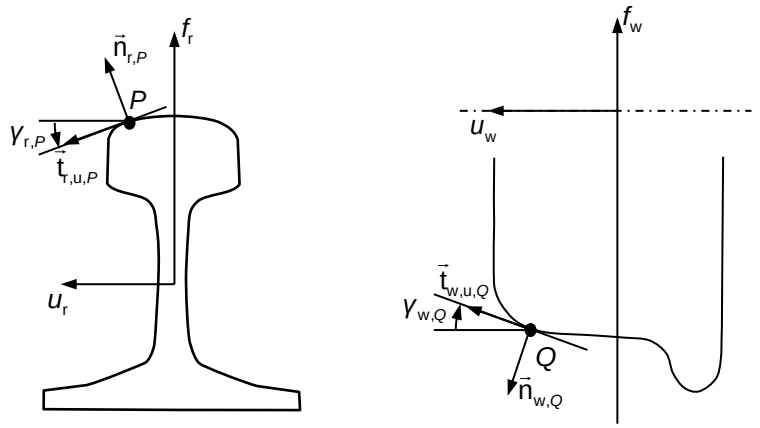

Figure 3.4 – Representation of an arbitrary point and normal and tangential vectors on (a) rail and (b) wheel profiles in their local coordinate system.

Based on the described surface parametrizations, represented in Figure 3.1, two arbitrary points, candidates to contact points, *P* and *Q*, can be defined in the rail and wheel surfaces, respectively, as a function of the surface parameters: $s_{r,P}^{side}$, $u_{r,P}^{side}$, $s_{w,Q}^{side}$ and $u_{w,Q}^{side}$. The position of point *P* is expressed in the global coordinate system as

$$\mathbf{r}_P^{side} = \mathbf{r}_r^{side} + \mathbf{r}_{r,P}^{side} \tag{3.1}$$

where $\mathbf{r}_r^{side}$ denotes the position vector of the origin of the rail profile, which is a function of the rail arc length $s_{r,P}^{side}$, and $\mathbf{r}_{r,P}^{side}$ represents the distance vector between the rail profile origin and point *P* that is calculated as

$$\mathbf{r}_{r,P}^{side} = \mathbf{A}_r^{side}\mathbf{r}_{r,P,r}^{side} \tag{3.2}$$

in which $\mathbf{r}_{r,P,r}^{side}$ denotes the vector $\mathbf{r}_{r,P}^{side}$ in the rail coordinate system and $\mathbf{A}_r^{side}$ is the rail transformation matrix associated with its local coordinate system. Both $\mathbf{r}_{r,P,r}^{side}$ and $\mathbf{A}_r^{side}$ can be defined as

$$\mathbf{r}_{r,P,r}^{side} = \begin{Bmatrix} 0 & u_{r,P}^{side} & f_{r,P}^{side} \end{Bmatrix}^T \tag{3.3}$$

$$\mathbf{A}_r^{side} = \begin{bmatrix} \mathbf{t}_r^{side} & \mathbf{n}_r^{side} & \mathbf{b}_r^{side} \end{bmatrix} \tag{3.4}$$

where $u_{r,P}^{side}$ is the rail lateral surface parameter of point *P*, $f_{r,P}^{side}$ denotes the ordinate of the rail profile function for the position $u_{r,P}^{side}$, as shown in Figure 3.4(a), and $\mathbf{t}_r^{side}$, $\mathbf{n}_r^{side}$ and $\mathbf{b}_r^{side}$ are, respectively, the tangent, normal and binormal vectors of the rail for a given $s_{r,P}^{side}$, as depicted in Figure 3.2.

In turn, an arbitrary point Q located on the wheel surface, following the representation provided in Figure 3.1, is calculated as

$$\mathbf{r}_Q^{side} = \mathbf{r}_{\mathrm{ws}} + \mathbf{h}_{\mathrm{w}}^{side} + \mathbf{r}_{\mathrm{w},Q}^{side} \tag{3.5}$$

in which $\mathbf{r}_{\mathrm{ws}}$ is the position vector of wheelset center of mass, $\mathbf{h}_{\mathrm{w}}^{side}$ represents the local position vector that define location of the origin of the wheel local coordinate system with respect to the wheelset center of mass, which is defined differently according whether it refers to the left or right side, i.e.,

$$\mathbf{h}_{\mathrm{w}}^{\mathrm{L}} = \mathbf{A}_{\mathrm{ws}} \begin{Bmatrix} 0 & H/2 & 0 \end{Bmatrix}^{\mathrm{T}} \qquad \text{or} \qquad \mathbf{h}_{\mathrm{w}}^{\mathrm{R}} = \mathbf{A}_{\mathrm{ws}} \begin{Bmatrix} 0 & -H/2 & 0 \end{Bmatrix}^{\mathrm{T}} \tag{3.6}$$

where H denotes the distance between left and right wheel profiles and $\mathbf{A}_{\mathrm{ws}}$ is the wheelset transformation matrix which defines the orientation of the wheelset local coordinate system relatively to the global coordinate system (Nikravesh, 1988). Moreover, the vector $\mathbf{r}_{\mathrm{w},Q}^{side}$ represents the distance between the wheel profile origin and point Q, which is defined as

$$\mathbf{r}_{\mathrm{w},Q}^{side} = \mathbf{A}_{\mathrm{ws}} \mathbf{A}_{\mathrm{w,s}}^{side} \mathbf{r}_{\mathrm{w},Q,\mathrm{w}}^{side} \tag{3.7}$$

where $\mathbf{r}_{\mathrm{w},Q,\mathrm{w}}^{side}$ is the vector $\mathbf{r}_{\mathrm{w},Q}^{side}$ in the wheel local coordinate system and it is given as

$$\mathbf{r}_{\mathrm{w},Q,\mathrm{w}}^{side} = \begin{Bmatrix} 0 & u_{\mathrm{w},Q}^{side} & f_{\mathrm{w},Q}^{side} \end{Bmatrix}^{\mathrm{T}} \tag{3.8}$$

in which, similarly to the rail case, $u_{\mathrm{w},Q}^{side}$ is the wheel lateral surface parameter of point Q and $f_{\mathrm{w},Q}^{side}$ denotes the ordinate of the wheel profile function for the position $u_{\mathrm{w},Q}^{side}$, as illustrated in Figure 3.4(b). The transformation matrix $\mathbf{A}_{\mathrm{w,s}}^{side}$ specifies the rotation around the wheel axis, which depends on the wheel angular surface parameter of point Q, $s_{\mathrm{w},Q}^{side}$, and is defined in a distinct manner for both wheels, since the left wheel profile is provided, when the right side is regarded, a symmetric profile must be considered. Thus, $\mathbf{A}_{\mathrm{w,s}}^{side}$ can be computed as

$$\mathbf{A}_{\mathrm{w,s}}^{\mathrm{L}} = \begin{bmatrix} \cos\left(s_{\mathrm{w},Q}^{\mathrm{L}}\right) & 0 & \sin\left(s_{\mathrm{w},Q}^{\mathrm{L}}\right) \\ 0 & 1 & 0 \\ -\sin\left(s_{\mathrm{w},Q}^{\mathrm{L}}\right) & 0 & \cos\left(s_{\mathrm{w},Q}^{\mathrm{L}}\right) \end{bmatrix} \quad \text{or} \quad \mathbf{A}_{\mathrm{w,s}}^{\mathrm{R}} = \begin{bmatrix} -\cos\left(s_{\mathrm{w},Q}^{\mathrm{R}}\right) & 0 & -\sin\left(s_{\mathrm{w},Q}^{\mathrm{R}}\right) \\ 0 & -1 & 0 \\ -\sin\left(s_{\mathrm{w},Q}^{\mathrm{R}}\right) & 0 & \cos\left(s_{\mathrm{w},Q}^{\mathrm{R}}\right) \end{bmatrix} \tag{3.9}$$

The definition of both normal and tangential vectors of the parametrized surfaces on the arbitrary points, P and Q, is required to perform the contact detection, whereas the local curvatures at the contact points can be necessary to solve the normal contact force problem. Regarding the rail surface, the tangential vectors on the longitudinal and lateral directions on point P are expressed, respectively, as

$$\mathbf{t}_{\mathrm{r,s},P}^{side} = \mathbf{t}_{\mathrm{r}}^{side} \tag{3.10}$$

$$\mathbf{t}_{\mathrm{r,u},P}^{side} = \mathbf{A}_{\mathrm{r}}^{side}\mathbf{t}_{\mathrm{r,u},P,\mathrm{r}}^{side} \tag{3.11}$$

in which the tangential vector of the rail in the lateral direction on point P in the rail local coordinate system is given by

$$\mathbf{t}_{\mathrm{r,u},P,\mathrm{r}}^{side} = \left\{0 \quad \cos\left(\gamma_{\mathrm{r},P}^{side}\right) \quad \sin\left(\gamma_{\mathrm{r},P}^{side}\right)\right\}^{\mathrm{T}} \tag{3.12}$$

where $\gamma_{\mathrm{r},P}^{side}$ is rail contact angle, which is defined by the angle between the tangent to the rail profile and the lateral direction, as shown in Figure 3.4(a). Thus, the contact angle is calculated as

$$\gamma_{\mathrm{r},P}^{side} = \arctan\left(f_{\mathrm{r},P}^{'side}\right) \tag{3.13}$$

It must be highlighted that the following notation is employed to denote the profile derivatives

$$f_{k,P}^{'side} = \frac{\mathrm{d}f_k^{side}\left(u_{k,P}^{side}\right)}{\mathrm{d}u_k^{side}} \qquad \text{and} \qquad f_{k,P}^{"side} = \frac{\mathrm{d}^2 f_k^{side}\left(u_{k,P}^{side}\right)}{\mathrm{d}u_k^{side\,2}}, \qquad k = \mathrm{w},\ \mathrm{r} \tag{3.14}$$

In a similar manner, the normal vector to the rail surface is calculated as

$$\mathbf{n}_{\mathrm{r},P}^{side} = \mathbf{A}_{\mathrm{r}}^{side}\mathbf{n}_{\mathrm{r},P,\mathrm{r}}^{side} \tag{3.15}$$

where

$$\mathbf{n}_{\mathrm{r},P,\mathrm{r}}^{side} = \left\{0 \quad -\sin\left(\gamma_{\mathrm{r},P}^{side}\right) \quad \cos\left(\gamma_{\mathrm{r},P}^{side}\right)\right\}^{\mathrm{T}} \tag{3.16}$$

Furthermore, the local lateral and longitudinal curvatures of rail surface in point P are computed, respectively, as

$$\kappa_{\mathrm{r},P}^{\mathrm{u},side} = \frac{1}{R_{\mathrm{r},P}^{\mathrm{u},side}} = -\frac{f_{\mathrm{r},P}^{"side}}{\left(1+\left(f_{\mathrm{r},P}^{'side}\right)^2\right)^{3/2}} \tag{3.17}$$

$$\kappa_{\mathrm{r},P}^{\mathrm{s},side} = 0 \tag{3.18}$$

It must be noticed that the rail longitudinal curvature is considered null since the slope variations of the rail path can be negligible for actual tracks.

In what concerns the wheel surface, the tangent vector in the longitudinal direction on point Q is

$$\mathbf{t}_{\mathrm{w,s},Q}^{side} = \mathbf{A}_{\mathrm{ws}}\mathbf{A}_{\mathrm{w,s}}^{side}\mathbf{t}_{\mathrm{w,s},Q,\mathrm{w}}^{side} \tag{3.19}$$

in which the tangent vector in the wheel local coordinate system is expressed differently for the left and right sides as

$$\mathbf{t}_{\mathrm{w,s},Q,\mathrm{w}}^{\mathrm{L}} = \left\{1 \quad 0 \quad 0\right\}^{\mathrm{T}} \qquad \text{or} \qquad \mathbf{t}_{\mathrm{w,s},Q,\mathrm{w}}^{\mathrm{R}} = \left\{-1 \quad 0 \quad 0\right\}^{\mathrm{T}} \tag{3.20}$$

while the tangent of the wheel surface in lateral direction is

$$\mathbf{t}_{\mathrm{w,u},Q}^{side} = \mathbf{A}_{\mathrm{ws}}\mathbf{A}_{\mathrm{w,s}}^{side}\mathbf{t}_{\mathrm{w,u},Q,\mathrm{w}}^{side} \tag{3.21}$$

in which

$$\mathbf{t}_{\mathrm{w,u},Q,\mathrm{w}}^{side} = \left\{0 \quad \cos\left(\gamma_{\mathrm{w},Q}^{side}\right) \quad \sin\left(\gamma_{\mathrm{w},Q}^{side}\right)\right\}^{\mathrm{T}} \tag{3.22}$$

where $\gamma_{\mathrm{w},Q}^{side}$ is the wheel contact angle on point Q, which is represented in Figure 3.4(b) and given by

$$\gamma_{\mathrm{w},Q}^{side} = \arctan\left(f_{\mathrm{w},Q}^{'side}\right) \tag{3.23}$$

Hence, the normal surface vector of the wheel is

$$\mathbf{n}_{\mathrm{w},Q}^{side} = \mathbf{A}_{\mathrm{ws}}\mathbf{A}_{\mathrm{w,s}}^{side}\mathbf{n}_{\mathrm{w},Q,\mathrm{w}}^{side} \tag{3.24}$$

in which

$$\mathbf{n}_{\mathrm{w},Q,\mathrm{w}}^{side} = \left\{0 \quad \sin\left(\gamma_{\mathrm{w},Q}^{side}\right) \quad -\cos\left(\gamma_{\mathrm{w},Q}^{side}\right)\right\}^{\mathrm{T}} \tag{3.25}$$

Finally, the local curvature of the wheel surface in the lateral direction is computed, in an analogous manner to the rail surface, as

$$\kappa_{\mathrm{w},Q}^{\mathrm{u},side} = \frac{1}{R_{\mathrm{w},Q}^{\mathrm{u},side}} = \frac{f_{\mathrm{w},Q}^{''side}}{\left(1+\left(f_{\mathrm{w},Q}^{'side}\right)^2\right)^{3/2}} \tag{3.26}$$

while the local curvature in the longitudinal direction is given by

$$\kappa_{\mathrm{w},Q}^{\mathrm{s},side} = \frac{1}{R_{\mathrm{w},Q}^{\mathrm{s},side}} = \frac{1}{\left|f_{\mathrm{w},Q}^{side}\right|\left(1+f_{\mathrm{w},Q}^{'side}\right)^{1/2}} \tag{3.27}$$

3.2. Wheel Profile Definition

The mathematical representations of wheel and rail profiles play an important role on the study of the wheel-rail contact interaction, since they not only affect significantly the location of contact points and the magnitude and orientation of the contact forces, but also the type of contact that develops. Whether the wheel and rail profiles are defined analytically or by a set of interpolated points, the transition zone between the tread and the flange is often neglected. In this case, the profile is simplified, and the concave region of the wheel is disregarded to avoid performing the contact detection in the negative curvature zone (Pombo et al., 2007; Marquis and Pascal, 2008; Sugiyama et al., 2009). Thus, the contact search is realized with convex surfaces only, which enables a more straightforward contact search leading

to a significant enhancement in terms of computational efficiency (Zhang et al., 2007; Wellmann et al., 2008; Gonçalves et al., 2017).

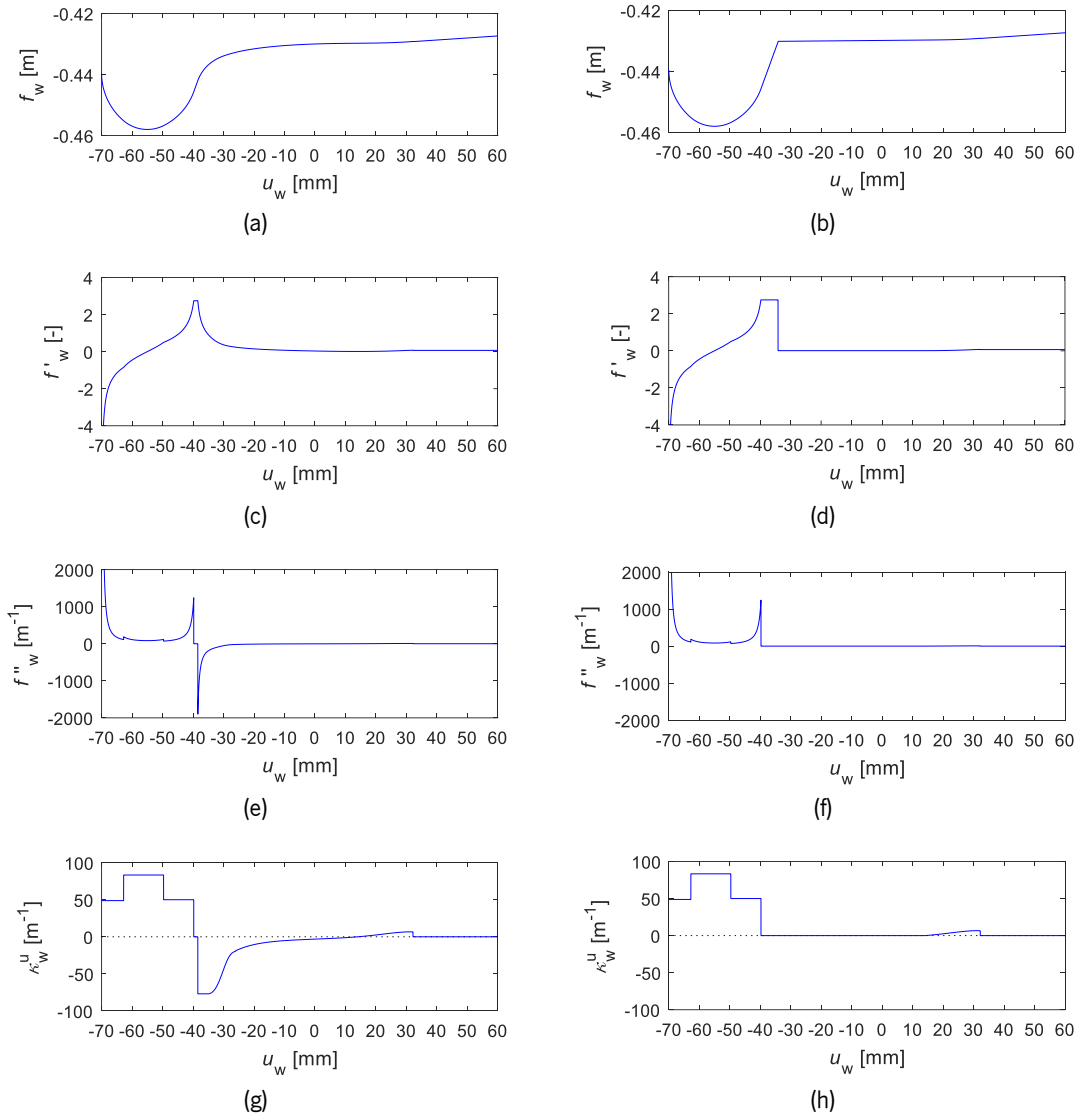

Figure 3.5 – Representation of an original S1002 profile and a modified non-conformal profile, respectively, (a)-(b) the profile function, (c)-(d) first derivative, (e)-(f) second derivative, and (g)-(h) curvature.

For a new wheel, the analytical definition of the profile is typically given in the respective standard as a piecewise function (UIC, 2004). Figure 3.5(a) depicts the S1002 wheel profile for a nominal radius equal to 0.43 m. It must be highlighted that, in contrast to the first derivative of the wheel profile, shown in Figure 3.5(c), its second derivative is not a continuous function, as observed in Figure 3.5(e). Based on the computed derivatives and resorting to Eq. (3.26), the profile curvature is displayed in Figure 3.5(g), which exhibits discontinuities. Hence, it is demonstrated that the curvature of the profile is negative where its lateral coordinate assumes values between -38.4 mm and 14.0 mm, approximately. Thus, to simplify the wheel profile in order to obtain a non-conformal or fully convex wheel surface, the profile curvature is

specified to be zero in this region, which means that two straight lines are drawn from the boundary points keeping the same slope until they intersect each other. The simplified wheel is profile plotted in Figure 3.5(b). This profile can easily be divided into two separate convex curves, one for the tread and another for the flange, each one used independently in the contact detection between wheel and rail. The boundary between these two regions may results in a singular point, however, it must be noted that it is not physically possible that the contact occurs in such a point due to the shape of the rail profile. This is a common geometric assumption that simplifies greatly the calculations but may be abusive for particular wheel profiles or operation conditions.

Since the new rail profile is always convex (BS, 2011), when using Eqs. (3.18) and (3.27) to evaluate the curvature of the surfaces in the rolling direction, it can be noticed that the modified wheel profile ensures that the resultant contacting surfaces are non-conformal. This property may have a paramount importance on the convergence of the contact detection methodologies. However, the assumptions for the modified profiles do not allow the detailed study of local wheel-rail interaction issues, as wear or rolling contact fatigue, being relevant to verify the actual influence of these approximated profiles on the dynamic response of railway systems.

3.3. Contact Detection – Minimum Distance Method

When using the elastic contact force models, as considered in this work, the bodies are allowed to have a slight interference in the contact zone, which symbolizes the elastic deformations due to the contact forces, and it is called virtual penetration (Flores and Lankarani, 2016). Thus, it is common to use the concept of a main contact point, which represents the local of the contact patch which exhibits the maximum penetration between the contacting surfaces. For the case of two arbitrary convex surfaces, as those represented in Figure 3.6, the contact points can be found through the minimum distance condition, that is, when the distance vector between the two points and their normal vectors to the surface are collinear. Since the mathematical definition of two collinear or parallel vectors is given by their null cross product, three mathematical expression can be obtained as

$$\begin{aligned} \mathbf{d}^{side} \times \mathbf{n}_{\mathrm{w},Q}^{side} &= \mathbf{0} \\ \mathbf{d}^{side} \times \mathbf{n}_{\mathrm{r},P}^{side} &= \mathbf{0} \\ \mathbf{n}_{\mathrm{r},P}^{side} \times \mathbf{n}_{\mathrm{w},Q}^{side} &= \mathbf{0} \end{aligned} \tag{3.28}$$

in which the distance vector is defined as

$$\mathbf{d}^{side} = \mathbf{r}_Q^{side} - \mathbf{r}_P^{side} \tag{3.29}$$

and the normal vectors are evaluated as described in section 3.1.

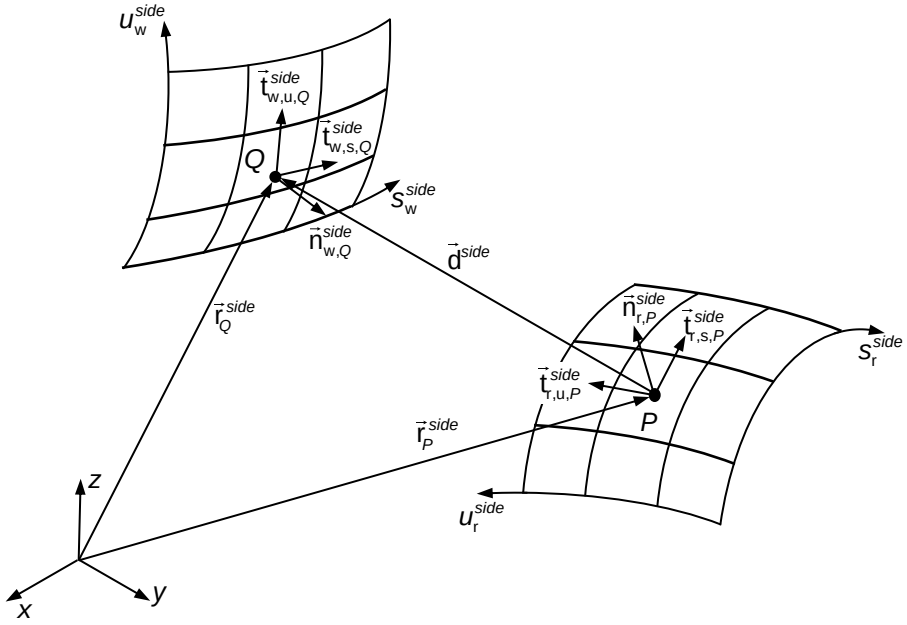

Figure 3.6 – Schematic representation of wheel and rail parametric surfaces for contact detection purposes.

The three constraints from Eq. (3.28) consist of a redundant set of equations, since two of them are enough to ensure the parallelism between the distance vector, $\mathbf{d}^{side}$, the normal vector to the wheel, $\mathbf{n}_{w,Q}^{side}$, and the normal vector to the rail, $\mathbf{n}_{r,P}^{side}$. Moreover, if just the first two conditions are selected, the constraint equations are satisfied, not only when the distance vector is parallel to the normal vectors, but also when the distance vector is null, which is an inappropriate contact detection case. Therefore, to obtain a proper non-redundant set of equations, one of the first two conditions given in Eq. (3.28) must be disregarded. Bearing this in mind, and using the equivalence between the cross product of a given vector and a normal vector to the surface and the inner products of this vector and the tangent vectors to that surface, the minimum distance condition establishes a system of four nonlinear equations (Pombo et. al., 2007; Magalhães et al., 2020), which can assume two different forms depending on which constraint is neglected, as

$$\mathbf{f}_{\text{nl}}\left(s_{r,P}^{side}, u_{r,P}^{side}, s_{w,Q}^{side}, u_{w,Q}^{side}\right) = \mathbf{0} \Leftrightarrow \begin{cases} \tilde{\mathbf{d}}^{side}\mathbf{n}_{w,Q}^{side} = \mathbf{0} \\ \tilde{\mathbf{n}}_{r,P}^{side}\mathbf{n}_{w,Q}^{side} = \mathbf{0} \end{cases} \Leftrightarrow \begin{cases} \left(\mathbf{d}^{side}\right)^{\text{T}}\mathbf{t}_{w,u,Q}^{side} = 0 \\ \left(\mathbf{d}^{side}\right)^{\text{T}}\mathbf{t}_{w,s,Q}^{side} = 0 \\ \left(\mathbf{n}_{r,P}^{side}\right)^{\text{T}}\mathbf{t}_{w,u,Q}^{side} = 0 \\ \left(\mathbf{n}_{r,P}^{side}\right)^{\text{T}}\mathbf{t}_{w,s,Q}^{side} = 0 \end{cases} \tag{3.30}$$

$$\mathbf{f}_{\mathrm{nl}}\left(s_{\mathrm{r},P}^{side}, u_{\mathrm{r},P}^{side}, s_{\mathrm{w},Q}^{side}, u_{\mathrm{w},Q}^{side}\right)=\mathbf{0} \Leftrightarrow \begin{cases} \tilde{\mathbf{d}}^{side}\mathbf{n}_{\mathrm{r},P}^{side}=\mathbf{0} \\ \tilde{\mathbf{n}}_{\mathrm{w},Q}^{side}\mathbf{n}_{\mathrm{r},P}^{side}=\mathbf{0} \end{cases} \Leftrightarrow \begin{cases} \left(\mathbf{d}^{side}\right)^{\mathrm{T}}\mathbf{t}_{\mathrm{r,u},P}^{side}=0 \\ \left(\mathbf{d}^{side}\right)^{\mathrm{T}}\mathbf{t}_{\mathrm{r,s},P}^{side}=0 \\ \left(\mathbf{n}_{\mathrm{w},Q}^{side}\right)^{\mathrm{T}}\mathbf{t}_{\mathrm{r,u},P}^{side}=0 \\ \left(\mathbf{n}_{\mathrm{w},Q}^{side}\right)^{\mathrm{T}}\mathbf{t}_{\mathrm{r,s},P}^{side}=0 \end{cases} \tag{3.31}$$

Each one of these sets of nonlinear equations can be solved by using a root finding algorithm to obtain the set of surface parameters, $s_{\mathrm{r},P}^{side}$, $u_{\mathrm{r},P}^{side}$, $s_{\mathrm{w},Q}^{side}$ and $u_{\mathrm{w},Q}^{side}$, that satisfies the minimum distance condition. For sake of computational efficiency, the modified Newton-Raphson method is employed here to iteratively solve Eq. (3.30) or, alternatively, Eq. (3.31). This method shows good convergency provided that the initial approximation is suitable, which is generally the case when the results obtained in the previous step are used as initial guess for the new equations. The solution of this problem returns two potential contact points, one on each surface, having the problem of the occurrence of contact to be properly checked. Three different scenarios can be identified according to the relative orientation of vectors $\mathbf{n}_{\mathrm{r},P}^{side}$ and $\mathbf{d}^{side}$, as shown in Figure 3.7. This verification can be performed by evaluating the inner product between those vectors. If $\left(\mathbf{n}_{\mathrm{r},P}^{side}\right)^{\mathrm{T}}\mathbf{d}^{side}>0$, there is no contact, as in Figure 3.7(a). In the case that $\left(\mathbf{n}_{\mathrm{r},P}^{side}\right)^{\mathrm{T}}\mathbf{d}^{side}=0$, the two surfaces are locally tangent, which means there is contact with no penetration, as shown in Figure 3.7(b). Finally, if $\left(\mathbf{n}_{\mathrm{r},P}^{side}\right)^{\mathrm{T}}\mathbf{d}^{side}<0$, the contact occurs and there is a virtual penetration or indentation of the surfaces, as observed in Figure 3.7(c).

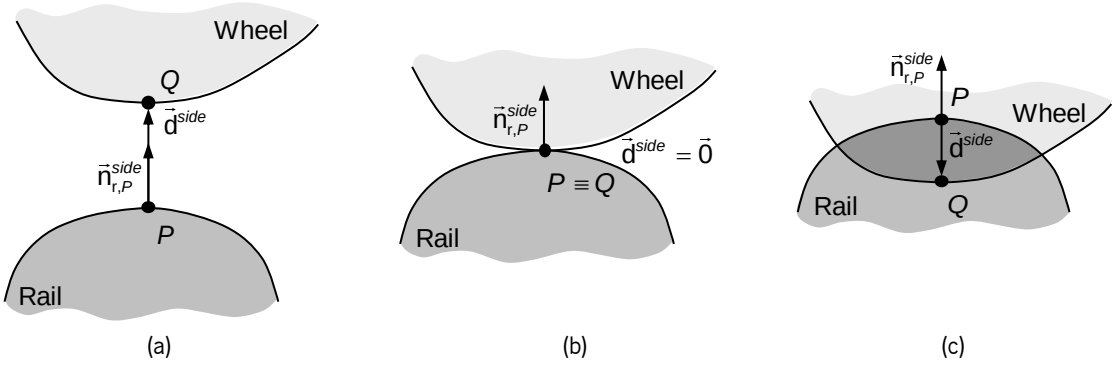

Figure 3.7 – Simplified representation of possible scenarios between convex wheel and rail profiles: (a) No contact; (b) Contact with no penetration; (c) Contact with penetration.

In the presence of two convex surfaces together with an appropriate initial approximation of the surface parameters, this methodology has proven to be effective and robust (Pombo et. al., 2007; Magalhães et al., 2020). However, actual wheels and rails may interact in a conformal region, where one of the surfaces has negative curvature. In this case, it may be not possible to find a solution for the geometric problem given by Eq. (3.30) or (3.31). To clarify this point, a scenario in which the wheel and

rail are aligned, i.e., without yaw, is used as a demonstrative example. Since both elements are aligned, it is easy to identify the plane where the contact points are located, that is, transversal to the rail surface and passing through the wheel axis, as represented in Figure 3.8. Hence, the search for potential contact points can be simplified, since for this plane the longitudinal surface parameter of the rail (s_r) and the angular surface parameter of the wheel (s_w) are kept constant. Thus, the contact detection problem is reduced to the finding of the lateral surface parameters (u_r and u_w) that verify the contact constraints.

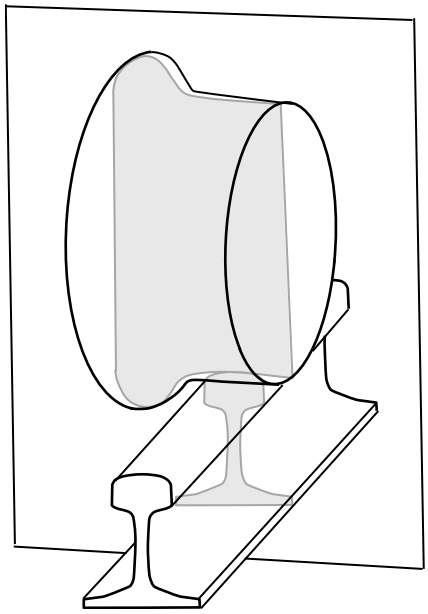

Figure 3.8 – Representation of a contact scenario in which the wheel and rail are aligned and the plane that contains the contact points.

In order to clarify the abovementioned point, the S1002 wheel profile and the UIC50 rail profile are selected. The two cases are depicted in Figure 3.9(a)-(b), where the top of the rail contacts the wheel tread, which leads to a non-conformal contact case, and where the rail corner contacts the tread/flange concordance zone, which is a conformal case. Then, the vector $\mathbf{f}_\mathrm{nl}$, which represents the residual of the contact equations, is evaluated for all possible combinations of the lateral surface parameters in the contact zone and its neighbourhood. Figure 3.9(c)-(d) presents a colormap of the norm of $\mathbf{f}_\mathrm{nl}$ as function of both lateral surface parameters, where a null value indicates that the contact constraint equations are satisfied and, therefore, a potential contact point is identified. For the non-conformal case, it can be observed in Figure 3.9(c) that only one well-defined minimum exists which marked with a dot. Regarding the conformal scenario shown in Figure 3.9(d), several combinations of the wheel and rail parameters spread through the domain closely satisfy the contact equations, meaning that the convergence for an optimal solution is not ensured, and often not possible. Therefore, an alternative methodology is required to solve the contact detection between wheel and rail surfaces when non-convex profiles are considered.

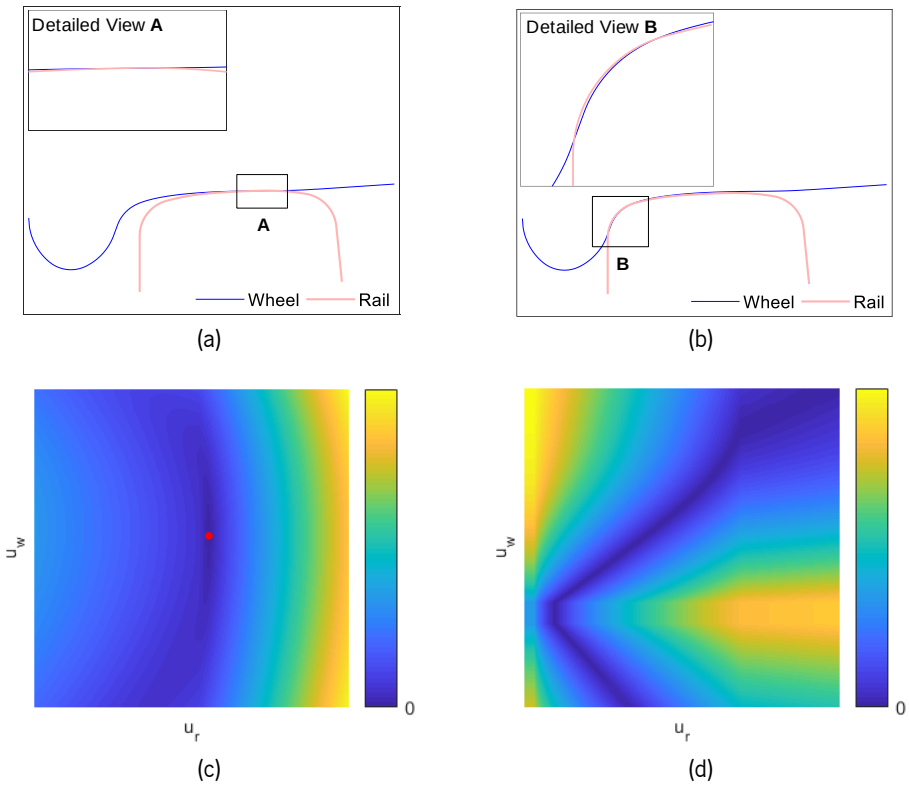

Figure 3.9 – Analysis of the existence of solution of the minimum distance problem for a non-conformal and conformal 2D cases: (a)-(b) wheel-rail relative position, and (c)-(d) norm of the residual of contact equations.

3.4. Contact Detection – Generalized Approach

In order to overcome the limitations of the minimum distance method, in what concerns the identification of the contact points for concave surfaces, a novel approach to deal with the contact detection between general wheel and rail profiles has been developed (Marques et al., 2020). The general idea of this methodology is to define the wheel surface as a set of strips or slices (Ambrósio et al., 2017; Ambrósio and Pombo, 2018) that represents circumferences with different radii, according to the wheel profile, as represented in Figure 3.10(a). Thus, the contact search can be performed between the rail surface and each strip of the wheel. Since the rail has a convex surface, a pair of points that satisfies the minimum distance condition between a wheel strip and the surface is guaranteed. For a given wheel lateral parameter, u_{w}, which defines one strip, the system of the contact constraint equations of (3.30) and (3.31) is reduced to three equations, that is

$$\mathbf{f}_{\mathrm{nl}}\left(s_{\mathrm{r},P}^{side}, u_{\mathrm{r},P}^{side}, s_{\mathrm{w},Q}^{side}\right)=\mathbf{0} \Leftrightarrow \begin{cases} \left(\mathbf{d}^{side}\right)^{\mathrm{T}} \mathbf{t}_{\mathrm{r,u},P}^{side}=0 \\ \left(\mathbf{d}^{side}\right)^{\mathrm{T}} \mathbf{t}_{\mathrm{r,s},P}^{side}=0 \\ \left(\mathbf{n}_{\mathrm{r},P}^{side}\right)^{\mathrm{T}} \mathbf{t}_{\mathrm{w,s},Q}^{side}=0 \end{cases} \tag{3.32}$$

Similarly to Eqs. (3.30) and (3.31), a root finding algorithm is required to solve the system of nonlinear equations defined by Eq. (3.32), namely the Newton-Raphson method is adopted. For each strip, the distance between the potential contact points obtained represents either the penetration, in case of contact, or the separation, otherwise, as observed in Figure 3.10(b). To find the main point of contact, the parameter $u_{\mathrm{w},Q}^{side}$, which identifies the wheel strip, that corresponds to the largest penetration value is found based on an optimization approach. It must be highlighted that for the evaluation of a given strip, Eq. (3.32) has to be solved, and the contact must be checked, being the penetration given by

$$\delta = \left\| \mathbf{d}^{side} \right\| \tag{3.33}$$

If the strip is not in contact with the rail surface, δ denotes the separation distance, otherwise, it denotes the penetration amount.

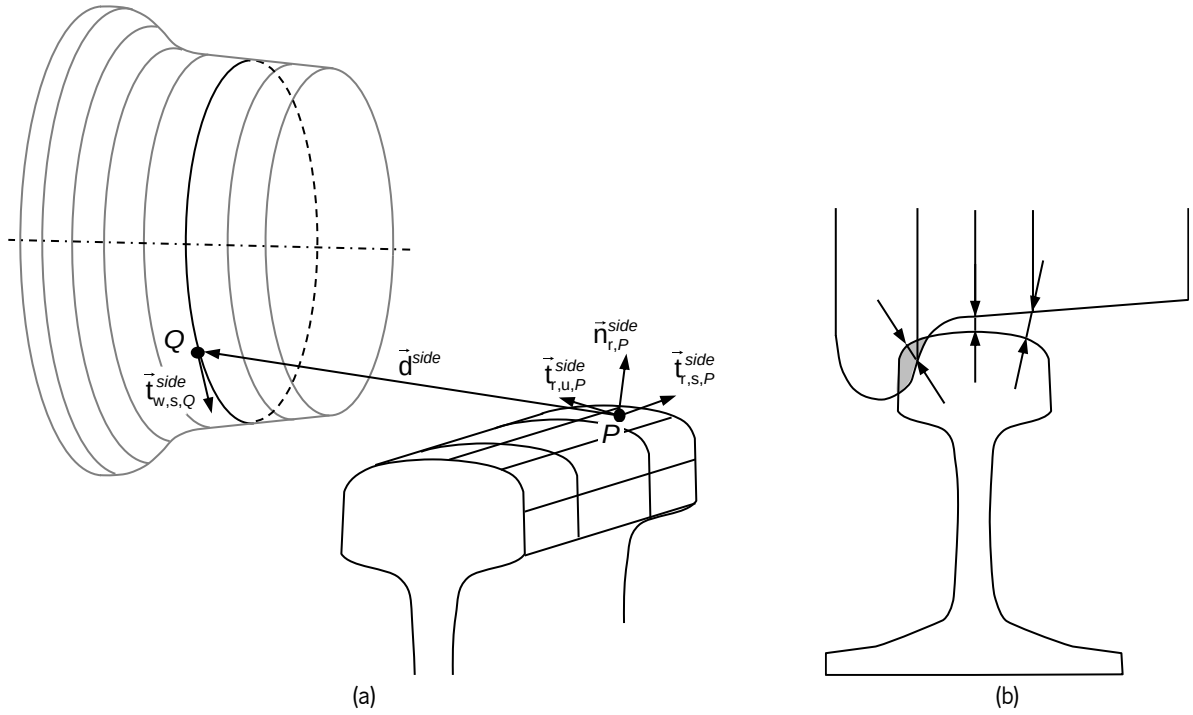

Figure 3.10 – Representation of the wheel divided into strips: (a) Contact evaluation between two arbitrary points; (b) Schematic 2D representation of the resultant candidate points.

The performance of this methodology is demonstrated for wheel-rail static cases (Marques et al., 2019a). However, for each wheel-rail pair, Eq. (3.32) has to be solved with respect to several wheel strips to find the maximum penetration point which leads to dynamic simulations that demand a high computational cost. To ensure an effective usability of this methodology, it is required to reduce the size of the problem to be solved in each step. One reasonable assumption to simplify the contact search is to consider that the rail is locally straight, i.e., the orientation of the rail coordinate frame is fixed during each

contact search. This is a suitable hypothesis, because the curvature of the rail path is very large when compared to the size of the local contact zone. In this contact detection procedure, the first step is to find the position and orientation of the rail local coordinate system to be used for the contact search, which varies along the rail longitudinal parameter, s_{r}^{side}, as represented for the right rail in Figure 3.11(a). Here, the point of the rail path, which is closest to the wheel center, must correspond to the rail coordinate frame. The value of parameter s_{r}^{side} that minimizes the distance between the wheel and rail profiles, represented by vector $\mathbf{d}_{\mathrm{rw}}^{side}$ shown in Figure 3.11, is evaluated as

$$\mathbf{d}_{\mathrm{rw}}^{side} = \mathbf{r}_{\mathrm{r}}^{side} - \mathbf{r}_{\mathrm{w}}^{side} \tag{3.34}$$

in which

$$\mathbf{r}_{\mathrm{w}}^{side} = \mathbf{r}_{\mathrm{ws}} + \mathbf{h}_{\mathrm{w}}^{side} \tag{3.35}$$

The minimum distance between the wheel center and the rail profile origin is obtained when the distance vector and tangent vector are perpendicular to each other, and, therefore, satisfy the condition

$$\left(\mathbf{d}_{\mathrm{rw}}^{side}\right)^{\mathrm{T}} \mathbf{t}_{\mathrm{r}}^{side} = 0 \tag{3.36}$$

This condition is a function of the rail longitudinal parameter, and it can be solved in an efficient manner using the parameter value obtained in the previous time step of integration as the initial approximation. Hence, the obtained s_{r}^{side} is used to find the rail profile location, $\mathbf{r}_{\mathrm{r}}^{side}$, and orientation, $\mathbf{A}_{\mathrm{r}}^{side}$, for the remaining steps of the contact search for which the rail is considered to be straight as pictured in Figure 3.11(b).

Subsequently, a wheel coordinate system aligned with the rail coordinate system is found, which allows a more immediate rotation from the wheel coordinate system to the rail coordinate system. So far, the wheel orientation is defined by the wheelset transformation matrix, $\mathbf{A}_{\mathrm{ws}}$, as in Eq. (3.7), which is decomposed into three unit vectors that represent the axes of the wheelset local frame, as displayed in Figure 3.12, that is,

$$\mathbf{A}_{\mathrm{ws}} = \begin{bmatrix} \mathbf{n}_{\mathrm{ws}} & \mathbf{a}_{\mathrm{ws}} & \mathbf{b}_{\mathrm{ws}} \end{bmatrix} \tag{3.37}$$

where $\mathbf{n}_{\mathrm{ws}}$ is the normal unit vector along the ξ_{ws} axis, $\mathbf{a}_{\mathrm{ws}}$ denotes the axial unit vector along the η_{ws} axis, and $\mathbf{b}_{\mathrm{ws}}$ represents the binormal unit vector along the ζ_{ws} axis. With the intent to obtain a wheel coordinate system aligned with the rail frame, this coordinate system is rotated about the wheelset axis a given angle β^{side}, as depicted in Figure 3.12 for the right wheel. The novel transformation matrix of the wheel is defined as

$$\mathbf{A}_{\mathrm{w}}^{side} = \left[\mathbf{n}_{\mathrm{w}}^{side} \quad \mathbf{a}_{\mathrm{w}}^{side} \quad \mathbf{b}_{\mathrm{w}}^{side} \right] \tag{3.38}$$

in which

$$\mathbf{a}_{\mathrm{w}}^{side} = \mathbf{a}_{\mathrm{ws}} \tag{3.39}$$

$$\mathbf{b}_{\mathrm{w}}^{side} = \frac{\tilde{\mathbf{t}}_{\mathrm{r}}^{side} \mathbf{a}_{\mathrm{w}}^{side}}{\left\| \tilde{\mathbf{t}}_{\mathrm{r}}^{side} \mathbf{a}_{\mathrm{w}}^{side} \right\|} \tag{3.40}$$

$$\mathbf{n}_{\mathrm{w}}^{side} = \tilde{\mathbf{a}}_{\mathrm{w}}^{side} \mathbf{b}_{\mathrm{w}}^{side} \tag{3.41}$$

The wheel transformation matrix allows the wheel angular coordinate, s_{w}^{side}, to be measured from the same position relatively to rail. This means that when $s_{\mathrm{w},Q}^{side} = 0$, point Q is located in the lower part of the wheel, since this coordinate system does not follow the wheel rolling motion. It must be noted that this coordinate system differs whether the contact search is performed in the left or right wheel, unless the tangent direction for both rails is exactly the same.

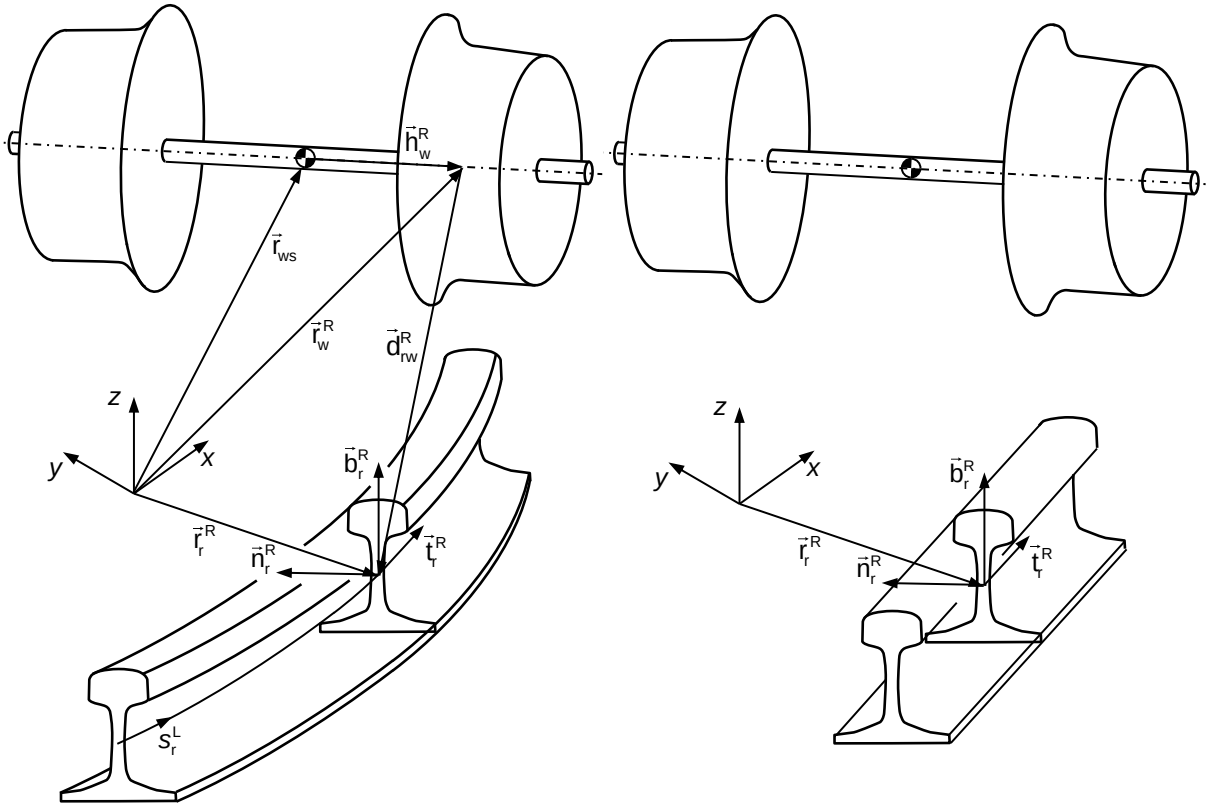

(a) (b)

Figure 3.11 – Representation of the determination of rail local coordinate system: (a) real rail and (b) straight rail approximation.

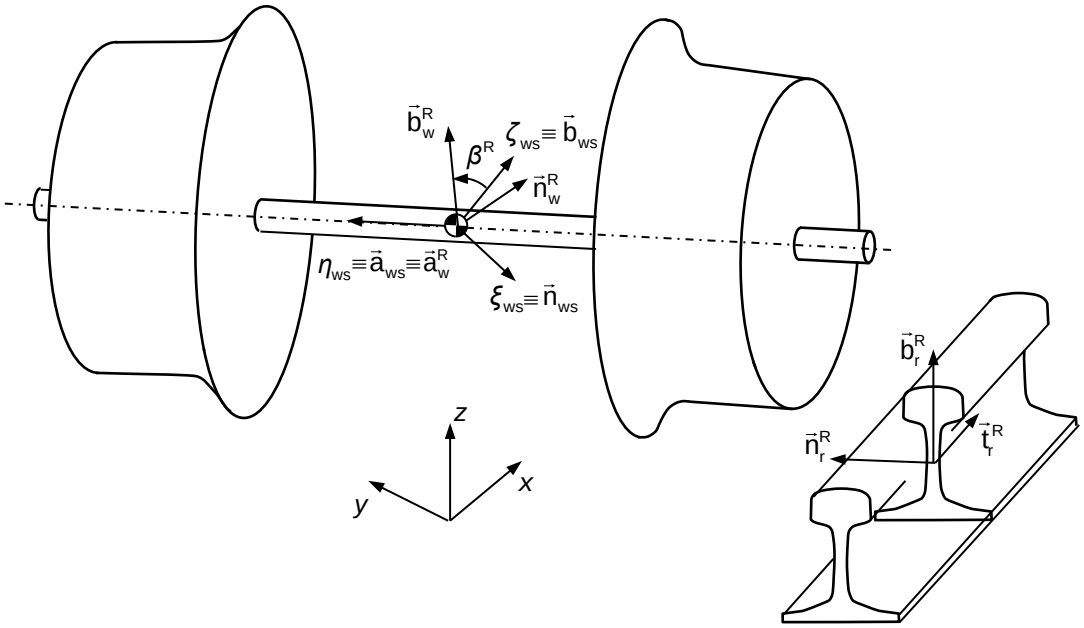

Figure 3.12 – Representation of wheel local coordinate system resulting from the rotation of the wheelset coordinate system.

Due to the introduction of the concept of wheel transformation matrix, the Eqs. (3.7), (3.19), (3.21) and (3.24) can be rewritten, respectively, as

$$\mathbf{r}_{\mathrm{w},Q}^{side} = \mathbf{A}_{\mathrm{w}}^{side}\mathbf{A}_{\mathrm{w,s}}^{side}\mathbf{r}_{\mathrm{w},Q,\mathrm{w}}^{side} \tag{3.42}$$

$$\mathbf{t}_{\mathrm{w,s},Q}^{side} = \mathbf{A}_{\mathrm{w}}^{side}\mathbf{A}_{\mathrm{w,s}}^{side}\mathbf{t}_{\mathrm{w,s},Q,\mathrm{w}}^{side} \tag{3.43}$$

$$\mathbf{t}_{\mathrm{w,u},Q}^{side} = \mathbf{A}_{\mathrm{w}}^{side}\mathbf{A}_{\mathrm{w,s}}^{side}\mathbf{t}_{\mathrm{w,u},Q,\mathrm{w}}^{side} \tag{3.44}$$

$$\mathbf{n}_{\mathrm{w},Q}^{side} = \mathbf{A}_{\mathrm{w}}^{side}\mathbf{A}_{\mathrm{w,s}}^{side}\mathbf{n}_{\mathrm{w},Q,\mathrm{w}}^{side} \tag{3.45}$$

Based on the relation between the wheel and rail coordinate systems, the roll angle, φ, and the yaw angle, α, are obtained through the successive rotation of the axial unit vector of the wheel, as displayed in Figure 3.13. First, the vector $\mathbf{a}_{\mathrm{w}}^{side}$ must be converted to rail local coordinates as

$$\mathbf{a}_{\mathrm{w,r}}^{side} = \mathbf{A}_{\mathrm{r}}^{side\ -1}\mathbf{a}_{\mathrm{w}}^{side} \tag{3.46}$$

Then, the roll angle can be evaluated as

$$\varphi^{side} = \arctan\left(\frac{a_{\mathrm{w,r},3}^{side}}{a_{\mathrm{w,r},2}^{side}}\right) \tag{3.47}$$

in which the last element of the subscript corresponds to the respective element of the vector. Thus, the rotation matrix relative to the roll angle is expressed as

$$\mathbf{R}_{\varphi}^{side}=\begin{bmatrix}1 & 0 & 0\\ 0 & \cos\left(\varphi^{side}\right) & -\sin\left(\varphi^{side}\right)\\ 0 & \sin\left(\varphi^{side}\right) & \cos\left(\varphi^{side}\right)\end{bmatrix} \tag{3.48}$$

To find the axial vector without roll in the local rail coordinate system, the rail has to be rotated the symmetric of the roll angle, i.e.,

$$\mathbf{a}_{\mathrm{w,r},\varphi}^{side}=\mathbf{R}_{-\varphi}^{side}\mathbf{a}_{\mathrm{w,r}}^{side} \tag{3.49}$$

Hence, vector $\mathbf{a}_{\mathrm{w,r},\varphi}^{side}$ is used to determine the yaw angle as

$$\alpha^{side}=\arctan\left(-\frac{a_{\mathrm{w,r},\varphi,1}^{side}}{a_{\mathrm{w,r},\varphi,2}^{side}}\right) \tag{3.50}$$

In a similar manner to the roll motion, the rotation matrix regarding the yaw angle is written as

$$\mathbf{R}_{\alpha}^{side}=\begin{bmatrix}\cos\left(\alpha^{side}\right) & -\sin\left(\alpha^{side}\right) & 0\\ \sin\left(\alpha^{side}\right) & \cos\left(\alpha^{side}\right) & 0\\ 0 & 0 & 1\end{bmatrix} \tag{3.51}$$

Since the obtained roll and yaw angles are associated with the relative position of each wheel and the rail, they must be calculated separately for the left and right wheels.

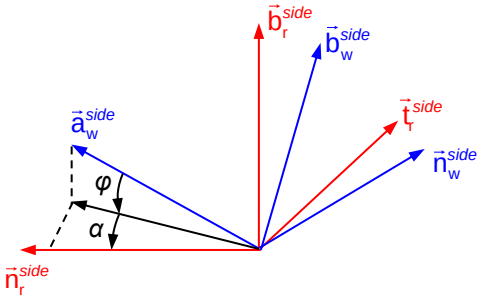

Figure 3.13 – Representation of the rotation of the wheel coordinate system to determine roll and yaw angles.

One of the constraints to find the contact points concerns the parallelism between both normal vectors. Since the rail is considered to be locally straight, the normal unit vector to the surface must be always in the plane formed by $\mathbf{n}_{\mathrm{r}}^{side}$ and $\mathbf{b}_{\mathrm{r}}^{side}$, regardless the rail lateral coordinate. This implies that the normal unit vector to the wheel surface is also on the referred plane, meaning that the first element of this vector in the rail local coordinate system is zero, i.e.,

$$n_{\mathrm{w},Q,\mathrm{r},1}^{side}=0 \tag{3.52}$$

Furthermore, the coordinates of a vector defined in the wheel coordinate system correlate to the rail coordinate system through the two rotations represented in Figure 3.13. Therefore, the normal unit vector to the wheel surface is given in the rail coordinate system as

$$\mathbf{n}_{\mathrm{w},Q,\mathrm{r}}^{side} = \mathbf{R}_{\varphi}^{side}\mathbf{R}_{\alpha}^{side}\mathbf{A}_{\mathrm{w,s}}^{side}\mathbf{n}_{\mathrm{w},Q,\mathrm{w}}^{side} \tag{3.53}$$

By introducing Eqs. (3.9), (3.25), (3.48) and (3.51), Eq. (3.53) is rewritten for the left and right sides, respectively, as

$$\mathbf{n}_{\mathrm{w},Q,\mathrm{r}}^{\mathrm{L}} = \begin{Bmatrix} -\mathrm{c}\left(\gamma_{\mathrm{w},Q}^{\mathrm{L}}\right)\mathrm{s}\left(s_{\mathrm{w},Q}^{\mathrm{L}}\right)\mathrm{c}\left(\alpha^{\mathrm{L}}\right)-\mathrm{s}\left(\gamma_{\mathrm{w},Q}^{\mathrm{L}}\right)\mathrm{s}\left(\alpha^{\mathrm{L}}\right) \\ -\mathrm{c}\left(\gamma_{\mathrm{w},Q}^{\mathrm{L}}\right)\mathrm{s}\left(s_{\mathrm{w},Q}^{\mathrm{L}}\right)\mathrm{s}\left(\alpha^{\mathrm{L}}\right)\mathrm{c}\left(\varphi^{\mathrm{L}}\right)+\mathrm{s}\left(\gamma_{\mathrm{w},Q}^{\mathrm{L}}\right)\mathrm{c}\left(\alpha^{\mathrm{L}}\right)\mathrm{c}\left(\varphi^{\mathrm{L}}\right)+\mathrm{s}\left(\varphi^{\mathrm{L}}\right)\mathrm{c}\left(\gamma_{\mathrm{w},Q}^{\mathrm{L}}\right)\mathrm{c}\left(s_{\mathrm{w},Q}^{\mathrm{L}}\right) \\ -\mathrm{c}\left(\gamma_{\mathrm{w},Q}^{\mathrm{L}}\right)\mathrm{s}\left(s_{\mathrm{w},Q}^{\mathrm{L}}\right)\mathrm{s}\left(\alpha^{\mathrm{L}}\right)\mathrm{s}\left(\varphi^{\mathrm{L}}\right)+\mathrm{s}\left(\gamma_{\mathrm{w},Q}^{\mathrm{L}}\right)\mathrm{c}\left(\alpha^{\mathrm{L}}\right)\mathrm{s}\left(\varphi^{\mathrm{L}}\right)-\mathrm{c}\left(\gamma_{\mathrm{w},Q}^{\mathrm{L}}\right)\mathrm{c}\left(s_{\mathrm{w},Q}^{\mathrm{L}}\right)\mathrm{c}\left(\varphi^{\mathrm{L}}\right) \end{Bmatrix} \tag{3.54}$$

$$\mathbf{n}_{\mathrm{w},Q,\mathrm{r}}^{\mathrm{R}} = \begin{Bmatrix} \mathrm{c}\left(\gamma_{\mathrm{w},Q}^{\mathrm{R}}\right)\mathrm{s}\left(s_{\mathrm{w},Q}^{\mathrm{R}}\right)\mathrm{c}\left(\alpha^{\mathrm{R}}\right)+\mathrm{s}\left(\gamma_{\mathrm{w},Q}^{\mathrm{R}}\right)\mathrm{s}\left(\alpha^{\mathrm{R}}\right) \\ \mathrm{c}\left(\gamma_{\mathrm{w},Q}^{\mathrm{R}}\right)\mathrm{s}\left(s_{\mathrm{w},Q}^{\mathrm{R}}\right)\mathrm{s}\left(\alpha^{\mathrm{R}}\right)\mathrm{c}\left(\varphi^{\mathrm{R}}\right)-\mathrm{s}\left(\gamma_{\mathrm{w},Q}^{\mathrm{R}}\right)\mathrm{c}\left(\alpha^{\mathrm{R}}\right)\mathrm{c}\left(\varphi^{\mathrm{R}}\right)+\mathrm{s}\left(\varphi^{\mathrm{R}}\right)\mathrm{c}\left(\gamma_{\mathrm{w},Q}^{\mathrm{R}}\right)\mathrm{c}\left(s_{\mathrm{w},Q}^{\mathrm{R}}\right) \\ \mathrm{c}\left(\gamma_{\mathrm{w},Q}^{\mathrm{R}}\right)\mathrm{s}\left(s_{\mathrm{w},Q}^{\mathrm{R}}\right)\mathrm{s}\left(\alpha^{\mathrm{R}}\right)\mathrm{s}\left(\varphi^{\mathrm{R}}\right)-\mathrm{s}\left(\gamma_{\mathrm{w},Q}^{\mathrm{R}}\right)\mathrm{c}\left(\alpha^{\mathrm{R}}\right)\mathrm{s}\left(\varphi^{\mathrm{R}}\right)-\mathrm{c}\left(\gamma_{\mathrm{w},Q}^{\mathrm{R}}\right)\mathrm{c}\left(s_{\mathrm{w},Q}^{\mathrm{R}}\right)\mathrm{c}\left(\varphi^{\mathrm{R}}\right) \end{Bmatrix} \tag{3.55}$$

in which ‘s’ and ‘c’ denote the sine and cosine functions, respectively, for sake of simplicity. By applying the constraint given by Eq. (3.52) to Eqs. (3.54) and (3.55), the following condition can be written for both left and right sides as

$$\sin\left(s_{\mathrm{w},Q}^{side}\right) = -\frac{\sin\left(\gamma_{\mathrm{w},Q}^{side}\right)\sin\left(\alpha^{side}\right)}{\cos\left(\gamma_{\mathrm{w},Q}^{side}\right)\cos\left(\alpha^{side}\right)} \tag{3.56}$$

Through some mathematical manipulation, and introducing Eq. (3.23), yields

$$s_{\mathrm{w},Q}^{side} = \arcsin\left(-\tan\left(\alpha^{side}\right) f_{\mathrm{w},Q}^{'side}\right) \tag{3.57}$$

Thus, it is possible to conclude that the angular coordinate of the wheel surface that allows the parallelism between the wheel and rail normal vectors can be calculated analytically as a function of the lateral surface parameter of the wheel, $u_{\mathrm{w},Q}^{side}$, and the yaw angle, α^{side}. This represents a significant gain in terms of efficiency, since this parameter does not need to be obtained when solving the contact conditions defined by Eq. (3.32). In that sense, since the wheel strip is a full circumference, Eq. (3.57) returns two solutions from which only the one close to the rail is considered. Hence, there is only one potential contact point for each wheel lateral coordinate, and the set of wheel potential contact points constitutes a three-dimensional curve. In order to check the existence of contact, this curve is projected onto the rail cross-section and the intersections between this curve and the rail profile represent zones of penetration and,

consequently, contact. Each of these zones represents a different contact patch, and their intersections indicate the lower and upper bounds of the interpenetration zone, $u_{\mathrm{w,lower}}^{side}$ and $u_{\mathrm{w,upper}}^{side}$ for the wheel, and $u_{\mathrm{r,lower}}^{side}$ and $u_{\mathrm{r,upper}}^{side}$ for the rail. The contact solution is obtained separately for each patch. Finally, if these curves do not intersect, there is no contact between the wheel and rail.

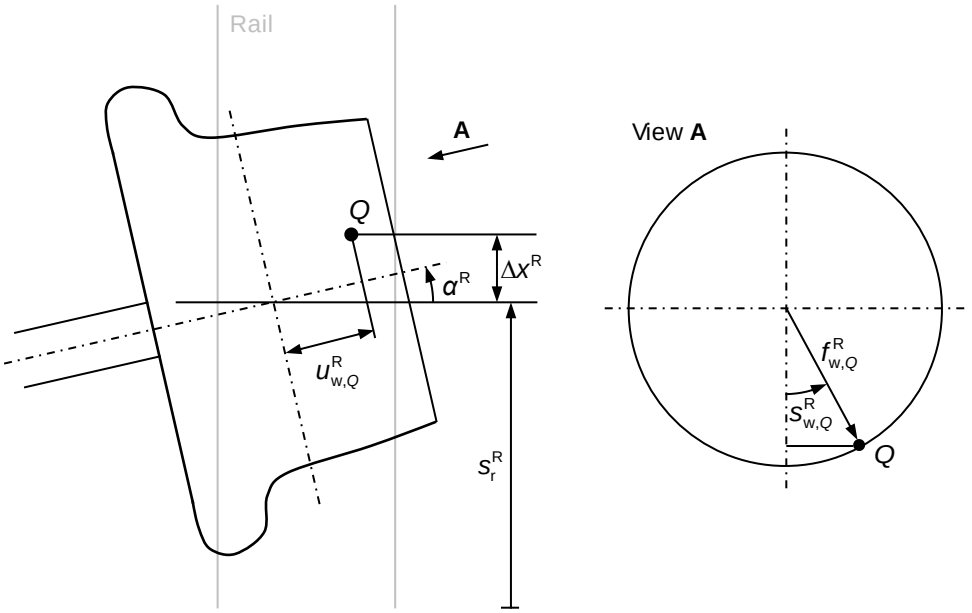

Figure 3.14 – Representation of the increment of the location of the contact point in the rail longitudinal direction.

The contact conditions also require that the distance vector between wheel and rail contact points and the normal unit vector to the rail surface are parallel. Thus, for a given wheel lateral position $u_{\mathrm{w},Q}^{side}$, using Eq. (3.57) and, then, Eq. (3.42), the position vector of point Q is calculated. Since the distance vector is given by Eq. (3.29) and the normal unit vector to the rail is within the plane formed by $\mathbf{n}_{\mathrm{r}}^{side}$ and $\mathbf{b}_{\mathrm{r}}^{side}$, it is mandatory that the wheel and rail contact points have the same coordinate along the rail tangential direction. This coordinate differs from the rail longitudinal parameter obtained through the solution of Eq. (3.36) due to the existence of a yaw angle, as shown in Figure 3.14 for the right side. Therefore, by considering the yaw angle and the wheel lateral coordinate, the increment of the location of the contact point in the rail longitudinal direction is found, following the representation of Figure 3.14, as

$$\Delta x^{\mathrm{R}} = u_{\mathrm{w},Q}^{\mathrm{R}} \sin\left(\alpha^{\mathrm{R}}\right) + \left| f_{\mathrm{w},Q}^{\mathrm{R}} \right| \sin\left(s_{\mathrm{w},Q}^{\mathrm{R}}\right) \cos\left(\alpha^{\mathrm{R}}\right) \tag{3.58}$$

hence, Eq. (3.57) is introduced, and Eq. (3.58) is generalized for both sides as

$$\Delta x^{\mathrm{L}} = \left(\left| f_{\mathrm{w},Q}^{\mathrm{L}} \right| f_{\mathrm{w},Q}^{'\mathrm{L}} - u_{\mathrm{w},Q}^{\mathrm{L}} \right) \sin\left(\alpha^{\mathrm{L}}\right) \quad \text{or} \quad \Delta x^{\mathrm{R}} = \left(u_{\mathrm{w},Q}^{\mathrm{R}} - \left| f_{\mathrm{w},Q}^{\mathrm{R}} \right| f_{\mathrm{w},Q}^{'\mathrm{R}} \right) \sin\left(\alpha^{\mathrm{R}}\right) \tag{3.59}$$

Accordingly, Eq. (3.3) must be replaced by

$$\mathbf{r}_{\mathrm{r},P,\mathrm{r}}^{side} = \left\{ \Delta x^{side} \quad u_{\mathrm{r},P}^{side} \quad f_{\mathrm{r},P}^{side} \right\}^{\mathrm{T}} \tag{3.60}$$

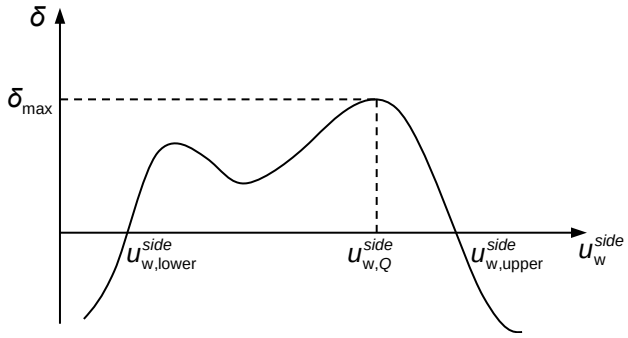

Figure 3.15 – Representation of the variation of penetration for each wheel strip.

At this stage, the potential contact points depend on the wheel and rail lateral coordinates only, because the wheel angular coordinate and the longitudinal position along the rail can be evaluated analytically. To find the wheel strip that returns the maximum penetration, only the rail lateral coordinate has to be found for each strip. Consequently, instead of solving a system of three non-linear equations presented in Eq. (3.32), only one equation must be satisfied, that is,

$$\left(\mathbf{d}^{side}\right)^{\mathrm{T}} \mathbf{t}_{\mathrm{r,u},P}^{side} = 0 \tag{3.61}$$

The substitution of Eq. (3.32) by Eq. (3.61) represents a substantial simplification in terms of computational efficiency, which leads to a feasible implementation of this methodology on the dynamic simulation of a railway vehicle running on a track. Overall, this approach consists of finding the wheel lateral parameter that maximizes the penetration between contact points of each contact zone, as represented in Figure 3.15. Therefore, an optimization problem is formulated as

$$\begin{aligned} &\min\left(-\delta\left(u_{\mathrm{w},Q}^{side}\right)\right) \\ &u_{\mathrm{w},Q}^{side} \in \left[u_{\mathrm{w,lower}}^{side} \quad u_{\mathrm{w,upper}}^{side}\right] \end{aligned} \tag{3.62}$$

Thus, for each strip, the wheel angular parameter is calculated using Eq. (3.57), the longitudinal position on the rail is computed employing Eq. (3.59), and the rail lateral parameter is found through Eq. (3.61). This nonlinear equation can be also solved using an iterative root finding algorithm such as the Newton-Raphson method.

3.5. Summary and Conclusions

In this chapter, the most relevant geometric aspects of the wheel-rail interaction are addressed. Both wheel and rail surfaces are described by parametric surfaces, which take advantage of the fact that the wheel is a solid of revolution and the rail is an extruded solid. Bearing in mind that the contact search

is more expeditious when the potentially colliding surfaces are convex, the wheel profiles geometric representation is commonly simplified to avoid the transition zone between the wheel tread and wheel flange, which is concave. Thus, the surface parametrization procedure used in the context of this work is presented, namely the position of an arbitrary point, the normal surface vector, the tangent vectors and the curvatures are defined as functions of both surface parameters. The simplification of the wheel profile to eliminate the concave region is explained and its consequences discussed.

In a multibody dynamic simulation of railway vehicles, the efficiency of the contact detection procedure has a preponderant role, therefore, a methodology that allows to search rapidly for the potential contact points in a continuous manner along the profile is pursued. The minimum distance method follows these requirements, although it demands that the contact is between convex surfaces to achieve a successful convergence. However, for more accurate studies, the real wheel profile must be considered, which presents some numerical problems, as demonstrated in section 3.3. These results show that, in a non-conformal zone, the main point of contact is well-defined with the contact conditions provided by the minimum distance method, while, in a conformal zone, the algorithm does not converge. Thus, an alternative approach to search for the contact points, which is based on the evaluation of the contact between each wheel strip and the rail, is provided here. This method allows for the existence of multiple contact patches in each wheel-rail pair and searches the strip which corresponds to the maximum virtual penetration for each patch. To improve the efficiency of the proposed methodology, the assumption that the rail is locally straight is used, which expedites the calculation of some of the surface's parameters. Although this novel approach requires more computational effort than the minimum distance method, it exploits the fact that the wheel is a solid of revolution to be divided into strips, which allows the search of contact points in its concave zone.

"*A man may imagine things that are false, but he can only understand things that are true.*"
Isaac Newton

4. CONTACT MECHANICS OF THE WHEEL-RAIL INTERACTION

The study of rolling contact has gained scientific relevance from the mechanics of materials point of view, essentially through the characterization of the relations between stresses and deformations arising from the contact between two solid surfaces (Johnson, 1985). Railway vehicles, journal and roller bearings, gears teeth, and cylinder seals are among the most investigated mechanical components, where the main focus is the improvement of efficiency and reliability on their design. In the context of multibody dynamics, most of the contact interactions can be modeled as point or line contact, where the contact patch is assumed to share the geometric and material properties of a single point. In these cases, the normal pressure and tangential tractions are neglected, and simplified to single force, which comprehensively lowers the computational cost while still being a suitable approximation in most dynamic studies of multibody mechanical systems. However, for a detailed analysis of the contact phenomena, such as wear or rolling contact fatigue predictions, the contact shape and size, as well as stress distributions must be computed (Halme and Andersson, 2010). Moreover, when the conformality between the contacting surfaces exists, most of the assumptions of the point contact approach can no longer be applied, since the contact patch tends to increase when compared with the characteristic dimension of the surfaces. Regarding the wheel-rail interaction, two main procedures can be adopted, namely the constraint and elastic approaches. In this chapter, three different methodologies, which use the elastic approach and, therefore, allow the local deformation of the contacting bodies, are presented. The ability of each model to compute the size, shape and pressure distribution on the contact patch is discussed in detail. First, a simple viscoelastic Hertzian-based model is described. Then, a non-Hertzian model which involves the discretization of the contact patch into strips over the longitudinal direction is addressed. Finally, a novel enhanced methodology to deal with conformal contact scenarios by considering a curved patch is introduced and its performance is compared with the remaining methods through several wheel-rail static configurations.

4.1. Hertzian-based Contact Model

The contact interaction between two elastic bodies can be treated according Hertz theory, thus evaluating the size and shape of the contact patch based on the information of the main contact point, namely where the maximum penetration occurs (Hertz, 1881). The application of Hertz theory simplifies in great measure the evaluation of normal contact forces, but its validity involves the fulfillment of several assumptions, i.e.: (i) the bodies have an isotropic linear elastic behavior; (ii) the strains are small enough to remain in the elastic range; (iii) the surfaces are continuous, and their curvature is constant across the contact patch; (iv) both bodies can be treated as elastic half-spaces and their surfaces cannot be conformal; (iv) the frictional effects do not affect the calculation of normal contact pressure (Hertz, 1881; Goldsmith, 1960; Johnson, 1985). Although most of these assumptions are violated for actual wheel-rail interactions, the Hertzian contact approach is still a suitable approximation for several railway applications as its results have small deviations with respect to those of more comprehensive approaches for many practical cases.

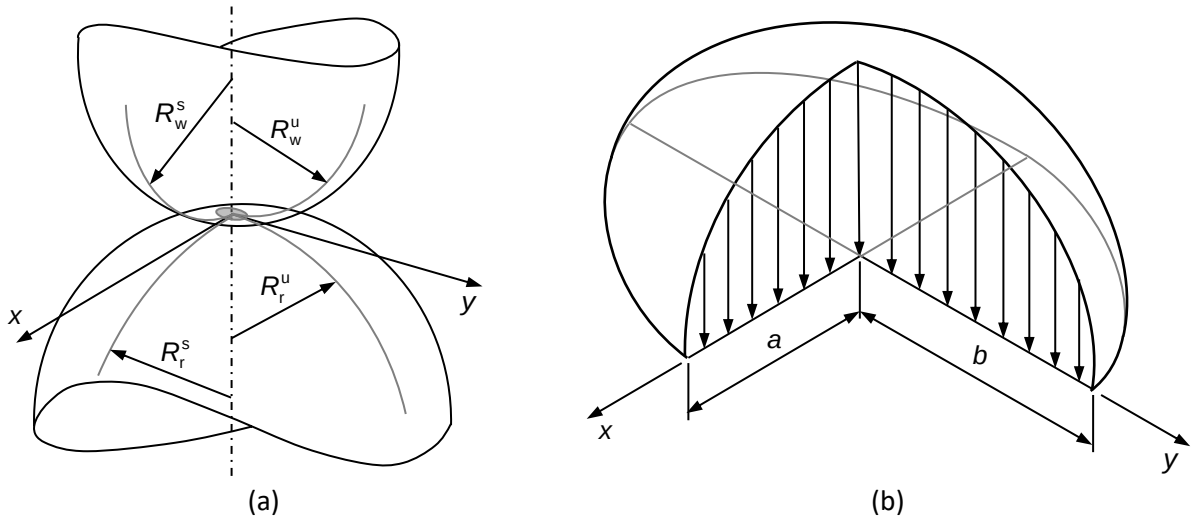

Figure 4.1 – Representation of Hertz contact: (a) geometry of contacting bodies, and (b) pressure distribution.

Since the curvature is considered constant in the lateral and longitudinal directions, in both contacting bodies, the distance between the undeformed surfaces in the vicinity of the contact can be approximated by a quadratic function, which is schematically represented in Figure 4.1(a) and mathematically expressed as

$$z(x, y) = Ax^2 + By^2 \tag{4.1}$$

where A and B represent the average curvatures of both surfaces in each principal direction and they can be computed as follows

$$A = \left(\kappa_{\mathrm{r},P}^{\mathrm{s}} + \kappa_{\mathrm{w},Q}^{\mathrm{s}}\right)/2 \tag{4.2}$$

$$B = \left(\kappa_{\mathrm{r},P}^{\mathrm{u}} + \kappa_{\mathrm{w},Q}^{\mathrm{u}}\right)/2 \tag{4.3}$$

The curvatures of each surface can be obtained resorting to Eqs. (3.17), (3.18), (3.26) and (3.27). It must be noted that the superscript $side$ is omitted in what follows in this Chapter for sake of simplicity, however, the difference between variables for left and right sides can be observed in Chapter 3. Considering the pseudo-penetration of both wheel and rail surfaces, their distance can be evaluated as

$$z_{\mathrm{p}}(x, y) = z(x, y) - \delta \tag{4.4}$$

where δ denotes the maximum penetration of both profiles defined by Eq. (3.33) and located on the origin of reference frame of the contact patch. It must be noted that z_{p} assumes negative values in the interpenetration region.

Using the assumptions for the Hertzian contact, the contact patch is planar and assumes an elliptical configuration, as pictured in Figure 4.1(b), its semi-ellipsoidal contact pressure distribution is

$$p(x, y) = p_0 \sqrt{1 - \left(\frac{x}{a}\right)^2 - \left(\frac{y}{b}\right)^2} \tag{4.5}$$

where a and b are the semi-axes of the contact ellipse and p_0 denotes the maximum contact pressure given as

$$p_0 = \frac{3 f_{\mathrm{n}}^{\mathrm{H}}}{2\pi a b} \tag{4.6}$$

in which $f_{\mathrm{n}}^{\mathrm{H}}$ is the magnitude of normal contact force that, according Hertz's law, it describes a nonlinear spring behavior as

$$f_{\mathrm{n}}^{\mathrm{H}} = K\delta^n \tag{4.7}$$

where K represents the generalized contact stiffness, and n is an exponent that defines the degree of nonlinearity determined from material properties, which is typically equal to 1.5 for metallic contacts. In what concerns the generalized contact stiffness, which depends on the local geometry of the contacting bodies and on their material characteristics, it is evaluated as

$$K = \frac{4C_\delta}{3\left(h_{\mathrm{w}} + h_{\mathrm{r}}\right)\sqrt{A+B}} \tag{4.8}$$

where the parameter C_δ is a function of the ratio A/B, which is tabulated in the references (Goldsmith, 1960; Lankarani, 1988; Pombo, 2004). The terms h_{w} and h_{r} are the wheel and rail material parameters, respectively, which can be given as

$$h_k = \frac{1-\sigma_k{}^2}{\pi E_k} \qquad \text{with} \qquad k = \mathrm{w, r} \tag{4.9}$$

where E is the Young's modulus, and σ represents the Poisson's ratio of respective element. Since the material properties are constant for the wheel-rail pair, this contact model ensures the continuity of the normal force unless there is a major change on the contact curvature between two consecutive time steps. The size of both longitudinal and lateral semi-axes of the contact ellipse can be evaluated, respectively, as

$$a = m\sqrt[3]{\frac{3\pi}{4}\frac{h_\mathrm{w}+h_\mathrm{r}}{A+B}\,f_\mathrm{n}^\mathrm{H}} \tag{4.10}$$

$$b = n\sqrt[3]{\frac{3\pi}{4}\frac{h_\mathrm{w}+h_\mathrm{r}}{A+B}\,f_\mathrm{n}^\mathrm{H}} \tag{4.11}$$

where m and n are tabulated values (Goldsmith, 1960; Lankarani, 1988; Pombo, 2004) and can be determined as function of

$$\theta = \arccos\left(\frac{B-A}{A+B}\right) \tag{4.12}$$

Regarding the normal contact force evaluation, the original pure elastic Hertz model is often modified to consider the energy dissipation (Machado et al., 2012; Alves et al., 2015). The viscoelastic contact model used here employs the coefficient of restitution to make a distinction between the contact force during the compression and restitution phases. The energy dissipated is given by the area inside the hysteresis loop of loading/unloading cycles, as represented in Figure 4.2. This modified version of Hertz contact model includes a tolerance velocity to smooth the discontinuity of the contact force in the transition between both phases (Ambrósio and Pombo, 2018). Hence, the normal force can be calculated as

$$f_\mathrm{n}^\mathrm{H,d} = f_\mathrm{n}^\mathrm{H} c_\mathrm{d} \tag{4.13}$$

where the damping factor is evaluated as

$$c_\mathrm{d} = \begin{cases} c_\mathrm{e} & \dot{\delta} \le -v_0 \\ \left[c_\mathrm{e} + \left(1-c_\mathrm{e}\right)\left(3r^2 - 2r^3\right)\right] & -v_0 < \dot{\delta} < v_0 \\ 1 & \dot{\delta} \ge v_0 \end{cases} \tag{4.14}$$

in which

$$r = \frac{\dot{\delta} + v_0}{2v_0} \tag{4.15}$$

where $\dot{\delta}$ expresses the penetration velocity, v_0 is the penetration velocity tolerance, and c_e represents the coefficient of restitution.

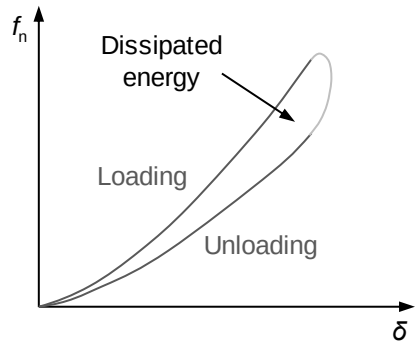

Figure 4.2 – Relation between force and penetration for the modified Hertz model.

The penetration velocity quantifies the rate of deformation in the normal contact direction, and it is expressed as

$$\dot{\delta} = \left(\dot{\mathbf{r}}_Q - \dot{\mathbf{r}}_P\right)^{\mathrm{T}} \mathbf{n}_{\mathrm{r},P} \tag{4.16}$$

in which $\dot{\mathbf{r}}_P$ and $\dot{\mathbf{r}}_Q$ denote the velocity vector of points *P* and *Q*, respectively. Here, $\dot{\mathbf{r}}_P$ is null, since the track is assumed to be rigid, while $\dot{\mathbf{r}}_Q$, according the rigid body theory, is calculated as

$$\dot{\mathbf{r}}_Q = \dot{\mathbf{r}}_{\mathrm{ws}} + \tilde{\boldsymbol{\omega}}_{\mathrm{ws}} \left(\mathbf{h}_{\mathrm{w}} + \mathbf{r}_{\mathrm{w},Q}\right) \tag{4.17}$$

where $\dot{\mathbf{r}}_{\mathrm{ws}}$ represents the velocity vector of the wheelset, and $\tilde{\boldsymbol{\omega}}_{\mathrm{ws}}$ is the skew-symmetric matrix associated with the angular velocity vector of the wheelset, $\boldsymbol{\omega}_{\mathrm{ws}}$.

4.2. Non-Hertzian Contact Patch

Although Hertz theory is widely used for the normal force evaluation in the dynamic simulation of wheel-rail contact, some of its assumptions are often violated. The wheel and rail can be treated as a revolution body and an extruded body, respectively, therefore, their curvature in the rolling direction can be expected to be constant. However, the hypothesis of constant curvature over the contact patch is recognizably not satisfied in the lateral direction, which leads to the adoption of a semi-Hertzian approach where the contact pressure distribution is elliptical only for the rolling direction (Piotrowski and Kik, 2008). This aspect is more evident in some particular wheel-rail configurations or when using worn profiles, which may lead to conformal or multipoint contact. Hence, the assumption of an elliptical contact patch tends to be a poor approximation of the normal pressure distribution which affects the reliability of the vehicle dynamics simulations.

4.2.1. Planar Contact Patch

In the general case of the interaction between two convex surfaces, assuming they are totally rigid, an interpenetration region appears as represented in Figure 4.3(a). However, considering the elasticity of the contacting bodies, their surfaces tend to deform and establish an effective contact area which is smaller than the interpenetration region. In this case, it is suitable to consider that the contact patch is planar, which means that the normal pressure distribution would have a constant direction over the entire contact zone.

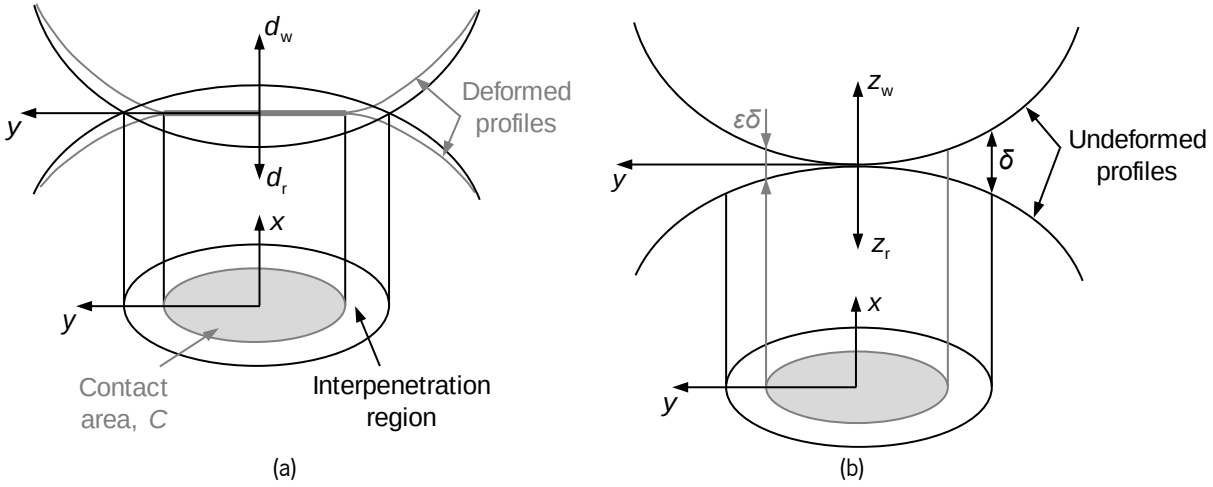

Figure 4.3 – Schematic representation of the contact between convex surfaces, namely (a) the deformed surfaces and actual planar contact region, and (b) the distance between undeformed profiles.

Assuming that the contacting bodies present local elasticity, the distance between the deformed wheel and rail profiles can be given as

$$d(x,y) = d_{\mathrm{w}}(x,y) + d_{\mathrm{r}}(x,y) \tag{4.18}$$

where the functions d_{w} and d_{r} are represented in Figure 4.3(a). Accordingly, the distance or separation between profiles is null inside the actual contact area as

$$d(x,y) = 0 \quad \text{if } (x,y) \in C \tag{4.19}$$

and it can be generally given as (Piotrowski and Kik, 2008)

$$d(x,y) = z_{\mathrm{wr}}(x,y) - \delta + w_{\mathrm{w}}(x,y) + w_{\mathrm{r}}(x,y) \tag{4.20}$$

in which w_{w} and w_{r} denote the displacement of both wheel and rail surfaces, respectively, and the distance between undeformed surfaces represented in Figure 4.3(b) and, for the non-Hertzian case, Eq.(4.1) is replaced by

$$z_{\mathrm{wr}}(x,y) = Ax^2 + f(y) \tag{4.21}$$

where A can be evaluated resorting to Eq. (4.2) and, consequently, to Eq. (3.18)

$$z_{\mathrm{wr}}(x,y)=\frac{x^2}{2R_{\mathrm{w}}^{\mathrm{s}}(y)}+f(y) \tag{4.22}$$

in which $R_{\mathrm{w}}^{\mathrm{s}}$ is the wheel radius in the rolling direction which varies along the lateral coordinate of the contact patch, and an arbitrary undeformed distance function $f(y)$ is taken into account instead of the quadratic function used in Eq. (4.1). It must be emphasized that the origin of the reference frame is located at the main point of contact, i.e., with maximum pseudo-penetration. However, in a more general case, the reference system can be placed in a different location, hereafter, the position of the main point of contact is regarded as y_{c}. Hence, at this point, the undeformed distance between both profiles is null, $z_{\mathrm{wr}}(0,y_{\mathrm{c}})=0$, as regarded in Figure 4.3(b).

Since the actual contact area is similar but smaller than the interpenetration region, as depicted in Figure 4.3, the identification of the shape of the contact patch must consider this feature. Therefore, one approach to handle this issue consists of assuming that the actual contact area is bounded by the boundary points for which the distance between the undeformed profiles is a given fraction of the total penetration. Thus, the limits of the contact patch can be obtained by solving the following equation

$$z(x_{\mathrm{L}}(y),y)=\varepsilon\delta \tag{4.23}$$

where ε is the correction factor for the penetration, which takes into account the deformation of the contacting surfaces that lead the actual contact area to be smaller than interpenetration region, as schematized in Figure 4.3. $x_{\mathrm{L}}(y)$ represents the leading edge of the contact patch for a given lateral coordinate that, combining Eq. (4.22) and Eq. (4.23), is calculated as

$$x_{\mathrm{L}}(y)=\sqrt{2R_{\mathrm{w}}^{\mathrm{s}}(y)\left[\varepsilon\delta-f(y)\right]} \tag{4.24}$$

It is now necessary to find the undeformed distance between profiles to identify the shape of contact patch. Considering an arbitrary interaction between the wheel and rail in a non-conformal region, as represented in Figure 4.4(a), the points *P*, on the rail, and *Q*, on the wheel, which return the maximum penetration, can be obtained with the contact detection methodology provided in the Chapter 3. Thus, the wheel and rail profiles must be evaluated according to the contact patch reference frame, which is exhibited in Figure 4.4(c), and defined resorting to the normal and tangent vectors to the surfaces, namely $x_{\mathrm{cp}}\equiv\mathbf{t}_{\mathrm{w,s},Q}$, $y_{\mathrm{cp}}\equiv\mathbf{t}_{\mathrm{w,u},Q}$ and $z_{\mathrm{cp}}\equiv\mathbf{n}_{\mathrm{r},P}$. To perform this evaluation the contact patch is discretized into strips, i.e. slices along the rolling direction, and the distance between profiles is measured in each strip.

This methodology is illustrated in Figure 4.4(c), where dots represent the center of each strip on both wheel and rail profiles, and all strips have the same width (Δs).

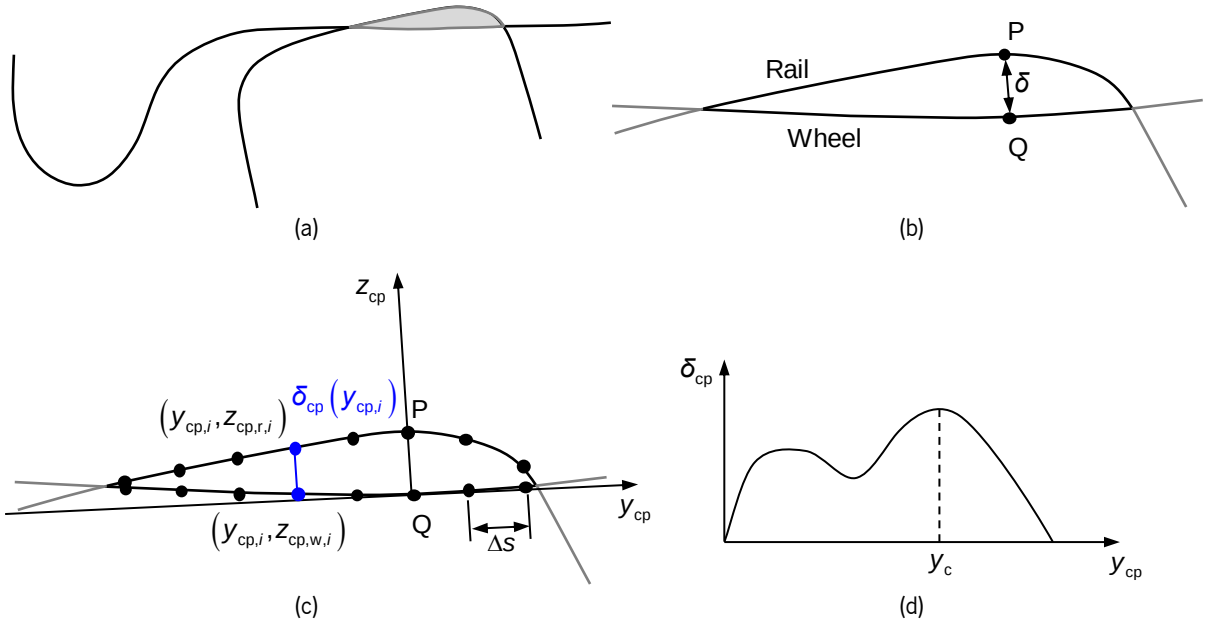

Figure 4.4 – Definition of the penetration along the interpenetration region in the wheel lateral direction for convex contacts: (a) interaction of wheel and rail in a non-conformal region; (b) representation of contact zone and main point of contact; (c) contact patch reference frame and identification of strips along the lateral direction; (d) representation of the penetration along the interference region.

Instead of evaluating the undeformed distance between the tangent profiles, the penetration along interference region is calculated for each strip, these two quantities are related as

$$\delta_{\mathrm{cp}}(y_{\mathrm{cp},i}) = \delta - f(y_{\mathrm{cp},i}) \tag{4.25}$$

in which $y_{\mathrm{cp},i}$ is the lateral coordinate of strip i in the contact patch reference system. Moreover, to save computation time, the evaluation of the penetration starts in the maximum penetration point and stops when it returns a negative value which means that the strip is outside of the interpenetration region. This procedure must be done for both directions to identify properly the boundaries of the contact area.

Assuming that the yaw angle between the wheel and the rail is null for the calculation of the contact patch (Magalhães et al., 2019), the center point of each strip for both wheel and rail is located on the plane $(y_{\mathrm{cp}} / z_{\mathrm{cp}})$, therefore, the coordinate x_{cp} is null for every strip.

Two approaches to obtain the position of the point of strip i on the wheel, either with its surface parameters as

$$\mathbf{r}_{y_i \mathrm{w}} = \mathbf{r}_{\mathrm{ws}} + \mathbf{h}_{\mathrm{w}} + \mathbf{r}_{\mathrm{w},y_i} \tag{4.26}$$

or by adding the distance vector to point Q using the contact patch reference system

$$\mathbf{r}_{y_i\mathrm{w}} = \mathbf{r}_{\mathrm{ws}} + \mathbf{h}_{\mathrm{w}} + \mathbf{r}_{\mathrm{w},Q} + \mathbf{r}_{\mathrm{cp,w},i} \tag{4.27}$$

where

$$\mathbf{r}_{\mathrm{cp,w},i} = \mathbf{A}_{\mathrm{cp}} \begin{Bmatrix} 0 & y_{\mathrm{cp},i} & z_{\mathrm{cp,w},i} \end{Bmatrix}^{\mathrm{T}} \tag{4.28}$$

in which the contact patch transformation matrix is given as

$$\mathbf{A}_{\mathrm{cp}} = \begin{bmatrix} \mathbf{t}_{\mathrm{w,s},Q} & \mathbf{t}_{\mathrm{w,u},Q} & \mathbf{n}_{\mathrm{r},P} \end{bmatrix} \tag{4.29}$$

Combining Eqs. (4.26) and (4.27), and introducing Eqs. (3.42) and (4.28), a system of equations is written as

$$\begin{Bmatrix} 0 & y_{\mathrm{cp},i} & z_{\mathrm{cp,w},i} \end{Bmatrix}^{\mathrm{T}} = \mathbf{B}_{\mathrm{w}} \begin{Bmatrix} 0 & \left(u_{\mathrm{w},i} - u_{\mathrm{w},Q}\right) & \left(f_{\mathrm{w},i} - f_{\mathrm{w},Q}\right) \end{Bmatrix}^{\mathrm{T}} \tag{4.30}$$

with

$$\mathbf{B}_{\mathrm{w}} = \mathbf{A}_{\mathrm{cp}}{}^{-1} \mathbf{A}_{\mathrm{w}} \mathbf{A}_{\mathrm{w,s}} \tag{4.31}$$

Although Eq. (4.30) is constituted by three equations, only two of them are linearly independent, and they can be used to calculate the two unknowns, $u_{\mathrm{w},i}$ and $z_{\mathrm{cp,w},i}$. The value of $f_{\mathrm{w},i}$ is also unknown, however, it is defined as function of $u_{\mathrm{w},i}$. Therefore, $u_{\mathrm{w},i}$ and $f_{\mathrm{w},i}$ can be found by iteratively solving the nonlinear equation that results from the second line of Eq. (4.31) as

$$B_{\mathrm{w}(2,2)}\left(u_{\mathrm{w},i} - u_{\mathrm{w},Q}\right) + B_{\mathrm{w}(2,3)}\left(f_{\mathrm{w},i} - f_{\mathrm{w},Q}\right) - y_{\mathrm{cp},i} = 0 \tag{4.32}$$

Then, these values are used to determine the coordinate of the point of strip i on the wheel as

$$z_{\mathrm{cp,w},i} = B_{\mathrm{w}(3,2)}\left(u_{\mathrm{w},i} - u_{\mathrm{w},Q}\right) + B_{\mathrm{w}(3,3)}\left(f_{\mathrm{w},i} - f_{\mathrm{w},Q}\right) \tag{4.33}$$

An analogous procedure is applied to determine the coordinates of the points of strips on the rail profile. Thus, the point on strip i can be expressed employing the surface parameters as

$$\mathbf{r}_{y_i\mathrm{r}} = \mathbf{r}_{\mathrm{r}} + \mathbf{r}_{\mathrm{r},y_i} \tag{4.34}$$

or through point P using the contact patch reference frame as

$$\mathbf{r}_{y_i\mathrm{r}} = \mathbf{r}_{\mathrm{r}} + \mathbf{r}_{\mathrm{r},P} + \mathbf{r}_{\mathrm{cp,r},i} \tag{4.35}$$

where

$$\mathbf{r}_{\mathrm{cp,r},i} = \mathbf{A}_{\mathrm{cp}} \begin{Bmatrix} 0 & y_{\mathrm{cp},i} & z_{\mathrm{cp,r},i} - \delta \end{Bmatrix}^{\mathrm{T}} \tag{4.36}$$

Similarly, combining Eqs. (4.34) and (4.35), and resorting to Eqs. (3.3) and (4.36), a new system of equations is formulated as

$$\left\{0 \quad y_{\mathrm{cp},i} \quad z_{\mathrm{cp,r},i}-\delta\right\}^{\mathrm{T}}=\mathbf{B}_{\mathrm{r}}\left\{0 \quad \left(u_{\mathrm{r},i}-u_{\mathrm{r},P}\right) \quad \left(f_{\mathrm{r},i}-f_{\mathrm{r},P}\right)\right\}^{\mathrm{T}} \tag{4.37}$$

in which

$$\mathbf{B}_{\mathrm{r}}=\mathbf{A}_{\mathrm{cp}}{}^{-1}\mathbf{A}_{\mathrm{r}} \tag{4.38}$$

Once more, based on Eq. (4.37), the $u_{\mathrm{r},i}$ is calculated by solving the nonlinear equation expressed as

$$B_{\mathrm{r}(2,2)}\left(u_{\mathrm{r},i}-u_{\mathrm{r},P}\right)+B_{\mathrm{r}(2,3)}\left(f_{\mathrm{r},i}-f_{\mathrm{r},P}\right)-y_{\mathrm{cp},i}=0 \tag{4.39}$$

and the remaining coordinate of the point of the strip on the rail profile is defined as

$$z_{\mathrm{cp,r},i}=B_{\mathrm{r}(3,2)}\left(u_{\mathrm{r},i}-u_{\mathrm{r},P}\right)+B_{\mathrm{r}(3,3)}\left(f_{\mathrm{r},i}-f_{\mathrm{r},P}\right)+\delta \tag{4.40}$$

Considering the effect of yaw angle between the wheel and rail on the determination of the distance of both profiles, the transformation matrix $\mathbf{A}_{\mathrm{w,s}}$ must be defined differently for each strip, since it depends on the wheel angular parameter, s_{w}, that varies with along the wheel lateral coordinate when yaw angle is not zero (see Eq. (3.57)). Hence, to compute the coordinate of the wheel point on strip i, Eq. (4.30) is replaced by

$$\left\{x_{\mathrm{cp},i} \quad y_{\mathrm{cp},i} \quad z_{\mathrm{cp,w},i}\right\}^{\mathrm{T}}=\mathbf{A}_{\mathrm{cp}}{}^{-1}\mathbf{A}_{\mathrm{w}}\left[\mathbf{A}_{\mathrm{w,s},i}\left\{0 \quad u_{\mathrm{w},i} \quad f_{\mathrm{w},i}\right\}^{\mathrm{T}}-\mathbf{A}_{\mathrm{w,s},Q}\left\{0 \quad u_{\mathrm{w},Q} \quad f_{\mathrm{w},Q}\right\}^{\mathrm{T}}\right] \tag{4.41}$$

where $u_{\mathrm{w},i}$, $x_{\mathrm{cp},i}$, and $z_{\mathrm{cp,w},i}$ are the unknown variables, that can be obtained by solving this nonlinear system of equations in which $\mathbf{A}_{\mathrm{w,s},i}$ and $f_{\mathrm{w},i}$ are function of $u_{\mathrm{w},i}$. Bearing in mind that the coordinate $x_{\mathrm{cp},i}$ must be equal for both wheel and rail profiles, and considering Eq. (3.60) instead of Eq. (3.3), the Eq. (4.37) is modified as

$$\left\{x_{\mathrm{cp},i} \quad y_{\mathrm{cp},i} \quad z_{\mathrm{cp,r},i}-\delta\right\}^{\mathrm{T}}=\mathbf{B}_{\mathrm{r}}\left\{\left(\Delta x_i-\Delta x_P\right) \quad \left(u_{\mathrm{r},i}-u_{\mathrm{r},P}\right) \quad \left(f_{\mathrm{r},i}-f_{\mathrm{r},P}\right)\right\}^{\mathrm{T}} \tag{4.42}$$

in which $u_{\mathrm{r},i}$, Δx_i and $z_{\mathrm{cp,w},i}$ are the variables to be calculated. To reduce the computational time, for both (4.41) and (4.42), the first two equations can be solved initially together as nonlinear system to find $u_{\mathrm{w},i}$ and $x_{\mathrm{cp},i}$, and $u_{\mathrm{r},i}$ and Δx_i, respectively. Then, the last equation is evaluated directly.

Consequently, the coordinates of the strips on both profiles are used to assess the penetration in each strip along the interference region, as seen in Figure 4.4(d), which is evaluated as

$$\delta_{\mathrm{cp}}(y_{\mathrm{cp},i})=z_{\mathrm{cp,r},i}-z_{\mathrm{cp,w},i} \tag{4.43}$$

The effective contact area is smaller than the interpenetration region due to the deformation of contacting surfaces, therefore, it is important to calculate the boundaries of the actual contact patch. In

the simplest case, when the penetration has only one maximum, as represented in Figure 4.5(a), it is considered that the maximum penetration is reduced by a factor ε as given in (4.23). Bearing that mind, combining Eqs. (4.22) and (4.25), the limits of contact patch are found by solving

$$\delta_{\mathrm{cp}}(y_{\mathrm{cp}}) = (1-\varepsilon)\delta \tag{4.44}$$

The boundaries of the contact patch are denoted by y_{s} and y_{e} for the starting and ending limits, respectively. Thus, the grey shaded area in Figure 4.5(b) represents the penetration taken into account for the assessment of the contact area. However, in a general case, the penetration function can have multiple maxima, for which Eq. (4.44) cannot be directly applied, otherwise, it may lead to significant discontinuities on the size of the contact area from one time step to the next. It must be highlighted that when the number of maxima is higher than 1, one interpenetration region can result in one or more contact patches. In order to deal with this issue, the methodology suggested by Sun et al. (2018) is followed in this work. First, the magnitude and location of each penetration maximum are identified, as schematized in Figure 4.5(c) for a case with two maxima. The magnitude of the penetration in each maximum is designated by δ_1, δ_2, ... , $\delta_{N_{\mathrm{m}}}$, where N_{m} is the total number of maxima, and their location along the y_{cp} direction of the contact patch is expressed by y_{c1}, y_{c2}, ... , $y_{\mathrm{c}N_{\mathrm{m}}}$. Moreover, the number of minima of the penetration function is $N_{\mathrm{m}}-1$, and their magnitude and location must also be identified. For a minimum that is located in between maxima k and $k+1$, its indentation is represented by $h_{k(k+1)}$ and its y_{cp} coordinate is $y_{\mathrm{h}_{k(k+1)}}$, as shown in Figure 4.5(c). Then, to evaluate the size and number of contact patches three different scenarios may occur between two adjacent peaks. The following explanation considers a function with two maxima, however, it can be applied in other cases without loss of generality. In the first place, the peak with higher penetration is determined, which, for the example in Figure 4.5, is δ_2, and the following scenarios can happen:

- $\delta_2 \leq h_{12}/(1-\varepsilon)$, as shown in Figure 4.5(d), which results in only one contact patch, and its limits can be found by solving Eq. (4.44).
- $\delta_2 > h_{12}/(1-\varepsilon) > \delta_1$, as shown in Figure 4.5(e), which produces two separate patches. The limits of the patch with the highest peak are also obtained with Eq. (4.44). However, the limits of the additional contact area are determined with $\delta_{\mathrm{cp}}(y_{\mathrm{cp}}) = h_{12}$, and one of them coincides with $y_{h_{12}}$, since the patch's size is constrained by the minimum of the penetration function.
- $\delta_1 \geq h_{12}/(1-\varepsilon)$, as shown in Figure 4.5(f), which originates two different contact patches. In this case, to find the limits of each contact patch, Eq. (4.44) is utilized in which the value of δ is associated with each peak.

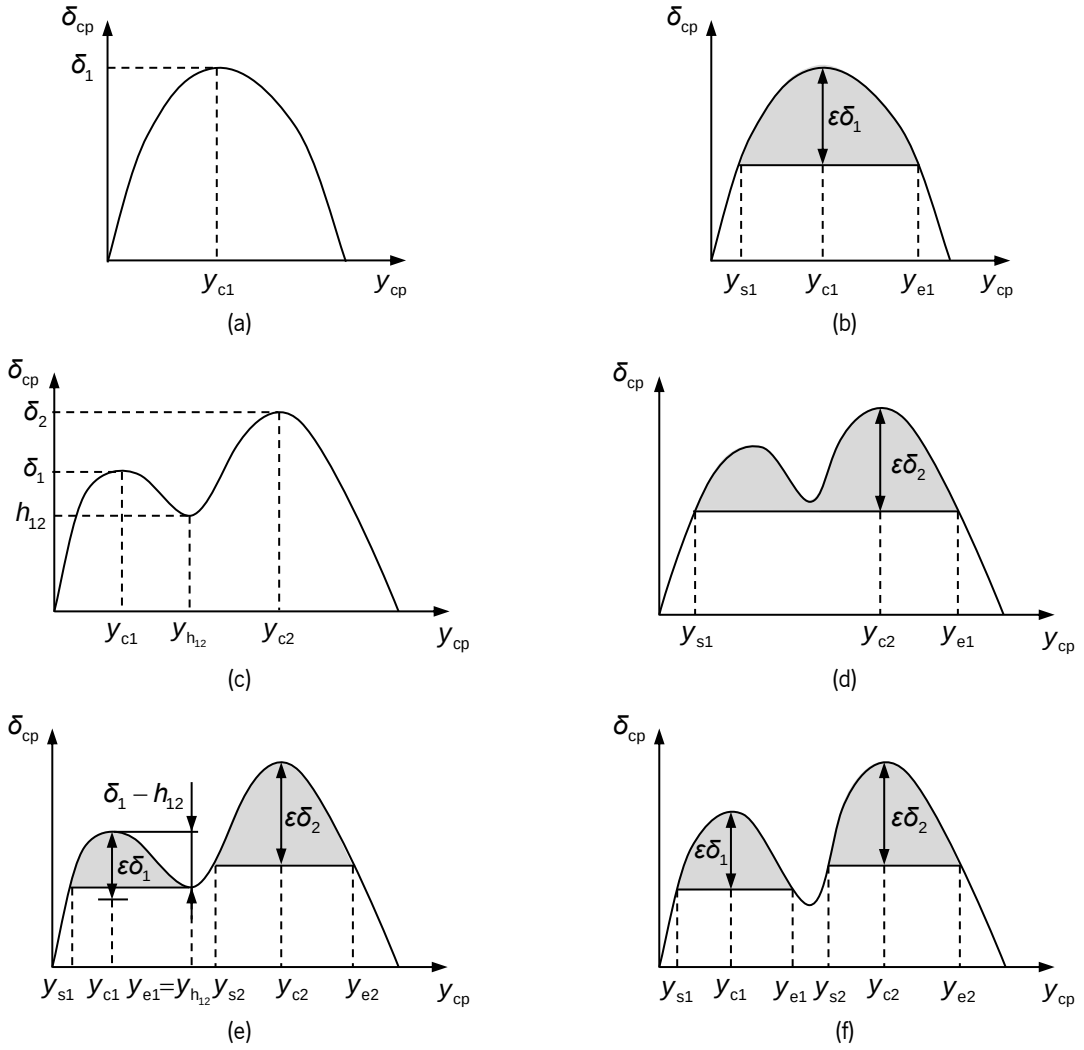

Figure 4.5 – Strategy to identify the actual size of the contact patch for one penetration maximum (a) the penetration function and (b) patch boundaries; and for multiple maxima (c) the penetration function and (d)-(f) the different scenarios of contact patch size.

It must be noted that if $\delta_1 > \delta_2$, the previous relations would be inverted. Moreover, the use of this method requires to correct Eq. (4.24), since the boundary of penetration depends on which case occurs first, and, therefore, the leading edge along the contact patch is calculated as

$$x_{\mathrm{L}}(y_{\mathrm{cp}}) = \sqrt{2R_{\mathrm{w}}^{\mathrm{s}}(y_{\mathrm{cp}})\left[\delta_{\mathrm{cp}}(y_{\mathrm{cp}}) - \delta_{\mathrm{cp}}(y_{\mathrm{s,e}})\right]} \tag{4.45}$$

where $\delta_{\mathrm{cp}}(y_{\mathrm{s,e}})$ represents the penetration in the start and end boundaries of the contact area which have the same value.

4.2.2. Curved Contact Patch

The hypothesis of planar contact patch, explored in Section 4.2.1, as well as in the Hertzian approach, exhibits limitations on modeling the conformal contact between surfaces. In the case of

interaction between a convex body and a concave body, as schematized in Figure 4.6, under the assumption of rigid bodies, an interpenetration region also exists, and the effective contact area is also smaller due to the elastic deformation of the surfaces. However, in the conformal case, the resultant contact patch tends to have a curved shape, as shown in Figure 4.6. It must be highlighted that the conformal contact only occurs if the radius of curvature of the concave surface is slightly larger than radius of curvature of the convex one.

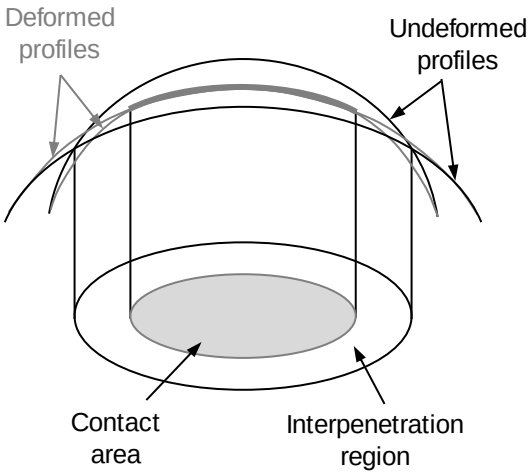

Figure 4.6 – Schematic representation of the contact between conformal surfaces.

The main difference between conformal and non-conformal contact lies on the fact that the contact area is no longer flat, which involves that there is no plane in which the contact patch can be projected on. Therefore, the concept of normal and tangential directions of the contact cannot be applied, since the contact angle varies along the contact patch.

The half-space approach is widely employed in the development of most wheel-rail contact theories, for which the only exception is when using the finite element method that is computationally intensive. This concept involves several assumptions, namely (i) the characteristic sizes of the contacting bodies are large compared to the size of the contact patch; (ii) the materials are homogeneous, isotropic and linearly elastic, and (iii) the strains are small, and the inertia effects can be neglected (Vollebregt and Segal, 2014). Having in mind that the size of the contact patch tends to increase due to the conformality between surfaces, the first assumption can be violated. However, the elastic half-space assumption can be kept since it is valid for smaller variations of the contact angle, as it is considered for the methodology presented in this work.

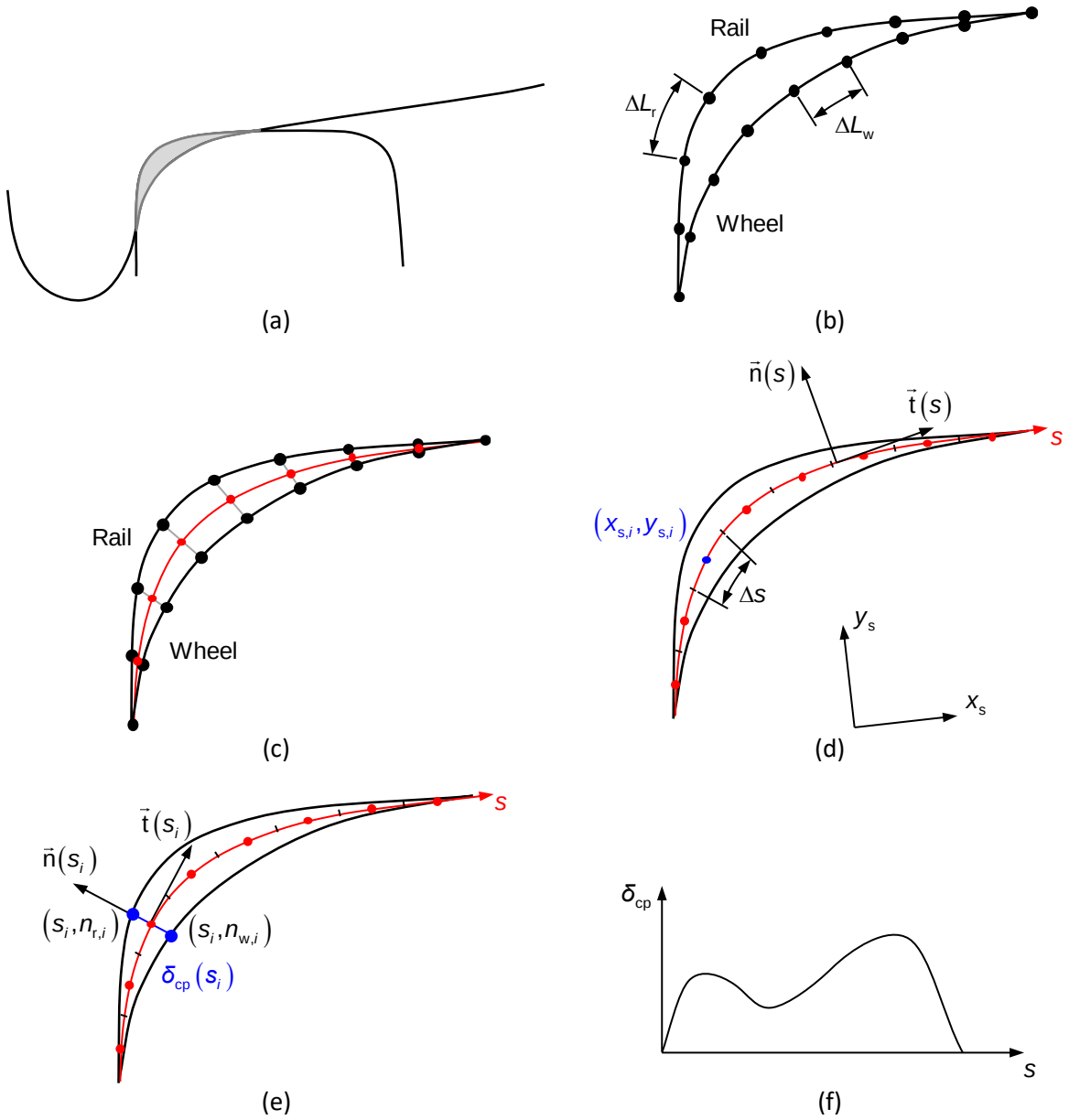

Figure 4.7 – Definition of the penetration along the interference region in the wheel lateral direction for conformal contacts: (a) interaction of wheel and rail in a conformal region; (b) discretization of the interpenetration zone by its arc length; (c) identification of the contact patch's curved axis; (d) establishment of size and center point of each strip; (e) evaluation of penetration in each strip; (f) representation of the penetration along the interference region.

The procedure proposed is here to compute the shape of a curved patch is illustrated in Figure 4.7, in which the contact dimension is exaggerated for sake of understandability. The first step consists of identifying the interpenetration region which limits are obtained with the methodology provided in Chapter 3 and denoted by $u_{w,lower}$ and $u_{w,upper}$ for the wheel lateral parameter, and by $u_{r,lower}$ and $u_{r,upper}$ for the rail lateral parameter. Since the patch is not flat, there is no preferential direction, therefore, the profiles must be parametrized according to their arc length. As seen in Chapter 3, the wheel potential contact points can be represented by a three-dimensional curve and the angular parameter, s_w, is given

as function of the lateral parameter and yaw angle (see Eq. (3.57)). Hence, to perform this length's parametrization, the wheel has to be projected into the rail profile plane, since the rail is considered an extruded body. This strategy transforms the identification of the contact patch in a two-dimensional problem, which simplifies the process of evaluation the penetration over the patch. To recall the formulation introduced previously, for a given wheel-rail relative configuration, the position of potential contact points, *P* and *Q*, are given as function of u_{r} and u_{w}, respectively, as

$$\mathbf{r}_P = \mathbf{r}_{\mathrm{r}} + \mathbf{A}_{\mathrm{r}}\mathbf{r}_{\mathrm{r},P,\mathrm{r}} \tag{4.46}$$

$$\mathbf{r}_Q = \mathbf{r}_{\mathrm{ws}} + \mathbf{h}_{\mathrm{w}} + \mathbf{A}_{\mathrm{w}}\mathbf{A}_{\mathrm{w,s}}\mathbf{r}_{\mathrm{w},Q,\mathrm{w}} \tag{4.47}$$

in which the only nonconstant variables are $\mathbf{r}_{\mathrm{r},P,\mathrm{r}}$, $\mathbf{r}_{\mathrm{w},Q,\mathrm{w}}$ and $\mathbf{A}_{\mathrm{w,s}}$.

Thus, to project both points of wheel and rail on the rail section plane, their position vectors must be premultiplied by the inverse of the rail transformation matrix. It must be noted that the roll and yaw angles relate both wheel and rail coordinate systems and the following relation can be employed

$$\mathbf{A}_{\mathrm{r}}^{-1} = \mathbf{R}_{\varphi}\mathbf{R}_{\alpha}\mathbf{A}_{\mathrm{w}}^{-1} \tag{4.48}$$

Hence, the coordinates of points *P* and *Q* on the rail and wheel, respectively, can be rotated to the contact patch evaluation, namely with the rail orientation. For sake of simplicity, it is also subtracted the position vector of the origin of the rail profile, and, thus, the coordinates can be expressed in the following form

$$\mathbf{r}_{\mathrm{r,p}} = \mathbf{A}_{\mathrm{r}}^{-1}\left(\mathbf{r}_P - \mathbf{r}_{\mathrm{r}}\right) = \mathbf{r}_{\mathrm{r},P,\mathrm{r}} \tag{4.49}$$

$$\mathbf{r}_{\mathrm{w,p}} = \mathbf{A}_{\mathrm{r}}^{-1}\left(\mathbf{r}_Q - \mathbf{r}_{\mathrm{r}}\right) = \mathbf{A}_{\mathrm{r}}^{-1}\left(\mathbf{r}_{\mathrm{ws}} + \mathbf{h}_{\mathrm{w}} - \mathbf{r}_{\mathrm{r}}\right) + \mathbf{R}_{\varphi}\mathbf{R}_{\alpha}\mathbf{A}_{\mathrm{w,s}}\mathbf{r}_{\mathrm{w},Q,\mathrm{w}} \tag{4.50}$$

It must be emphasized that these position vectors define spatial curves parametrized as function of u_{r} and u_{w}, respectively. Moreover, these vectors can be divided into constant terms, which are null for the rail, being denoted by

$$\mathbf{c}_{\mathrm{r}} = \mathbf{0} \tag{4.51}$$

$$\mathbf{c}_{\mathrm{w}} = \mathbf{A}_{\mathrm{r}}^{-1}\left(\mathbf{r}_{\mathrm{ws}} + \mathbf{h}_{\mathrm{w}} - \mathbf{r}_{\mathrm{r}}\right) \tag{4.52}$$

and variable terms, which can be rewritten recurring to Eqs. (3.3), (3.8), (3.9), (3.48) and (3.51), and rearranging the expression in the form

$$\mathbf{r}_{\mathrm{r},P,\mathrm{r}} = \begin{Bmatrix} 0 & u_{\mathrm{r}} & f_{\mathrm{r}} \end{Bmatrix}^{\mathrm{T}} \tag{4.53}$$

$$\mathbf{R}_{\varphi}\mathbf{R}_{\alpha}\mathbf{A}_{\mathrm{w,s}}\mathbf{r}_{\mathrm{w},Q,\mathrm{w}}=\begin{Bmatrix}\mp\sin\alpha\left(f_{\mathrm{w}}^{'}f_{\mathrm{w}}+u_{\mathrm{w}}\right)\\ \pm\cos\varphi\cos\alpha\left(u_{\mathrm{w}}-\tan^{2}\alpha\,f_{\mathrm{w}}^{'}f_{\mathrm{w}}\right)-\sin(\varphi)\sqrt{1-\tan^{2}\alpha\,f_{\mathrm{w}}^{'\,2}}\,f_{\mathrm{w}}\\ \pm\sin\varphi\cos\alpha\left(u_{\mathrm{w}}-\tan^{2}\alpha\,f_{\mathrm{w}}^{'}f_{\mathrm{w}}\right)+\cos(\varphi)\sqrt{1-\tan^{2}\alpha\,f_{\mathrm{w}}^{'\,2}}\,f_{\mathrm{w}}\end{Bmatrix} \tag{4.54}$$

where $\pm$ and $\mp$ refer to the differences between the left and right wheels, respectively.

Next, the two curves are parametrized as function of their arc length inside the interpenetration region. In a general case, the length of the curve is calculated as

$$L_{k}\left(u_{k}\right)=\int_{u_{k,\mathrm{lower}}}^{u_{k}}\sqrt{\left(\frac{\mathrm{d}r_{k,\mathrm{p},x}}{\mathrm{d}u_{k}}\right)^{2}+\left(\frac{\mathrm{d}r_{k,\mathrm{p},y}}{\mathrm{d}u_{k}}\right)^{2}+\left(\frac{\mathrm{d}r_{k,\mathrm{p},z}}{\mathrm{d}u_{k}}\right)^{2}}\,\mathrm{d}u_{k}\,,\qquad k=\mathrm{w},\,\mathrm{r} \tag{4.55}$$

in which the arc length is assumed to be zero in the starting point of the interpenetration region. However, since the profiles are projected in the rail cross-section, the contribution of x direction must be neglected, which yields

$$L_{k}\left(u_{k}\right)=\int_{u_{k,\mathrm{lower}}}^{u_{k}}\sqrt{\left(\frac{\mathrm{d}r_{k,\mathrm{p},y}}{\mathrm{d}u_{k}}\right)^{2}+\left(\frac{\mathrm{d}r_{k,\mathrm{p},z}}{\mathrm{d}u_{k}}\right)^{2}}\,\mathrm{d}u_{k}\,,\qquad k=\mathrm{w},\,\mathrm{r} \tag{4.56}$$

The arc length, defined by Eq. (4.56), only depends on the derivatives of Eqs. (4.49) and (4.50), and, therefore, only the variable terms described in Eqs. (4.53) and (4.54) need to be considered. Hence, after some mathematical manipulation, the expressions to obtain the arc length for rail and the wheel interpenetration region are

$$L_{\mathrm{r}}\left(u_{\mathrm{r}}\right)=\int_{u_{\mathrm{r,lower}}}^{u_{\mathrm{r}}}\sqrt{1+f_{\mathrm{r}}^{'}}\,\mathrm{d}u_{\mathrm{r}} \tag{4.57}$$

$$L_{\mathrm{w}}\left(u_{\mathrm{w}}\right)=\int_{u_{\mathrm{w,lower}}}^{u_{\mathrm{w}}}\sqrt{\begin{aligned}&-\sin^{2}\alpha\left(f_{\mathrm{w}}^{'\,4}+2f_{\mathrm{w}}f_{\mathrm{w}}^{'\,2}f_{\mathrm{w}}^{''}+2f_{\mathrm{w}}^{'\,2}+2f_{\mathrm{w}}f_{\mathrm{w}}^{''}\right)+\cos^{2}\alpha\\&\quad+f_{\mathrm{w}}^{'\,2}+\tan^{2}\alpha\,f_{\mathrm{w}}{}^{2}f_{\mathrm{w}}^{''2}\left(\frac{\tan^{2}\alpha\,f_{\mathrm{w}}^{'\,2}}{1-\tan^{2}\alpha\,f_{\mathrm{w}}^{'\,2}}+\sin^{2}\alpha\right)\end{aligned}}\,\mathrm{d}u_{\mathrm{w}} \tag{4.58}$$

It must be noticed that the rail's arc length just depends on the profile shape and the boundaries of the interpenetration region, while the wheel's arc length also depends on the yaw angle and, therefore, requires its identification for each wheel-rail configuration. Moreover, the total length of the profiles on the interpenetration region is calculated by evaluating Eqs. (4.57) and (4.58) on the upper bounds of the interference zone. Then, both profiles are discretized in N_{s} equally sized spaces, as schematized in Figure 4.7(b). The length of each space is different for both wheel and rail and given as

$$\Delta L_k = \frac{L_k\left(u_{k,\text{upper}}\right)}{N_\text{s}}, \qquad k = \text{w, r} \tag{4.59}$$

The definition of a fixed number of spaces would yield large intervals in a case of a particularly broad interpenetration zone and would lead to unnecessary refinement in case of small contact areas. Therefore, to mitigate the changes in size of the discretized elements, it is preferable to specify a suitable size for these intervals, Δs_0. Using this dimension, the resultant number of intervals may not only differ for both profiles, but also not to be an integer number. Therefore, the appropriate number of intervals which results in the arc length close to the specified value. Thus, the number of intervals must be evaluated based on the average length of both profiles as

$$N_\text{s} = \text{round}\left(\frac{L_\text{r}\left(u_{\text{r,upper}}\right) + L_\text{w}\left(u_{\text{w,upper}}\right)}{2\Delta s_0}\right) \tag{4.60}$$

where the function $\text{round}(x)$ returns the nearest integer. In order to be able to employ this procedure to determine shape of a curved contact patch, it is defined that the minimum number of intervals is 5. Hence, if Eq. (4.60) returns a lower number, five intervals must be considered in the discretization. Moreover, the value of arc length in the set of equally spaced points represented in Figure 4.7(b) is obtained by

$$L_{k,i} = i\Delta L_k, \qquad i = 0,\ 1,\ \ldots,\ N_\text{s} \quad \text{and} \quad k = \text{w, r} \tag{4.61}$$

in which $L_{\text{r},i}$ and $L_{\text{w},i}$ denote the arc length value on the i^{th} point on the rail and wheel interpenetration region, respectively.

Since the arc length functions given by Eqs. (4.57) and (4.58) are strictly monotonic functions and, hence, injective, their inverse functions exist. Therefore, it is possible to obtain the parameters u_r and u_w for a given a given arc length. To apply this methodology, Eqs. (4.57) and (4.58) are solved with a variable step integration algorithm which allows to obtain the value of arc length for a set of points. Then, using this data, a set of cubic splines are established to interpolate the values of the profile parameters in the points defined in Eq. (4.61), which consequently allow to calculate their coordinates employing Eqs. (4.49) and (4.50). Once again the problem is reduced to the bidimensional space and, only the second and third coordinates are considered and expressed in a planar reference system in x_s and y_s directions, respectively, as represented in Figure 4.7.

Bearing that in mind, the curved surface in which the contact patch is contained can be determined through the evaluation of the middle position between the wheel and rail points, as pictured

in red in Figure 4.7(c). Since the points obtained are not necessarily equally spaced in this curve, they are used to generate cubic splines of the type $y_{\mathrm{s}}(x_{\mathrm{s}})$ and, then, parameterized according to the arc length. Hereafter, the curve is divided in N_{s} equally sized spaces, that represent the locally planar strips in which the contact patch is to be discretized, being these points specified in the center of each strip. Furthermore, $(x_{\mathrm{s},i}, y_{\mathrm{s},i})$ expresses the coordinates of the i^{th} strip, also denoted by the vector $\mathbf{r}_{\mathrm{s},i}$, and Δs is the width of each strip, as depicted in Figure 4.7(d).

A curved axis s is established representing the direction along the contact patch for which the normal and tangential directions are variable. Thus, the normal and tangential vectors are found for each strip as

$$\mathbf{n}_{\mathrm{s},i} = \left\{ -\sin\theta_i \quad \cos\theta_i \right\}^{\mathrm{T}} \tag{4.62}$$

$$\mathbf{t}_{\mathrm{s},i} = \left\{ \cos\theta_i \quad \sin\theta_i \right\}^{\mathrm{T}} \tag{4.63}$$

in which the angle of each strip is defined as

$$\theta_i = \arctan\left(y'_{\mathrm{s},i} \right) \tag{4.64}$$

where $y'_{\mathrm{s},i}$ denotes the derivative of y_{s} in $x_{\mathrm{s},i}$ that is calculated from the splines produced.

Now, the penetration along the curved contact patch, which is measured in the normal direction of each strip, as represented in Figure 4.7(e), is evaluated. Both points on rail and wheel which define the limits of the interference of a given strip can be obtained through the intersection between a straight line normal to the patch surface and the rail and wheel profiles, respectively.

The line normal to the patch surface on each strip can be defined in a vector equation form using the coordinate of the corresponding strip along with the normal vector established in Eq. (4.62). Hence, the conditions for the intersection points are prescribed by equalizing the line equation to the second and third elements of Eqs. (4.49) and (4.50), respectively, for the rail and wheel cases. Here, these conditions are expressed as

$$\mathbf{r}_{\mathrm{s},i} + n_{\mathrm{r},i}\mathbf{n}_{\mathrm{s},i} = \mathbf{r}_{\mathrm{r,p,2:3}} \tag{4.65}$$

$$\mathbf{r}_{\mathrm{s},i} + n_{\mathrm{w},i}\mathbf{n}_{\mathrm{s},i} = \mathbf{r}_{\mathrm{w,p,2:3}} \tag{4.66}$$

in which $n_{\mathrm{r},i}$ and $n_{\mathrm{w},i}$ denote the distance from the strip center point to the intersection point in the rail and wheel profiles, respectively, as illustrated in Figure 4.7(e). It should be highlighted that, following the proposed reference frames, $n_{\mathrm{r},i}$ must assume positive values, while $n_{\mathrm{w},i}$ is always negative. Equations (4.65) and (4.66) are rewritten in an expanded form as

$$\begin{Bmatrix} x_{\mathrm{s},i} \\ y_{\mathrm{s},i} \end{Bmatrix} + n_{\mathrm{r},i} \begin{Bmatrix} -\sin\theta_i \\ \cos\theta_i \end{Bmatrix} = \begin{Bmatrix} u_{\mathrm{r},i} \\ f_{\mathrm{r},i} \end{Bmatrix} \tag{4.67}$$

$$\begin{Bmatrix} x_{\mathrm{s},i} \\ y_{\mathrm{s},i} \end{Bmatrix} + n_{\mathrm{w},i} \begin{Bmatrix} -\sin\theta_i \\ \cos\theta_i \end{Bmatrix} = \begin{Bmatrix} c_{\mathrm{w},2} \\ c_{\mathrm{w},3} \end{Bmatrix} + \begin{Bmatrix} \pm\cos\varphi\cos\alpha\left(u_{\mathrm{w},i} - \tan^2\alpha\, f'_{\mathrm{w},i} f_{\mathrm{w},i}\right) - \sin(\varphi)\sqrt{1-\tan^2\alpha\, f'^{\,2}_{\mathrm{w},i}}\, f_{\mathrm{w},i} \\ \pm\sin\varphi\cos\alpha\left(u_{\mathrm{w},i} - \tan^2\alpha\, f'_{\mathrm{w},i} f_{\mathrm{w},i}\right) + \cos(\varphi)\sqrt{1-\tan^2\alpha\, f'^{\,2}_{\mathrm{w},i}}\, f_{\mathrm{w},i} \end{Bmatrix} \tag{4.68}$$

This results in a set of two equations for each element in which the unknowns are $n_{\mathrm{r},i}$ and $u_{\mathrm{r},i}$, for the rail case, and $n_{\mathrm{w},i}$ and $u_{\mathrm{w},i}$, for the wheel case. Thus, combining each set of equations and considering Eq. (4.64), the following nonlinear equations are given

$$\left(f_{\mathrm{r},i} - y_{\mathrm{s},i}\right) y'_{\mathrm{s},i} + u_{\mathrm{r},i} - x_{\mathrm{s},i} = 0 \tag{4.69}$$

$$\begin{aligned} &\left(\pm\sin\varphi\cos\alpha\left(u_{\mathrm{w},i} - \tan^2\alpha\, f'_{\mathrm{w},i} f_{\mathrm{w},i}\right) + \cos(\varphi)\sqrt{1-\tan^2\alpha\, f'^{\,2}_{\mathrm{w},i}}\, f_{\mathrm{w},i} - y_{\mathrm{s},i} + c_{\mathrm{w},3}\right) y'_{\mathrm{s},i} \\ &\pm\cos\varphi\cos\alpha\left(u_{\mathrm{w},i} - \tan^2\alpha\, f'_{\mathrm{w},i} f_{\mathrm{w},i}\right) - \sin(\varphi)\sqrt{1-\tan^2\alpha\, f'^{\,2}_{\mathrm{w},i}}\, f_{\mathrm{w},i} - x_{\mathrm{s},i} + c_{\mathrm{w},2} = 0 \end{aligned} \tag{4.70}$$

Each of these equations only contains one unknown which is the lateral profile parameter of the corresponding element for the i^{th} strip, that is, $u_{\mathrm{r},i}$ and $u_{\mathrm{w},i}$, respectively. Therefore, they can be solved independently recurring to an iterative procedure, such as the Newton-Raphson method. Consequently, the parameters obtained are introduced in Eqs. (4.67) and (4.68) to determine $n_{\mathrm{r},i}$ and $n_{\mathrm{w},i}$, which can be employed to find the penetration of each strip as

$$\delta_{\mathrm{cp}}(s_i) = n_{\mathrm{r},i} - n_{\mathrm{w},i} \tag{4.71}$$

Following this procedure for the N_{s} strips, the penetration function for the whole interference region considering a curved contact patch is obtained, as represented in Figure 4.7(f). It must be highlighted that this penetration function has similar characteristics to the one generated for the planar patch, although, in this case, it is measured through a curved surface.

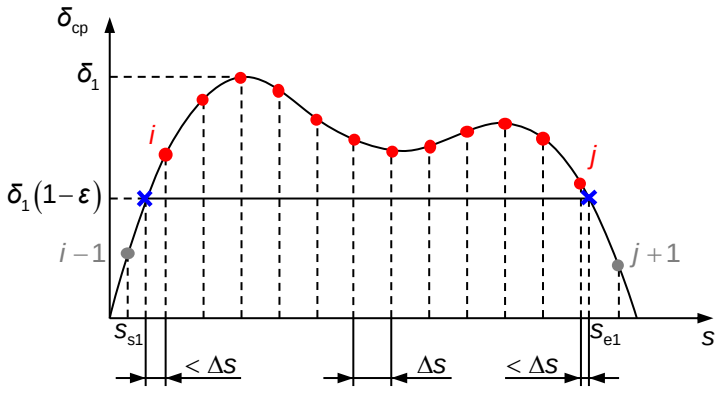

Figure 4.8 – Schematic representation of the identification of the contact patch limits

After obtaining the penetration function, the number and size of contact patches within each interpenetration region is evaluated with the procedure presented in the previous section and illustrated in Figure 4.5 (Sun et al., 2018). It must be mentioned that, in this case, the maximum penetration point and the start and end boundaries of the i^{th} patch are denoted by s_{ci}, s_{si} and s_{ei}, respectively. Furthermore, since the patches' limits are not exactly located in the end of a given strip, their evaluation is done through the linear interpolation between the strips immediately before and after the penetration limit (Magalhães et al., 2020). This procedure is presented in Figure 4.8 in which the red points represent the strips above the penetration threshold, the grey points denote the strips below it, and blue crosses indicate the boundaries of the contact patch. Hence, denoting by i and j the first and last strips inside the contact patch, the start and end limits of the contact patch are given by the following expressions

$$s_{\text{s1}} = s_i - \frac{\delta_{\text{cp}}(s_i) - \delta_1(1-\varepsilon)}{\delta_{\text{cp}}(s_i) - \delta_{\text{cp}}(s_{i-1})}\Delta s \tag{4.72}$$

$$s_{\text{e1}} = s_j + \frac{\delta_{\text{cp}}(s_j) - \delta_1(1-\varepsilon)}{\delta_{\text{cp}}(s_j) - \delta_{\text{cp}}(s_{j+1})}\Delta s \tag{4.73}$$

This amendment implies that the width of the first and last strips of the contact patch is lower than Δs, which is of paramount importance in terms of numerical stability. When this correction is not performed, the size of the contact patch does not change smoothly over time and it is a multiple of Δs. Consequently, such discontinuity on the contact area induces a discontinuity on the contact forces which has two main drawbacks. First, when using integration algorithms with variable time step, which is the most suitable option, such discontinuities force the algorithm to reduce drastically the step size and, consequently, to reduce the numerical simulation efficiency. Second, it is not physically plausible that the contact force magnitude changes abruptly due to an insignificant variation of the size of the contact patch.

4.3. Non-Hertzian Contact Pressure

Subsequently to the identification of the shape and size of the contact patches, the evaluation of the normal pressure distribution on each patch, which assumes a significant importance on the dynamic modeling of railway vehicles, is required. The sum of the pressure distribution allows to obtain the normal contact forces, which must vary smoothly through the contact region unless impact occurs. Some numerical models present a non-smooth variation of the contact force for similar wheel-rail relative positions which is not plausible from the physical point of view and introduces numerical instability on

the simulations. A representative example of this problem is the use of Hertzian contact models when the surface curvature changes abruptly, since these models only consider the properties of the main point of contact and, therefore, the contact forces immediately suffer from the curvature variations. Another problem is that the pressure distributions are responsible for the limits of the tangential tractions in the lateral and longitudinal directions, which affects the ability of the vehicle to accelerate, brake or turn. The accurate determination of surface tractions allows to predict the components' damage, namely wear or rolling contact fatigue.

In this section, a semi-Hertzian methodology is considered to evaluate the normal pressure distribution which complies with the procedure presented for the identification of the contact patch shape (Piotrowski and Kik, 2008). Although this method is widely used in the literature (Liu et al., 2016; Magalhães et al., 2020), it may present a non-smooth behavior when the penetration function, inside an interference region, has more than one maximum. Bearing that in mind, the methodology proposed by Sun et al. (2018) is used here to deal with multiple maxima.

As has been assumed, during contact interaction, both wheel and rail surfaces deform and their distance in the normal direction is given by Eq. (4.20). In the case of a planar contact patch, the distance between surfaces is measured in a fixed direction (y) which is the normal direction in the maximum penetration point. For a curved contact patch, the distance is measured normal to a curved line (s) that can be obtained with the procedure explained in section 4.2.2. The difference between these approaches is outlined in Figure 4.9. These numerical techniques used to evaluate the contact pressure distribution, applied in flat contacts, are adapted to be employed in either planar or curved contact patches. Hence, the lateral direction y is replaced by a variable direction along the contact patch s.

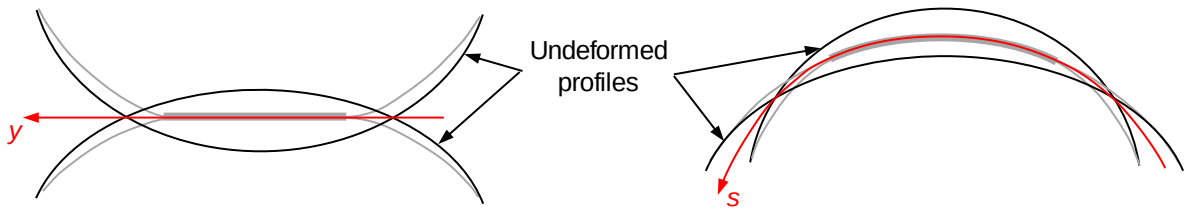

Figure 4.9 – Representation of contact direction for planar and curved contact.

Assuming that contact occurs between two elastic half-spaces, the subsurface stresses and the displacements produced by a set of surface tractions are obtained through continuum mechanics theory using Boussinesq-Cerruti approximation (Johnson, 1985). In this context, the displacements in the normal direction relative to the contact are expressed as

$$w(x,y,z)=\frac{1}{4\pi G}\left[\iint_C \frac{2(1-\sigma)\,p(\xi,\eta)\mathrm{d}\xi\mathrm{d}\eta}{\left((x-\xi)^2+(y-\eta)^2+z^2\right)^{1/2}}+\iint_C \frac{z^2\,p(\xi,\eta)\mathrm{d}\xi\mathrm{d}\eta}{\left((x-\xi)^2+(y-\eta)^2+z^2\right)^{3/2}}\right] \tag{4.74}$$

where x and y denote the tangential directions, and z represents the normal direction. In addition, G is the shear modulus which relates to the Young's modulus and Poisson's ratio as

$$G=\frac{E}{2(1+\sigma)} \tag{4.75}$$

Thus, to obtain the displacements at the contact surface, Eq. (4.74) must be evaluated when $z=0$, which produces

$$w(x,y)=\frac{1-\sigma^2}{\pi E}\iint_C \frac{p(\xi,\eta)}{\sqrt{(x-\xi)^2+(y-\eta)^2}}\mathrm{d}\xi\mathrm{d}\eta \tag{4.76}$$

Based on Eq. (4.76) and, since the pressure distribution p and the contact area C are equal for two contacting bodies, if the wheel and rail have the same material, their displacements are symmetrical. Bearing this hypothesis in mind, the displacements of wheel and rail surfaces, which were distinguished in Eq. (4.20), are equalized as $w_{\mathrm{wr}}(x,y)=w_{\mathrm{w}}(x,y)=w_{\mathrm{r}}(x,y)$. Since inside the contact area, the distance between surfaces is null, Eq. (4.20) is rewritten as

$$w_{\mathrm{wr}}(x,y)=\frac{\delta-z_{\mathrm{wr}}(x,y)}{2} \tag{4.77}$$

Hence, as the contact patch is discretized into strips which have a semi-elliptical pressure distribution, the deformation on the maximum pressure point in each strip is obtained using $x=0$. Therefore, employing Eq. (4.22), the deformation is expressed as

$$w_{\mathrm{wr}}(0,y)=\frac{\delta-f(y)}{2} \tag{4.78}$$

which can be simplified introducing Eq. (4.25) as

$$w_{\mathrm{wr}}(0,y)=\frac{\delta_{\mathrm{cp}}(y)}{2} \tag{4.79}$$

Thus, the displacement of both surfaces in each strip is dependent on the pseudo-penetration in the respective strip, which is obtained distinctively for a planar or curved patch, as demonstrated in section 4.2.

4.3.1. Kik-Piotrowski Method – Main Point of Contact

The methodology proposed by Kik and Piotrowski (1996) (KP) assumes that the maximum pressure in each strip is proportional to the strip length, therefore, the maximum pressure on the whole contact area p_0 is located in the point of maximum penetration y_c. Hereupon, the elliptical pressure distribution is given by

$$p(x,y)=\frac{p_0}{x_L(y_c)}\sqrt{x_L^2(y)-x^2} \tag{4.80}$$

As the size of each strip has been already determined via Eq. (4.45), it is necessary to evaluate the value of maximum pressure to assess the pressure in any point of the contact zone and, consequently, the normal contact force. Taking into account the Boussinesq-Cerruti approximation, given by Eq. (4.76), to estimate the displacement and introducing Eq. (4.80), leads to

$$w(x,y)=\frac{\left(1-\sigma^2\right)p_0}{\pi E x_L(y_c)}\iint_C\frac{\sqrt{x_L^2(\eta)-\xi^2}}{\sqrt{\left(x-\xi\right)^2+\left(y-\eta\right)^2}}\mathrm{d}\xi\mathrm{d}\eta \tag{4.81}$$

This equation is employed using the deformation of the maximum penetration point, and noticing that $\delta_{cp}(y_c)=\delta$, which yields

$$w(0,y_c)=\frac{\delta}{2}=\frac{\left(1-\sigma^2\right)p_0}{\pi E x_L(y_c)}\iint_C\sqrt{\frac{x_L^2(\eta)-\xi^2}{\xi^2+\left(y_c-\eta\right)^2}}\,\mathrm{d}\xi\mathrm{d}\eta \tag{4.82}$$

Rearranging Eq. (4.82) and including the limits of integration, the maximum normal contact pressure is expressed as

$$p_0=\frac{\pi E\delta x_L(y_c)}{2\left(1-\sigma^2\right)}\left(\int_{y_s}^{y_e}\int_{-x_L}^{x_L}\sqrt{\frac{x_L^2(\eta)-\xi^2}{\xi^2+\left(y_c-\eta\right)^2}}\,\mathrm{d}\xi\mathrm{d}\eta\right)^{-1} \tag{4.83}$$

It must be highlighted that the integral term from Eq. (4.83) not only cannot be solved analytically which forces its numerical evaluation, but also the function to integrate has a singularity at $(\xi,\eta)=(0,y_c)$, since it tends to infinity. Thus, when discretizing the contact area in small rectangular elements with constant sizes in the lateral direction and constant number in the longitudinal direction, as shown in Figure 4.10, the numerical integration is performed by evaluating the function to integrate in the middle of each element. If the number of elements in each strip is even, as represented in Figure 4.10, the singular point is avoided since the middle point of each element cannot be located in the y axis, which will not happen if the number of elements is odd. Although the integral can be evaluated, this

strategy makes its value dependent of the element size, eventually preventing convergence. Therefore, the direct integration of the function is not feasible. To overcome this difficulty, there are two possibilities: either to convert the cartesian coordinate system into a polar coordinate system (Magalhães et al., 2020); or, to approximate the function to integrate (Kalker, 1990; Kalker, 2001). Although the use of polar coordinates eliminates the singularity, it is only appropriate if the contact patch shape is close to an ellipse, which is not in the general case. Consequently, the integral is evaluated based on an approximation function suggested by Kalker (2001).

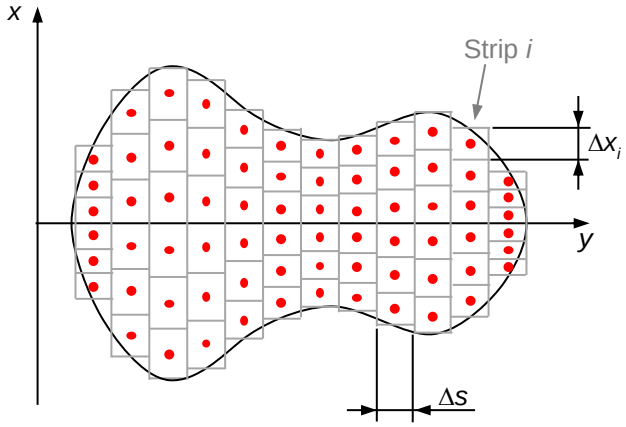

Figure 4.10 – Contact patch discretization.

Subsequently to the calculation of the maximum pressure, the normal contact force is found performing the integration of the pressure distribution over the contact patch. Thus, integrating the pressure given by Eq. (4.80), the normal force is calculated as

$$f_{\mathrm{n}}^{\mathrm{KP}} = \frac{p_0}{x_{\mathrm{L}}(y_{\mathrm{c}})} \int_{y_{\mathrm{s}}}^{y_{\mathrm{e}}} \int_{-x_{\mathrm{L}}}^{x_{\mathrm{L}}} \sqrt{x_{\mathrm{L}}^2(y) - x^2}\,\mathrm{d}x\mathrm{d}y \tag{4.84}$$

Hence, partially solving the integral and introducing Eq. (4.83), the normal contact force is expressed in a general form as

$$f_{\mathrm{n}}^{\mathrm{KP}} = \frac{\pi^2 E\delta}{4\left(1-\sigma^2\right)} \int_{y_{\mathrm{s}}}^{y_{\mathrm{e}}} x_{\mathrm{L}}^2(y)\mathrm{d}y \left(\int_{y_{\mathrm{s}}}^{y_{\mathrm{e}}} \int_{-x_{\mathrm{L}}}^{x_{\mathrm{L}}} \sqrt{\frac{x_{\mathrm{L}}^2(\eta) - \xi^2}{\xi^2 + \left(y_{\mathrm{c}} - \eta\right)^2}}\,\mathrm{d}\xi\mathrm{d}\eta \right)^{-1} \tag{4.85}$$

which is used to calculate the normal force in a planar contact patch because the normal direction to the contact area is constant, therefore, the resultant force is just the sum of the contact pressure. In the case of the curved contact patch, that procedure is not valid, since the normal direction varies along the s coordinate and an alternative approach must be taken.

Bearing in mind that each strip is considered locally planar, the pressure is integrated separately for each strip. Thus, the magnitude of normal force for the i^{th} strip is

$$f_{\mathrm{n},i}^{\mathrm{KP}} = \frac{p_0}{x_{\mathrm{L}}(s_{\mathrm{c}})} \int_{s_i-\Delta s/2}^{s_i+\Delta s/2} \int_{-x_{\mathrm{L}}}^{x_{\mathrm{L}}} \sqrt{x_{\mathrm{L}}^2(s) - x^2}\ \mathrm{d}x\mathrm{d}s \tag{4.86}$$

solving the integral, Eq. (4.86) leads to

$$f_{\mathrm{n},i}^{\mathrm{KP}} = \frac{\pi p_0}{2x_{\mathrm{L}}(s_{\mathrm{c}})} \int_{s_i-\Delta s/2}^{s_i+\Delta s/2} x_{\mathrm{L}}^2(s)\ \mathrm{d}s \tag{4.87}$$

and, since the size of each strip is constant in the longitudinal direction, Eq. (4.87) is written as

$$f_{\mathrm{n},i}^{\mathrm{KP}} = \frac{\pi p_0 x_{\mathrm{L}}^2(s_i)\Delta s}{2x_{\mathrm{L}}(s_{\mathrm{c}})} \tag{4.88}$$

In the case of curved contact, Eq. (4.83) is modified accordingly, and the maximum pressure is rewritten as follows

$$p_0 = \frac{\pi E \delta x_{\mathrm{L}}(s_{\mathrm{c}})}{2\left(1-\sigma^2\right)} \left(\int_{s_{\mathrm{s}}}^{s_{\mathrm{e}}} \int_{-x_{\mathrm{L}}}^{x_{\mathrm{L}}} \sqrt{\frac{x_{\mathrm{L}}^2(\eta) - \xi^2}{\xi^2 + \left(s_{\mathrm{c}} - \eta\right)^2}}\ \mathrm{d}\xi\mathrm{d}\eta \right)^{-1} \tag{4.89}$$

Having calculated the fractions of normal force for each strip, the total force due to the normal pressure is evaluated through the vector sum of the contribution of each strip, which is expressed as

$$\mathbf{f}_{\mathrm{n}}^{\mathrm{KP}} = \sum_{i=1}^{N_{\mathrm{s}}} f_{\mathrm{n},i}^{\mathrm{KP}} \mathbf{n}_{\mathrm{s},i} \tag{4.90}$$

Regarding the planar contact patch scenario, the normal force is also given in vector form as

$$\mathbf{f}_{\mathrm{n}}^{\mathrm{KP}} = f_{\mathrm{n}}^{\mathrm{KP}} \mathbf{n}_{\mathrm{r},P} \tag{4.91}$$

Moreover, Eqs. (4.90) and (4.91) represent the resultant normal contact force that is applied on the wheel surface. The normal force acting on the rail is the symmetrical to that acting on the wheel.

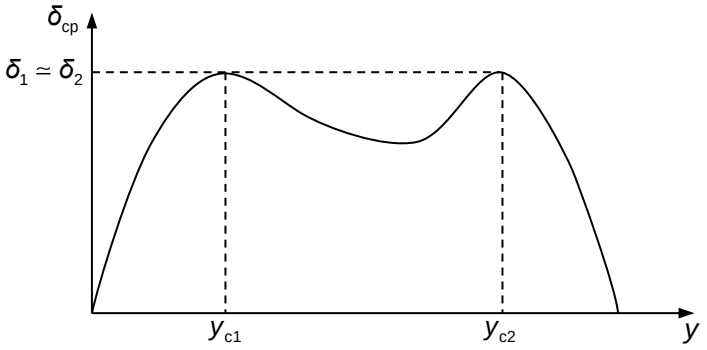

Figure 4.11 – Schematic representation of a general the penetration function with two similar maxima.

From the analysis of the normal force equation, it is significant to mention that the force magnitude is highly dependent on the location of the maximum penetration point y_c, which can lead to substantial discontinuities on the contact force during a dynamic analysis. This problem occurs when the location of the main point of contact changes abruptly, which results from the existence of similar penetration maxima over the same interpenetration region, as schematized in Figure 4.11. In that case, when the wheel-rail relative position changes slightly, although the maximum penetration and the contact patch area vary marginally, the location maximum penetration point may jump from y_{c1} to y_{c2} or vice versa. This means that, for similar contact conditions, Kik-Piotrowski method can predict similar patches with distinct forces. These differences represent a noteworthy limitation of this contact force model, since the discontinuous force variation is not physically plausible and introduces numerical instabilities. This issue is common in the presence of worn wheel or rail profiles, but it can still occur with new profiles.

4.3.2. Sun et al. Method – Without a Main Point of Contact

In order to overcome the problem displayed by Kik-Piotrowski model associated with its sensitivity to the location of the main contact model, Sun et al. (2018) proposed an extension which avoids this discontinuity. While, in the Kik-Piotrowski model, the pressure distribution is calculated based on the maximum pressure on the strip with most penetration and the pressure in the remaining strips is obtained proportionally to the strip size, the Sun et al. model (SZG) calculates the semi-elliptical pressure distribution in each strip using the corresponding maximum pressure which is computed independently for each strip. Thus, in this case, Eq. (4.80) can be replaced by

$$p(x,y) = p_0(y)\sqrt{1-\left(\frac{x}{x_L(y)}\right)^2} \tag{4.92}$$

To determine the maximum pressure for each lateral coordinate, the Boussinesq-Cerruti approximation is also employed using the corresponding lateral coordinate as reference point. Hence, the pressure distribution to introduce in Eq. (4.76) to calculate the maximum pressure at any coordinate y' is given as

$$p(x,y) = \frac{p_0(y')}{x_L(y')}\sqrt{x_L^2(y)-x^2} \tag{4.93}$$

Equation (4.93) is analogous to the Eq. (4.80), used in the Kik-Piotrowski model. However, the reference point from which the pressure is obtained replaces the maximum penetration point. Thus, the maximum pressure for each lateral coordinate is now expressed as

$$p_0(y)=\frac{\pi E x_{\mathrm{L}}(y)\delta_{\mathrm{cp}}(y)}{2\left(1-\sigma^2\right)}\left(\int_{y_{\mathrm{s}}}^{y_{\mathrm{e}}}\int_{-x_{\mathrm{L}}}^{x_{\mathrm{L}}}\sqrt{\frac{x_{\mathrm{L}}^2(\eta)-\xi^2}{\xi^2+\left(y-\eta\right)^2}}\,\mathrm{d}\xi\mathrm{d}\eta\right)^{-1} \tag{4.94}$$

It is worth to mention that, in this methodology, the integral of Eq. (4.94) has to be evaluated for each strip of the contact patch since it depends of its lateral coordinate. This issue is highly relevant since the numerical assessment of the integral involves a significant computational cost which may compromise the efficiency of railway dynamics simulations.

The normal contact force estimated using this method is obtained through the integration of the pressure distribution, given by Eq. (4.92), over the contact area as

$$f_{\mathrm{n}}^{\mathrm{SZG}}=\int_{y_{\mathrm{s}}}^{y_{\mathrm{e}}}\int_{-x_{\mathrm{L}}}^{x_{\mathrm{L}}}p_0(y)\sqrt{1-\left(\frac{x}{x_{\mathrm{L}}(y)}\right)^2}\,\mathrm{d}x\mathrm{d}y \tag{4.95}$$

introducing Eq. (4.94), it yields

$$f_{\mathrm{n}}^{\mathrm{SZG}}=\frac{\pi E}{2\left(1-\sigma^2\right)}\int_{y_{\mathrm{s}}}^{y_{\mathrm{e}}}\int_{-x_{\mathrm{L}}}^{x_{\mathrm{L}}}\delta_{\mathrm{cp}}(y)\sqrt{x_{\mathrm{L}}^2(y)-x^2}\left(\int_{y_{\mathrm{s}}}^{y_{\mathrm{e}}}\int_{-x_{\mathrm{L}}}^{x_{\mathrm{L}}}\sqrt{\frac{x_{\mathrm{L}}^2(\eta)-\xi^2}{\xi^2+\left(y-\eta\right)^2}}\,\mathrm{d}\xi\mathrm{d}\eta\right)^{-1}\mathrm{d}x\mathrm{d}y \tag{4.96}$$

and solving the integral in the x direction, the normal contact force is formulated as

$$f_{\mathrm{n}}^{\mathrm{SZG}}=\frac{\pi^2 E}{4\left(1-\sigma^2\right)}\int_{y_{\mathrm{s}}}^{y_{\mathrm{e}}}\delta_{\mathrm{cp}}(y)x_{\mathrm{L}}^2(y)\left(\int_{y_{\mathrm{s}}}^{y_{\mathrm{e}}}\int_{-x_{\mathrm{L}}}^{x_{\mathrm{L}}}\sqrt{\frac{x_{\mathrm{L}}^2(\eta)-\xi^2}{\xi^2+\left(y-\eta\right)^2}}\,\mathrm{d}\xi\mathrm{d}\eta\right)^{-1}\mathrm{d}y \tag{4.97}$$

Similar to the Kik-Piotrowski model, this expression is only valid to the evaluation of the normal contact force in planar contact patches. For the case of a curved contact region, the normal force has to be integrated independently in each strip as

$$f_{\mathrm{n},i}^{\mathrm{SZG}}=\frac{\pi^2 E}{4\left(1-\sigma^2\right)}\int_{s_i-\Delta s/2}^{s_i+\Delta s/2}\delta_{\mathrm{cp}}(s)x_{\mathrm{L}}^2(s)\left(\int_{s_{\mathrm{s}}}^{s_{\mathrm{e}}}\int_{-x_{\mathrm{L}}}^{x_{\mathrm{L}}}\sqrt{\frac{x_{\mathrm{L}}^2(\eta)-\xi^2}{\xi^2+\left(s-\eta\right)^2}}\,\mathrm{d}\xi\mathrm{d}\eta\right)^{-1}\mathrm{d}s \tag{4.98}$$

Assuming that a given strip possesses constant length and penetration, Eq. (4.98) is simplified as

$$f_{\mathrm{n},i}^{\mathrm{SZG}}=\frac{\pi^2 E\delta_{\mathrm{cp}}(s_i)x_{\mathrm{L}}^2(s_i)\Delta s}{4\left(1-\sigma^2\right)}\left(\int_{s_{\mathrm{s}}}^{s_{\mathrm{e}}}\int_{-x_{\mathrm{L}}}^{x_{\mathrm{L}}}\sqrt{\frac{x_{\mathrm{L}}^2(\eta)-\xi^2}{\xi^2+\left(s_i-\eta\right)^2}}\,\mathrm{d}\xi\mathrm{d}\eta\right)^{-1} \tag{4.99}$$

The total normal contact force is also given by the vector sum of the force originated in each strip of contact and, written as

$$\mathbf{f}_{\mathrm{n}}^{\mathrm{SZG}} = \sum_{i=1}^{N_{\mathrm{s}}} f_{\mathrm{n},i}^{\mathrm{SZG}} \mathbf{n}_{\mathrm{s},i} \tag{4.100}$$

For the planar contact patch, an expression identical to Eq. (4.91) is used as

$$\mathbf{f}_{\mathrm{n}}^{\mathrm{SZG}} = f_{\mathrm{n}}^{\mathrm{SZG}} \mathbf{n}_{\mathrm{r},P} \tag{4.101}$$

In short, this contact force model allows to calculate the normal force magnitude based on the Boussinesq-Cerruti approximation without discontinuities when the location of the maximum penetration point changes abruptly. However, it requires the evaluation of the integral of Eq. (4.94) for each contact strip, which means that the computational cost of this model is N_{s} times higher than that of the Kik-Piotrowski model. It must be noted that these two contact models (Kik-Piotrowski and Sun et al.) are purely elastic, since the contact force only depends on the relative positions between the contacting surfaces. Hence, a damping effect can be added by multiplying the respective normal force by the damping factor given by Eq. (4.14), as demonstrated for the Hertzian model.

4.4. Application Example

In this section, a case of static interaction between a wheel and a rail is used as an example of application to investigate the advantages and limitations of the contact methodologies discussed throughout this chapter. Thus, five different contact modelling approaches are compared, namely Hertzian contact, non-Hertzian planar contact with both KP and SZG models, and non-Hertzian curved contact with both KP and SZG models. In order to proceed to the static analysis, the wheel and rail profiles used are the S1002 and UIC50, respectively, which are displayed in Figure 4.12. The material properties and geometrical characteristics of the vehicle track interaction employed here are listed in Table 4.1.

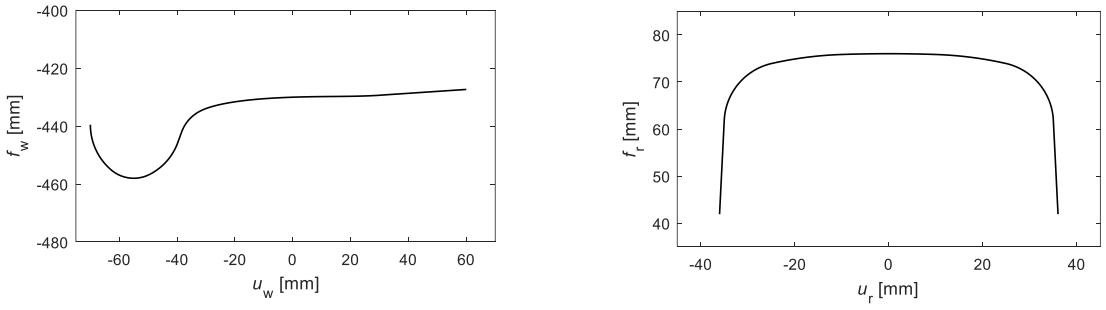

Figure 4.12 – Profiles utilized in the static analysis: (a) Wheel S1002 and (b) Rail UIC50.

Table 4.1 – Geometric and material properties for the static analysis.

Parameter	Value
Nominal wheel radius, R_0	0.43 m
Distance between wheel profiles, H	1.5 m
Track gauge	1.435 m
Rail cant	1:40 and 1:20
Young modulus, E	206 GPa
Poisson ratio, σ	0.296

Although the methodologies described in the previous sections enable the calculation of the contact patches and, hence, the normal contact forces, in these static analyses, the contact is evaluated for a specified normal force. Therefore, for a fixed lateral displacement, the vertical position of the wheelset is iteratively identified to ensure that the specified normal force is obtained. It must be noted that the wheelset lateral displacement is estimated relative to its nominal position as described in Figure 4.13, in which Δy is measured from the track centerline until the wheelset center of mass in the lateral direction.

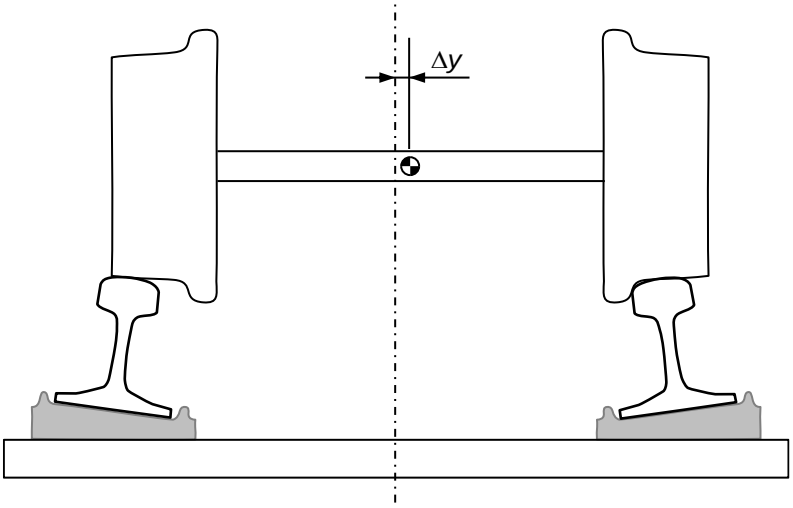

Figure 4.13 – Representation of the lateral displacement of the wheelset.

In the following sections, three main aspects are studied. First, the shape and size of the contact patch obtained with different approaches are examined for different wheel-rail configurations. It must be mentioned that two different rail cant configurations are used here, which allow to simulate the interaction between wheel and rail for distinct relative positions. Second, the effects of normal load variation are analyzed. Finally, the problems associated with contact force discontinuities are identified, and the capability of each methodology to deal with them is investigated.

4.4.1. Static Analysis – Rail Cant 1:40

The wheel-rail interaction is evaluated for five different wheelset lateral positions considering a 1:40 rail cant (1.43°). The normal load specified for this case is 48 kN, and the vertical position of the wheel is adjusted until the normal force error is less than 0.1 N. In order to facilitate the comparison of the contact modelling approaches, only three methodologies are examined, namely the Hertzian model, non-Hertzian model with flat patch and the non-Hertzian model with curved patch. Both non-Hertzian approaches are computed using the SZG model presented in section 4.3.2. Since the main goal of this analysis is to assess the influence of the modeling approaches on the shape of contact patch, the comparison between KP and SZG model is performed later in this section.

Bearing in mind that this analysis is static and there is no relative velocity between the contacting bodies, only purely elastic models are considered, therefore, the damping factor proposed in Eq. (4.14) is not used. Regarding the non-Hertzian approaches, the penetration correction factor used is 0.55 and the width of the strips is 0.1 mm (Magalhães et al., 2020). The static simulations are computed without yaw motion for five different relative positions, in which the wheel lateral displacement is -1, 0, 1, 4 and 5 mm, being the corresponding contact patches displayed from Figure 4.14 to Figure 4.18. Each figure shows the location and size of each contact patch on the wheel and rail profiles for Hertzian contact patch, non-Hertzian planar contact patch and non-Hertzian curved contact patch. They also compare the shape of the three contact patches, in which the curved contact patch is projected onto a plane to facilitate the comparison and the point of maximum penetration is used as the origin of the reference systems.

The results show that, for the tested cases, the Hertzian contact model present significantly different contact patches when compared with the non-Hertzian approaches, mainly for a lateral displacement of -1, 0 and 5 mm, as depicted in Figure 4.14, Figure 4.15 and Figure 4.18. Moreover, Table 4.2 contains the contact patches area for the 15 evaluated cases, and the specified differences are more noticeable. In what concerns to the aspect of the contact patch, the Hertzian model tends to produce narrower contact regions but longer in the longitudinal direction. These results agree with the maximum pressure obtained for each contact modeling procedure, since the Hertzian contact patches exhibit higher maximum pressure, as demonstrated in Table 4.3. Regarding both non-Hertzian approaches, they present identical results, either in shape or size of the contact patches.

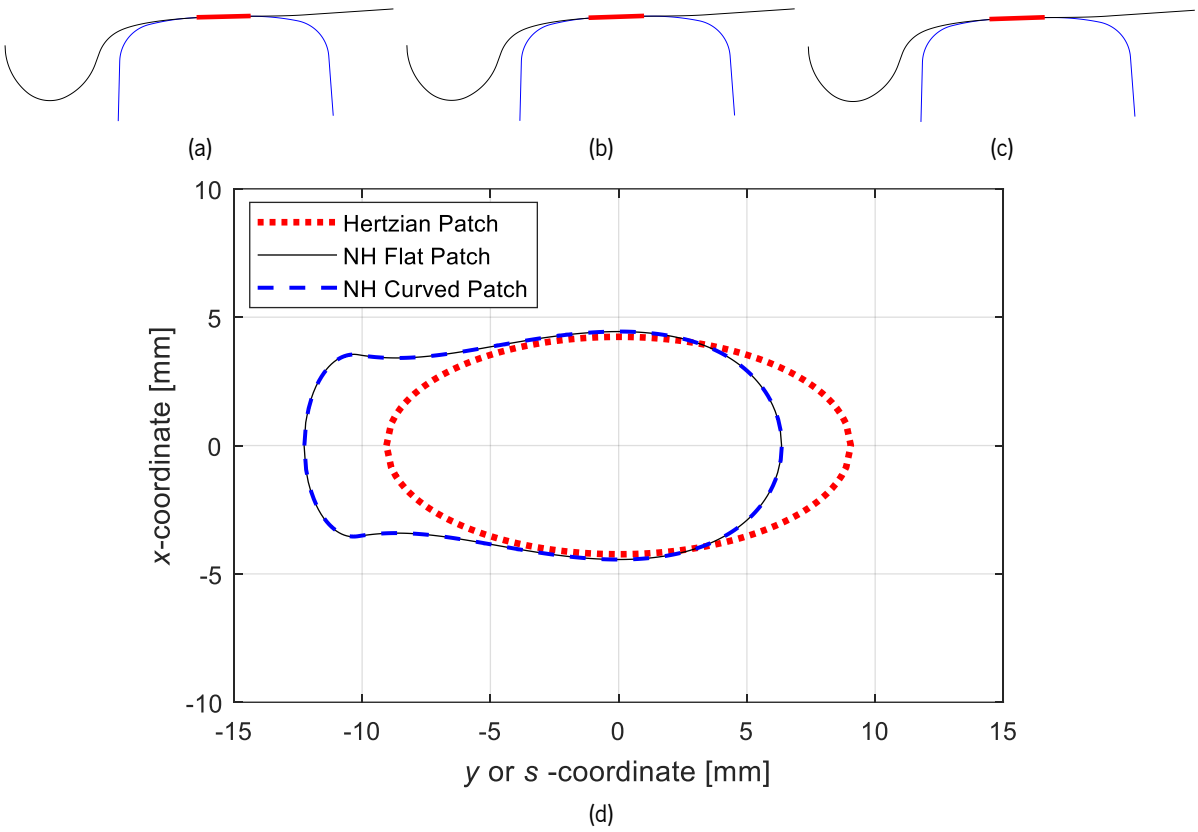

Figure 4.14 – Location and size of contact zones for (a) Hertzian, (b) non-Hertzian flat and (c) non-Hertzian curved contact, and (d) corresponding contact patches for a 1:40 rail cant, 48 kN normal load and Δy = -1 mm.

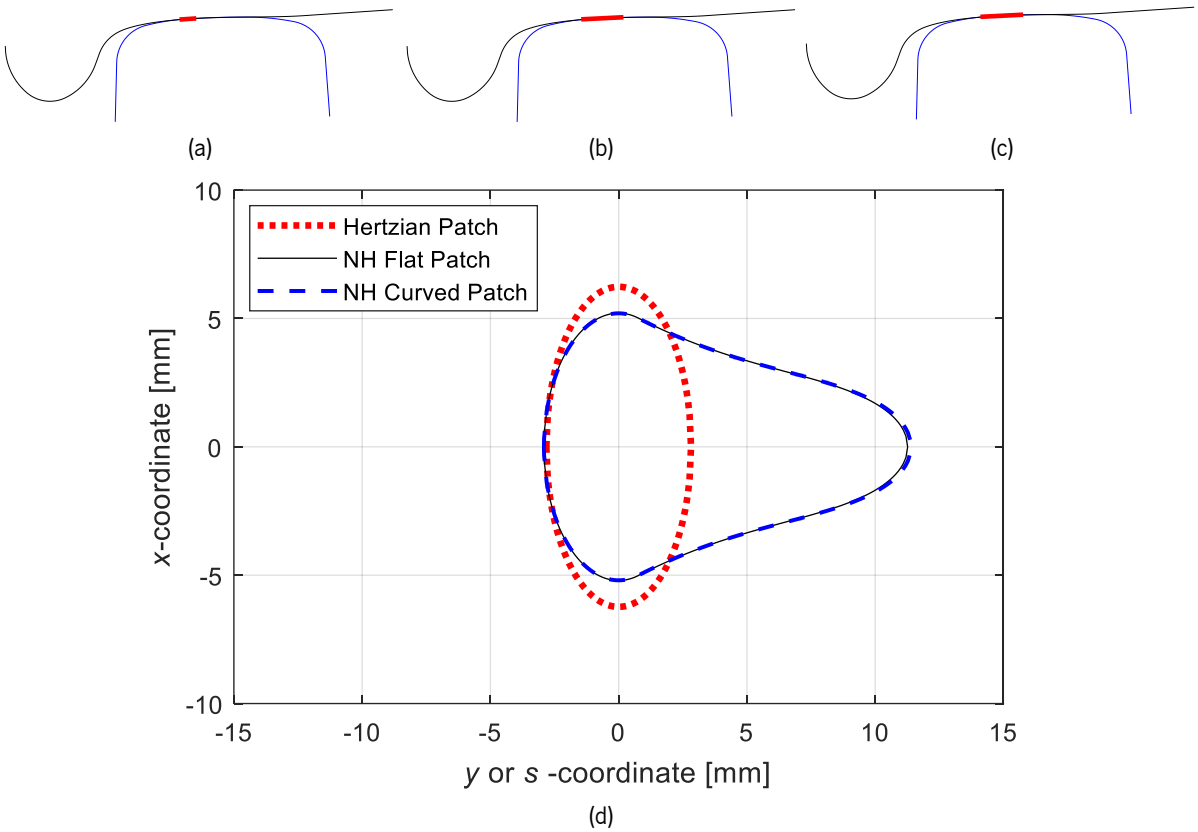

Figure 4.15 – Location and size of contact zones for (a) Hertzian, (b) non-Hertzian flat and (c) non-Hertzian curved contact, and (d) corresponding contact patches for a 1:40 rail cant, 48 kN normal load and Δy = 0 mm.

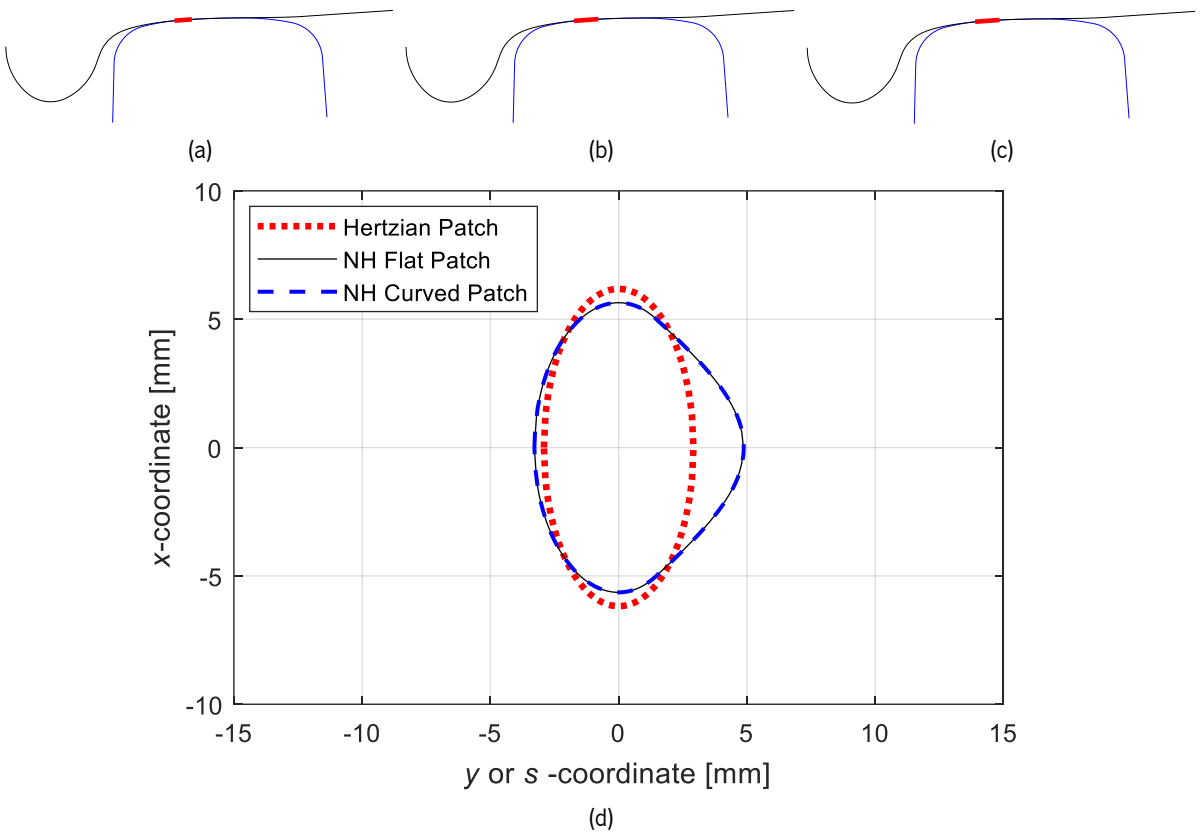

Figure 4.16 – Location and size of contact zones for (a) Hertzian, (b) non-Hertzian flat and (c) non-Hertzian curved contact, and (d) corresponding contact patches for a 1:40 rail cant, 48 kN normal load and $\Delta y = 1$ mm.

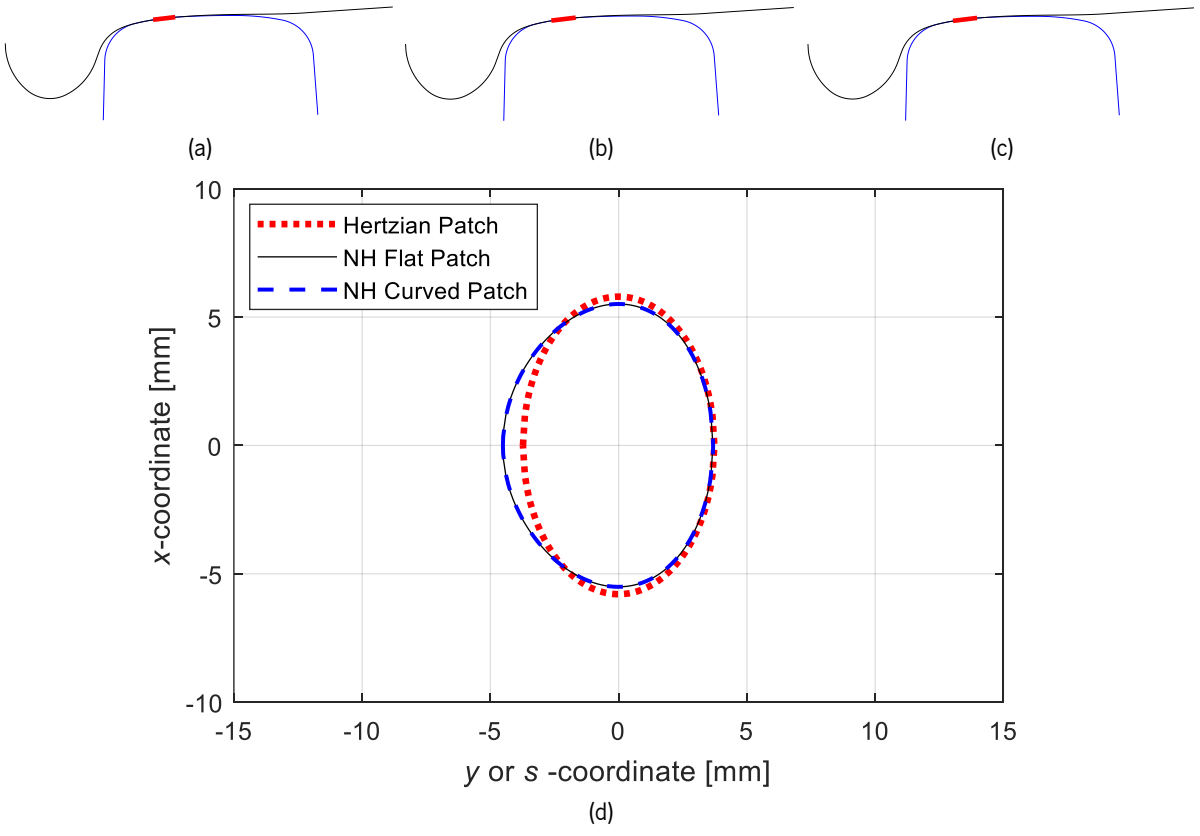

Figure 4.17 – Location and size of contact zones for (a) Hertzian, (b) non-Hertzian flat and (c) non-Hertzian curved contact, and (d) corresponding contact patches for a 1:40 rail cant, 48 kN normal load and $\Delta y = 4$ mm.

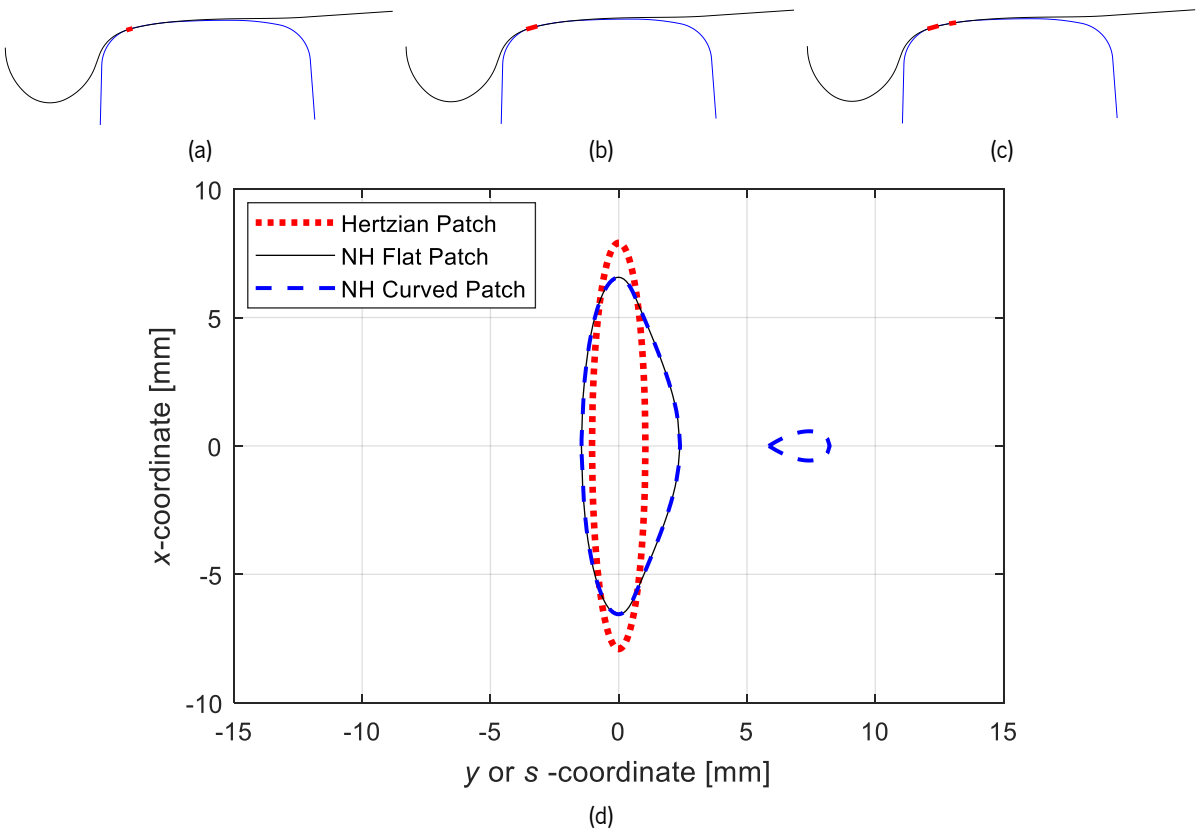

Figure 4.18 – Location and size of contact zones for (a) Hertzian, (b) non-Hertzian flat and (c) non-Hertzian curved contact, and (d) corresponding contact patches for a 1:40 rail cant, 48 kN normal load and Δy = 5 mm.

Table 4.2 – Contact patch area [mm^2] for different lateral wheel positions with Hertzian contact, non-Hertzian flat contact and non-Hertzian curved contact for a 1:40 rail cant and a normal load of 48 kN.

Lateral Displacement, Δy	**-1 mm**	**0 mm**	**1 mm**	**4 mm**	**5 mm**
Hertzian Contact	120.42	55.24	56.59	67.93	25.86
Non-Hertzian Flat Contact	136.18	95.56	66.50	70.20	35.54
Non-Hertzian Curved Contact	136.15	96.16	66.50	70.38	37.31

Table 4.3 – Maximum pressure [MPa] for different lateral wheel positions with Hertzian contact, non-Hertzian flat contact and non-Hertzian curved contact for a 1:40 rail cant and a normal load of 48 kN.

Lateral Displacement, Δy	**-1 mm**	**0 mm**	**1 mm**	**4 mm**	**5 mm**
Hertzian Contact	597.90	1303.44	1272.41	1059.91	2783.89
Non-Hertzian Flat Contact	522.62	927.44	1169.65	1045.58	2295.55
Non-Hertzian Curved Contact	522.69	924.94	1168.88	1045.69	2292.96

It must be highlighted that the only case in which more than one contact patch takes place is when using the non-Hertzian curved contact patch for a lateral displacement of 5 mm as shown in Figure 4.18. In this case, the wheel and rail have only one interference region, however, as the contact occurs in a more conformal zone, the computation of the penetration function using the planar and curved approaches presents significant differences, as depicted in Figure 4.19. Since the penetration function of

the curved contact holds two peaks, following the methodology illustrated in Figure 4.5, the total contact area will contain two separate patches.

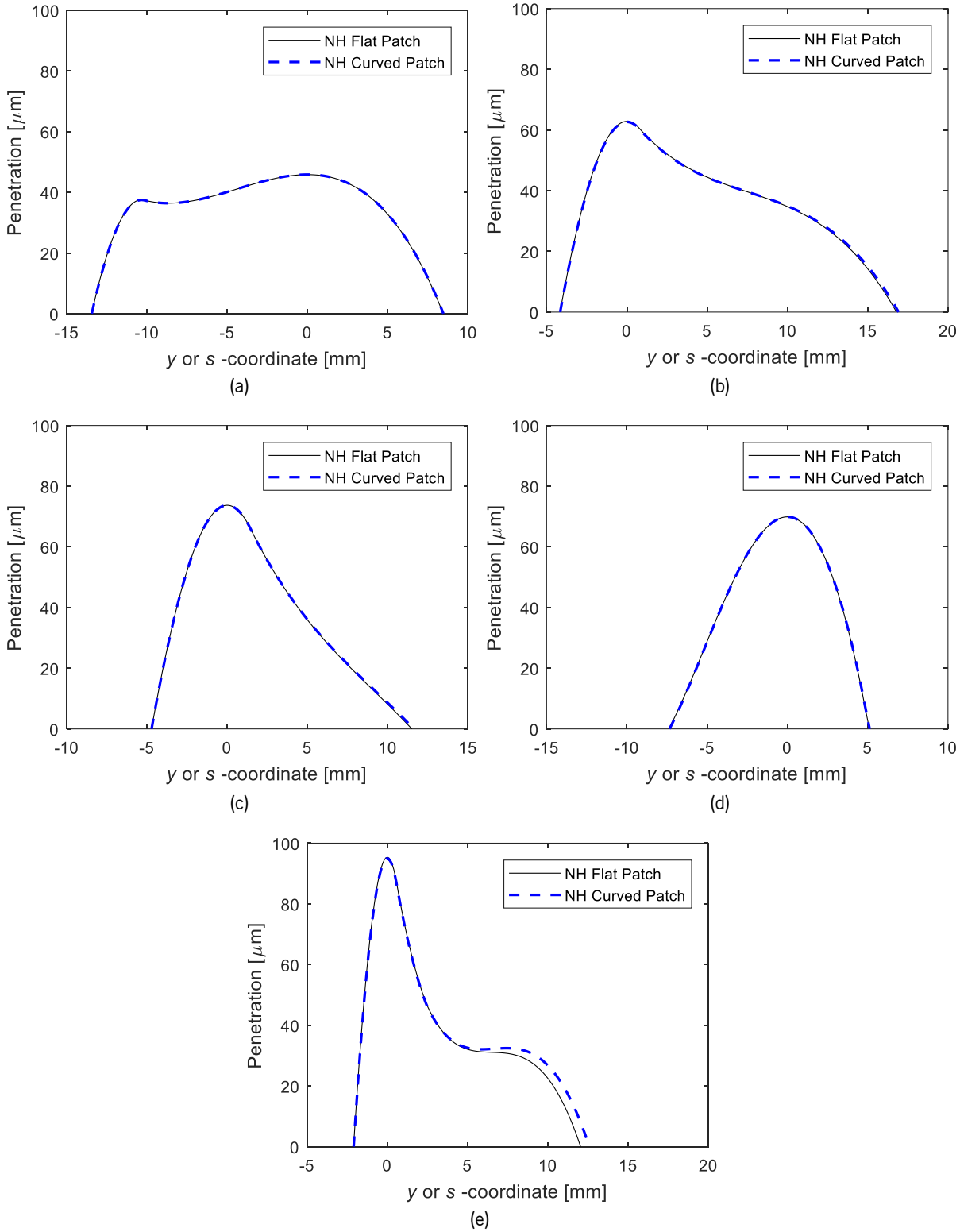

Figure 4.19 – Penetration function obtained with both flat and curved contact patch approaches for 1:40 rail cant and 48 kN normal load, (a) Δy = -1 mm, (b) Δy = 0 mm, (c) Δy = 1 mm, (d) Δy = 4 mm, and (e) Δy = 5 mm.

Table 4.4 – Contact angle variation in non-Hertzian curved contact patch for different lateral wheel positions for a 1:40 rail cant and a normal load of 48 kN.

Lateral Displacement, Δy	**-1 mm**	**0 mm**	**1 mm**	**4 mm**	**5 mm**
Contact Angle Variation, $\Delta\gamma$	3.94°	3.97°	3.21°	4.92°	12.61°

Table 4.4 shows the variation of the contact angle on the curved contact patches for the five different lateral positions. In the last case, the variation of the contact angle represents the total angular variation from the start of the first patch until the end of the second patch, since both areas belong to the same interpenetration which would return just one direction on the planar approach. Nonetheless, the contact angle variation for each patch is 8.06° and 1.55°, respectively, for the first and second patches. From these results, it is possible to conclude that the contact angle variation tends to increase when the contact approaches the wheel conformal zone. The greater this variation, the greater the need of considering a curved contact patch. Moreover, since the maximum variation is 12.61°, the half-space assumption can be held without introducing substantial inaccuracy.

4.4.2. Static Analysis – Rail Cant 1:20

In order to accomplish a detailed analysis of the contact modelling methodologies, the evaluation of the contact patches for different wheel lateral positions is performed again considering the same profiles but a different rail cant. In this case, a greater cant angle is examined, namely 1:20 rail cant (2.86°). Regarding the simulation parameters, the same data of previous case is considered here, therefore, a 48 kN normal load is imposed. Nevertheless, a new wheel-rail relative position is also included, besides the five different positions previously examined. Thus, a lateral displacement of 6.4 mm is used to investigate a more conformal situation.

The obtained locations and shapes of the contact patches for the Hertzian contact, non-Hertzian planar contact and non-Hertzian curved contact are displayed in Figure 4.20 to Figure 4.25. From their analysis, it is possible to verify some of the conclusions collected from the previous application case, namely the Hertzian approach based on the curvatures of the maximum penetration point tends to produce a longer patch on the longitudinal direction and a narrower patch on the lateral direction. Regarding the whole contact area, the values displayed in Table 4.5 show that both non-Hertzian approaches provide similar results for the case analyzed. In terms of the maximum pressure, the same tendency is observed as demonstrated by the results presented in Table 4.6. However, the differences between them and the Hertzian methodology are larger when compared with the results from previous section, mainly in the case of Δy is equal to 5 mm where two contact patches coexist. It should be

mentioned that it is the only lateral wheel position which returned two distinct contact patches, and both contact areas are found to be in different interpenetration regions. This is a significant issue, since, unlike the case in the previous example, it allows that the non-Hertzian flat contact approach to compute two separate contact areas in two different planes of contact which explain the similar results obtained with a curved contact patch.

Table 4.5 – Contact patch area [mm^2] for different lateral wheel positions with Hertzian contact, non-Hertzian flat contact and non-Hertzian curved contact for a 1:20 rail cant and a normal load of 48 kN.

Lateral Displacement, Δy	**-1 mm**	**0 mm**	**1 mm**	**4 mm**	**5 mm**	**6.4 mm**
Hertzian Contact	45.57	46.08	46.57	47.92	48.37	37.56
Non-Hertzian Flat Contact	55.40	56.88	58.85	71.88	92.72	42.84
Non-Hertzian Curved Contact	55.69	56.77	58.79	72.08	92.70	42.43

Table 4.6 – Maximum pressure [MPa] for different lateral wheel positions with Hertzian contact, non-Hertzian flat contact and non-Hertzian curved contact for a 1:20 rail cant and a normal load of 48 kN.

Lateral Displacement, Δy	**-1 mm**	**0 mm**	**1 mm**	**4 mm**	**5 mm**	**6.4 mm**
Hertzian Contact	1580.12	1562.61	1546.08	1502.37	1488.38	1917.08
Non-Hertzian Flat Contact	1383.03	1352.16	1311.83	1087.59	893.15	1760.02
Non-Hertzian Curved Contact	1381.58	1350.90	1310.81	1086.21	891.86	1773.04

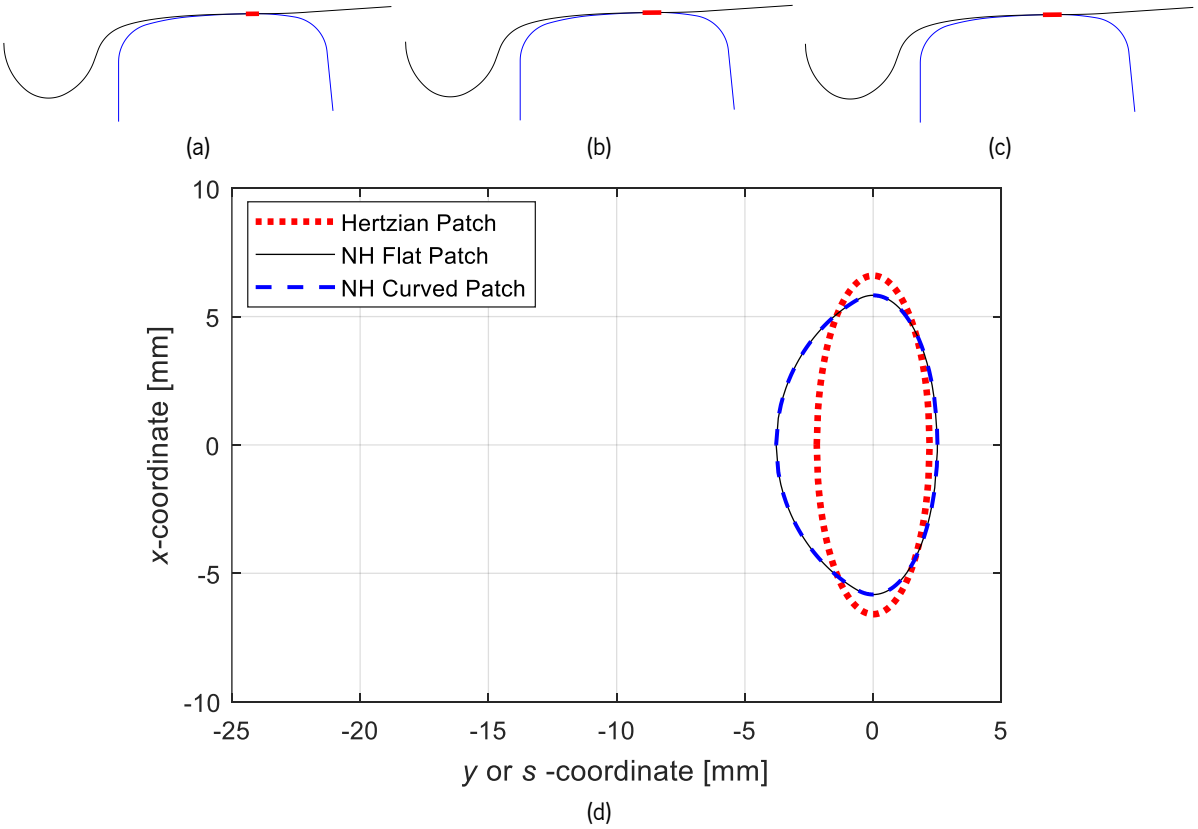

Figure 4.20 – Location and size of contact zones for (a) Hertzian, (b) non-Hertzian flat and (c) non-Hertzian curved contact, and (d) corresponding contact patches for a 1:20 rail cant, 48 kN normal load and Δy = -1 mm.

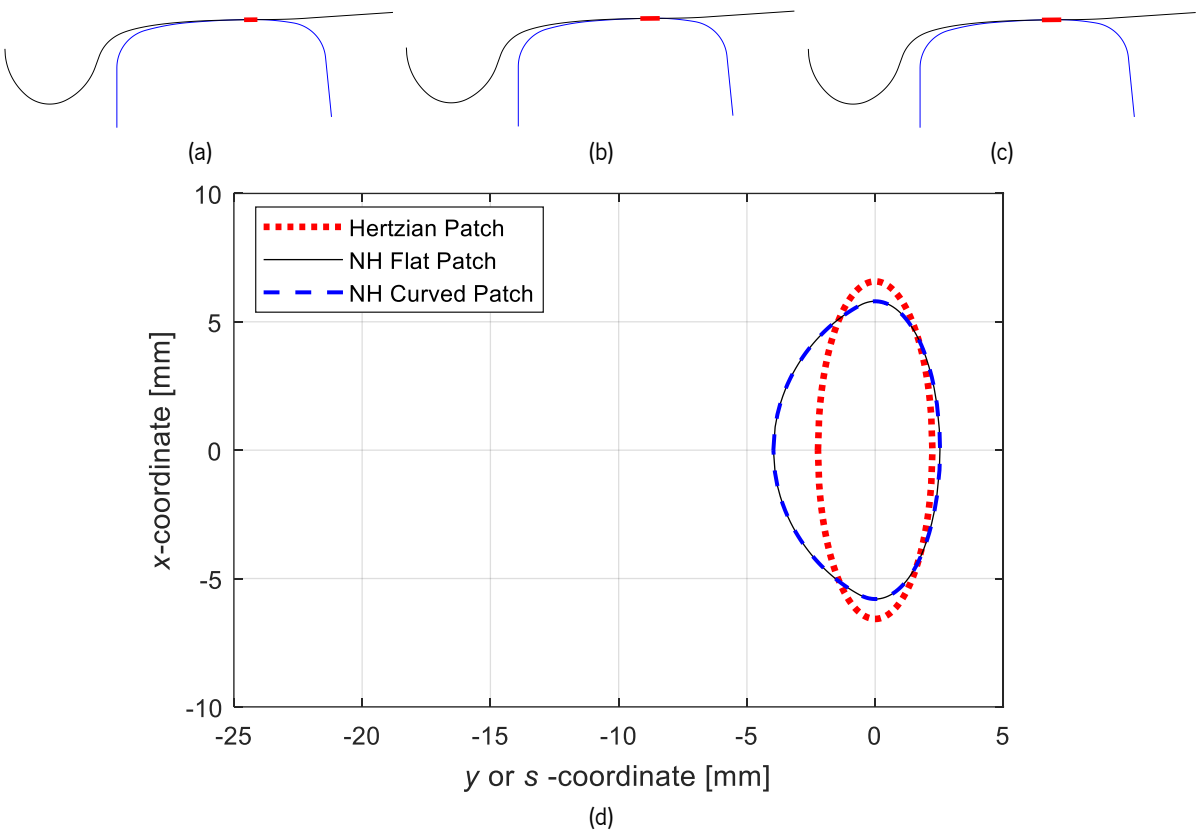

Figure 4.21 – Location and size of contact zones for (a) Hertzian, (b) non-Hertzian flat and (c) non-Hertzian curved contact, and (d) corresponding contact patches for a 1:20 rail cant, 48 kN normal load and $\Delta y = 0$ mm.

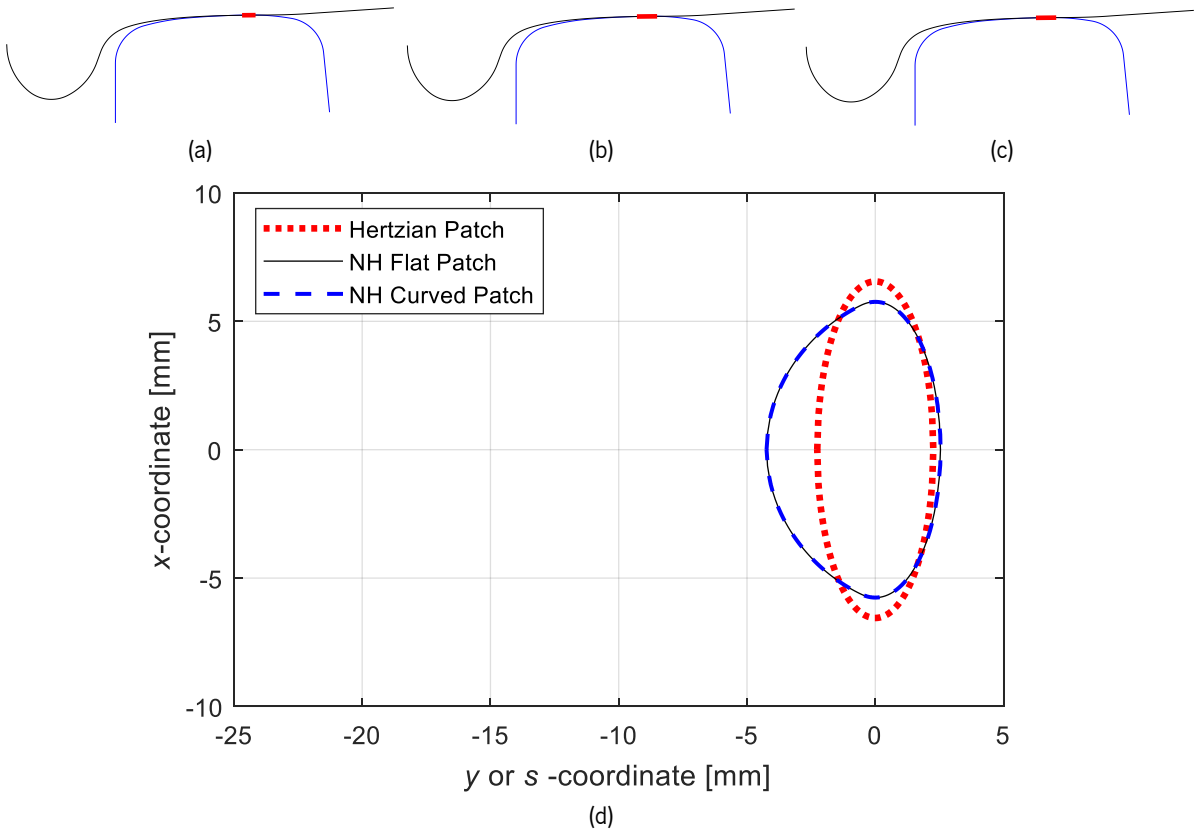

Figure 4.22 – Location and size of contact zones for (a) Hertzian, (b) non-Hertzian flat and (c) non-Hertzian curved contact, and (d) corresponding contact patches for a 1:20 rail cant, 48 kN normal load and $\Delta y = 1$ mm.

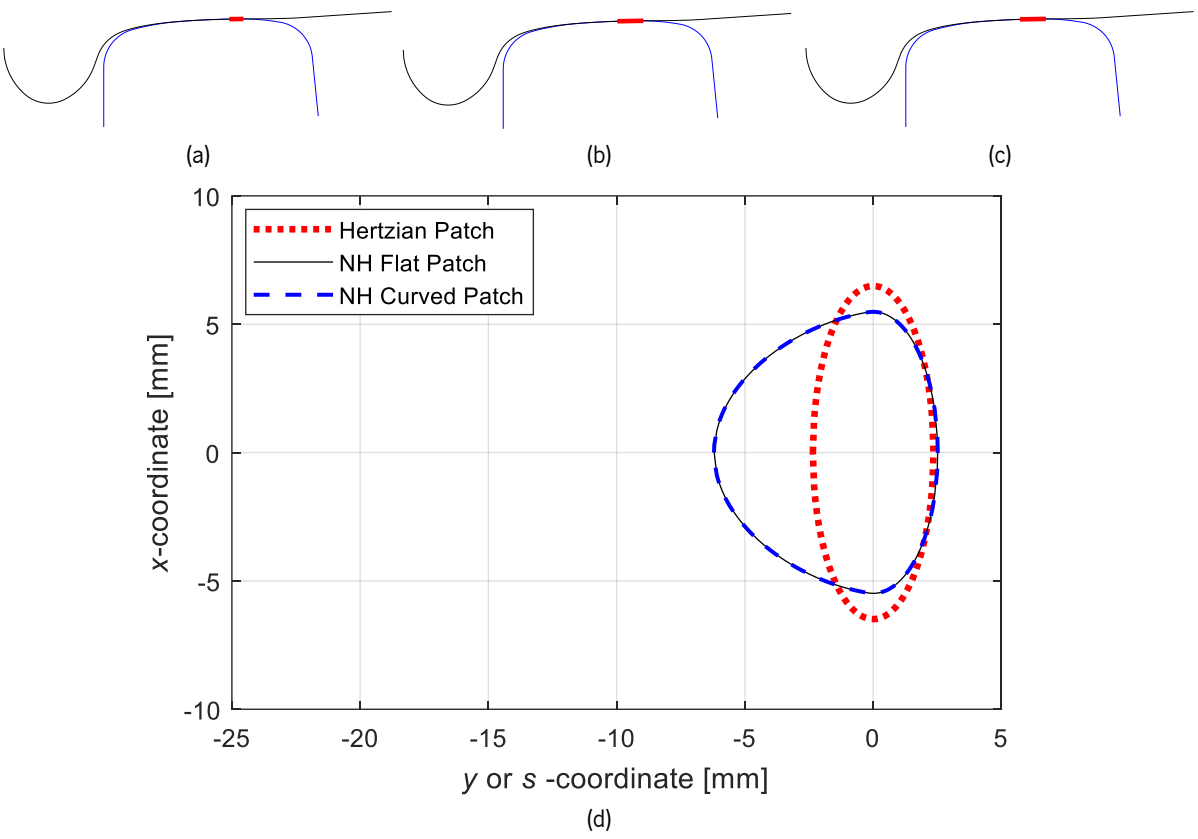

Figure 4.23 – Location and size of contact zones for (a) Hertzian, (b) non-Hertzian flat and (c) non-Hertzian curved contact, and (d) corresponding contact patches for a 1:20 rail cant, 48 kN normal load and $\Delta y = 4$ mm.

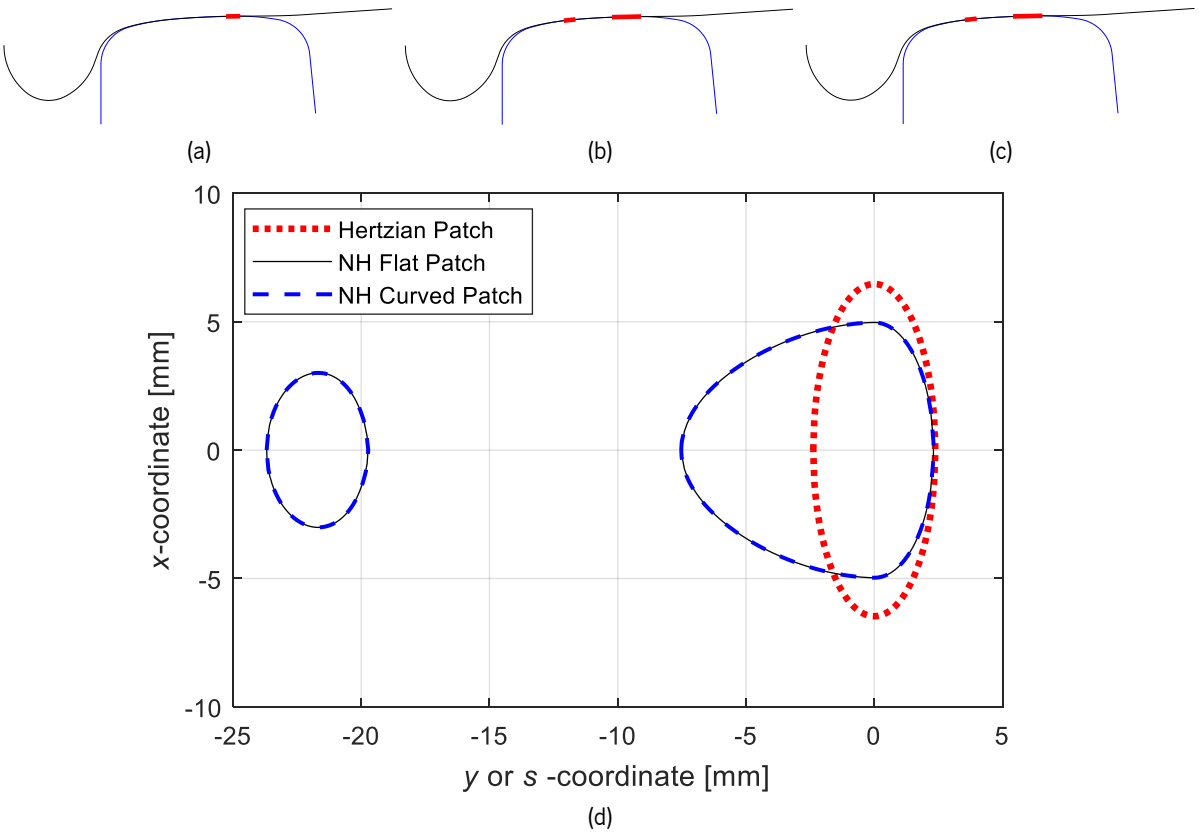

Figure 4.24 – Location and size of contact zones for (a) Hertzian, (b) non-Hertzian flat and (c) non-Hertzian curved contact, and (d) corresponding contact patches for a 1:20 rail cant, 48 kN normal load and $\Delta y = 5$ mm.

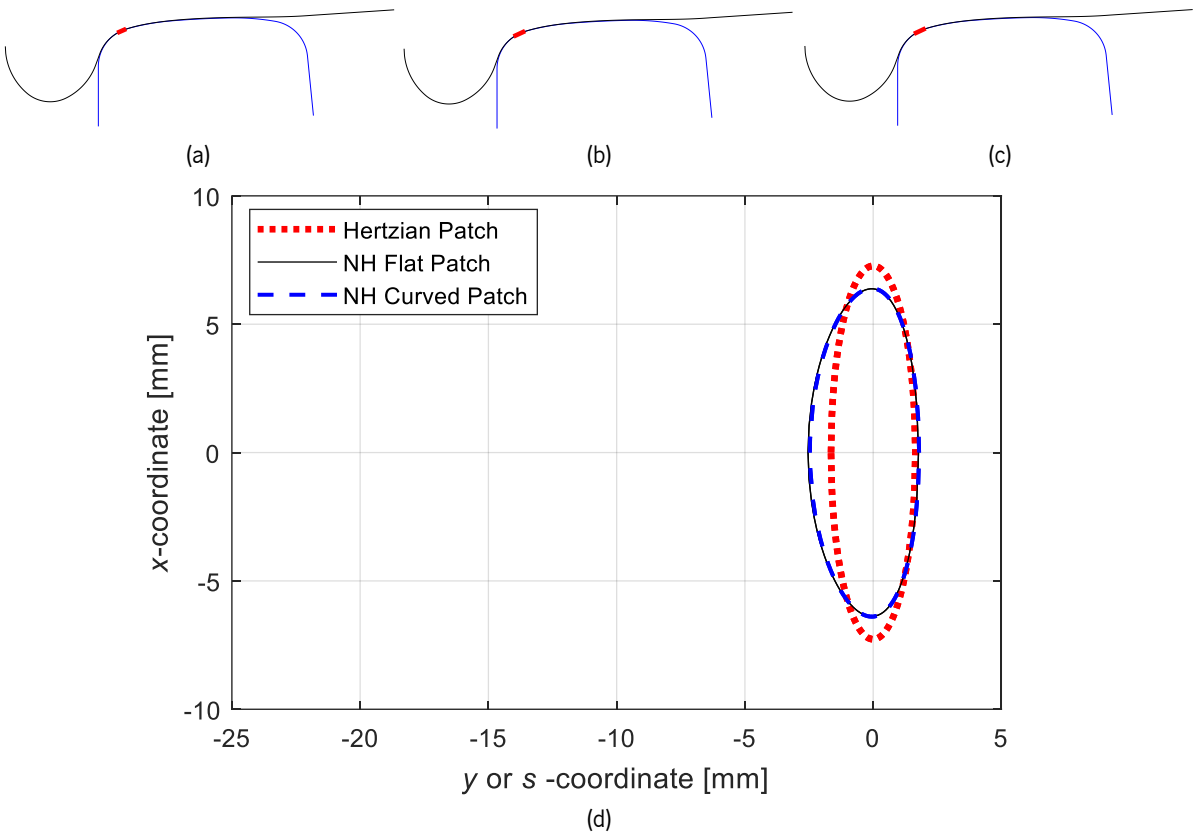

Figure 4.25 – Location and size of contact zones for (a) Hertzian, (b) non-Hertzian flat and (c) non-Hertzian curved contact, and (d) corresponding contact patches for a 1:20 rail cant, 48 kN normal load and Δy = 6.4 mm.

In terms of the location of the contact patches on the wheel profile, it can be seen from Figure 4.20 to Figure 4.24 that, although the wheel lateral position changes, the contact always takes place on the wheel tread. Moreover, despite the fact that nearly half of the wheel tread has negative curvature, as seen Figure 3.5, it cannot be stated that it produces a conformal contact in most cases. Bearing that in mind, the case in which Δy is equal to 6.4 mm was also studied, since the interpenetration occurs in the wheel transition zone as depicted in Figure 4.25. The conformality of this contact interaction is evident, mainly when compared with the remaining ones, through the analysis of contact angle variation using the non-Hertzian curved contact approach. Table 4.7 demonstrates that, in this case, the contact angle variation is approximately 16.32°, which is substantially higher than in the remaining scenarios. It must be noted that two variations of the contact angle are provided for the case in which Δy is equal to 5 mm which concern to the two separate interpenetration regions. The existence of small contact angle variations for the curved patch approach leads to minor differences relatively to the planar patch results, since the penetration is measured with just slight changes of direction. In that sense, Figure 4.26 depicts the penetration function of the wheel and rail profiles only for the last scenario, since it is shows the most significative differences, mainly when moving away from the point of maximum penetration. As this

contact scenario generates a significant degree of conformity, it would be expected to produce a larger contact patch in the lateral direction. However, the increase of wheel profile slope in the flange region reduces the longitudinal curvature of the wheel surface (see Eq. (3.27)) which increases the length of the patch in that direction. Hence, with a lower width, the same normal load is produced. This issue allows to conclude that the conformal contact might become more evident when the contact occurs in the wheel tread between worn profiles, since the surface longitudinal curvature keeps a high value.

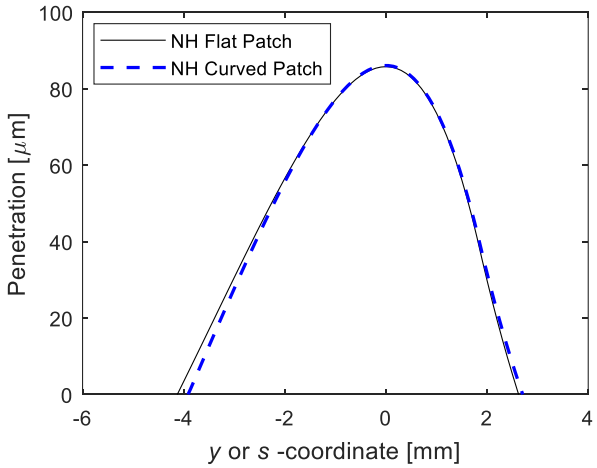

Figure 4.26 – Penetration function obtained with both flat and curved contact patch approaches for 1:20 rail cant and 48 kN normal load with a lateral wheel displacement of Δy = 6.4 mm.

Table 4.7 – Contact angle variation in non-Hertzian curved contact patch for different lateral wheel positions for a 1:20 rail cant and a normal load of 48 kN.

Lateral Displacement, Δy	**-1 mm**	**0 mm**	**1 mm**	**4 mm**	**5 mm**	**6.4 mm**
Contact Angle Variation, $\Delta\gamma$	1.47°	1.56°	1.65°	2.04°	2.07° and 2.22°	16.32°

4.4.3. Effect of Normal Load

In this section, two of the previous cases are used to verify the effects of normal load variation the obtained contact patches. Thus, for 1:40 rail cant, the case of Δy equal to -1 mm is selected and, for the 1:20 rail cant, the scenario where Δy is equal to 5 mm is used. For this analysis, apart from the case with a normal load of 48 kN which was previously discussed, two additional cases are simulated here, namely with 24 kN and 72 kN.

Regarding the first example, the contact patches obtained are depicted in Figure 4.27, which can be compared with Figure 4.14 that presents the results for 48 kN. This case is chosen due to the large width of the contact patch when compared with the remaining ones. The increase of normal load leads to the expected rise of the contact patch area. This growth is also demonstrated in Table 4.8, which

shows that the relative difference of contact area between Hertzian and non-Hertzian approaches is lower for higher normal load values. From the analysis of Figure 4.27, it is possible to conclude that the increase of the contact area is higher on the longitudinal direction than in the lateral direction. Since this contact occurs in wheel tread, the utilization of a curved patch did not become relevant, as can be demonstrated by the obtained contact angle variations listed in Table 4.8. Although the angle increases with the increasing of the normal load, the changes are not significant.

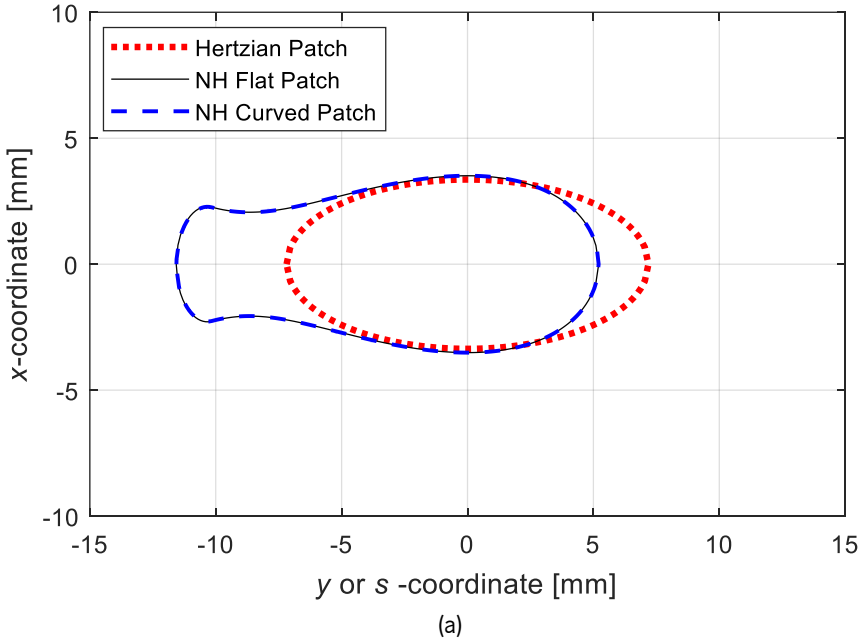

(a)

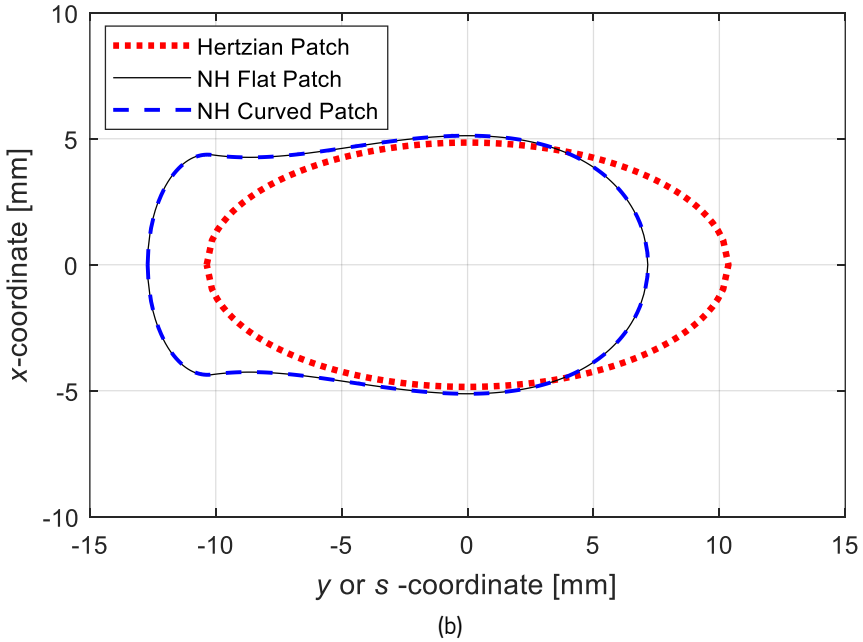

(b)

Figure 4.27 – Contact patches obtained for a 1:40 rail cant and Δy = -1 mm with normal load of (a) 24 kN and (b) 72 kN.

Figure 4.28 show the interpenetration function for the three different values of normal load, and it exhibits great similarities between both planar and curved approaches regardless of the normal force.

This figure includes an enlarged view of the maximum penetration region for each case, and it can be verified that the maximum penetration is always slightly higher for non-Hertzian model with curved contact patch. This is related to the fact that, due to the inclination of the contact patch, in the curved approach, there is a component of the normal pressure which does not contribute to the total normal force. Therefore, the model requires more penetration to achieve the same normal force.

Table 4.8 – Contact area, maximum pressure and cant angle variation for a 1:40 rail cant and Δy = -1 mm with different normal loads.

Normal Load		**24 kN**	**48 kN**	**72 kN**
Contact Area [mm^2]	Hertzian Contact	75.87	120.42	157.78
	Non-Hertzian Flat Contact	90.10	136.18	171.51
	Non-Hertzian Curved Contact	90.14	136.15	171.42
Maximum Pressure [MPa]	Hertzian Contact	474.48	597.90	684.51
	Non-Hertzian Flat Contact	414.52	522.62	607.87
	Non-Hertzian Curved Contact	414.52	522.69	607.98
Contact Angle Variation		3.47°	3.94°	4.29°

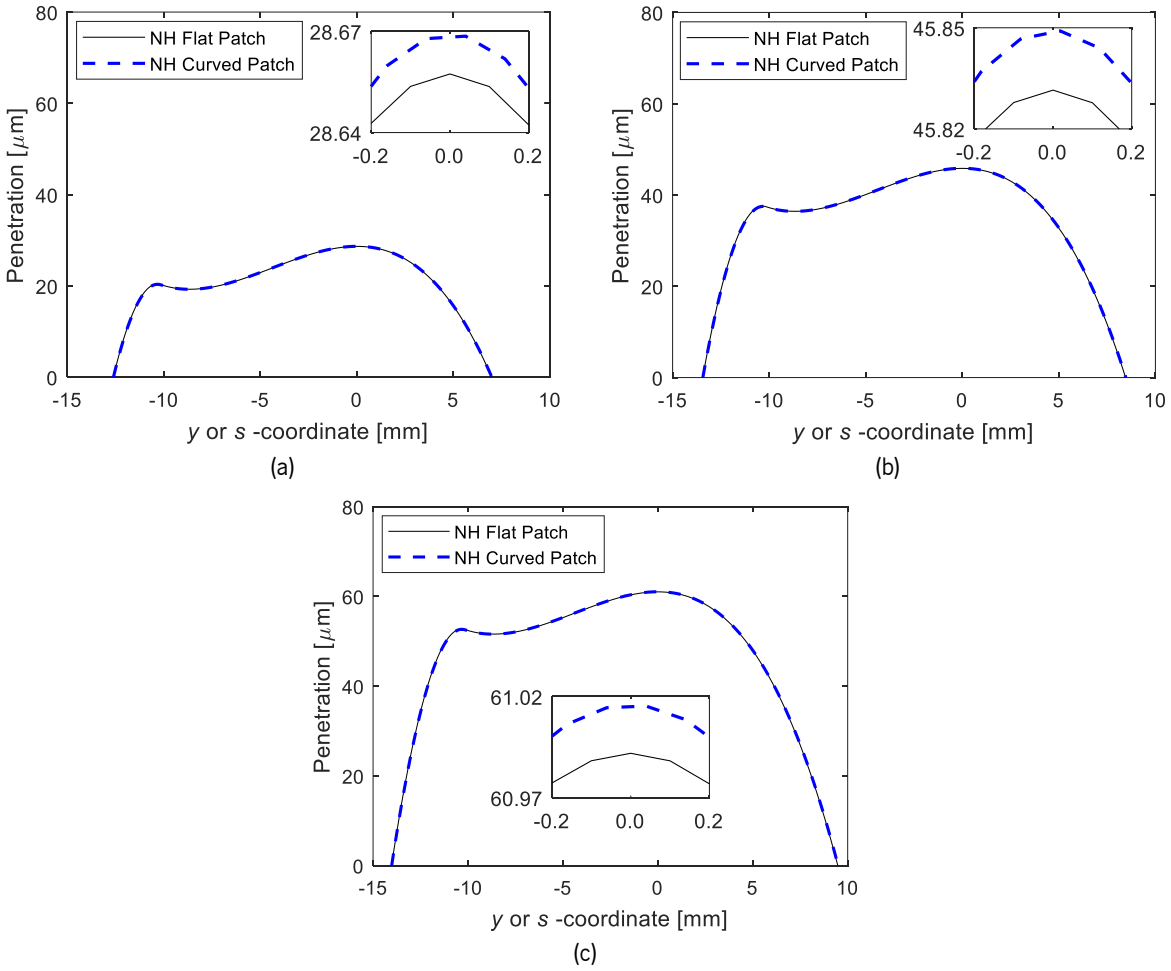

Figure 4.28 – Penetration function obtained with both flat and curved contact patch approaches for 1:40 rail cant and Δy = -1 mm, (a) 24 kN mm, (b) 48 kN, and (c) 72 kN.

The second example to study the variation of normal force is the scenario with 5 mm wheel lateral displacement and a rail cant 1:20, which exhibited two distinct contact patches in Figure 4.24. Similar to the previous example, the contact is tested for 24 kN and 72 kN and the obtained patches are displayed in Figure 4.29. In what concerns to the Hertzian model, although it returns two separate contact patches for a normal load of 24 kN, for higher load values it produces only one contact patch. This is not physically plausible, and the explanation relies on the fact that to obtain a normal force of 24 kN, two interpenetration regions are detected, thus, the contact model produces one patch in each region. Moreover, to achieve higher forces, the penetration is increased, and the two interpenetration regions merge together, crating one larger interpenetration zone which only produces one contact patch. This is a very significant issue, since this transition from two to one patch, or vice-versa, is obviously discontinuous and introduces numerical problems in the dynamic simulations.

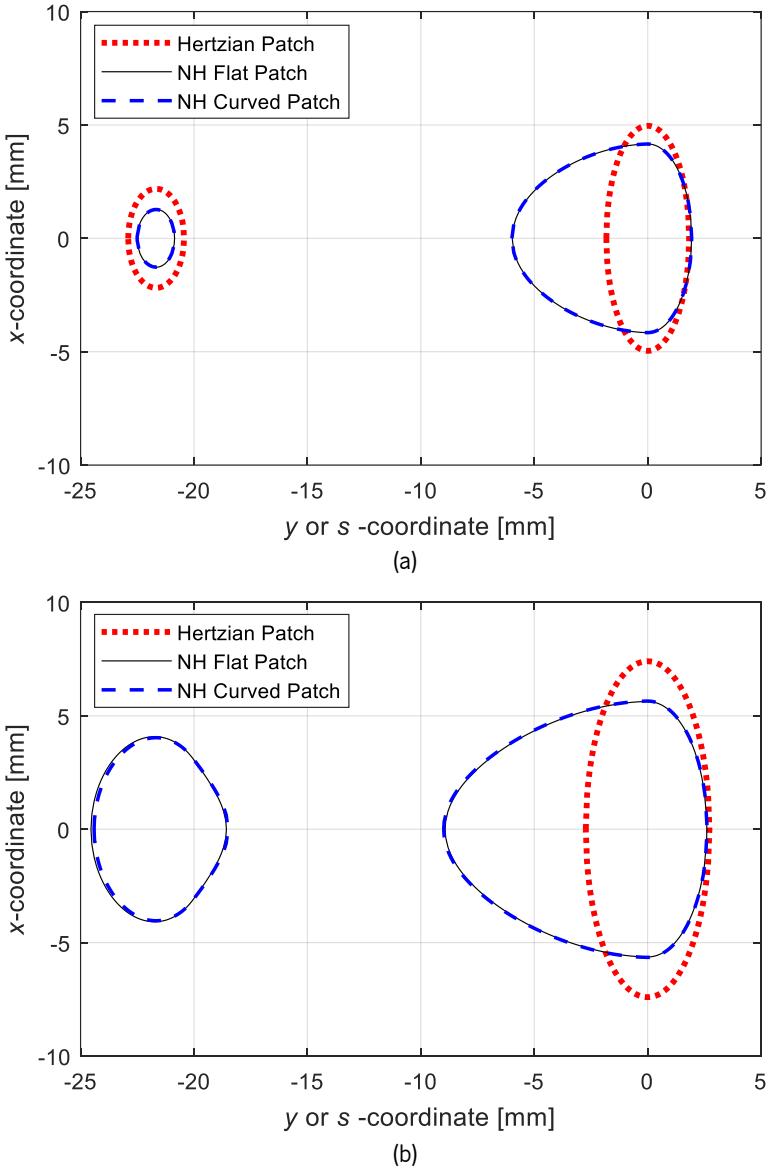

Figure 4.29 – Contact patches obtained for a 1:20 rail cant and Δy = 5 mm with normal load of (a) 24 kN and (b) 72 kN.

In terms of comparison between both non-Hertzian approaches, it must be noted that they present very similar results for the cases in which the normal force is 24 kN and 48 kN. For these conditions, two separate interpenetrations regions are found, thus, as previously discussed, the planar contact approach computed two distinct contact directions. For 72 kN, the penetration increases and both contact patches are located in the same interpenetration region. In that situation, the penetration function of the planar contact is evaluated using the normal direction of the maximum penetration point. This effect is magnified the greater the distance to the location where the contact direction was defined and the greater the conformality of the surfaces. In that sense, the shape of the contact patch for both non-Hertzian models tends to diverge far from the maximum penetration point, as illustrated in Figure 4.29(b). Table 4.9 summarizes the contact area, maximum pressure and contact angle variation for the simulated cases. The contact area represents the sum of the contact area of each contact patch when more than one patch is detected.

Table 4.9 – Contact area, maximum pressure and cant angle variation for a 1:20 rail cant and Δy = 5 mm with different normal loads.

Normal Load		**24 kN**	**48 kN**	**72 kN**
Contact Area [mm^2]	Hertzian Contact	36.90	48.37	63.39
	Non-Hertzian Flat Contact	53.67	92.72	134.39
	Non-Hertzian Curved Contact	53.73	92.70	134.13
Maximum Pressure [MPa]	Hertzian Contact	1141.37	1488.38	1703.78
	Non-Hertzian Flat Contact	754.77	893.15	973.41
	Non-Hertzian Curved Contact	753.57	891.86	976.16
Contact Angle Variation		0.91° and 1.76°	2.07° and 2.22°	7.61°

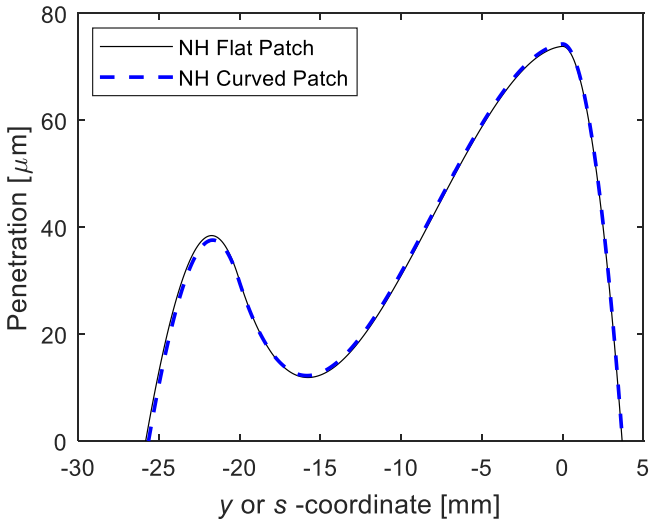

Figure 4.30 – Penetration function obtained with both flat and curved contact patch approaches for 1:20 rail cant, 72 kN normal load and Δy = 5 mm.

In order to perform a detailed comparison between the planar and curved approaches, the penetration function computed for both methods is plotted in Figure 4.30. From its analysis, it can be demonstrated that there are significative differences between them, and that the planar contact patch approach tends to overestimate the penetration far from the reference point. The most relevant issue lies in the fact that both procedures produce similar patches when they are originated from different interpretation regions, and present considerable differences when they are identified from the same interference region. This represents a meaningful discontinuity in the context of a dynamic analysis, since the flat contact procedure would produce an abrupt normal load variation when two interpenetration regions merge into one.

4.4.4. Contact Force Discontinuities

The main limitation associated with the planar contact approach relies on the fact that the penetration is evaluated with the direction of the maximum penetration point in the whole interference region. Therefore, whenever the maximum penetration point changes its location, there is an abrupt variation on the contact patch shape. Hence, the discontinuity on the contact shape affects the contact force computed. Moreover, as aforementioned, the change on the location of the maximum penetration point also produces a discontinuity on the contact force obtained with KP model, since it depends on its position to evaluate the maximum pressure.

In order to verify how both flat and curved approaches deal with the discontinuity on the location of the maximum penetration point, two scenarios where two similar penetration maxima are found within the same interpenetration region are considered. In these examples, the normal force is not imposed, but the wheel position relative to the rail is set. They consist of contact cases similar to the ones analyzed in the previous section, although the penetration maxima are balanced. The first scenario has a 1:40 rail cant, and the wheelset lateral displacement is -0.764247 mm (Δy_0) which returns the maximum penetration on the left peak. Then, keeping the same vertical position, with a slight decrease of the wheelset lateral displacement (1 nm), the maximum penetration is detected on the right peak. It must be noted that this variation on the wheel position is almost imperceptible in real operation, therefore, it must not correspond to a measurable change on the contact force.

In this example, the contact occurs in the middle of the wheel tread, as shown in Figure 4.31(a), thus, the contact angle does not vary significantly through the contact patch. Bearing that in mind, the evaluation of the flat contact patch shape using different maximum penetration points does not produce

large discrepancies, as illustrated in Figure 4.31(b). However, the use of curved approaches returns the same contact patch before and after this discontinuity, as expected in real operation. From the analysis of Figure 4.31, it can be recognized that the curved approach presents more resemblance to the flat patch obtained with the direction of the right peak, since it better represents the overall direction of the contact patch.

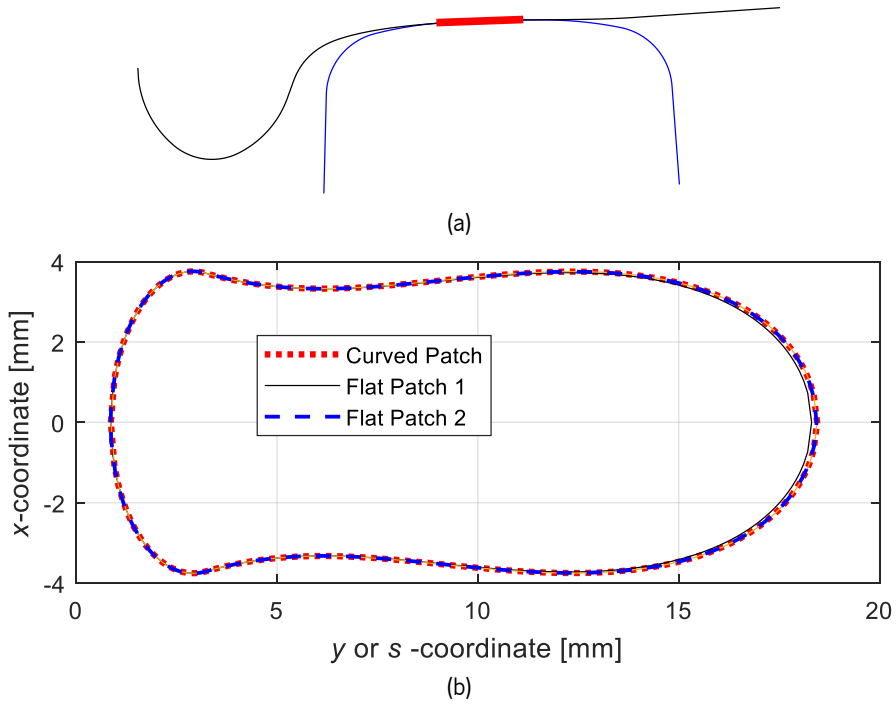

Figure 4.31 – Contact patches obtained in a scenario with two similar penetration maxima in the same interpenetration region which results in one contact patch: (a) location; (b) contact shape for curved approach and for flat approach before and after discontinuity.

For a given wheel-rail relative position, the contact patch obtained does not depend on the model used to compute the normal pressure, therefore, the contact patches presented are valid for both KP and SZG models. In order to compare the performance of the contact patch's methodologies and the contact force models, the contact force is computed for eight different cases, namely for both curved and flat patches before and after the discontinuity using KP and SZG models. Hence, the contact forces obtained are listed in Table 4.10. The KP model shows large discontinuities on the contact force for both planar (16%) and curved (17%) patches, which certainly causes difficulties on the integration process of the equations of motion. In turn, the use of SZG model with flat patch reduces the discontinuity of the contact force to 1%, since the contact direction does not change extensively. Finally, using the SZG model combined with the curved contact patch, the discontinuity is fully eliminated, since this methodology does not depend either on the direction or the location of the maximum penetration point to evaluate the

contact force. Bearing in mind that the curved patch and the flat patch using the right peak as a reference point have a similar shape, as expected they also present identical normal forces, namely 0.02% with KP model and 0.29% with SZG model. Conversely, comparing the flat patch when the maximum penetration is detected in the left peak with the curved patch, the differences are slightly higher, that is, 1.13% with KP model and 1.02% with SZG model.

Table 4.10 – Contact force and contact area obtained with both KP and SZG models for flat and curved contact patches in a scenario with two similar penetration maxima in the same interpenetration region which results in one contact patch.

		Area [mm^2]	**Force KP [N]**	**Force SZG [N]**
Δy_0	Non-Hertzian Flat Contact	114.12	38563	33255
	Non-Hertzian Curved Contact	115.42	39003	33597
Δy_0 - 1 nm	Non-Hertzian Flat Contact	115.46	32988	33693
	Non-Hertzian Curved Contact	115.42	32981	33597

Regarding the normal pressure distribution, Figure 4.32 presents the results obtained with KP contact model for both flat and curved contact before and after the discontinuity. Although the contact patches present similar shape, the origin of the reference system varies according the contact case. For the flat contact approach, the origin coincides with the maximum penetration point, while, in the curved patch, the origin is located where the interference zone starts. From the analysis of Figure 4.32, it is possible to verify that both planar and curved approaches present a significant variation when using different locations as the reference point for the KP method. However, in these cases, the differences between the flat and curved contact are less meaningful. This fact is demonstrated by the maximum pressure in each scenario, Figure 4.32(a) and Figure 4.32(c) exhibit that the planar and curved approaches have 476 MPa and 474 MPa as the maximum pressure, respectively, while Figure 4.32(b) and Figure 4.32(d) present 402 MPa and 401 MPa.

The second example of discontinuity is obtained with 1:20 rail cant, and the wheelset lateral displacement is 5.406630 mm. This case also shows two similar peaks on the penetration function over the interference region, however, the minimum between them is lower which produces two separate contact patches. As in the previous example, with small decrease of the wheelset lateral position, the contact detection methodology tends to consider a different peak as the maximum penetration point which leads to discontinuity of the contact models.

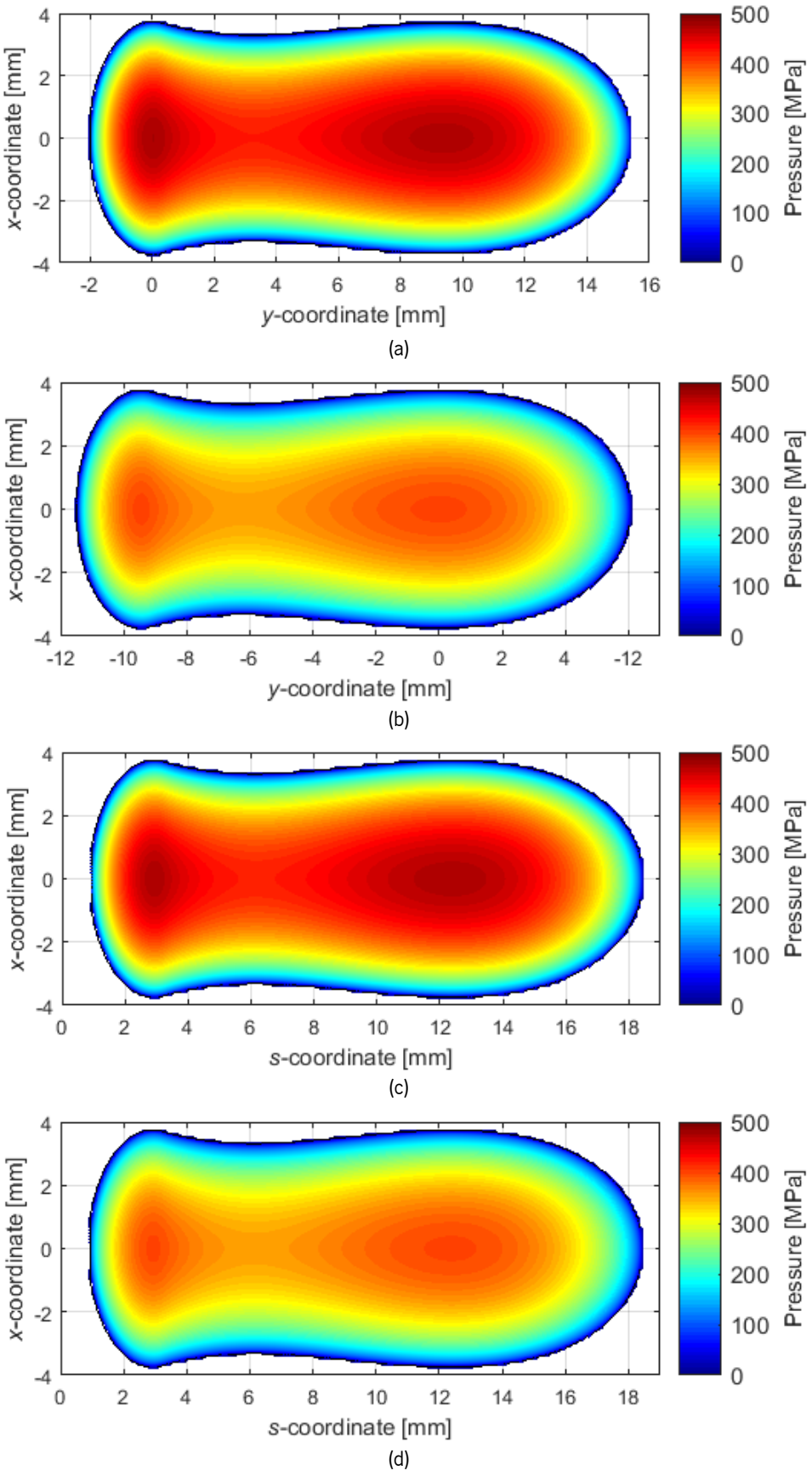

Figure 4.32 – Contact pressure distribution obtained with KP model in a scenario with two similar penetration maxima in the same interpenetration region which results in one contact patch: (a) flat contact with Δy_0; (b) flat contact with Δy_0 - 1 nm; (c) curved contact with Δy_0; (d) curved contact with Δy_0 - 1 nm.

For the identification of the contact patches shape, the curved approach is not affected by the discontinuity on the maximum penetration point, while two different configurations are obtained when using the planar contact method with different maxima, as illustrated in Figure 4.33. From the analysis of the results, it is possible to establish that when the left peak is taken as reference direction, the left contact patch resembles with the one obtained with the curved approach, on the other hand, when the right peak is used as the reference direction of the contact, the right contact patch coincides with the one achieved with the curved method. Figure 4.33(a) represents the position of both contact patches and, although the left patch is located closely to the flange fillet zone, both patches are situated in the wheel tread and the contact angle does not change largely within each patch. Nonetheless, the contact angle varies significantly between both contact zones which does not allow enough accuracy when evaluation the penetration of one patch using the direction of the maximum penetration from the other.

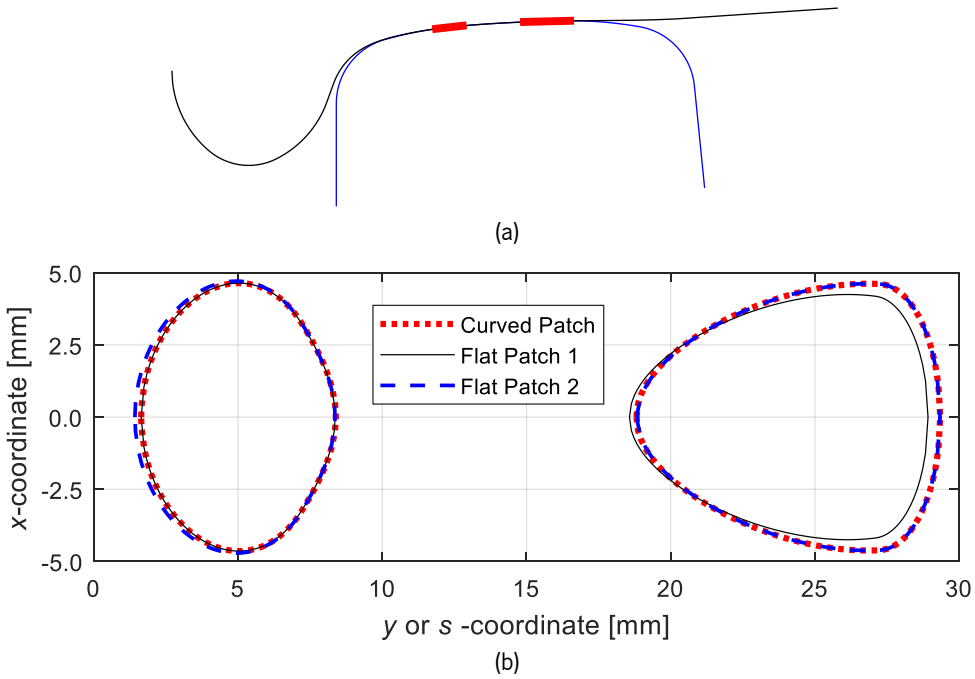

Figure 4.33 – Contact patches obtained in a scenario with two similar penetration maxima in the same interpenetration region which results in two contact patches: (a) location; (b) contact shape for curved approach and for flat approach before and after discontinuity.

For this second example, the same eight scenarios were computed, and the results are detailed in Table 4.11. Once again, the curved contact patch approach combined with SZG model is the only modelling methodology that does not present any discontinuity on the contact force when changing the maximum penetration from the left to the right peak. Regarding the KP contact model, the curved contact approach shows a discontinuity of 11.7% on the contact force, while the planar contact only varies around 1.7%. The reason for the lower variation when using the planar contact might be associated with the fact

that the discontinuity produced by the change of the contact patch area may compensate the discontinuity provoked by the KP model. Although the normal force magnitude does not change greatly, there is still a significant discontinuity on the direction of application of this contact force which certainly induces numerical problems in the progression of dynamic simulations. In the case of planar contact with SZG force model, the normal force variation before and after the discontinuity is approximately 13.1%, which, in addition to being unrealistic, introduces problems from the numerical point of view. In what concerns to the differences between the planar and curved approaches, they are more significant when the maximum penetration is detected in the left patch, namely 7.92% with KP model and 10.81% with SZG model. When the maximum penetration is obtained in the right contact patch, since this patch has larger area, the differences on the computed normal force are lower, that is, 2.08% with KP model and 2.26% with SZG model.

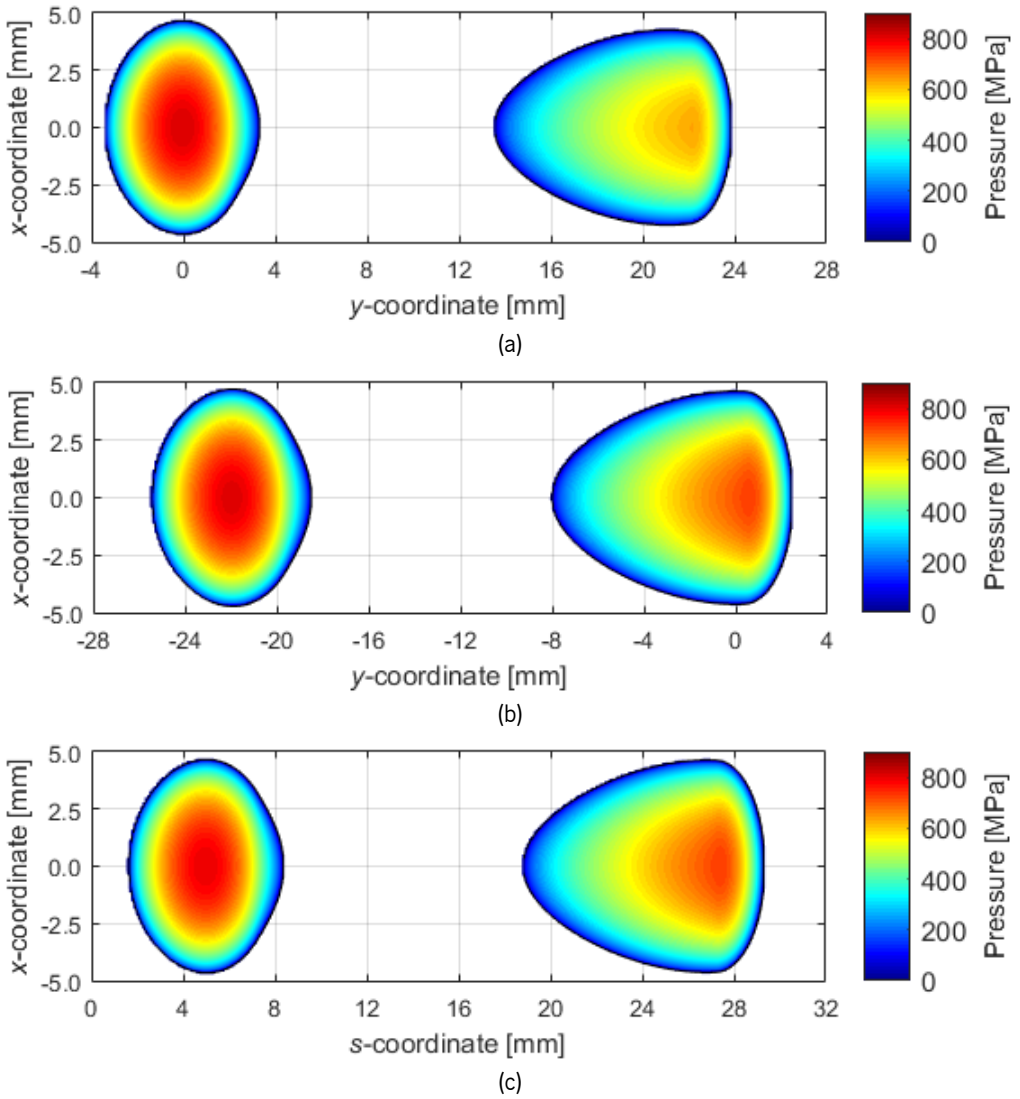

Figure 4.34 – Contact pressure distribution obtained with SZG model in a scenario with two similar penetration maxima in the same interpenetration region which results in one contact patch: (a) flat contact with Δy_0; (b) flat contact with Δy_0 - 1 nm; (c) curved contact.

Table 4.11 – Contact force and contact area obtained with both KP and SZG models for flat and curved contact patches in a scenario with two similar penetration maxima in the same interpenetration region which results in two different contact patches.

		Area [mm^2]	Force KP [N]	Force SZG [N]
Δy_0	Non-Hertzian Flat Contact	115.53	59165	51476
	Non-Hertzian Curved Contact	121.97	64046	57359
Δy_0 - 1 nm	Non-Hertzian Flat Contact	123.95	58172	58671
	Non-Hertzian Curved Contact	121.97	56977	57359

Figure 4.34 presents the normal pressure distribution obtained with SZG contact model for the planar contact approach when the maximum penetration occurs on the left patch, Figure 4.34(a), and on the right patch, Figure 4.34(b), and for the curved contact approach, Figure 4.34(c). Since there is no discontinuity using the curved contact with SZG model, only one result is provided. From the analysis of the normal pressure distributions displayed, the effects of the different modelling approaches are evident, mainly when comparing Figure 4.34(a) with the remaining ones. Although the three cases computed show similar maximum local pressure, that is, 815 MPa for the planar approach using the left penetration maximum as the reference direction, 811 MPa for the planar approach considering the right peak and 801 MPa for the curved contact approach, the overall distribution present significant discrepancies. It must be emphasized that the differences between Figure 4.34(a) and Figure 4.34(b) are obtained through the variation of the wheelset lateral position by 1 nm, which may provoke an almost undetectable change on the normal contact, hence these discrepancies are not admissible during a railway dynamic simulation.

4.5. Summary and Conclusions

In the context of the wheel and rail interaction, different methodologies to evaluate the shape and size of the contact patches are proposed and compared throughout this chapter. Bearing that in mind, the Hertzian methodology based on the local surface curvatures is compared with more advanced non-Hertzian approaches which require the evaluation of the penetration over the contact region. Regarding the non-Hertzian methods, two main approaches are studied, namely planar and curved contact patches. The former considers that the contact area lies on a single plane and the penetration between profiles is measured using the direction of the maximum penetration point, while the latter defines a curved reference surface between the two contacting bodies in which the contact patch is contained. Both approaches perform a discretization of the contact region into longitudinal strips and, in the curved contact, the normal direction is different for each strip, hence, the penetration is measured through those directions. Although, in most cases, the planar approach comprehends a suitable approximation for non-

conformal contact, it provides discontinuities on the contact when the maximum penetration point changes, and it does not capture the variation of the contact angle mainly for closely conformal contacts.

The normal pressure distribution over the contact area is also a very important aspect in this study, since it not only influences the dynamics of the vehicle but also allows to investigate the localized contact phenomena, such wear or rolling contact fatigue. The Hertzian approach naturally assumes an elliptical pressure distribution, while, for the non-Hertzian approaches, this elliptical pressure is only considered in the longitudinal direction. Although the pressure distribution in lateral direction for the non-Hertzian models depends on the penetration along the profiles, it can be computed in different ways, and two of them are explored here. The Kik-Piotrowski contact model uses the value and location of the maximum penetration point to compute the pressure distribution. On the other hand, the model proposed by Sun et al. calculates the maximum pressure in each strip independently recurring to the corresponding penetration. In that sense, this contact model does not depend uniquely of the location of the maximum penetration point which avoids discontinuities on the contact force when the maximum penetration point suddenly changes location.

The performance of the aforementioned contact modeling approaches is verified through several static application examples, in which several modeling issues were addressed. Wheel and rail profiles were selected for this investigation, and the influence of their relative position was assessed using different wheelset lateral positions and rail cant inclinations. The variation of the surfaces' relative configuration demonstrated to be a relevant issue, since the type of the obtained contact patches is highly dependent on that. In these results, it was confirmed that in most cases the Hertzian approach is not a suitable approximation, and the both non-Hertzian planar and curved methods present similar results except for contact cases in which the surfaces tend to be more conformal. Furthermore, scenarios where two similar penetration peaks exist in the same interpenetration region were utilized to evaluate the occurrence discontinuities on the computation of the normal contact force. From this analysis, it is possible conclude that, with the planar approach, a different shape of contact is obtained when the maximum of penetration changes and, hence, there is a significant change on the normal force magnitude. It is also verified that, with Kik-Piotrowski model, it exists an abrupt variation of contact force with a slight change of the wheel's position due to the change of location of the maximum penetration point, which is used in the computation of the force as a reference position. Finally, the curved contact approach combined with the SZG model showed to be the most appropriate methodology to deal with the contact force discontinuities and, therefore, to be applied in railway vehicles' dynamic simulations.

"*When you have exhausted all possibilities, remember this - you haven't.*"
Thomas Edison

5. LOOKUP TABLES FOR WHEEL-RAIL CONTACT PROBLEMS

The ultimate goal of developing a new wheel-rail contact model for dynamic analysis purposes is to provide high accuracy by capturing most of tribological phenomena while keeping a low computation cost, or alternatively to decrease computational cost while maintaining accuracy. Yet, more advanced nonlinear models (Kalker, 1967; Kalker, 1982a; Kalker,1982b; Kalker, 1990) are required for situations where large creepages or conformal contact exist, for instance, and to study contact damage phenomena, such as wear or rolling contact fatigue. In contrast, simplified linear models (Shen et al., 1983; Polach, 1999; Vollebregt and Wilders, 2011) are more suitable when the local contact phenomena are not particularly relevant. The use of computational efficient models has a special interest for real-time or long-time simulations. In this framework, the implementation of LuT based approaches is a valuable and common alternative for the efficiency improvement of railway dynamic simulations when compared with online wheel-rail contact force evaluation. A LuT allows to obtain an approximation of the function evaluation through the interpolation of pre-calculated values. However, the generation of LuTs with multiple inputs and multiple outputs is a challenging task for which aspects such as their minimal size and a uniform accuracy over the LuT domain have not been systematically addressed in the literature. In this chapter, a LuT for the evaluation of creep forces and moment in non-Hertzian contact patches is studied. Then, a comprehensive methodology for a detailed analysis of general LuT is presented. With this purpose in mind, an analysis of the variation of the input parameters for the LuT is made and the interpolation error is assessed on the cells and edges of the original table. Finally, based on this analysis, two novel enhanced LuTs are proposed.

5.1. Lookup Table Description

The interpolation of a LuT consists of an approximation of the exact evaluation of a time-consuming and complex function. Hence, the error introduced by the interpolation process varies over

the LuT domain, i.e., it should be null at the pre-calculated points and tends to increase when moving away from those points. Despite of the fact that the generation of a more refined LuT leads to more accurate interpolations, not only the search and interpolation procedures become slower, but also the memory required and the time for the LuT generation increase, since the exact function must be evaluated at more points. The discretization of a LuT domain with multiple input and multiple output is commonly performed empirically based on the experience and judgment, since that methodologies to deal with the tradeoff between accuracy and size in these cases are not commonly used and, thus, the LuT accuracy is not controlled over its domain (Marques et al., 2019b).

A general function with n inputs and m outputs can be written as

$$\mathbf{f}\left(x_1,...,x_n\right) \equiv \left\{ f_1\left(x_1,...,x_n\right),..., f_m\left(x_1,...,x_n\right)\right\} \tag{5.1}$$

The domain of this function can be represented by an orthogonal reference frame with n axes. In order to construct a LuT to approximate this function, a domain of interest must be selected for each dimension, or input variable of the LuT, and the lower and upper limits must be defined, for a given dimension i, as x_i^{L} and x_i^{U}, respectively. Moreover, for each dimension, a set of points must be defined, where the m outputs of the function $\mathbf{f}\left(x_1,...,x_n\right)$ are exactly calculated. These points characterize the refinement of the LuT and, consequently, its accuracy. For instance, Figure 5.1 shows a general LuT where the dots represent the set of points that define the LuT domain. For sake of simplicity, Figure 5.1 refers to a two-dimensional problem, however, the same concept can be generalized for *n*-dimensional problems.

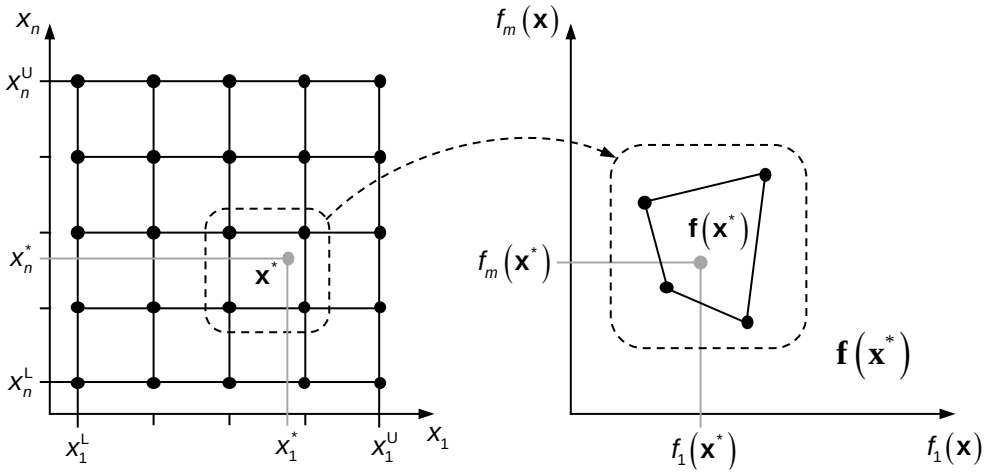

Figure 5.1 – Schematic representation of a generic lookup table (LuT) with n inputs and m outputs

To interpolate a given point $\mathbf{x}^*$, the cell in which this point is contained must be first identified. Figure 5.1 shows the point $\mathbf{x}^*$ in grey and the cell is defined by the black dots encircled by the dashed line. The output values of the points of this cell are represented in the right image of Figure 5.1. Thus, to

obtain the j^{th} element of the output vector, the linear interpolation of the values of the cell points stored is performed as

$$f_j\left(\mathbf{x}^*\right)=\sum_{k_1=1}^{2}\cdots\sum_{k_n=1}^{2}\left(w_1^{k_1}\ldots w_n^{k_n}\,f_j\left(x_1^{k_1},\ldots,x_n^{k_n}\right)\right) \tag{5.2}$$

where the weight coefficients are defined as

$$w_i^1=\frac{x_i^2-x_i^*}{x_i^2-x_i^1}\quad,\quad w_i^2=1-w_i^1 \tag{5.3}$$

in which x_i^1 and x_i^2 are, respectively, the lower and upper values of the cell in dimension i and the subscript i ranges from 1 to n.

Therefore, the domain and size of the lookup table are defined by the refinement of the input variables $x_1,\ldots,x_n$. It must be noted that the example depicted in Figure 5.1 shows an equal spacing grid, however, in a general case, the interval between points is not fixed since the LuT refinement needs to be higher in zones of the domain that demonstrate a more nonlinear behaviour.

5.2. Kalker Book of Tables for Non-Hertzian Contact

The contact between the rail and the wheel tread, in normal operating conditions with regular wheel and rail profiles, is characterized by a configuration such as that illustrated in Figure 5.2. Thus, in order to build a LuT for the evaluation of creep forces and spin moment, a regularization of non-elliptical contact patches was introduced by Piotrowski et al. (2017; 2019), being the contact patch regularized to be a Simple Double-Elliptical Contact region (SDEC), as represented in Figure 5.3(b). This LuT is based in CONTACT software (Kalker, 1990) and designated as the Kalker Book of Tables for Non-Hertzian contact (KBTNH).

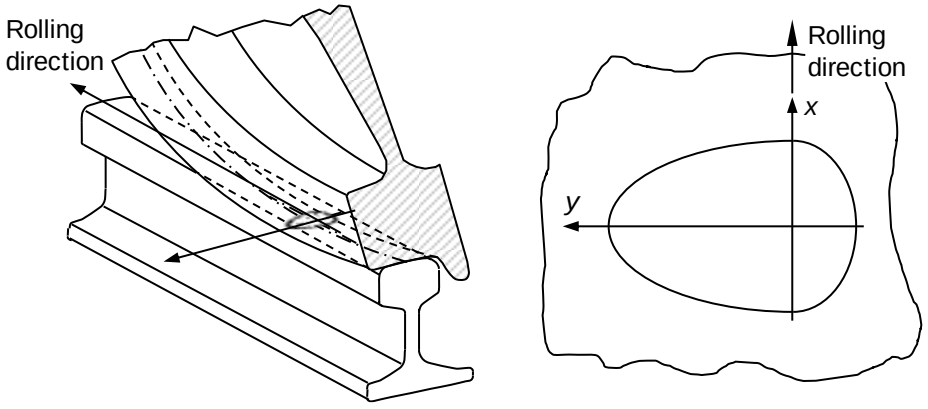

Figure 5.2 – Representation of the wheel-rail interaction and respective contact region.

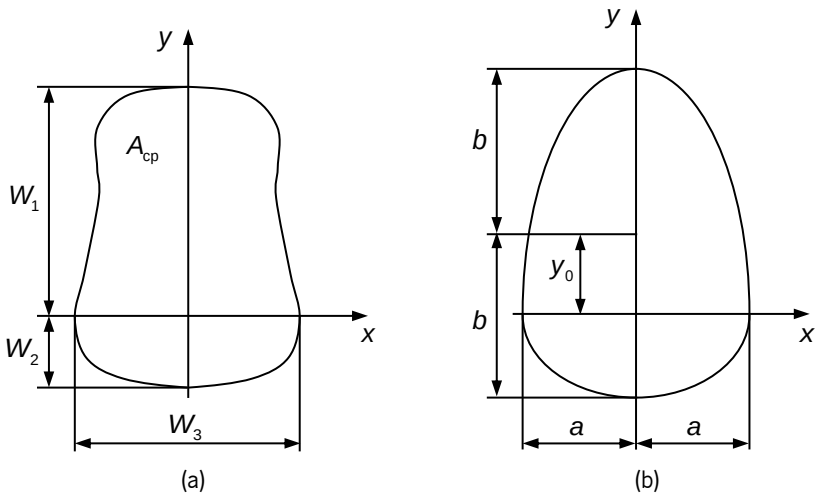

Figure 5.3 – Regularization of a general non-Hertzian contact patch into a SDEC region.

Notice that the SDEC shape holds some quasi-Hertzian properties and symmetry relations, and it requires a small number of parameters to be fully described. Hence, in a nondimensionalized analysis, it can be characterized by the semi-axes ratio as

$$g = a / b \tag{5.4}$$

and the shape number as

$$\psi = y_0 / b \tag{5.5}$$

where a and b are the semi-axes of the SDEC region. This shape is particularly suitable to be regularized from most of the contact shapes obtained with approximate non-Hertzian methods for normal contact problem, as can be noticed by the contact patches obtained in Chapter 4. Hence, with the area of the contact patch, A_{cp}, and its dimensions, W_1, W_2 and W_3, obtained from a given non-Hertzian model and depicted in Figure 5.3(a), the dimensions of the SDEC region can be calculated as

$$a = \sqrt{\frac{A_{cp}}{\pi}\frac{W_3}{(W_1 + W_2)}} \tag{5.6}$$

$$b = \sqrt{\frac{A_{cp}}{\pi}\frac{(W_1 + W_2)}{W_3}} \tag{5.7}$$

$$y_0 = b\frac{W_1 - W_2}{W_1 + W_2} \tag{5.8}$$

For a given pair of contacting surfaces, resorting to the parametrization of variables, the creep forces and moment generated due to wheel-rail interaction only depend on the contact patch geometry,

characterized by g and ψ, and the parametrized longitudinal, lateral and spin creepages. Moreover, the parametrized creepages, designated by ξ, η and χ, respectively, are defined as

$$\xi = \frac{\rho \upsilon_x}{\mu c} \tag{5.9}$$

$$\eta = \frac{\rho \upsilon_y}{\mu c} \tag{5.10}$$

$$\chi = \frac{\rho \varphi}{\mu} \tag{5.11}$$

in which ρ is a characteristic length of the elliptical contact patch, μ denotes the friction coefficient, υ_x represents the longitudinal creepage, υ_y is the lateral creepage, φ denotes the spin creepage, and c is the equivalent radius of the SDEC region that can be calculated as

$$c = \sqrt{ab} \tag{5.12}$$

In turn, the characteristic length of the elliptical contact patch, which can be seen as the average radius of curvature of the two contacting surfaces in both directions, are evaluated as

$$\rho = \frac{4E}{3\left(1-\sigma^2\right) f_{\mathrm{n}}} \left(\frac{A_{\mathrm{cp}}}{\pi n_{\mathrm{a}} n_{\mathrm{b}}} \right)^{\frac{3}{2}} \tag{5.13}$$

in which E represents the Young's modulus, σ is the Poisson ratio, f_{n} denotes the normal contact force, and n_{a} and n_{b} are tabulated coefficients that are dependent of θ, which is given by

$$\theta = \max\left(\frac{a}{b}, \frac{b}{a} \right) \tag{5.14}$$

Thus, the product of these tabulated coefficients can be approximated by the following empirical formula

$$n_a n_b = k_3 \theta^3 + k_2 \theta^2 + k_1 \theta + k_0 \tag{5.15}$$

where $k_3 = 3.618652 \times 10^{-5}$, $k_2 = -2.687505 \times 10^{-3}$, $k_1 = 9.5658 \times 10^{-2}$ and $k_0 = 8.872736 \times 10^{-1}$.

For the sake of simplicity, the regularized longitudinal and lateral creepages are replaced by the creepage angle and modulus of creepage, which are defined as

$$\nu = \sqrt{\xi^2 + \eta^2} \tag{5.16}$$

$$\alpha = \arctan\left(\frac{\eta}{\xi} \right) \tag{5.17}$$

For this case, the generation of the lookup table involves five input variables, illustrated in Figure 5.4, each one with a characteristic domain defined by:

$\chi \in [0,2]$ - parametrized spin creepage;

$g \in [0.2,5]$ - semi-axes ratio;

$\alpha \in [-\pi/2, \pi/2]$ - creepage angle;

$\nu \in [0,12]$ - parametrized creepage modulus;

$\psi \in [-0.9, 0.9]$ - shape number;

and three output quantities:

f_x - normalized longitudinal creep force;

f_y - normalized lateral creep force;

m_z - normalized moment.

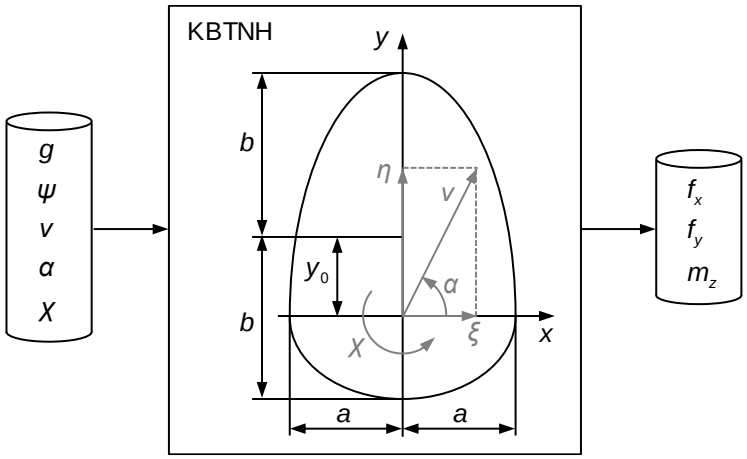

Figure 5.4 – Representation of input and output variables of KBTNH.

The normalized creep forces and moment, stored in the LuT, are obtained as

$$f_x(\chi, g, \alpha, \nu, \psi) = \frac{F_x}{\mu f_n} \tag{5.18}$$

$$f_y(\chi, g, \alpha, \nu, \psi) = \frac{F_y}{\mu f_n} \tag{5.19}$$

$$m_z(\chi, g, \alpha, \nu, \psi) = \frac{M_z}{\mu c f_n} \tag{5.20}$$

where F_x, F_y and M_z are, respectively, the longitudinal and lateral creep forces and the moment computed by CONTACT (Kalker, 1990). The genesis of this program is associated with continuum mechanics concepts in which the mechanical behavior of materials is modeled by mathematical relations involving stresses, strains and displacements. Notice that the CONTACT program uses the boundary element method in which the elasticity equations of the interior material are converted to equations on its surfaces. Hence, the relation between surface tractions and displacements are established. This involves the discretization of the potential contact area, as represented in Figure 5.5, in which the size of the elements plays an important role on the accuracy and simulation time of the software.

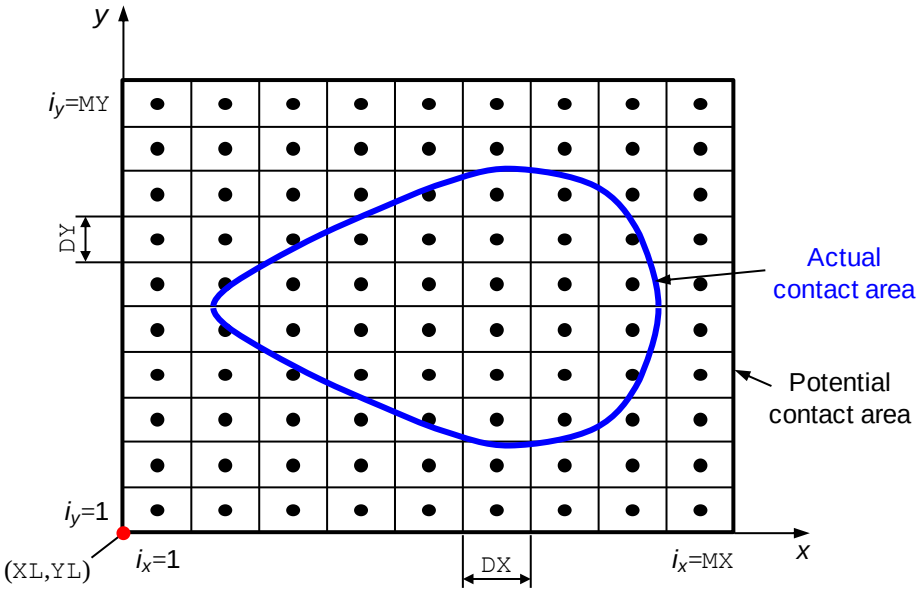

Figure 5.5 – Representation of potential contact area discretization on CONTACT.

This LuT represents the simulation of non-Hertzian contact scenarios, therefore, the distance between the undeformed surfaces must be provided. Thus, the undeformed distance function, illustrated in Figure 5.6(a), which characterizes the distance between the two original profiles when they are tangent in the main point of contact, must be defined in the lateral direction through a set of equally spaced points, shown in Figure 5.6(b).

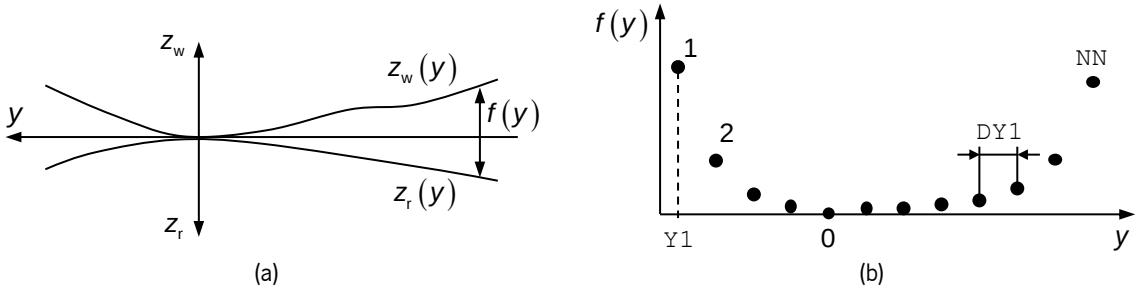

Figure 5.6 – Representation of (a) the undeformed distance function between wheel rail profiles and (b) its discretization.

Since a SDEC shape is considered, the separation between the two undeformed surfaces is elliptical in the rolling direction and defined by two circular arcs in the lateral direction. Hence, the separation function is defined as

$$z(x,y)=\frac{x^2}{2R}+f(y) \tag{5.21}$$

where the distance between the two profiles, which is schematized in Figure 5.7, is mathematically defined as

$$f(y)=\begin{cases}\dfrac{y^2}{2R_1} & \text{if} \quad y>0\\[2ex] \dfrac{y^2}{2R_2} & \text{if} \quad y\le 0\end{cases} \tag{5.22}$$

Thus, it is necessary to obtain the values of R, R_1 and R_2 that originate a SDEC contact patch of a given a, b, y_0 and δ, in which δ denotes the virtual penetration between profiles. The radii obtained from a geometrical analysis without taking to account the bodies' deformation is used as initial approximation, i.e.,

$$R=\frac{a^2}{2\delta_0} \tag{5.23}$$

$$R_1=\frac{(b+y_0)^2}{2\delta_0} \tag{5.24}$$

$$R_2=\frac{(b-y_0)^2}{2\delta_0} \tag{5.25}$$

where $\delta_0=0.55\delta$. An iterative tuning process is adopted to adjust the values for the radii using CONTACT. The process is stopped when the differences between the prescribed dimensions and the ones obtained with CONTACT are less than the size of each cell of the domain.

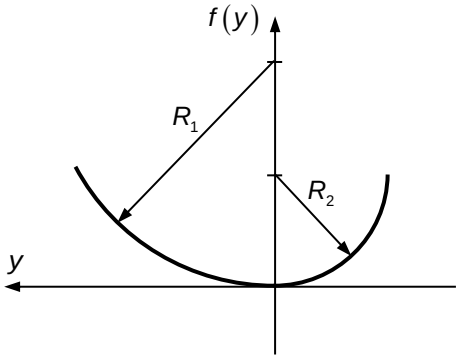

Figure 5.7 – The undeformed distance function for the SDEC patch.

A functional LuT is built spaning the complete domain in which the expected contact configurations for typical wheel-rail interaction are included. The domain of the spin creepage and creepage angle are reduced to half due to the symmetry that is inherent to the SDEC shape (Piotrowski et al., 2017; Magalhães et al., 2019), thus decreasing significantly the size of the table.

Table 5.1 shows the distribution of points of the LuT proposed by Piotrowski et al. (2017). It is observed that a different number of points is used for the different independent parameters. In this case, the selection of the number and position of the LuT points was done empirically, resulting from the developer experience. The most refined parameter is, by far, the parametrized creepage modulus. Thus, the total number of LuT points, and runs of program CONTACT required to compute the forces to construct the LuT, is calculated as the combination of these points

$$N_{\mathrm{p}} = \prod_{i=1}^{5} n_i = 113\,344 \tag{5.26}$$

The number given by Eq. (5.26) represents the LuT size and it has direct impact on the storage size and on the time required to search the table. It seems obvious that it is of great interest to keep the number of LuT points as low as possible. Thus, the evaluation of the creep forces and moment during a multibody simulation is performed through the assessment of the LuT values and the subsequent linear interpolation performed in the five-dimensional space. The use of interpolation schemes of higher order would require a preprocessing of the polynomial coefficients for the interpolation, which is not reasonable for multiple inputs, five in this particular case.

Table 5.1 – Domain of the Kalker Book of Tables for Non-Hertzian contact in Piotrowski et. al. (2017).

Parameter	No. of Points
$\chi = \begin{Bmatrix} 0.00 & 0.25 & 0.50 & 1.00 \\ 1.25 & 1.50 & 1.75 & 2.00 \end{Bmatrix}$	$n_\chi = 8$
$g = \left\{ \frac{1}{5} \quad \frac{1}{2} \quad \frac{3}{4} \quad 1 \quad 2 \quad 3 \quad 4 \quad 5 \right\}$	$n_g = 8$
$\alpha = \left\{ -\frac{\pi}{2} \quad -\frac{\pi}{3} \quad -\frac{\pi}{6} \quad 0 \quad \frac{\pi}{6} \quad \frac{\pi}{3} \quad \frac{\pi}{2} \right\}$	$n_\alpha = 7$
$\nu = \begin{Bmatrix} 0.0 & 0.1 & 0.2 & 0.3 & 0.4 & 0.5 & 0.7 & 0.9 \\ 1.1 & 1.4 & 1.7 & 2.0 & 2.5 & 3.0 & 3.5 & 4.0 \\ 5.0 & 6.0 & 7.0 & 8.0 & 9.0 & 10.0 & 12.0 \end{Bmatrix}$	$n_\nu = 23$
$\psi = \begin{Bmatrix} -0.9 & -0.8 & -0.6 & -0.4 & -0.2 \\ 0.0 & 0.2 & 0.4 & 0.6 & 0.8 & 0.9 \end{Bmatrix}$	$n_\psi = 11$

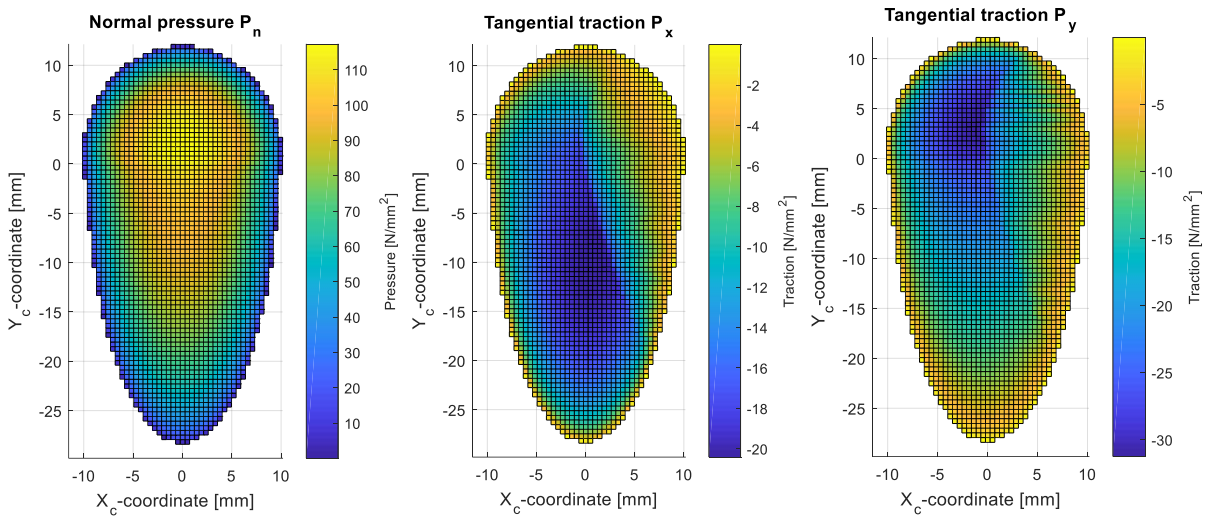

Figure 5.8 – Example of the normal pressure distribution and tangent tractions obtained with CONTACT

For each point of the LuT, the CONTACT program is used to evaluate the contact stresses, being the global values of the normal and tangential forces calculated and stored. Figure 5.8 shows the obtained normal pressure distribution and tangent tractions for a point of the LuT ($\chi=0.5$; $g=1/2$; $\alpha=\pi/3$; $\nu=1.1$; $\psi=-0.4$) obtained with CONTACT.

5.3. Methodology for Assessment of Lookup Table Accuracy

A comprehensive evaluation of the LuT accuracy is performed by analyzing the variation of its input parameters and by quantifying how each parameter influences the calculation of the creep forces. In a first stage, a mesh of 60×60 elements is used in CONTACT to discretize the complete contact patch. Then, the assessment of the interpolation error is performed by comparing the exact value of the contact force evaluated with CONTACT and the approximated value obtained with linear interpolation of LuT data. The center point of each cell and the middle point of each edge are used to quantify the error of the LuT interpolation.

5.3.1. Analysis of the Variation of the Input Parameters

The variation of each output parameter, namely, the force components and moment, with respect to each one of the input parameters is evaluated in order to assess which parameters need finer or coarser discretization. A design of experiments technique (Myers et al., 2016) is applied, in particular, a Latin Hypercube Sampling (LHS) is selected with 10 points inside the domain of the lookup table, as listed in Table 5.2. This sampling technique allows for a suitable inspection of the domain.

Table 5.2 – Points of the Lookup Table selected for the sensitivity analysis using a Latin Hypercube Sampling

Point	χ	g	α	ν	ψ
1	7.60×10^{-1}	6.34×10^{-1}	7.85×10^{-1}	9.00×10^{0}	3.78×10^{-1}
2	1.88×10^{0}	4.52×10^{0}	-1.48×10^{0}	1.10×10^{1}	-7.02×10^{-1}
3	5.00×10^{-1}	1.90×10^{0}	1.13×10^{0}	3.12×10^{0}	-9.00×10^{-1}
4	1.72×10^{0}	1.18×10^{0}	1.48×10^{0}	6.60×10^{0}	6.12×10^{-1}
5	9.60×10^{-1}	3.24×10^{-1}	-6.28×10^{-2}	3.84×10^{0}	-2.52×10^{-1}
6	1.36×10^{0}	2.38×10^{-1}	-7.54×10^{-1}	0.00×10^{0}	9.00×10^{-2}
7	1.48×10^{0}	4.20×10^{0}	-3.14×10^{-1}	1.02×10^{1}	-1.62×10^{-1}
8	1.40×10^{-1}	4.87×10^{-1}	1.57×10^{-1}	7.32×10^{0}	-3.60×10^{-1}
9	2.80×10^{-1}	2.61×10^{0}	5.34×10^{-1}	1.44×10^{0}	3.42×10^{-1}
10	1.02×10^{0}	2.07×10^{-1}	-1.26×10^{0}	5.28×10^{0}	8.28×10^{-1}

The sensitivity of the output quantities, namely the three forces, to each of the five input parameters are calculated over each one of the 10 sampling points by varying one of the input parameters while maintaining the other four unchanged. Figure 5.9 shows the results of this variation in which each parameter is tested for one hundred values within its domain. The variation of the input parameters for the LuT values is also included for purpose of comparison. Since both lines are undistinguishable in the full scale, a representative plot of each input parameter is zoomed to better observe the existence of the error caused by the linear interpolation.

The analysis of the plots depicted in Figure 5.9 provides useful indications on the requirements for finer or coarser discretization of the input parameters. The spin creepage shows a more pronounced nonlinear behavior in the left side of the domain, while being almost linear in the right side. The semi-axes ratio seems to have a logarithmic like behavior, which suggests having an equivalent refinement from 1/5 to 1 and from 1 to 5. The creepage angle leads to a force and moment response that resembles a sinusoidal behavior. It is observed that the creepage modulus is highly nonlinear for low values, which suggests refinement, while becoming almost linear for high values of creepage, which suggests coursing the mesh. The shape number leads to a very moderate nonlinear behavior, thus, a small number of points is required to provide a good approximation. It is also clear that some plots present noisy curves, as in the case of the variations of the semi-axes ratio and the shape number. This is expected, since the change of these parameters implies a modification of the contact patch shape, which results in an adjustment of the mesh used in CONTACT which causes a non-smooth variation of the output quantities due to the use of cells of finite size to estimate the contact patch geometry. In short, the analysis of the variations allows to identify which are the variables that produce a more pronounced nonlinear response of the output quantities and, therefore, the ones that require a finer discretization of the LuT.

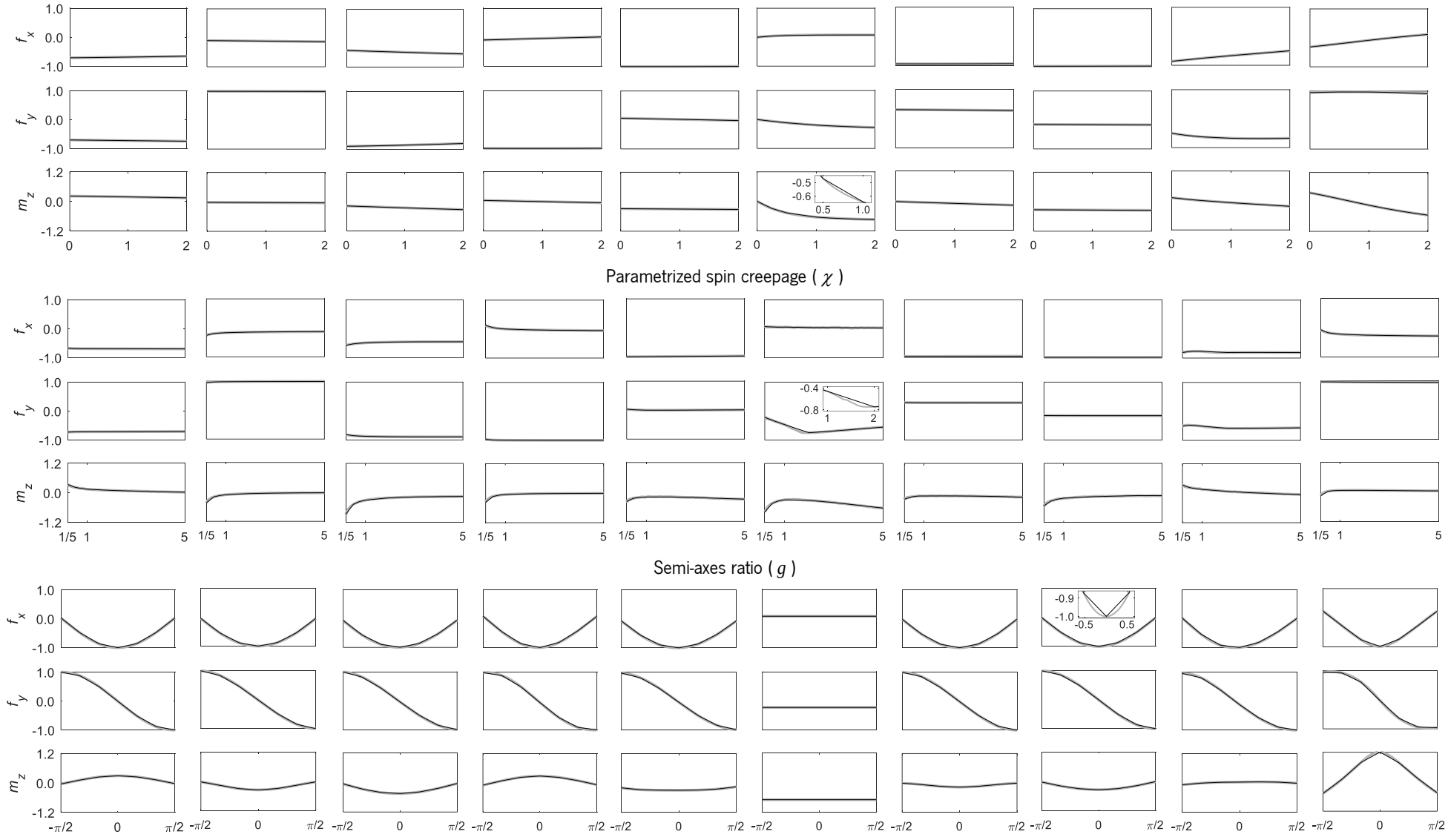

Figure 5.9 – Analysis of the variation of the output quantities of the function used to generate the KBTNH using a LHS with 10 points listed in Table 5.2 (— solid thick grey line - results for 100 values of each input parameter; — solid thin black line - results for the LuT values) (continued).

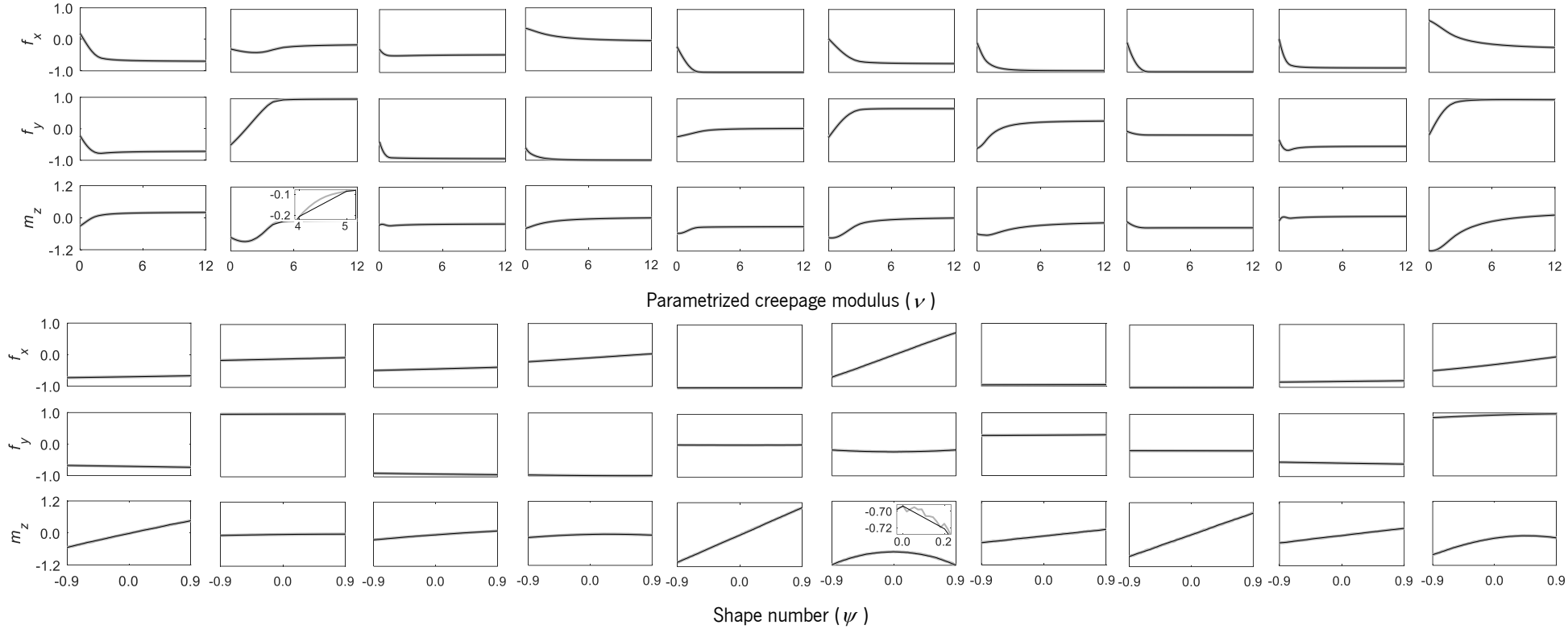

Figure 5.9 – (continued) Analysis of the variation of the output quantities of the function used to generate the KBTNH using a LHS with 10 points listed in Table 5.2 (– solid thick grey line - results for 100 values of each input parameter; – solid thin black line - results for the LuT values).

5.3.2. Interpolation Error in Cells

The assessment of the accuracy of the current LuT is performed by the evaluation of the interpolation error measured as the difference between the exact value of the forces and moments obtained from CONTACT and the value for the same quantities interpolated from the LuT. In order to have a proper error analysis, it is of paramount importance to select suitable points where the error evaluation is quantified. In the LuT points the interpolation error is null as the forces and moments in these points are exact. Thus, the best candidates for points with maximum errors are those in the vicinity of the LuT cell center, as shown in Figure 5.10, for a case in which only 3 inputs are considered. It must be noted that in the current case there are 5 input parameters making the graphical representation of the LuT cell center impossible. Assuming that the distance between LuT points is sufficiently small so that the error introduced by the interpolation is inversely proportional to the distance to them. In this case, the point in the center of each cell would lead to the output with the highest error, since it is the one farthest from the lookup table points, for which the output is exact.

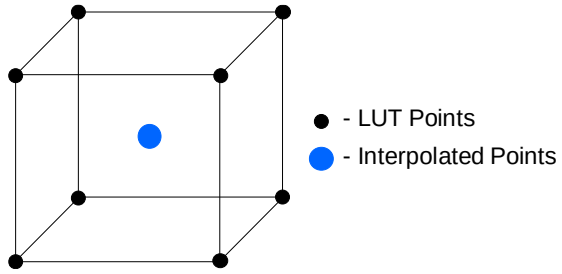

Figure 5.10 – Schematic representation of the error evaluation at the center of a cell of a 3D lookup table.

For the LuT with the points presented in Table 5.1, the number of cells defined in the space that it spans is

$$N_c = \prod_{i=1}^{5}(n_i - 1) = 64\ 680 \tag{5.27}$$

The errors of interpolation for the center of each cell of the LuT are presented in Figure 5.11 for the three output quantities. The cell number, that defines the order where each input parameter is spanned, is evaluated as

$$n_c = i_\chi + (n_\chi - 1)(i_g - 1 + (n_g - 1)(i_\alpha - 1 + (n_\alpha - 1)(i_\nu - 1 + (n_\nu - 1)(i_\psi - 1)))) \tag{5.28}$$

where i_k is the i^{th} space of the parameter k. Moreover, the interpolation error for each output quantity is evaluated as the absolute difference between the interpolated value using LuT data and the exact value obtained with Eqs. (5.18)-(5.20), that is

$$Error\ f_x(n_c) = \left| f_x(\chi_c, g_c, \alpha_c, \nu_c, \psi_c) - f_x^{\text{int}}(\chi_c, g_c, \alpha_c, \nu_c, \psi_c) \right| \tag{5.29}$$

$$Error\ f_y(n_c) = \left| f_y(\chi_c, g_c, \alpha_c, \nu_c, \psi_c) - f_y^{\text{int}}(\chi_c, g_c, \alpha_c, \nu_c, \psi_c) \right| \tag{5.30}$$

$$Error\ m_z(n_c) = \left| m_z(\chi_c, g_c, \alpha_c, \nu_c, \psi_c) - m_z^{\text{int}}(\chi_c, g_c, \alpha_c, \nu_c, \psi_c) \right| \tag{5.31}$$

where χ_c, g_c, α_c, ν_c, and ψ_c are the values of the input variables in the center of the cell n_c and f_x^{int}, f_y^{int} and m_z^{int} denote the creep forces and moment obtained through linear interpolation of the LuT data.

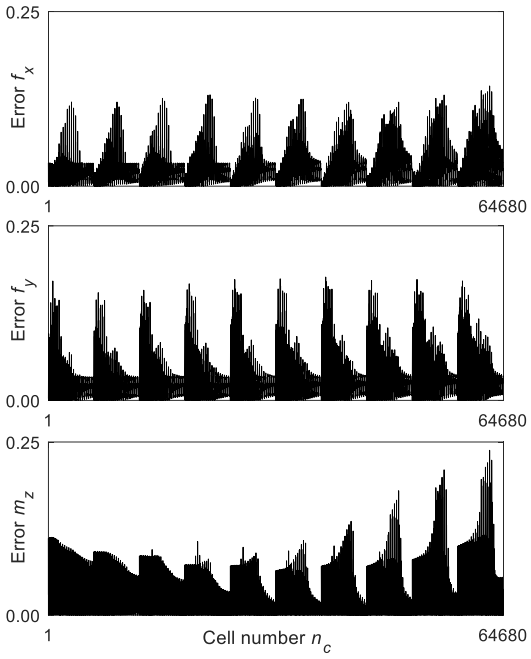

Figure 5.11 – Interpolation error at the center of the LuT cells for different outputs over the domain.

Since all the parameters are interpolated at the same time, it is not possible to check which is the main source of error. The results only allow to identify the order of magnitude of the maximum interpolation error of each output quantity.

5.3.3. Interpolation Error in Edges

In order to improve the LuT design, it is necessary to identify which are the parameters that need to be more refined and the ones that can have a coarser distribution. To address this issue, the interpolation error is evaluated at the points in the middle of the LuT edges as represented in Figure 5.12. Note that when interpolating at any edge of the LuT, four input parameters are kept constant, and the interpolation is performed with the variation of a single parameter. Thus, the evaluation of the error in the

middle point of the edges allows to determine the error introduced by the discretization of each individual input parameter.

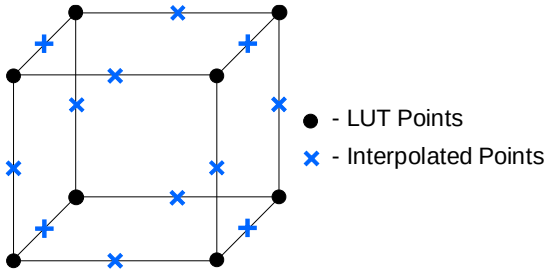

Figure 5.12 – Schematic representation of the error evaluation at the middle point of the edges of a cell of a 3D lookup table.

The number of edges of the LuT is significantly higher than the number of cells, which can be given, for the LuT with the structure presented in Table 5.1, as

$$N_{\mathrm{e}} = \sum_{i=1}^{5} \frac{(n_i - 1)\prod_{j=1}^{5} n_j}{n_i} = 506\,960 \tag{5.32}$$

The maximum and mean errors of the normalized creep forces and moment are evaluated for each edge of the lookup table domain, and summarized in Figure 5.13 and Figure 5.14, respectively. Thus, the values of the interpolation error at the middle point of each edge are obtained using a similar approach as for the interpolation error in the center of the cells, as represented by Eqs. (5.29)-(5.31). In each plot, all the outputs are presented with the same scale, for easier readability and comparison.

From the analysis of the maximum interpolation errors, displayed in Figure 5.13, the peak value is found for the interpolation of the spin creepage, which suggests that additional points should be used in the LuT. The higher values of spin creepages present lower interpolation error, suggesting that less points can be used in the LuT for the higher values.

It should be noted that the semi-axis ratio must be analyzed in a logarithmic scale, where it can be concluded the highest errors occur for larger intervals. This observation suggests that a finer refinement is required for the lower semi-axis ratio values and that a coarser refinement can be used in the highest values.

The creepage angle and modulus and the shape number exhibit consistently distributed errors for the entire domain. However, the interpolation error from the creepage modulus and the shape number present a maximum error magnitude much lower than that of the remaining parameters, which means that a coarser refinement without damaging the LuT accuracy can be considered.

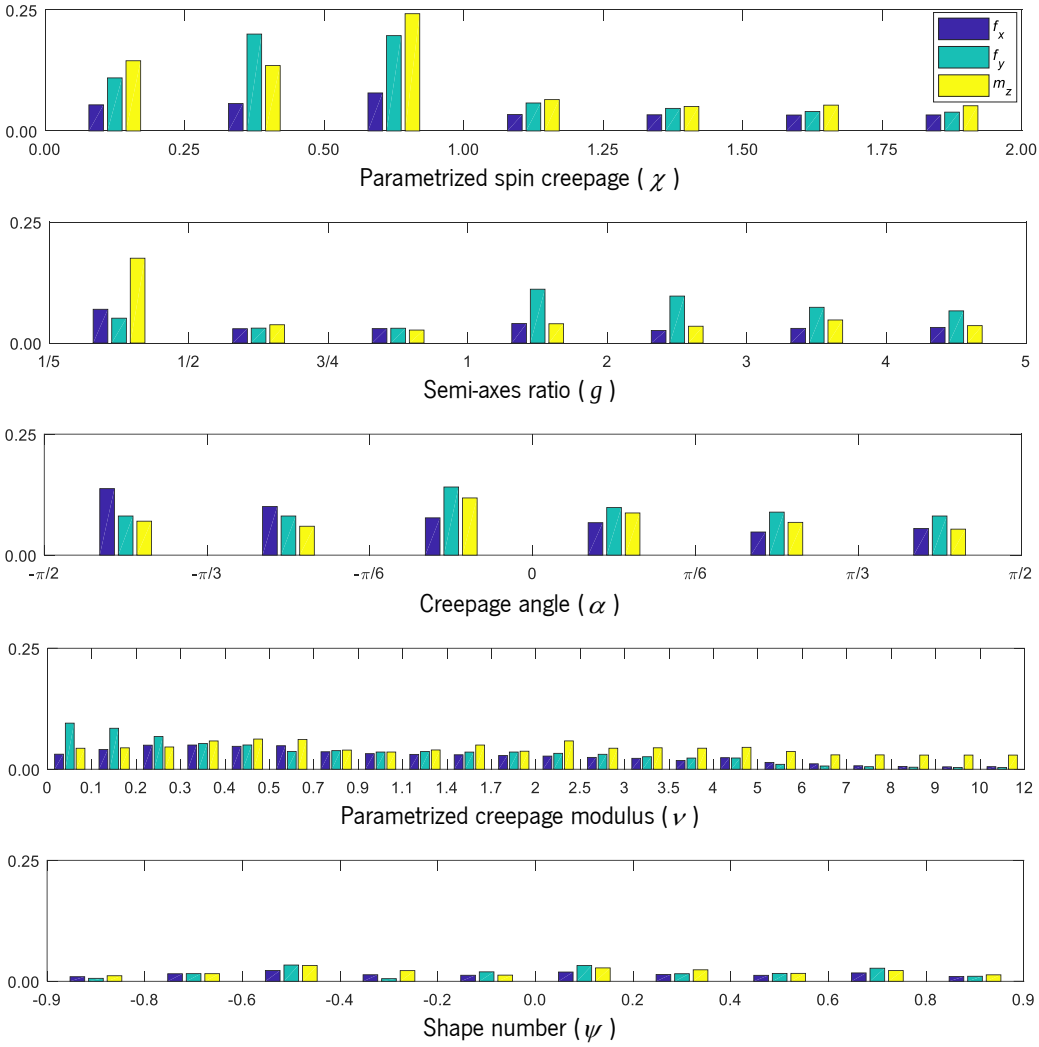

Figure 5.13 – Maximum interpolation error between two consecutive points of the same independent parameter for each output quantity.

In what concerns the mean error, the magnitude of error is significantly lower, as it is shown in the plots of Figure 5.14. A similar analysis to that made for the maximum error can be made. The maximum mean error is found to be for the lower values of the semi-axis ratio. For the remaining input variables, it can be said that they have discretization which favor uniform error distributions. However, the creepage angle exhibits the highest interpolation error.

It must be mentioned that there is no advantage of having different levels of error for different input parameters, since the accuracy of the table is limited by the variable that introduces the highest error. In principle, it would be possible to design the LuT so that it has smaller errors for the cases having a higher probability of occurrence. However, the probability of occurrence of the input variables is closely linked with the type of train, characteristics of the track, running conditions, hence with a balanced interpolation error, the LuT would be more suitable for a wide range of simulation scenarios. Thus, the

design of the LuT can be enhanced either by improving the discretization where the error is higher, thus increasing accuracy, or by using a coarser discretization where the error is smaller, which reduces the size of the LuT and enhances efficiency.

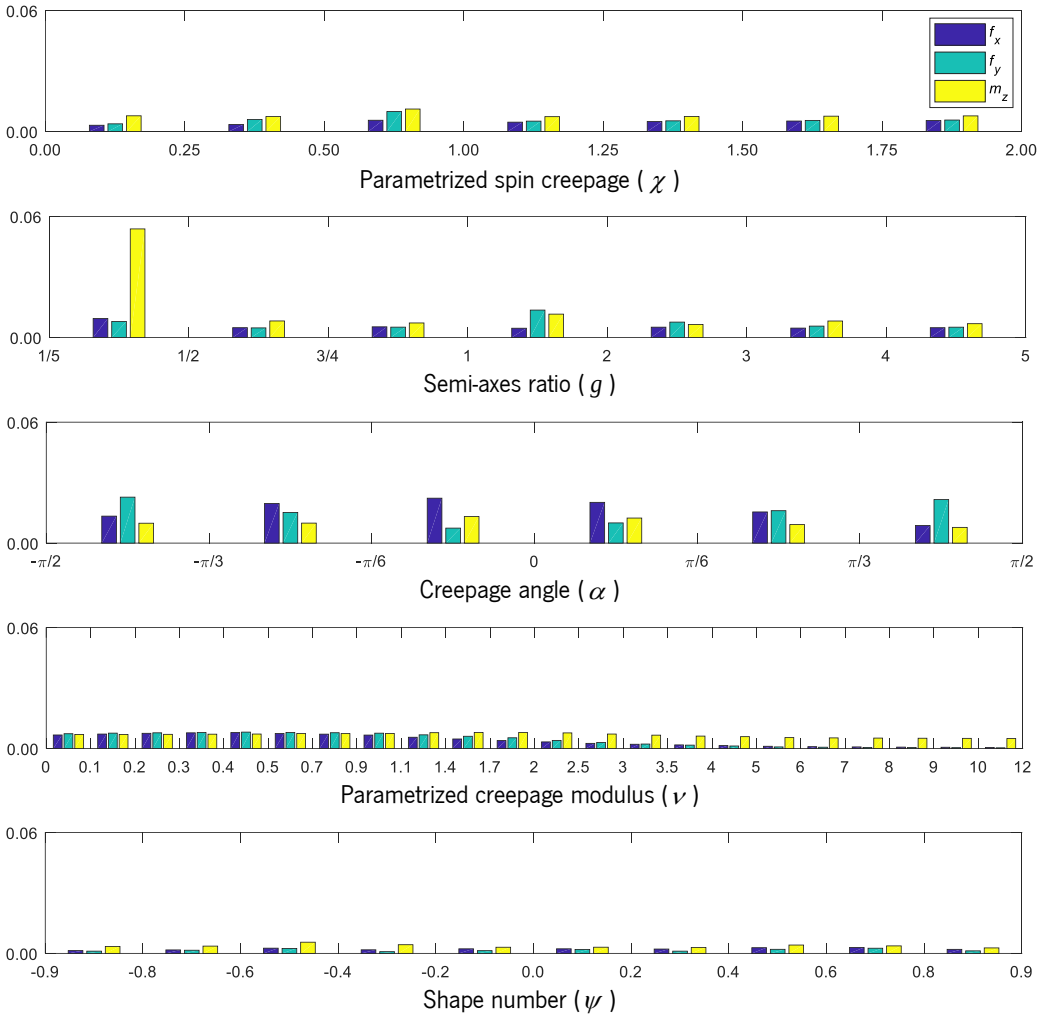

Figure 5.14 – Mean interpolation error between two consecutive points of the same independent parameter for each output quantity.

5.4. Generation of Enhanced Lookup Tables

It is demonstrated, in section 5.3, that the current KBTNH has an unbalanced interpolation error for the different input parameters. Based on the analysis made, two novel LuT designs are proposed. The options are either to have a smaller sized table keeping the error level of the current LuT or to improve its accuracy while preserving the LuT size. A trial and error procedure, which involves the generation of table and error analysis, is used here to obtain the enhanced LuTs. In any form of LuT enhancement, it must be taken into account that the creepage angle and shape factor have the same range of errors for

the positive and negative parts of their domains, and, therefore, their discretization must be symmetric. The distribution of points of the semi-axis ratio must also be symmetric around 1 in a logarithmic scale.

5.4.1. Reduced Size Enhanced LuT

In order to preserve the same accuracy of the original LuT, the parameters that lead to the higher values must be kept with the same discretization in the region of such error. Thus, the creepage angle, which is equally spaced, is maintained unchanged. The spin creepage may have a coarser discretization for higher values. Regarding the semi-axis ratio, the points must be redistributed to achieve the symmetry around 1. The number of points used for the creepage modulus and shape number can be significantly reduced, since the current error on the output quantities is much lower when compared with other input parameter.

Table 5.3 – Domain of the enhanced Kalker Book of Tables for Non-Hertzian (KBTNH) contact with reduced size.

Parameter	No. of Points	Deviation
$\chi = \begin{Bmatrix} 0.00 & 0.25 & 0.50 & 1.00 \\ 1.25 & 1.50 & 1.75 & 2.00 \end{Bmatrix}$	$n_\chi = 7$	-1
$g = \left\{ \frac{1}{5} \quad \frac{1}{3} \quad \frac{1}{2} \quad 1 \quad 2 \quad 3 \quad 5 \right\}$	$n_g = 7$	-1
$\alpha = \left\{ -\frac{\pi}{2} \quad -\frac{\pi}{3} \quad -\frac{\pi}{6} \quad 0 \quad \frac{\pi}{6} \quad \frac{\pi}{3} \quad \frac{\pi}{2} \right\}$	$n_\alpha = 7$	0
$\nu = \begin{Bmatrix} 0.0 & 0.2 & 0.4 & 0.7 & 1.2 \\ 2.0 & 3.5 & 5.0 & 8.0 & 12.0 \end{Bmatrix}$	$n_\nu = 10$	-13
$\psi = \begin{Bmatrix} -0.9 & -0.6 & -0.3 \\ 0.0 & 0.3 & 0.6 & 0.9 \end{Bmatrix}$	$n_\psi = 7$	-4

Bearing in mind the interpretations of the errors due to the discretization of the input parameters, an enhanced version of the KBTNH is proposed here, being its discretization presented in Table 5.3. The number of points used for the discretization of each parameter is reduced when compared to the original LuT. Thus, the total number of data points in the enhanced LuT is expressed as

$$N_p = \prod_{i=1}^{5} n_i = 24\,010 \tag{5.33}$$

Analyzing the size of the enhanced LuT with the size of the original LuT, given in Eq. (5.33), a compression ratio of 4.72 is obtained for a table with similar accuracy. This has a substantial impact on the computational time to generate the LuT and on the time to search and interpolate the LuT in dynamic analyses.

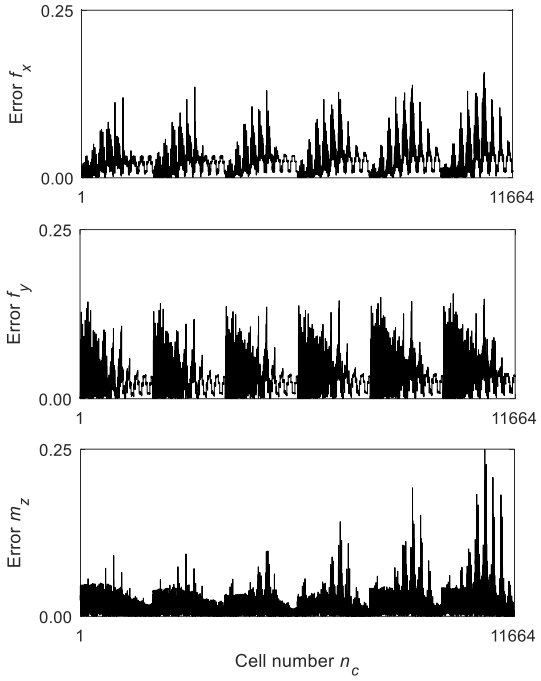

Figure 5.15 – Interpolation error at the center of the LuT cells for different outputs over the domain of the enhanced LuT with reduced size.

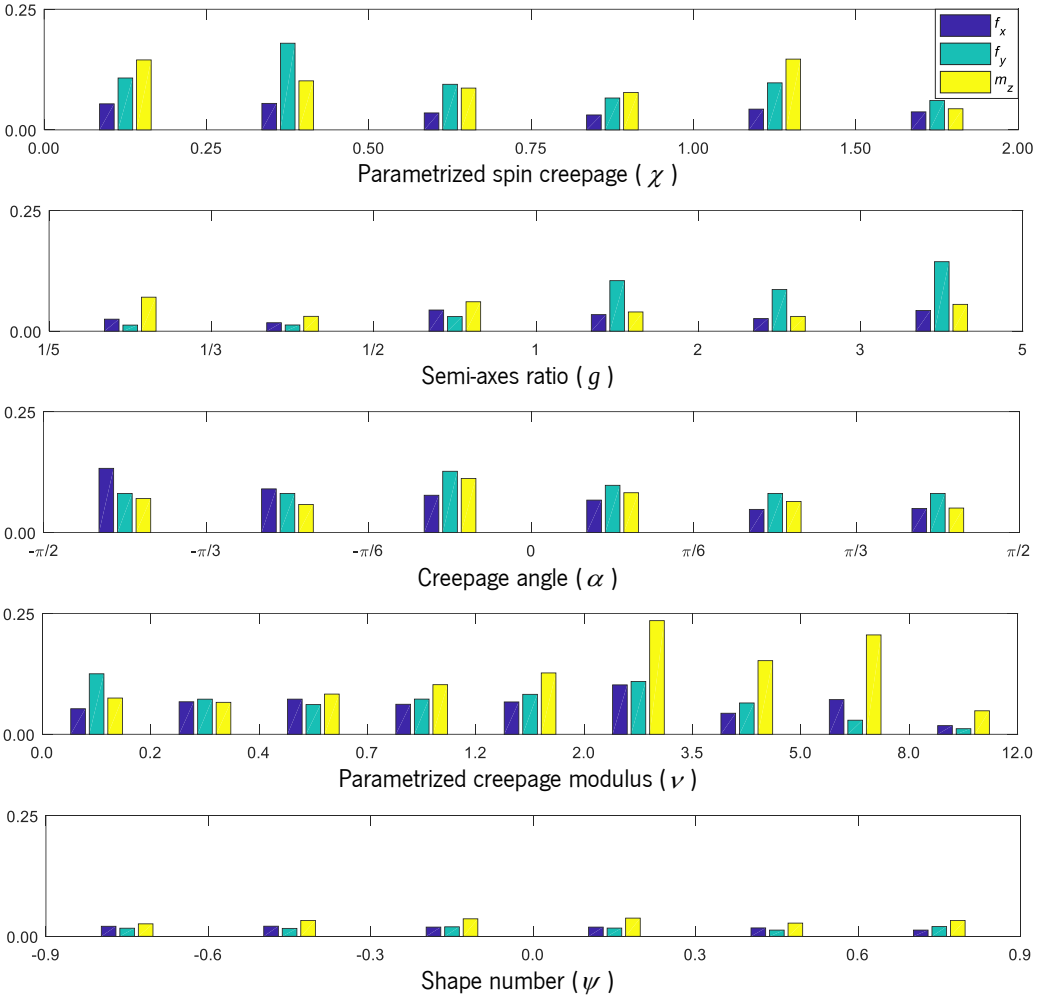

Figure 5.16 – Maximum interpolation error between two consecutive points of the same independent parameter for each output quantity of the enhanced LuT with reduced size.

In order to assess the accuracy of the enhanced KBTNH and compare it with the original one, the evaluation of the interpolation error at the center of the cells and at the middle point of the edges is performed using a procedure similar to the one described in Sections 5.3.2 and 5.3.3, respectively. The error of interpolation at the center of the cells of the LuT proposed in Table 5.3 is displayed in Figure 5.15. Moreover, Figure 5.16 and Figure 5.17 depict, respectively, the maximum and mean errors of interpolation for the normalized creep forces and moment. Through the comparison of the plots of Figure 5.11 and Figure 5.15, it can be recognized that a similar level of error in the center of the cells can be achieved with a significant reduction of the size of the LuT if a careful selection of its discretization points is made. By observing Figure 5.16 and Figure 5.17, it can be concluded that the level of maximum error is similar to that of the original LuT, i.e., lower than 0.25. However, the maximum mean error is reduced even with the decrease of the number of points used in the discretization of some of its input parameters. Moreover, the two parameters that are more affected by this change, i.e., the creepage modulus and shape number, keep their interpolation error lower than the creepage angle, as plotted in Figure 5.17.

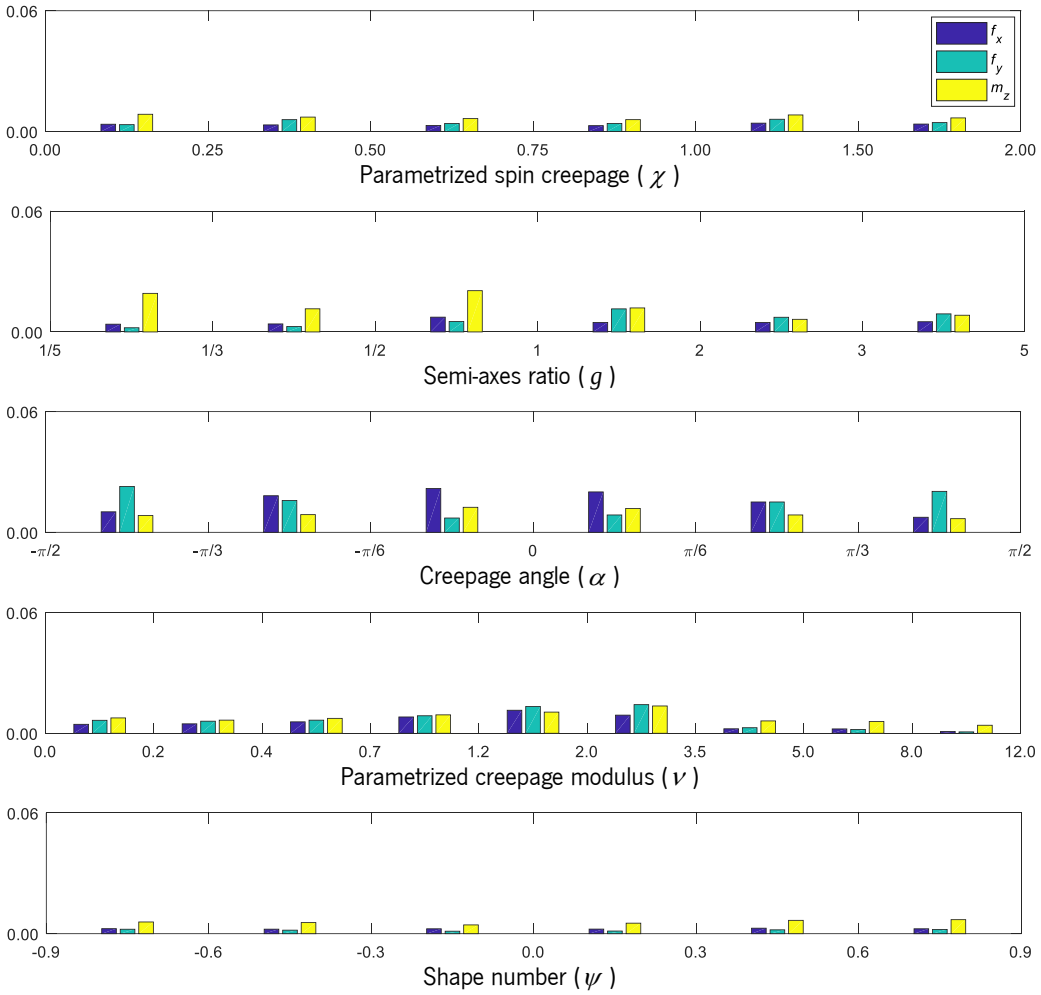

Figure 5.17 – Mean interpolation error between two consecutive points of the same independent parameter for each output quantity of the enhanced LuT with reduced size.

5.4.2. Improved Accuracy Enhanced LuT

By keeping the size of the LuT and redistributing the LuT points, a higher accuracy of the interpolation is obtained. Some points are removed from the zones with lower error to be placed where the error is higher. In addition, the guidelines gathered from the analysis of variation of the input parameters are taken into account for the selection of LuT points. For this purpose, the spin creepage is refined for values between 0 and 1 in order to reduce the maximum interpolation error. Then, a higher number of points is added to the semi-axis ratio to maintain the same target. Since the creepage angle leads to one of the major sources of error, two additional points are considered in the discretization, keeping the constant spacing distribution. As for the enhanced LuT presented in section 5.4.1, the number of points for the creepage modulus and shape factor can be reduced due to original low interpolation error associated with them.

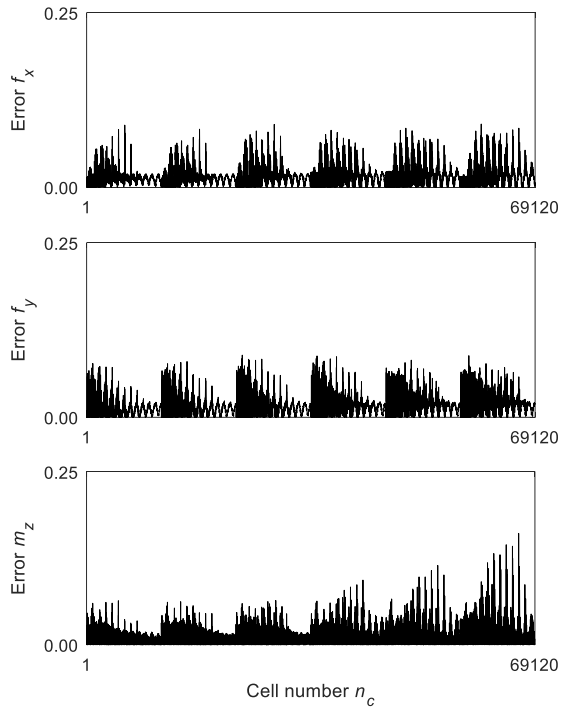

Figure 5.18 – Interpolation error at the center of the LuT cells for different outputs over the domain of the enhanced LuT with improved accuracy.

Based on the observations made, an enhanced KBTNH described in Table 5.4 is proposed here. The number of points used in the discretization is increased for the spin creepage, semi-axis ratio and creepage angle, while it is decreased for the discretization of the creepage modulus and shape number. The total number of LuT entries is now expressed by

$$N_p = \prod_{i=1}^{5} n_i = 117\ 117 \tag{5.34}$$

The new enhanced LuT is, approximately, 1.03 times larger than the original KBTNH, which is acceptable. To verify the accuracy improvement of the table, the interpolation error at the center of the LuT cells is evaluated, and its values presented in Figure 5.18. From the error analysis, it is evident that a significant reduction of the error is accomplished comparatively to the original LuT. In addition, the assessment of the interpolation error at the middle point of LuT edges is performed, being the maximum and mean interpolation errors for the normalized creep forces and moment shown in Figure 5.19 and Figure 5.20, respectively. The results indicate that the maximum error is below 0.12, which is less than half of that exhibited by the original KBTNH. It can be recognized that, for this enhanced LuT, the interpolation error is much more balanced than in the original one, i.e., the order of magnitude of the error is similar for the five parameters. Moreover, this significant decrease of the error ensures higher confidence for the use of this new LuT on railway vehicle dynamics, since it has higher resemblance with the online use of CONTACT, deemed as the correct representation of the rail-wheel contact forces.

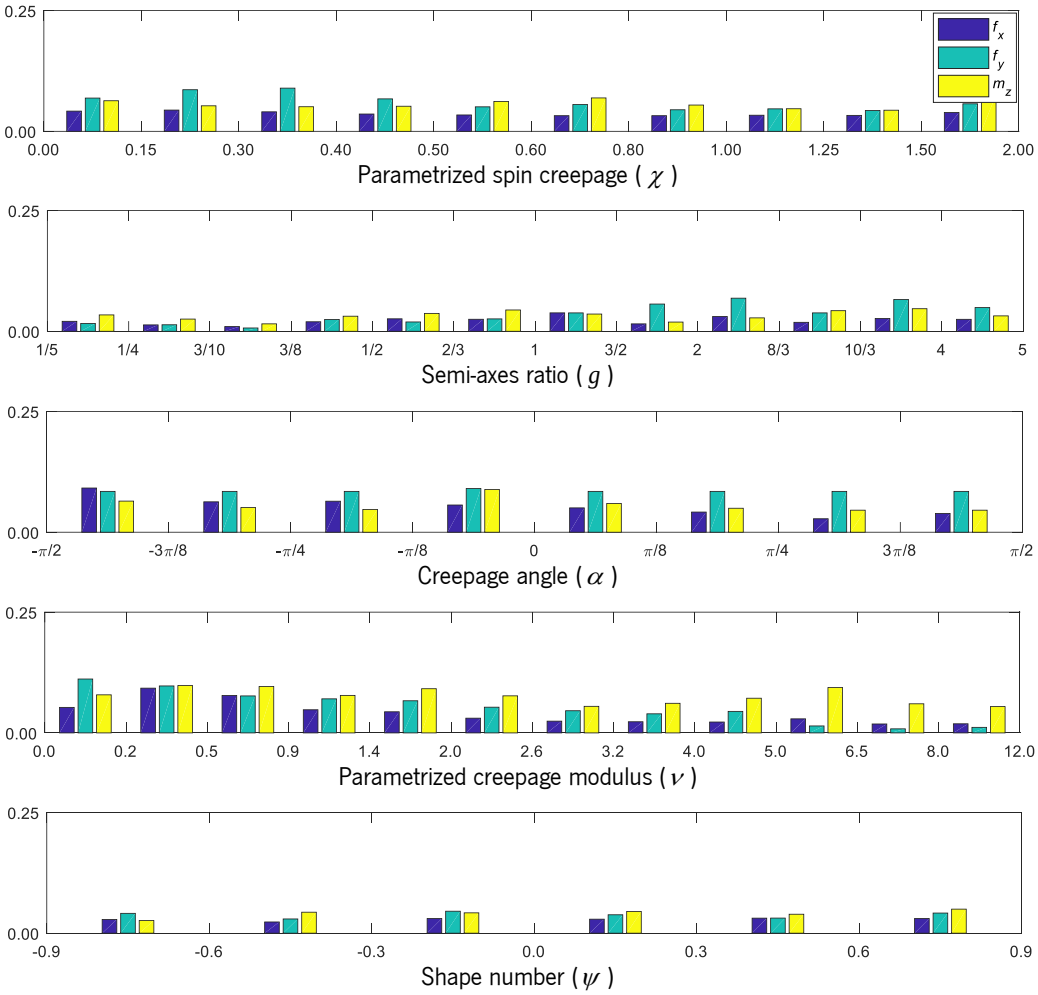

Figure 5.19 – Maximum interpolation error between two consecutive points of the same independent parameter for each output quantity of the enhanced LuT with improved accuracy.

Table 5.4 – Domain of the enhanced Kalker Book of Tables for Non-Hertzian (KBTNH) contact with improved accuracy.

Parameter	No. of Points	Deviation
$\chi = \{0.00 \quad 0.15 \quad 0.30 \quad 0.40 \quad 0.50 \quad 0.60 \quad 0.80 \quad 1.00 \quad 1.25 \quad 1.50 \quad 2.00\}$	$n_\chi = 11$	+3
$g = \left\{\frac{1}{5} \quad \frac{1}{4} \quad \frac{3}{10} \quad \frac{3}{8} \quad \frac{1}{2} \quad \frac{2}{3} \quad 1 \quad \frac{3}{2} \quad 2 \quad \frac{8}{3} \quad \frac{10}{3} \quad 4 \quad 5\right\}$	$n_g = 13$	+5
$\alpha = \left\{-\frac{\pi}{2} \quad -\frac{3\pi}{8} \quad -\frac{\pi}{4} \quad -\frac{\pi}{8} \quad 0 \quad \frac{\pi}{8} \quad \frac{\pi}{4} \quad \frac{3\pi}{8} \quad \frac{\pi}{2}\right\}$	$n_\alpha = 9$	+2
$\nu = \{0.0 \quad 0.2 \quad 0.5 \quad 0.9 \quad 1.4 \quad 2.0 \quad 2.6 \quad 3.2 \quad 4.0 \quad 5.0 \quad 6.5 \quad 8.0 \quad 12.0\}$	$n_\nu = 13$	-10
$\psi = \{-0.9 \quad -0.6 \quad -0.3 \quad 0.0 \quad 0.3 \quad 0.6 \quad 0.9\}$	$n_\psi = 7$	-4

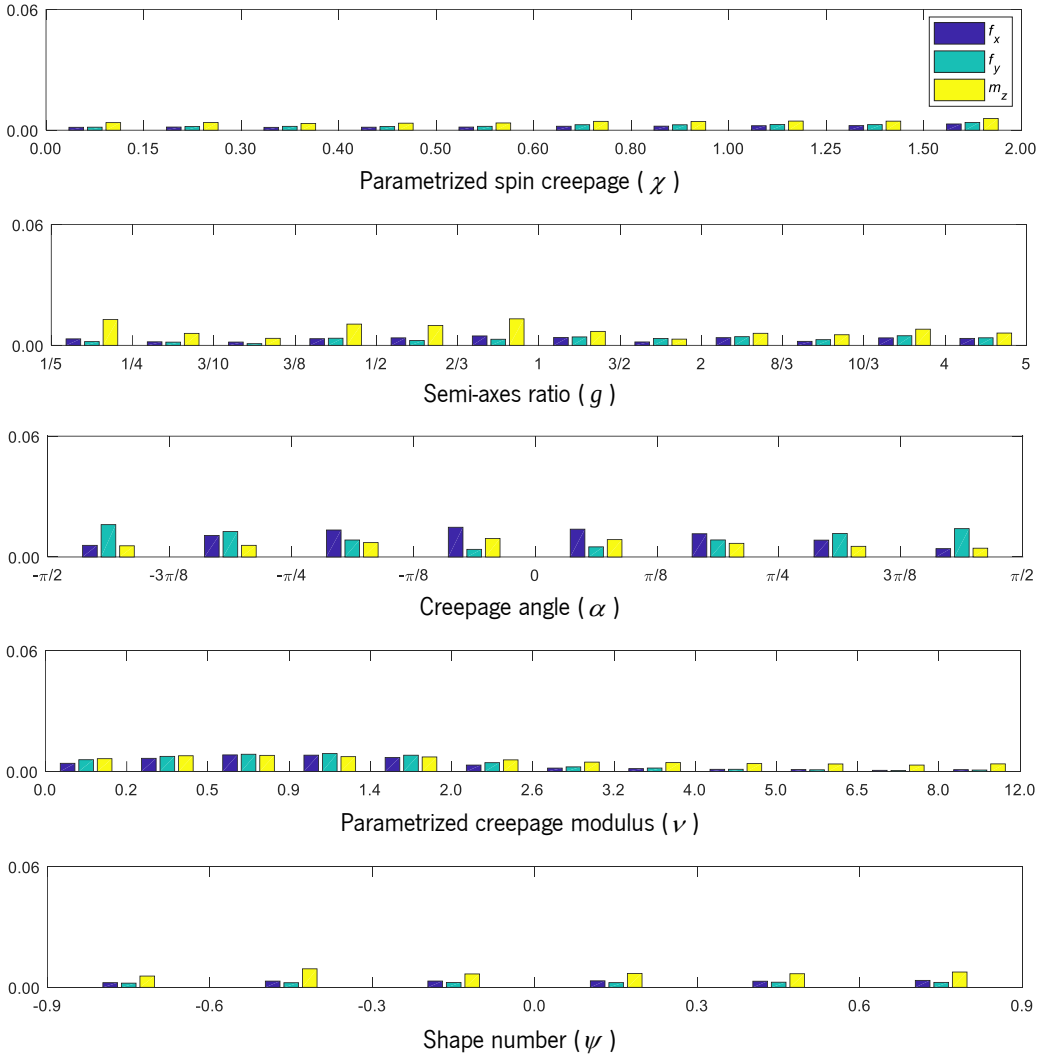

Figure 5.20 – Mean interpolation error between two consecutive points of the same independent parameter for each output quantity of the enhanced LuT with improved accuracy.

5.5. Summary and Conclusions

In this chapter, the use of Lookup Tables with the purpose of decreasing the computational time to replace the online evaluation of a given function is addressed. Here, a LuT based on CONTACT software is used to evaluate the creep forces and moment at the wheel-rail interaction considering a regularization with a simple double-elliptical contact patch. This LuT is called Kalker Book of Tables for Non-Hertzian contact, and involves five input parameters, namely the parametrized spin creepage, the semi-axes ratio, the creepage angle, the parametrized creepage modulus and the shape number. The process of regularization of a general non-Hertzian contact patch, and the generation of the contact LuT using CONTACT, are discussed.

The application of LuT methodologies presents some limitations as the prior definition of a finite domain and the error introduced by the linear interpolation of LuT data. The selection of LuT points for each input variable defines the available domain and the degree of accuracy of the LuT, thus, a suitable discretization is of paramount importance. This work presents a comprehensive methodology for a detailed analysis of a general LuT and proposes a methodology for its improvement. An analysis of the variation of the input parameters is made and the interpolation error is assessed on the center of the cells and at the middle point of the edges of the original table.

The assessment of the LuT accuracy shows that the interpolation error introduced by the distribution of the LuT points is significantly different for the several input parameters. This observation allows to redistribute the location of the LuT points, and even eliminate some of them where the LuT is too refined. Based on this error analysis methodology, two enhanced LuTs are generated, one with a reduced size but similar accuracy to the original table and another with the same size of the original LuT but with improved accuracy. The former LuT, with similar accuracy, has its size decreased by a ratio of 4.72. The latter LuT, with a size identical to that of the original, exhibits a maximum interpolation error reduced by half. With respect to the memory consumption of different LuTs, this is directly related with the number of points of the LuT. In the specific case of the current table, it is around 2.2 MB (113 344 points) for the original LuT, 460 kB (24 010 points) for the table developed in section 5.4.1 and 2.3 MB (117 117 points) for the table obtained in section 5.4.2. Certainly, the larger the number of inputs parameters for the LuT the more important is the selection of the sampling points, in terms of accuracy, and the size of the table, in terms of computational efficiency.

This page is intentionally left blank.

"*I was gratified to be able to answer promptly, and I did. I said I didn't know.*"
Mark Twain

6. ENHANCED WHEEL-RAIL CONTACT MODEL FOR DYNAMIC ANALYSIS

The wheel-rail contact interaction involves several transient phenomena that cannot be assessed with static or quasi-static analyses. The normal and creep forces generated in the contact and the motion of the railway vehicle are naturally coupled, which makes the contact modeling to have a significant impact on the evaluation of the vehicle performance. During a dynamic analysis of a multibody railway vehicle, the contact evaluation must be somewhat fast, and ensure a smooth variation of the contact forces, which not only is more realistic but also allows the expeditious evolution of the integration process. To verify the effectiveness and reliability of the contact modeling methodologies proposed in the previous chapters, it is necessary to analyze their consequence on the behavior of railway vehicles in different running conditions (Marques et al., 2020). For this purpose, a simple multibody model of a trailer railway vehicle is presented and used in the dynamic analyses developed in this chapter. The results of these analyses support the assessment of the different modeling simplifications, such as for the geometry description or for the contact pressure distribution. Three different running scenarios are used as application cases to demonstrate the validity and robustness of the contact detection procedure proposed, i.e., the curved contact patch approach and the enhanced look-up tables for the creep forces.

6.1. Multibody Model of the Vehicle

The trailer vehicle of the ML95 trainset, proposed by Pombo et al. (2004), is used in this work to study the behavior of the contact modeling methodologies proposed in the context of multibody dynamics simulations. This train is operated by the Lisbon subway company, and the driving vehicles are not considered for this study in order to focus the analysis results on the contact modeling avoiding dealing with other issues such as the coupling between vehicles or the traction systems. In the remaining of this section, a detailed description of the multibody model of this vehicle is provided (Pombo, 2004).

A schematic representation of the multibody model is given in Figure 6.1. In the vehicle model, three main subsystems are highlighted, that is, the carbody, and the front and rear bogies. The carbody is treated as a single rigid body while both bogies are similar subsystems, schematized in Figure 6.2. Each bogie is constituted of a bogie frame, two wheelsets, four axleboxes and suspension systems. The primary suspension is responsible for supporting the bogie frame and it is constituted of four sets of two Chevron springs connecting each axlebox and the bogie frame. The secondary suspension, which supports the vertical loads from the carbody and reduces the vibrations transmitted from the track to the passengers, is composed by two airsprings that operate in parallel with two hydraulic vertical dampers. The connection between the bogie and the carbody is done by means of a center plate attached to the carbody which is connected to the center of the bogie frame through two traction rods and two transversal dampers. These connection elements are represented in Figure 6.3, and ensure the vehicle steering functions by providing a stable rotation of the bogie system with respect to the carbody.

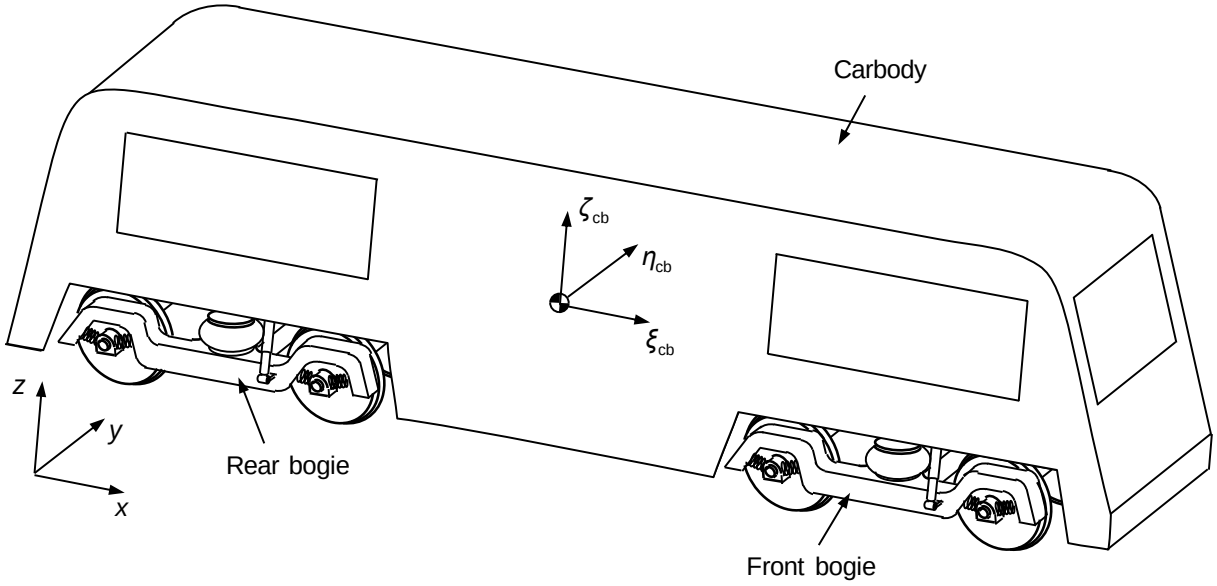

Figure 6.1 – Schematic representation of the multibody model of ML95 trailer vehicle.

The multibody model of the ML95 trailer vehicle is constituted by a set of rigid bodies connected by kinematic joints or force elements, and its motion is modeled according to the multibody dynamics formulation presented in Section 2.1. The vehicle model consists of 11 rigid bodies, that is, one carbody, two bogie frames, four pair of axleboxes and four wheelsets. It must be noted that each pair of axleboxes connected with the same wheelset is considered a single rigid body reducing in this form the total number of bodies without affecting the system dynamics. For the multibody model, it is necessary to define the mass and moment of inertia in all principal directions for each body, as provided in Table 6.1. The initial

conditions are defined through the position, orientation and velocity of the local reference frame of each body, attached to their center of mass. Table 6.1 lists the position of the center of mass of each rigid body with respect to the global reference system. Regarding their orientation, all rigid bodies start the simulation aligned with the global reference system and, hence, that data is provided. The initial translational and angular velocities of the rigid bodies is provided in Section 6.2, since they vary in consonance with the running scenarios.

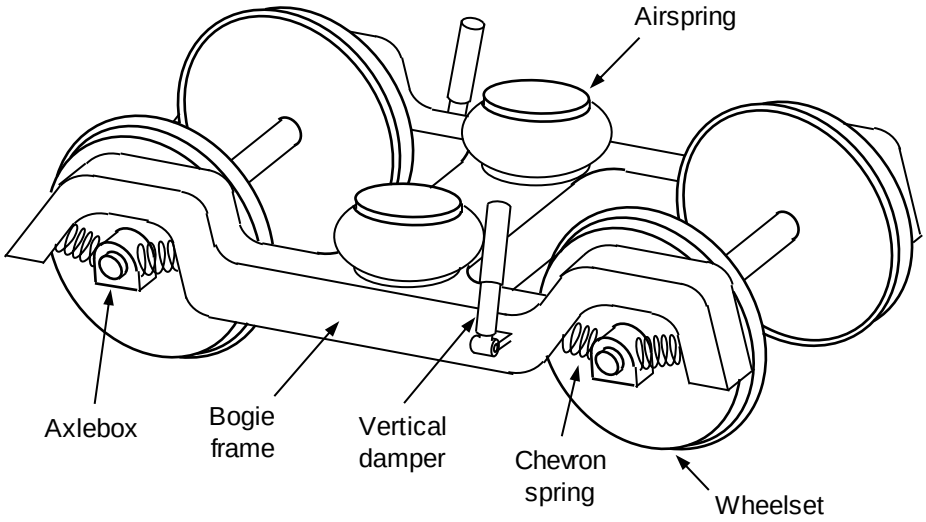

Figure 6.2 – Schematic representation of the bogie subsystem utilized in the multibody model of ML95 trailer vehicle.

Table 6.1 – Inertial properties and initial position of each body of the multibody model of the vehicle.

No.	Body		Mass [kg]	Inertia Properties [kg·m^2]			Initial Position [m]		
				$I_{\xi\xi}$	$I_{\eta\eta}$	$I_{\zeta\zeta}$	x_0	y_0	z_0
1	Rear Bogie	Rear Wheelset	933	461.4	61.6	461.4	0.95	0.0	0.430
2		Front Wheelset	933	461.4	61.6	461.4	3.05	0.0	0.430
3		Rear Axleboxes	176	144.5	2.2	144.5	0.95	0.0	0.430
4		Front Axleboxes	176	144.5	2.2	144.5	3.05	0.0	0.430
5		Bogie Frame	1982	1398.5	2667.0	2667.0	2.00	0.0	0.460
6	Front Bogie	Rear Wheelset	933	461.4	61.6	461.4	12.05	0.0	0.430
7		Front Wheelset	933	461.4	61.6	461.4	14.15	0.0	0.430
8		Rear Axleboxes	176	144.5	2.2	144.5	12.05	0.0	0.430
9		Front Axleboxes	176	144.5	2.2	144.5	14.15	0.0	0.430
10		Bogie Frame	1982	1398.5	2667.0	2667.0	13.10	0.0	0.460
11		Carbody	11160	14952.9	225365.4	224994.9	7.55	0.0	1.849

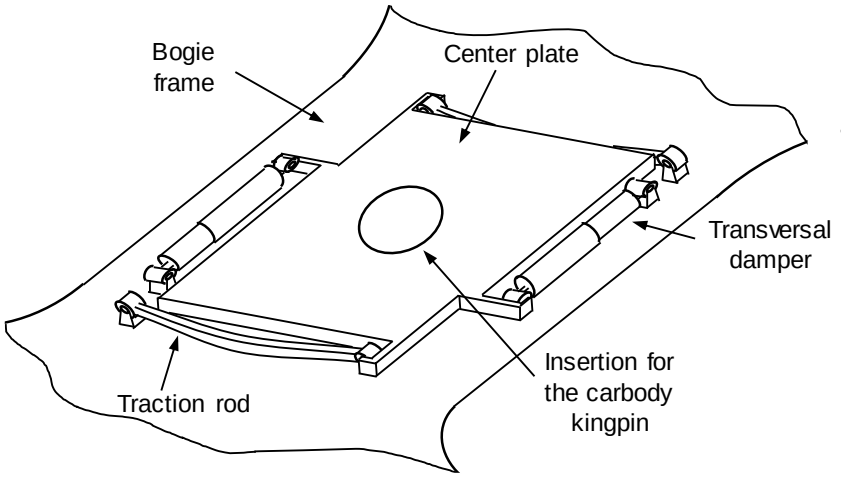

Figure 6.3 – Schematic representation of the carbody-bogie connection elements for the ML95 trailer vehicle.

The model has four kinematic revolute joints between each pair of axleboxes and the corresponding wheelset. These revolute joints only allow the relative rotation around the wheelset axis, which represents the existence of roller bearings in their ends. The remaining bodies are interconnected through force elements, as further detailed in this section.

Regarding the primary suspension, each pair of Chevron springs connecting each individual axlebox with the bogie frame are modeled as four three-dimensional spring-damper elements, as schematized in Figure 6.4. Thus, two longitudinal, one vertical and one lateral force elements are considered for each wheel, which results in a total of 16 spring-damper connection for each bogie. In order to implement these spring-damper elements, it is necessary to define their stiffness, damping coefficient and the location where they are attached to both bodies, in their local reference frame. This data is provided in Table 6.2 for the rear bogie system, where the bodies' indexes refer to the numbering provided in Table 6.1. The primary suspension on the front bogie is equal to that of the rear bogie and only the bodies' indexes change.

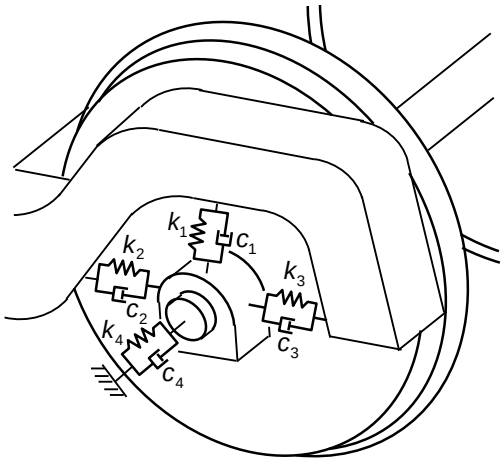

Figure 6.4 – Representation of spring-damper elements used on the modeling of the primary suspension.

Table 6.2 – Properties of spring-damper elements from the primary suspension, secondary suspension and bogie-carbody connection elements.

	Element	Spring Stiffness [kN/m]	Damping Coefficient [kN·s/m]	Bodies		Bodies Local Coordinates [m]					
						Body *i*			Body *j*		
				i	*j*	ξ_i	η_i	ζ_i	ξ_j	η_j	ζ_j
Primary Suspension	Vertical (1)	1280	55.41	3	5	0.0	-0.9	0.0	-1.05	-0.9	0.22
				3	5	0.0	0.9	0.0	-1.05	0.9	0.22
				4	5	0.0	-0.9	0.0	1.05	-0.9	0.22
				4	5	0.0	0.9	0.0	1.05	0.9	0.22
	Longitudinal (2)	6210	86.29	3	5	0.0	-0.9	0.0	-0.775	-0.9	-0.03
				3	5	0.0	0.9	0.0	-0.775	0.9	-0.03
				4	5	0.0	-0.9	0.0	0.775	-0.9	-0.03
				4	5	0.0	0.9	0.0	0.775	0.9	-0.03
	Longitudinal (3)	6210	86.29	3	5	0.0	-0.9	0.0	-1.325	-0.9	-0.03
				3	5	0.0	0.9	0.0	-1.325	0.9	-0.03
				4	5	0.0	-0.9	0.0	1.325	-0.9	-0.03
				4	5	0.0	0.9	0.0	1.325	0.9	-0.03
	Lateral (4)	2060	70.29	3	5	0.0	-0.9	0.0	-1.05	-1.1	-0.03
				3	5	0.0	0.9	0.0	-1.05	1.1	-0.03
				4	5	0.0	-0.9	0.0	1.05	-1.1	-0.03
				4	5	0.0	0.9	0.0	1.05	1.1	-0.03
Secondary Suspension	Airspring Vertical (5)	250	47.54	5	11	0.0	-0.935	0.09	-5.55	-0.935	-1.009
				5	11	0.0	0.935	0.09	-5.55	0.935	-1.009
				10	11	0.0	-0.935	0.09	5.55	-0.935	-1.009
				10	11	0.0	0.935	0.09	5.55	0.935	-1.009
	Airspring Longitudinal (6)	75	26.04	5	11	0.2	-0.935	0.38	-5.55	-0.935	-1.009
				5	11	0.2	0.935	0.38	-5.55	0.935	-1.009
				10	11	-0.2	-0.935	0.38	5.55	-0.935	-1.009
				10	11	-0.2	0.935	0.38	5.55	0.935	-1.009
	Airspring Lateral (7)	750	26.04	5	11	0.0	-1.135	0.38	-5.55	-0.935	-1.009
				5	11	0.0	1.135	0.38	-5.55	0.935	-1.009
				10	11	0.0	-1.135	0.38	5.55	-0.935	-1.009
				10	11	0.0	1.135	0.38	5.55	0.935	-1.009
	Vertical Damper (8)	-	21.00	5	11	0.48	-1.130	-0.07	-5.07	-1.130	-1.009
				5	11	-0.48	1.130	-0.07	-6.03	1.130	-1.009
				10	11	0.48	-1.130	-0.07	6.03	-1.130	-1.009
				10	11	-0.48	1.130	-0.07	5.07	1.130	-1.009
Connection Elements	Traction Rod (9)	1905	-	5	11	0.245	-0.44	-0.21	-5.795	-0.44	-1.599
				5	11	-0.245	0.44	-0.21	-5.305	0.44	-1.599
				10	11	0.245	-0.44	-0.21	5.305	-0.44	-1.599
				10	11	-0.245	0.44	-0.21	5.795	0.44	-1.599
	Transversal Damper (10)	-	12.00	5	11	0.225	-0.285	-0.27	-5.325	0.04	-1.599
				5	11	-0.225	0.285	-0.27	-5.775	-0.04	-1.599
				10	11	0.225	-0.285	-0.27	5.775	0.04	-1.599
				10	11	-0.225	0.285	-0.27	5.325	-0.04	-1.599

The secondary suspension supports the vertical loads from the carbody and transmit them to the bogie frame. This suspension system is composed of four airsprings and four vertical dampers, half of these components are placed in each bogie. Once again, these connection parts are modeled as force elements, that is, the each airspring is replaced by three three-dimensional spring-damper elements, for vertical, longitudinal and lateral directions, and the vertical hydraulic damper is treated as single damper. This modeling approach is represented in Figure 6.5 for an airspring and a vertical damper, and the data for the implementation of these elements for the whole secondary suspension is given in Table 6.2.

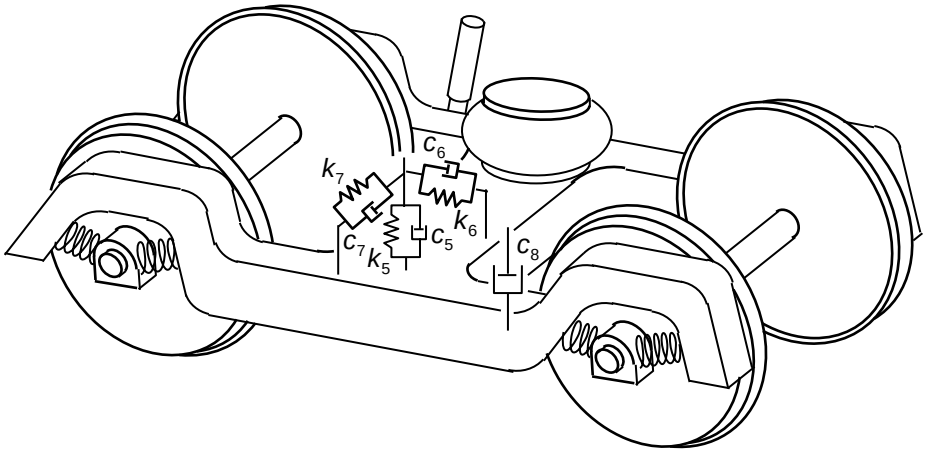

Figure 6.5 – Representation of spring-damper elements used on the modeling of the secondary suspension.

The traction rods and lateral hydraulic dampers are used to transmit the traction and braking loads and to perform the lateral stabilization of the carbody, respectively. These connection elements between bogie frame and the carbody allow some steering functions, but do not have a role on the vertical dynamics of the vehicle. In order to model the contribution of these parts, the traction rods are treated as three-dimensional longitudinal springs and the hydraulic dampers are replaced by simple three-dimensional dampers, as schematized in Figure 6.6. The stiffness, damping coefficient and location of the connection points are listed in Table 6.2.

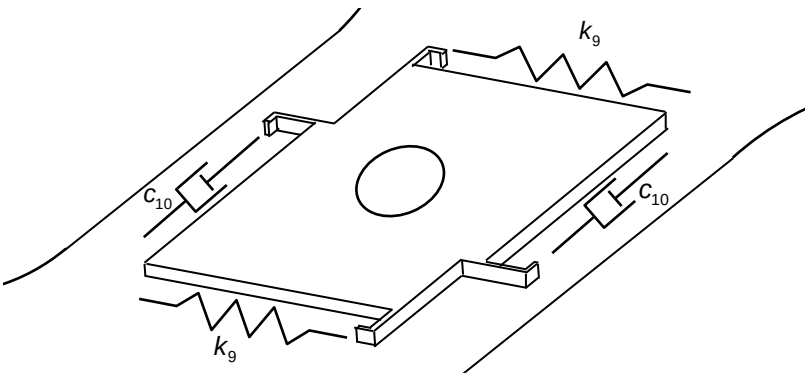

Figure 6.6 – Representation of spring-damper elements used on the modeling of the connection components between the carbody and bogie frame.

It must be noted that the undeformed length of each spring is not given in Table 6.2, although it is required for the calculation of elastic forces. Therefore, the undeformed length of the lateral and longitudinal springs must be found so that these spring elements do not produce force for the initial conditions of the vehicle model. Moreover, the undeformed length of the vertical springs must be defined in way that the vehicle starts the dynamic simulation in static equilibrium, i.e., the vertical springs of the secondary suspension carry the weight of the carbody, while the vertical springs of the primary suspension support the load of the carbody plus the bogies frames.

6.2. Description of Running Scenarios

In this section, the wheel and rail properties selected for the contact models utilized in the dynamic analyses are described, and characteristics of three running scenarios are specified. The wheel and rail profiles employed for this investigation are the S1002 and UIC50, respectively, as shown in Figure 6.7. Depending on the procedure used for the wheel-rail contact problem a simplified version of the wheel profile, as proposed in Chapter 3, in which the transition zone between the tread and the flange is removed avoiding numerical issues associated with the existence of negative curvature, may be used. The remaining geometrical and material parameters of the wheel and rail elements are listed in Table 6.3.

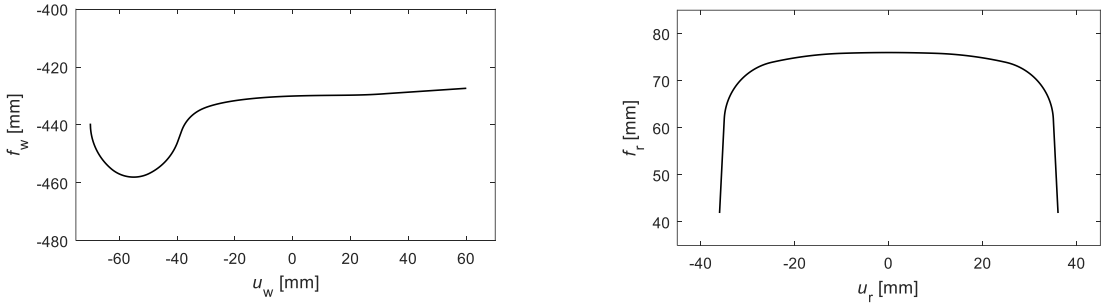

Figure 6.7 – Profiles utilized in the dynamic analysis: (a) Wheel S1002 and (b) Rail UIC50.

In order to test the effectiveness of the contact detection procedures, i.e., the normal contact force evaluation method and LuT approach, three different scenarios are tested: a wheelset running on a tangent track; a bogie running on a tangent track; and the trailer vehicle running on a curved track. In the first scenario, only one wheelset is considered, i.e., body 1 from Table 6.1, with an initial forward velocity of 10 m/s. In this case, there are no force elements or kinematic constraints, and the average load per wheel is around 4576 N. The second running scenario includes a single bogie, i.e., bodies 1 to 5 from Table 6.1, running on tangent track with an initial forward velocity of 18.3 m/s. Since this system includes

one suspension level, i.e., the primary suspension, it can have higher forward speed without destabilizing. Thus, the resulting load per wheel is 10301 N. The final application example consists of the ML95 trailer vehicle, described in the previous section, negotiating a left curve with a radius of 300 m, as described in Figure 6.8. In this scenario, the vehicle also initiates the simulation with a forward speed of 18.3 m/s, and the load per wheel represents an effective real case with approximately 23985 N. The simulation time adopted in the tangent and curved track scenarios are 10 and 41 s, respectively. It must be highlighted that these simulations are carried considering perfect tracks, i.e., without including structural flexibility or irregularities.

Table 6.3 – Geometric and material properties for the dynamic analysis.

Parameter	**Value**
Nominal wheel radius, R_0	0.43 m
Distance between wheel profiles, H	1.5 m
Track gauge	1.435 m
Rail cant	1:20
Young modulus, E	206 GPa
Poisson ratio, σ	0.296
Coefficient of friction, μ	0.25
Coefficient of restitution, c_e	0.75

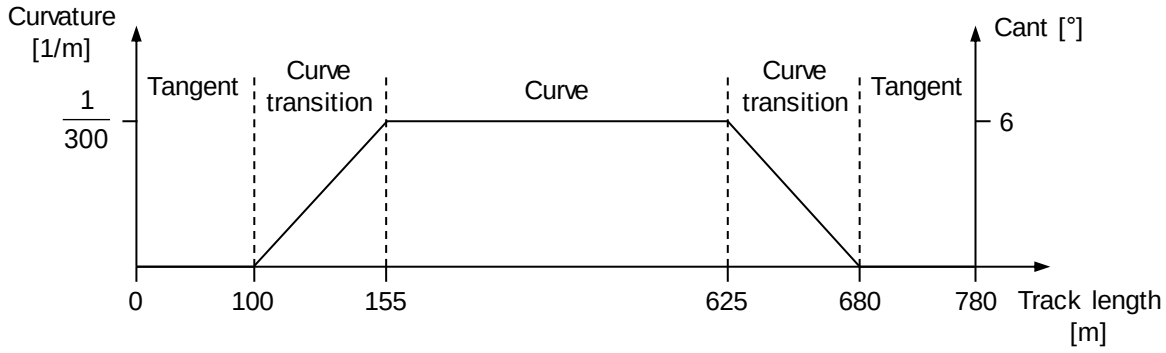

Figure 6.8 – Curvature and cant angle of the curved track.

For the three examples of application, the initial configuration of the multibody models includes a lateral misalignment of 2 mm, between the wheelsets and track center lines, to promote the hunting motion of the system. Therefore, the initial position in y-direction is shifted for all bodies with respect to the initial positions provided in Table 6.1. In what concerns to the vertical position, it must also be adjusted in the sense that the simulations start with no contact between the wheels and the rails, but just slightly separated. In this way, all wheel-rail pairs are in a situation of imminent contact which is initiated less

than a millisecond after the beginning of the simulation. Due to the needs for positioning the vehicle in an 'almost contact' with the rails the first milliseconds of the dynamic analysis results are disregarded from any consideration. The initial velocities of the rigid bodies in x-direction are defined according to the initial forward speed of the system for each case, and all bodies have null velocity in y and z directions. Regarding the angular motion, wheelsets have angular velocity around y axis, calculated by considering them with pure rolling motion.

The simulations are performed in an in-house MATLAB code devoted to the dynamic analysis of spatial multibody systems, called MUBODYNA, in which the methodologies presented for wheel-rail contact modelling are implemented. In each time step, Eq. (2.13) is solved, for which the gravitational forces, the spring-damper connection forces and the wheel-rail contact forces are treated as external forces acting on the bodies. The numerical integration process is performed using the MATLAB '*ode45*' solver, and the optimization problem depicted in Eq. (3.62) is solved using the MATLAB '*fmincon*'. The settings used for each of the MATLAB functions are listed in Table 6.4.

Table 6.4 – Parameters for the numerical integrator scheme and optimization algorithm.

Function	**Parameter**	**Value**
ode45	Relative error tolerance	10^{-5}
	Absolute error tolerance	10^{-5}
	Maximum step size	0.001 s
	Report time step	0.001 s
fmincon	Optimization algorithm	sqp
	Step tolerance	10^{-8}
	Function Tolerance	10^{-10}

6.3. Contact Detection Methodology Assessment

In order to analyze the use of simplified profiles and validate the contact detection methodology proposed in Chapter 3, the railway dynamic simulations are performed for three different conditions, namely, (i) convex wheel profiles with the minimum distance method; (ii) convex wheel profiles with the proposed contact detection method; (iii) real wheel profiles with the proposed contact detection method. The convex wheel profiles refer to the modification proposed in Section 3.2, and illustrated in Figure 3.5(b), which eliminates the transition zone between the wheel tread and wheel flange, with negative curvature, for which the utilization of the minimum distance method for the contact search is applicable.

Therefore, using both contact detection methods with the modified wheel profile, it is possible to assess whether their outcomes are in agreement. Finally, the third scenario allows to verify the suitability and efficiency of the approach presented for realistic wheel profiles. For these simulations, the Hertzian contact model with damping described in Section 4.1 is applied to compute the normal contact forces, and the creep forces are evaluated with Polach method (Polach, 1999), which also assumes an elliptical contact area.

Regarding the scenario of a single wheelset running on a tangent track, Figure 6.9 shows the lateral position of the center of mass of the wheelset relatively to the center of the track in which three different curves are depicted. It can be observed in Figure 6.9 that the use of different methodologies for the contact detection considering the modified convex wheel profiles barely affects the lateral response of the wheelset, since both lines are overlapped. Moreover, the augmented view shown in Figure 6.9 demonstrates that the differences of using the minimum distance method or the novel proposed methodology are less than 10 nm almost at the end of the simulation, which is negligible. On the other hand, it is clear that the use of different wheel profiles has a substantial influence on the frequency of the lateral oscillation, as illustrated in Figure 6.9.

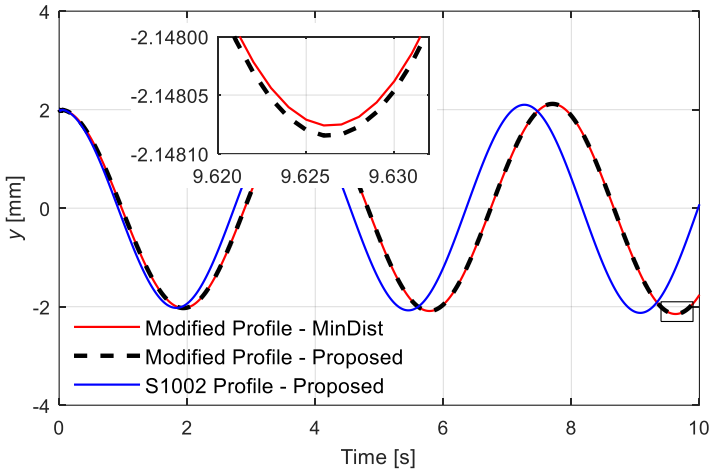

Figure 6.9 – Lateral position of the wheelset for the three tested scenarios of the wheelset running on a tangent track.

The location of the contact points on the wheel surface is also analyzed to demonstrate the differences obtained with the use of real and simplified profiles. The results are displayed only for the simulations with the methodology proposed for the contact search, since the minimum distance method exhibits similar outcomes to the ones when using the modified wheel profiles. Figure 6.10 illustrates the location of the contact points for both actual and simplified wheel profiles in the left wheel. As the wheelset is running on tangent track without irregularities with a small hunting motion, the contact location does not

vary extensively. Although the lateral position of the contact points present some similarities between Figure 6.10(a) and Figure 6.10(b), it includes the modified zone of the wheel surface and, therefore, the computed contact angle differs, which affects the dynamic results in a significant manner.

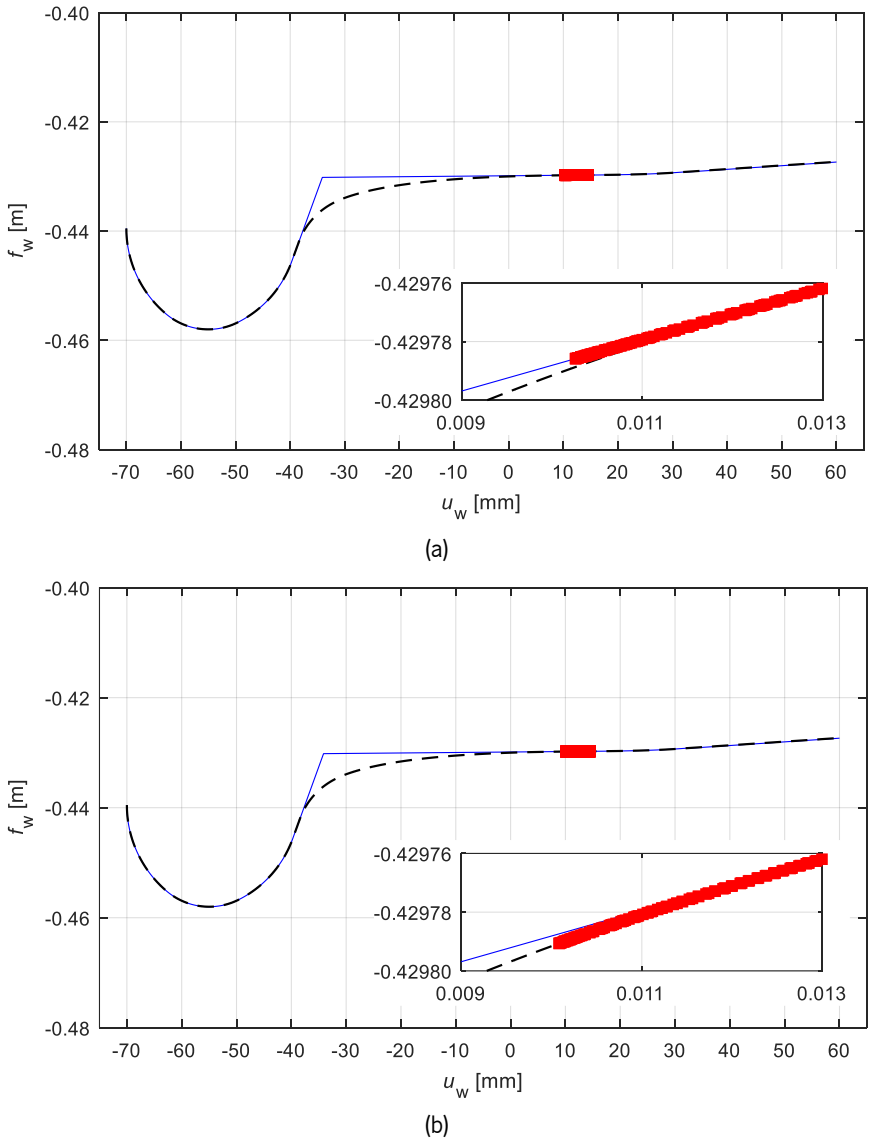

Figure 6.10 – Representation of both actual (**- - -**) and modified (**–**) wheel profiles, and the location of the wheel contact point (■) every 0.05 s for (a) modified and (b) actual profiles of the wheelset running on a tangent track in the left wheel.

In what concerns the normal contact force, Figure 6.11 shows the evolution of the magnitude of normal force on the left wheel for the three cases, suggesting that its oscillation frequency is slightly influenced by the change in the profile, which correlates with the hunting motion variation depicted in Figure 6.9. It must be noticed that, since the wheelset is dropped into the track, at the beginning of the simulation the contact force exhibits high frequency due to the initial impact which is only damped by the normal contact model. Therefore, the results are displayed only after one second of simulation, i.e., after the

numerical perturbation due to the need to start the simulations with wheels and rails without contact vanishes.

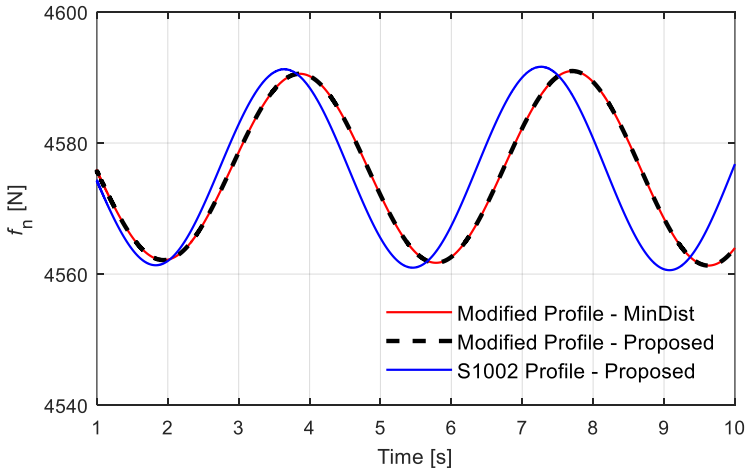

Figure 6.11 – Normal force magnitude in the left wheel for the three tested scenarios of the wheelset running on a tangent track.

In the second case of application, a single bogie running on a tangent track is tested for the same three different scenarios, being the lateral position of the leading wheelset displayed in Figure 6.12. These results show, once more, that the proposed methodology can replace the minimum distance method for fully convex profiles. In addition, it can be observed that the magnitude of the lateral oscillation of the system decreases faster, when compared with the single wheelset case, in Figure 6.9. This fact is related to the increase of the critical velocity due to the presence of the primary suspension.

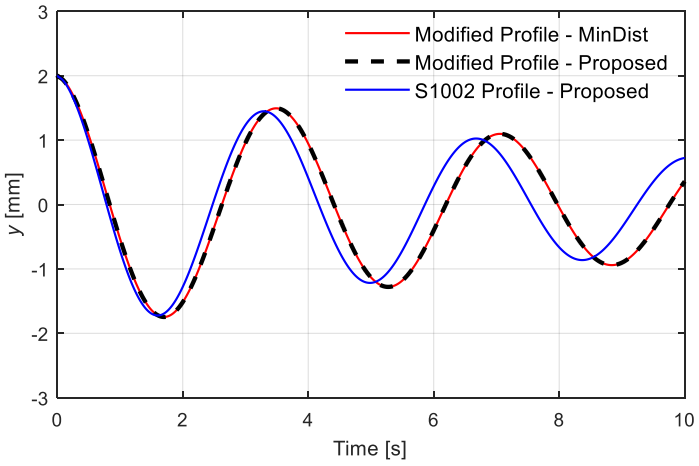

Figure 6.12 – Lateral position of the leading wheelset for the three tested scenarios of the bogie running on a tangent track.

As observed in the case of the wheelset running on a tangent track, here, the wheelsets of the bogie system, present only one contact patch in each wheel. The normal contact force on the left wheel of the leading wheelset is plotted in Figure 6.13. The use of the modified wheel profile affects the frequency of the

normal force oscillation, although its magnitude remains similar. It must be noted that the amplitude of oscillation of normal force is lower than for the single wheelset case not only due to damping introduced by the primary suspension but also due to the cumulative damping associated to the two wheelsets hunting motion.

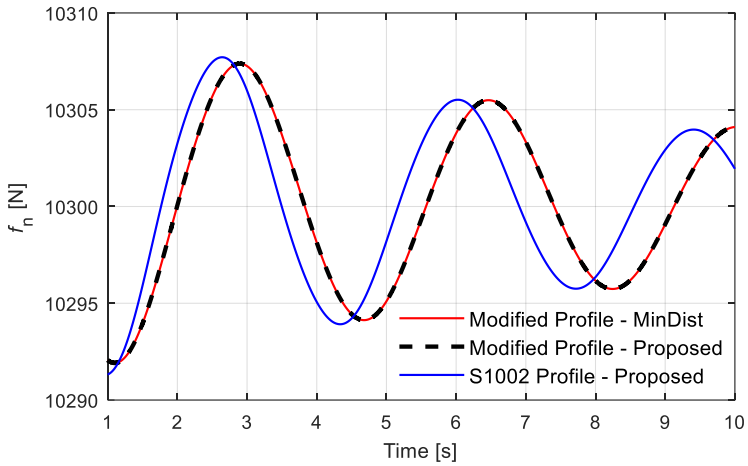

Figure 6.13 – Normal force magnitude in the left wheel of the leading wheelset for the three tested scenarios of the bogie running on a tangent track.

Relatively to the location of the contact points, both the lateral rail coordinate and lateral wheel coordinate are plotted for the simulations with modified and actual profiles in Figure 6.14. Henceforth, the simulations with the minimum distance method are disregarded since, as previously demonstrated, the usage of different contact detection methods does not affect the results. From the analysis of Figure 6.14(a), it can be observed that the location of the contact point in the rail profile is almost fixed when the simplified profile is considered. Regarding the location of the contact point in the wheel profile, it is not much affected by the change in the wheel profile description, as displayed in Figure 6.14(b). This corroborates the results obtained for the wheelset case in Figure 6.10.

Finally, the case of the trailer vehicle negotiating a left curve is evaluated. Since in the two previous examples it was observed that the minimum distance method and the proposed methodology provide similar results, in this case, only the novel approach is considered for both types of profile. Due to the curve negotiation, the dynamic simulations present flange contact and, therefore, multiple contact points occur several times for both cases.

For this application example, the contact in the right wheel of the leading wheelset of the front bogie is analyzed in detail, because it is the external wheel relatively to the curve where the flange contact occurs. Thus, Figure 6.15(a) and Figure 6.16(a) display the location of the center of the several contact patches in

the wheel profile over time for both modified and actual profiles, respectively. The remaining subplots represent the location and shape of the contact patches for some specific moments.

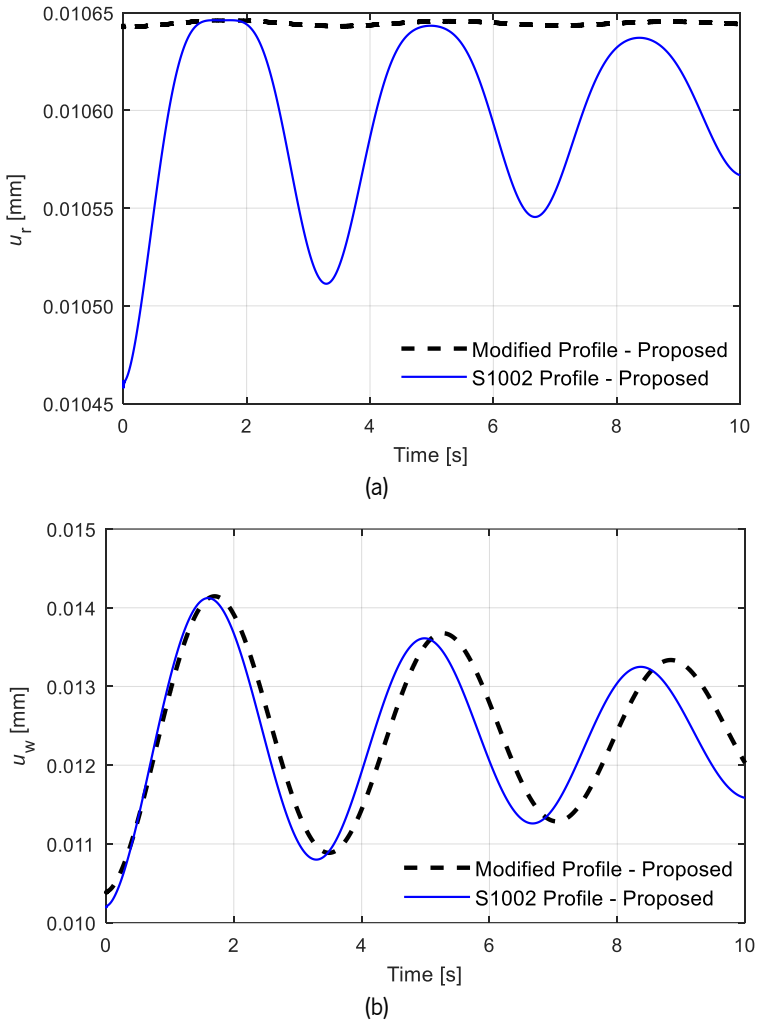

Figure 6.14 – Location of the contact point in the left wheel of the leading wheelset using modified and real profiles for the bogie running on a tangent track: (a) lateral rail coordinate and (b) lateral wheel coordinate.

Relatively to the simulation with a wheel simplified profile, since the wheel tread and wheel flange are considered as two independent convex surfaces, it can be observed that at most one contact can occur in each of these segments. The flange contact occurs uninterruptedly during the curve negotiation, it is initiated at 5.2 s and ends at 37.1 s, as demonstrated in Figure 6.15(a). Although a constant location on the wheel profile is observed, its normal force magnitude suffers some variations on the initial and final stages of the flange contact due to the transition curves. These variations can be demonstrated by the different sizes of the contact ellipses in the beginning, Figure 6.15 (c), middle, Figure 6.15 (d), and end, Figure 6.15(e), of flange contact. It must be noted that, before and after the curve negotiation, there is only one contact in the wheel tread and, therefore, the vehicle exhibits a hunting motion which is not constrained by the wheel flange.

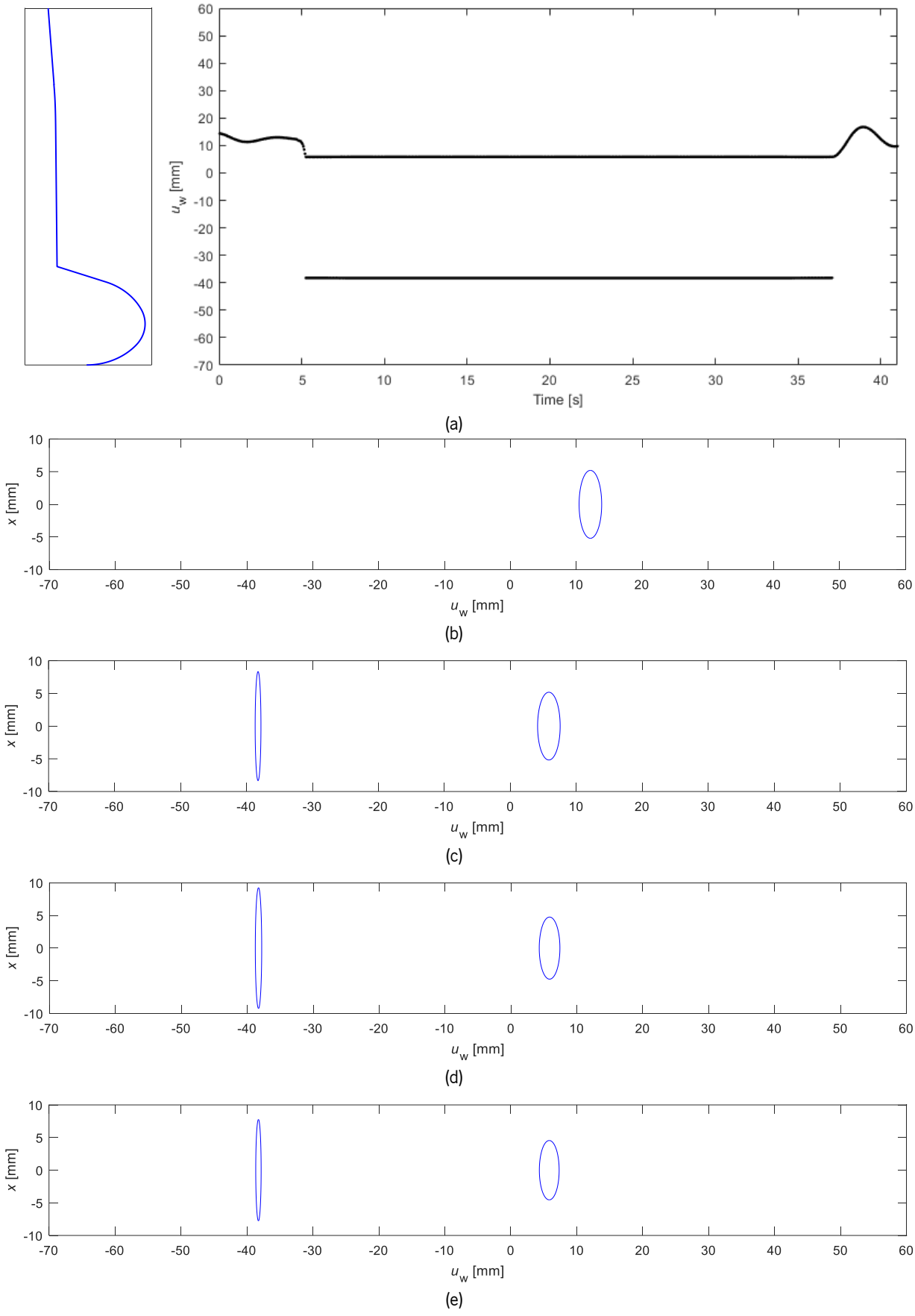

Figure 6.15 – Representation of (a) the location of the main point of contact for each patch over time and shape of the contact patches for (b) $t = 1$ s (c) $t = 6$ s (d) $t = 20$ s and (e) $t = 36.4$ s for the right wheel of the leading wheelset of the front bogie considering the modified wheel profile and Hertzian approach.

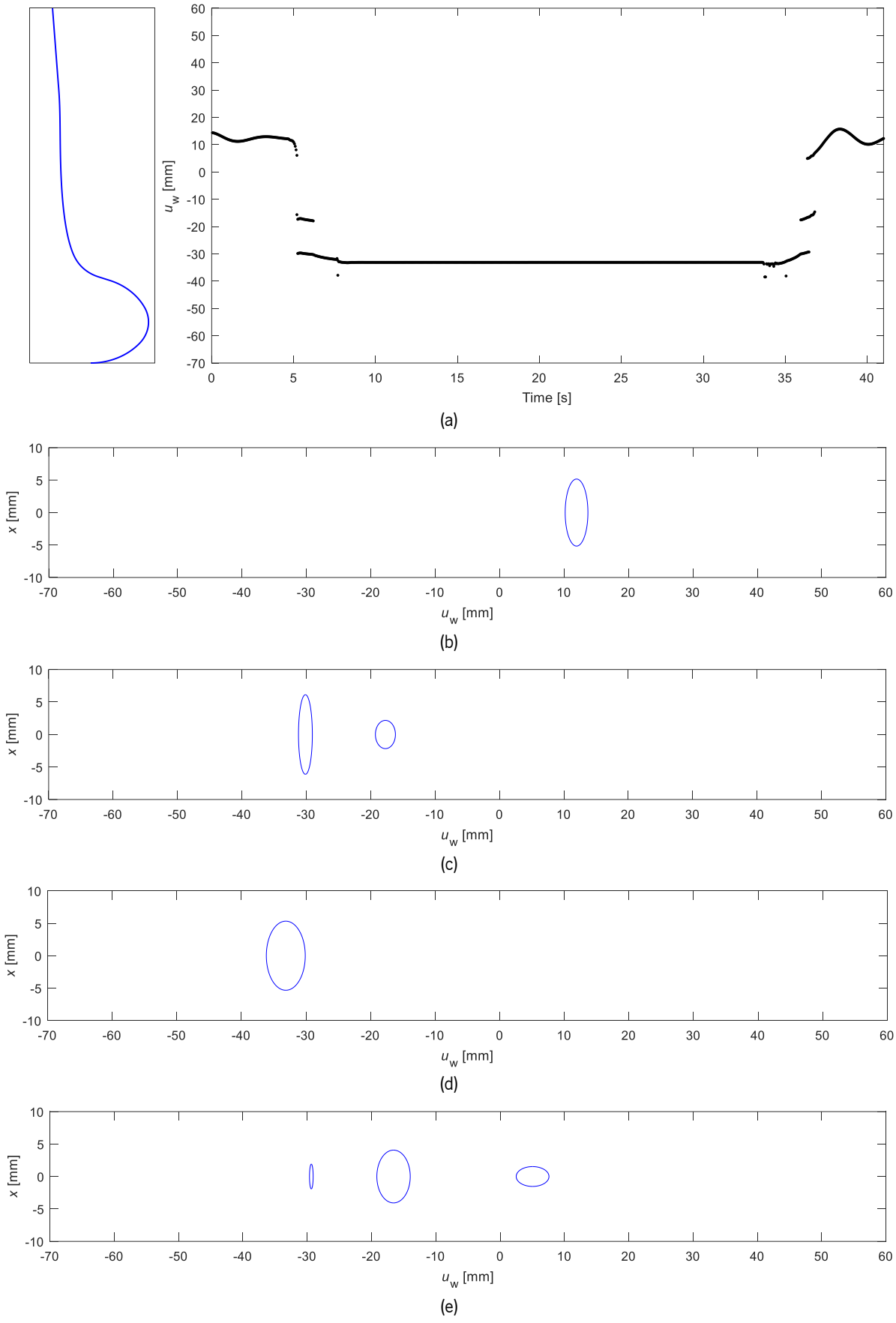

Figure 6.16 – Representation of (a) the location of the main point of contact for each patch over time and shape of the contact patches for (b) $t = 1$ s (c) $t = 6$ s (d) $t = 20$ s and (e) $t = 36.4$ s for the right wheel of the leading wheelset of the front bogie considering the S1002 wheel profile and Hertzian approach.

In what concerns to the simulation of the trailer vehicle negotiating a curve with a realistic wheel profiles, it is shown that the contact is not treated independently in the wheel tread and wheel flange. One of the major differences, when compared to the previous case, is that, during most of the curve negotiation, only one contact patch exists, which is in the transition zone with negative curvature, as represented in Figure 6.16(a) and Figure 6.16(d). For this case, the curve negotiation starts approximately at the same instant, i.e., 5.2 s, and it ends slightly sooner at 36.5 s. Moreover, the proposed methodology demonstrates the capability to detect multiple contacts at the same type for one wheel-rail pair. This is verified either in the initial or final phase of the curve negotiation, as shown in Figure 6.16(c) and Figure 6.16(e), respectively. It must be highlighted that, in the latter case, even three different contact patches are detected at the same time. Overall, the contact detection in the wheel transition zone corroborates the importance of considering the actual wheel profiles. This significantly affects both the shape of the contact patch and vehicle dynamics.

Table 6.5 – Computational time ratio for the three scenarios tested

Simulation	Modified Wheel Profile Minimum Distance Method	Modified Wheel Profile Proposed Method	S1002 Wheel Profile Proposed Method
Wheelset	1.00	2.39	2.41
Bogie	1.00	2.37	2.40
Vehicle	1.00	2.11	2.21

In terms of computational efficiency, the ratio of CPU time for the three simulation scenarios is presented in Table 6.5. As expected, the minimum distance method is the most efficient approach, since it takes advantage of being only applied to pairs of convex surfaces. In turn, for the same wheel profile, the computational cost is more than two times higher for the proposed contact detection methodology. Moreover, the use of a real wheel profile with concave zone slightly increases the computational effort of simulation with respect to that of using a simplified profile. It must be noted that, in the simulation of the full vehicle, the CPU time ratio for the proposed methodology is lower since the importance of contact detection in the whole simulation is also lower due to vehicle modeling. Moreover, the simulation time is affected by the algorithms and corresponding parameters employed for solving the nonlinear equations and optimization problems, these aspects can be a source of improvement.

6.4. Contact Force Model Assessment

In this section, the main goal is to verify the suitability and robustness of the contact force model developed in Chapter 4, in which the contact patch is contained in a curved surface, and the enhanced

LuT strategy provided in Chapter 5 to evaluate the creep forces. The three scenarios described are tested with the S1002 wheel profile. For the normal contact model, it is employed the non-Hertzian curved contact approach combined with the SZG model which had demonstrated to have better performance in the static cases tested. Regarding the tangential or creep forces, two methodologies are compared, namely the Polach method and the KBTNH, which consider an elliptical contact and a simple double-elliptical contact, respectively. To apply these methodologies, it is mandatory to regularize the contact patch obtained with the normal contact model. For the SDEC region, according to Figure 5.3, Eqs. (5.6)-(5.8) are employed to find the semi-axes, a and b, and the deviation from the region's center, y_0. In the case of an elliptical contact, only the semi-axes need to be computed, therefore, only two equations are required. Thus, to keep the contact patch width and area, the following equations are applied

$$a = \frac{2A_{cp}}{\pi\left(W_1 + W_2\right)} \tag{6.1}$$

$$b = \frac{W_1 + W_2}{2} \tag{6.2}$$

This comparison allows to evaluate the utilization of a non-Hertzian approach in the computation of creep forces. Regarding the LuT approach, it is used the KBTNH proposed in section 5.4.2, which showed improved accuracy after rearranging the location of LuT points. For the normal contact model, the penetration correction factor (ε) is 0.55 and the approximated width of the strips (Δs_0) is 0.1 mm, as defined in Chapter 4.

First, the case of a single wheelset running on a tangent track is studied, and Figure 6.17 shows its lateral motion using both Polach and KBTNH methods to evaluate the creep forces. From the analysis of this figure, it seems that, for this example, the wheelset displays similar motion with respect to the results presented in Figure 6.9 in which a Hertzian contact model is applied in the normal contact. In what concerns to the influence of the methodology used to compute the creep force, it is observed that the use of KBTNH slightly increases the oscillation magnitude and frequency.

In this example, only one contact patch is found for the whole simulation, which is already expected since the contact occurs always in the wheel tread and the normal force is low due to the weight of the wheelset. As in the previous section, the results are provided only after one second of simulation, since the motion starts without contact and the impact of the wheelset on the rails provide large contact forces with high frequency that are just numerical artifacts. Thus, the normal contact force on the contact patch of the left wheel is plotted in Figure 6.18, and both curves show identical behavior since the creep

force does not influence the normal force computation. From the analysis of these curves, it is observed the existence of some noise on the results, as can be verified with a magnified view. The reason behind these oscillations on the normal force relies on the discontinuities that arrive from the use of a methodology based on strips which consist on a discretization of the contact region. Although Eqs. (4.72) and (4.73) are used to correct the width of the first and last strips, respectively, which effectively smooths the variation of contact patch's width, as shown in Figure 6.19(a), the normal force still shows discontinuities. This occurs when the number of strips, given by Eq. (4.60), changes due to the increase or decrease of the interpenetration region, which disposes the strips in slightly different positions and, therefore, influences the evaluation of their length. This variation ultimately affects the calculation of the contact patch area, as demonstrated in Figure 6.19(b). It must be noted that the oscillation of contact area depicted in the magnified view of Figure 6.19(b) represents only 0.10%, and corresponds to the fluctuation of normal force magnitude of approximately 0.07% displayed in Figure 6.18. After this shift of normal force, there is an oscillatory behavior of the force in order to achieve anew the vertical equilibrium. The normal force oscillation due to these discontinuities is short being its influence on the wheelset motion negligible. In this simulation, the normal load is extremely small which, in turn, reduces the size of the contact patch. Therefore, this problem exhibits lower prevalence in case of simulating the bogie and the full vehicle, since larger contact areas are expected. Moreover, the magnitude of these variations can be mitigated by reducing the strips' width, although it, consequently, increases the computational effort.

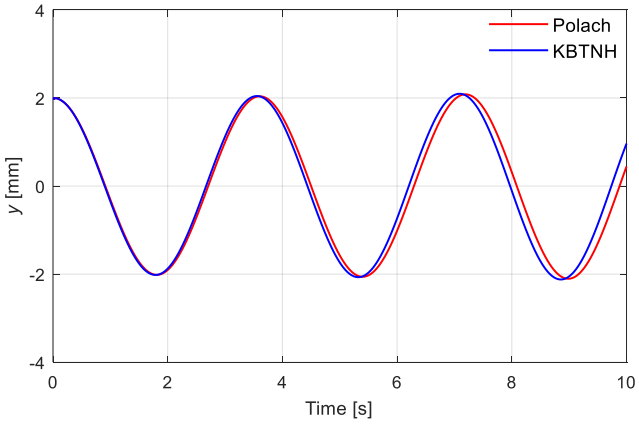

Figure 6.17 – Lateral position of the wheelset using a curved contact patch with both Polach and KBTNH methods for the case of a single wheelset running on a tangent track.

Figure 6.20 displays the lateral creep forces evaluated with both Polach and KBTNH methods, which shows that the oscillations of normal force resonate on the calculation of creep forces, as would be expected. Furthermore, the KBTNH presents higher lateral creep forces which shows the importance

of using a non-Hertzian approach to capture this aspect. Thus, the higher level of creep forces explains the higher frequency of hunting motion exhibited in Figure 6.17.

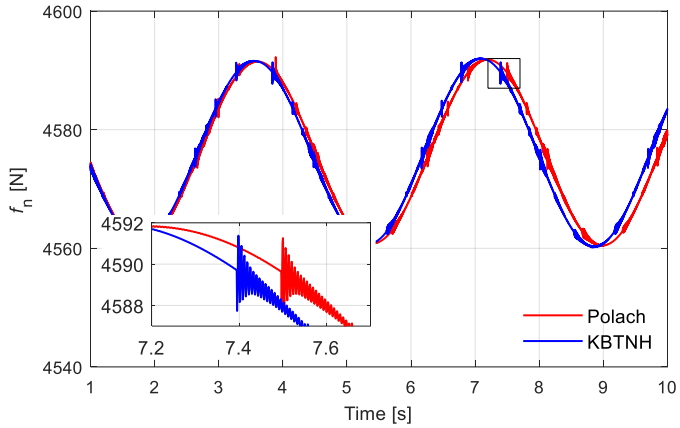

Figure 6.18 – Normal force magnitude in the left wheel using a curved contact patch with both Polach and KBTNH methods for the case of a single wheelset running on a tangent track.

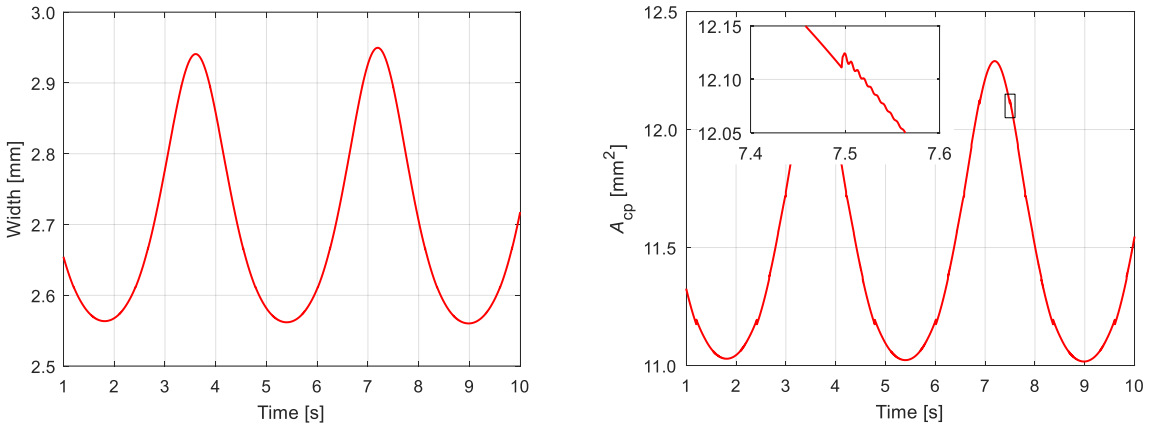

Figure 6.19 – Characteristics of the contact patch on the left wheel using a curved contact with Polach method for the case of a single wheelset running on a tangent track: (a) Width, and (b) Area.

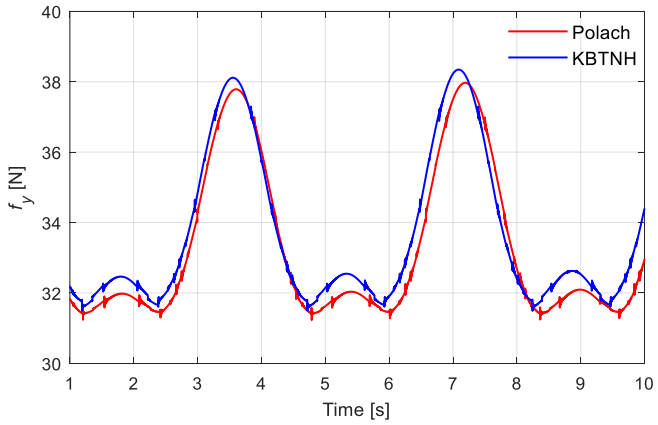

Figure 6.20 – Lateral creep forces computed with both Polach and KBTNH methods on the left wheel for the case of a single wheelset running on a tangent track.

The bogie system running on a tangent track is also used to evaluate the performance of the contact force models. Figure 6.21 depicts the lateral position of the leading wheelset, in which the simulation with KBTNH shows higher frequency than using Polach method and corroborates the results obtained in the previous case. Also, the KBTNH methodology produces larger oscillations, which seems to decrease the critical velocity of the system.

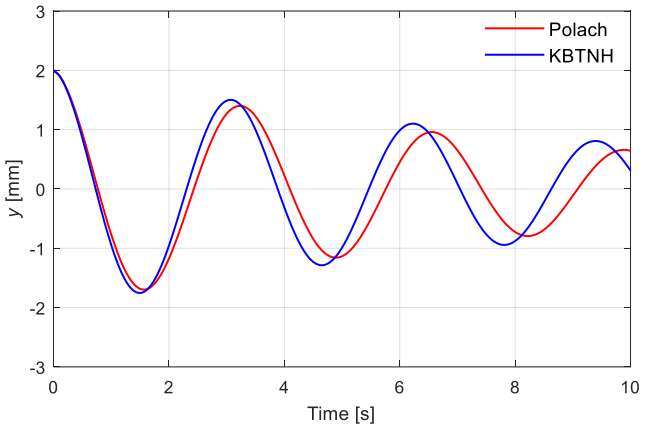

Figure 6.21 – Lateral position of the leading wheelset using a curved contact patch with both Polach and KBTNH methods for the case of a bogie system running on a tangent track.

As in the previous case, since the bogie runs in a straight track without irregularities under its critical velocity, the contact always occurs on the wheel tread with only one contact patch for each wheel-rail pair. The left wheel of the leading wheelset is used to analyze the evolution of the contact forces, therefore, the normal force magnitude is plotted in Figure 6.22. The variation of normal force for each simulation corresponds to the wheelset's motion displayed in Figure 6.21. The discontinuities of the normal force due to the discretization of the contact patch into strips are also identified, however, in this case, as the average normal load is higher, these fluctuations have lower significance and represent approximately 0.04% of the total force.

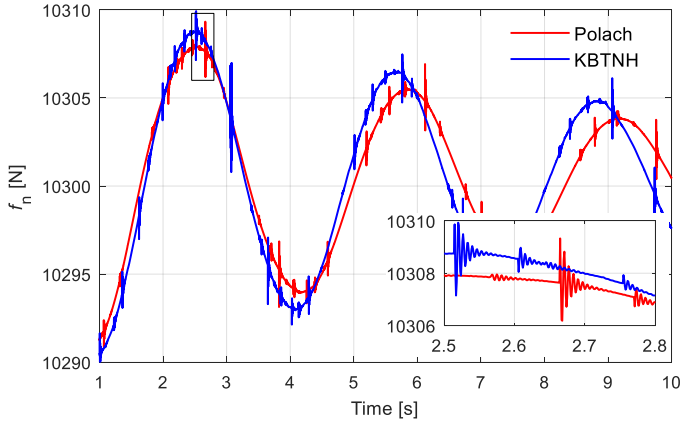

Figure 6.22 – Normal force magnitude on the left wheel of the leading wheelset using a curved contact patch with both Polach and KBTNH methods for the case of a bogie system running on a tangent track.

The lateral and longitudinal creep forces evaluated with both methods are provided in Figure 6.23 and Figure 6.24, respectively. Again, KBTNH produced larger lateral forces which promotes the lateral oscillation of the system. Regarding the longitudinal forces, Figure 6.24 shows similar values with both strategies. It must be noted that, in these results, the influence of the discontinuities in the normal force are almost imperceptible, since the creep forces presents a higher variation of magnitude when compared to the normal force. Furthermore, in the magnified views, it is verified that the discontinuities are more noticeable for the KBTNH method due its nature and the existence of interpolations.

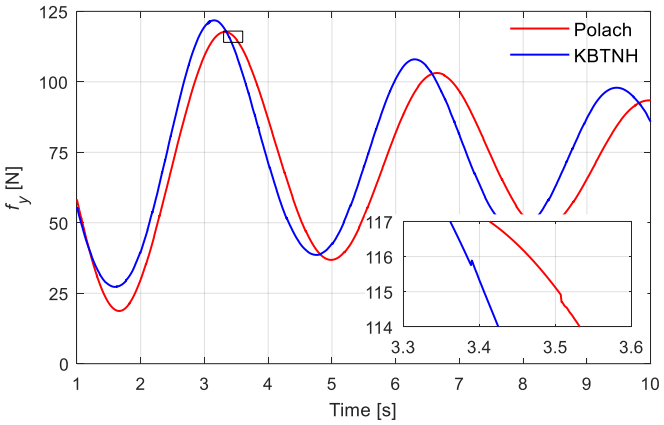

Figure 6.23 – Lateral creep forces computed with both Polach and KBTNH methods on the left wheel of the leading wheelset for the case of a bogie system running on a tangent track.

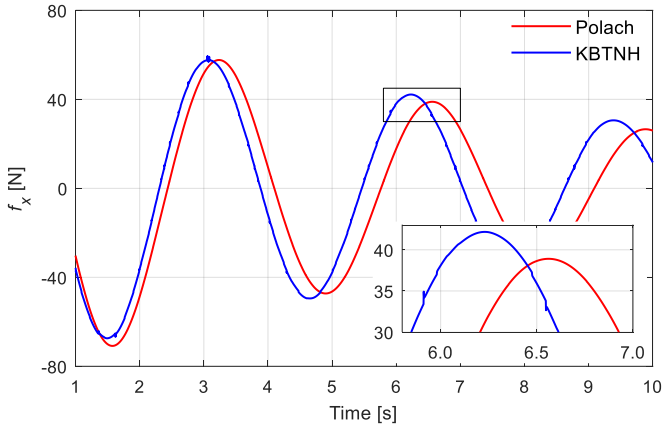

Figure 6.24 – Longitudinal creep forces computed with both Polach and KBTNH methods on the left wheel of the leading wheelset for the case of a bogie system running on a tangent track.

One strategy to verify the suitability of this LuT for the computation of the creep forces in the simulations performed consists of checking whether the limits of the domain were reached and, therefore, if the creep forces are properly evaluated. The values of the LuT's input variables are plotted in Figure 6.25. Due to symmetry properties (Magalhães et al., 2020), only some of the boundaries of the domain may need to be extended, i.e., the parametrized spin creepage and the parametrized creepage modulus

can only have positive values and the creepage angles already covers the whole possible domain. The values displayed in Figure 6.25 are far from the boundaries of the LuT defined in Chapter 5, and, therefore, the KBTNH seems appropriate for the conditions simulated.

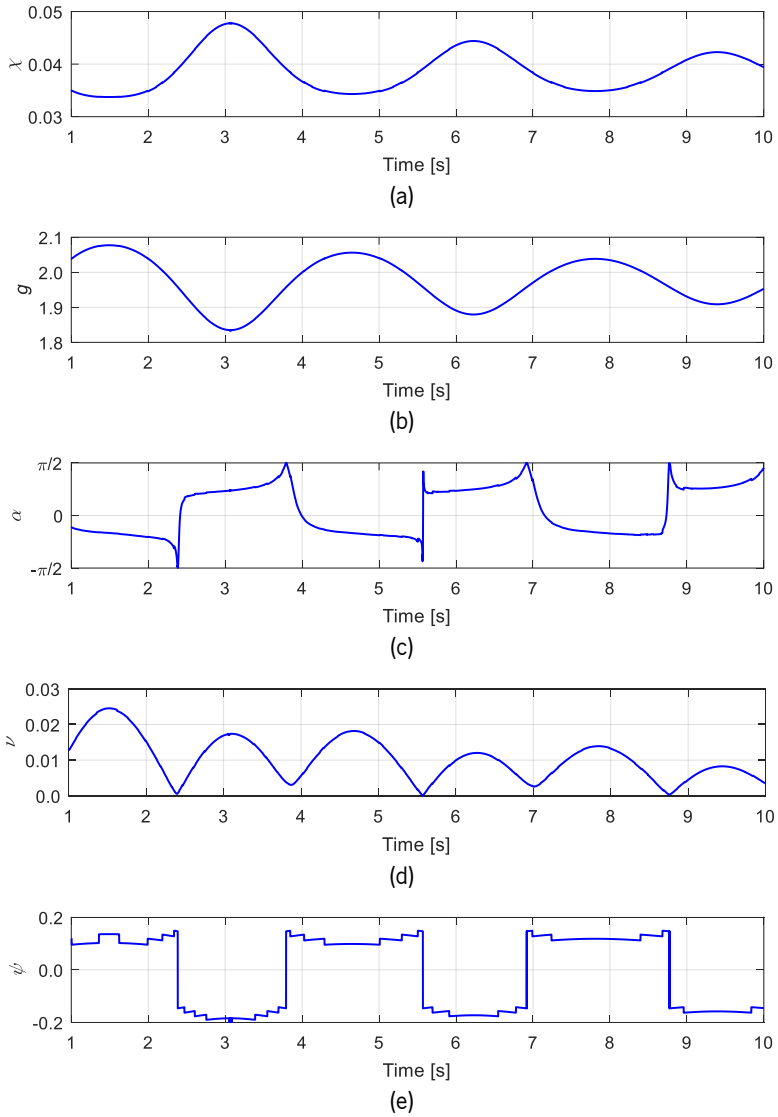

Figure 6.25 – Inputs of KBTNH in the contact of the left wheel of the leading wheelset for the case of a bogie system running on a tangent track. (a) parametrized spin creepage; (b) semi-axes ratio; (c) creepage angle; (d) parametrized creepage modulus; and (e) shape number.

In the last application example, the trailer vehicle described in section 6.1 negotiating a left curve, the contact is again analyzed in detail in the right wheel of the leading wheelset of the front bogie, since it is external with respect to the curve and experiences flange contact. Figure 6.26 and Figure 6.27 present the location of the several contact patches on the wheel profile during the whole simulation using Polach and KBTNH methods, respectively.

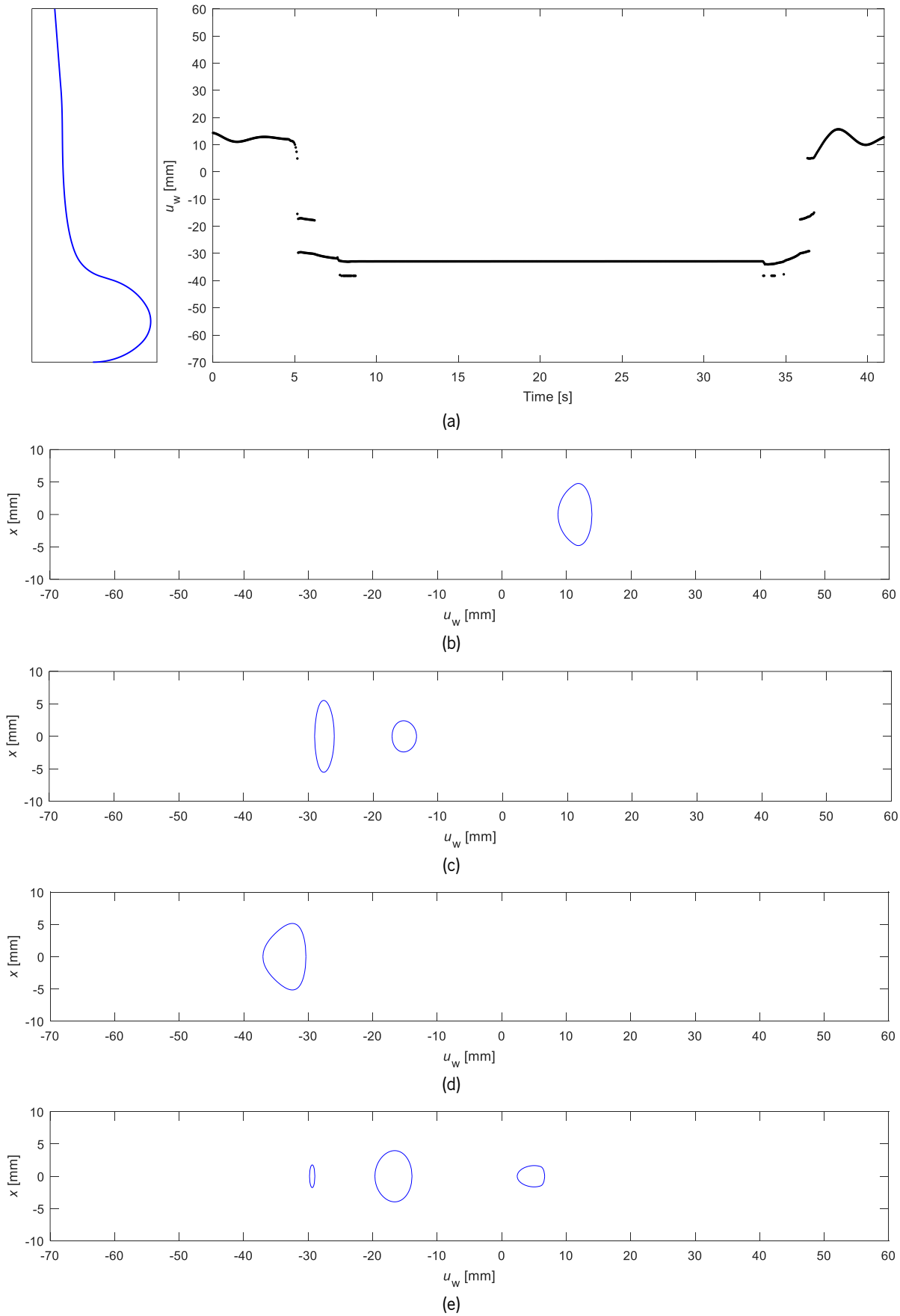

Figure 6.26 – Representation of (a) the location of the main point of contact for each patch over time and shape of the contact patches for (b) $t = 1$ s (c) $t = 6$ s (d) $t = 20$ s and (e) $t = 36.4$ s for the right wheel of the leading wheelset of the front bogie considering the non-Hertzian curved contact and Polach method.

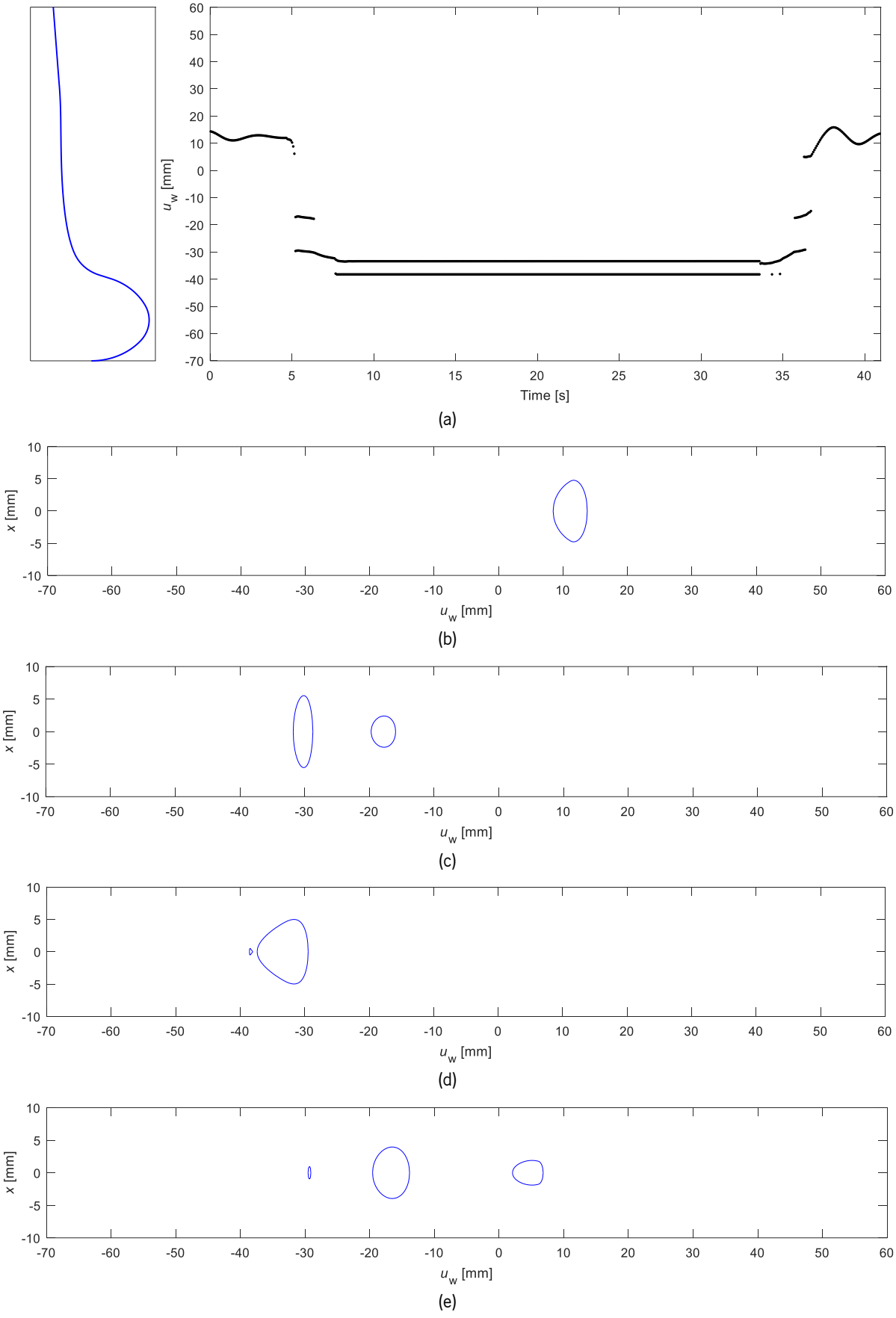

Figure 6.27 – Representation of (a) the location of the main point of contact for each patch over time and shape of the contact patches for (b) $t = 1$ s (c) $t = 6$ s (d) $t = 20$ s and (e) $t = 36.4$ s for the right wheel of the leading wheelset of the front bogie considering the non-Hertzian curved contact and KBTNH.

From the results obtained, it is possible to conclude that the location of contact patches achieved with the curved non-Hertzian patch and Polach method is similar to the one reached with the Hertzian contact model and presented in Figure 6.16. The main exception deals with cases in which, within the same interpenetration region, more than one patch is identified, since this aspect is not possible to capture in the Hertzian approach. In terms of number of contact patches, Figure 6.26(a) demonstrates that most of the time just one patch is identified. However, during the transition curves, multiple contact patches are identified simultaneously, as depicted Figure 6.26(c) and Figure 6.26(e). As in the previous analysis, the shape of the contact patches is displayed in four different moments, namely in the straight zone, in the transition curve before the curve, during the curve negotiation and in the transition curve after the curve. Although some of the contact patches resembles an elliptical shape, as in Figure 6.26(c), most of them shows significant differences, which demonstrates again the importance of using non-Hertzian approaches.

The outcomes of the simulation with KBTNH method exhibit some differences, mainly during the curve negotiation, since in this period two patches are identified, as illustrated in Figure 6.27(d). It must be noted that this difference results from the appearance of an additional contact patch inside the same interference region. Regarding the shape of the captured contact areas, they show a good suitability to be regularized with a SDEC region and, therefore, to apply KBTNH for the creep forces calculations.

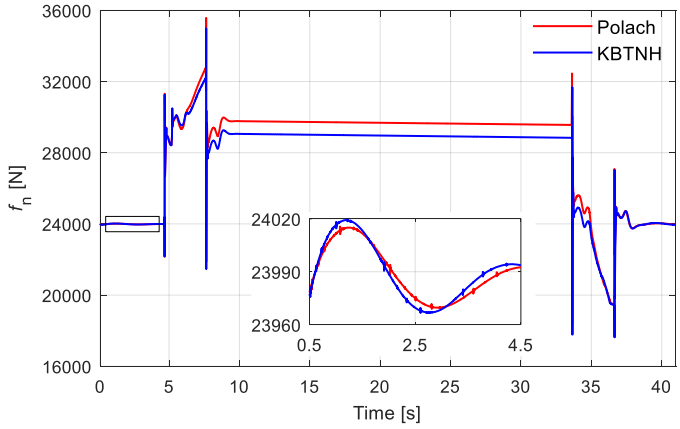

Figure 6.28 – Normal force magnitude on the right wheel of the leading wheelset of the front bogie using a curved contact patch with both Polach and KBTNH methods for the case of a trailer vehicle running on a curved track.

In order to compare the simulation with both methods, the sum of the normal force magnitude in all patches for each time-step is displayed in Figure 6.28. Although the same methodology is used to calculate the normal load, different results are obtained, since the creep forces significantly influence the motion of the vehicle. Figure 6.28 demonstrates that the main differences occur during curve negotiation,

when the simulation with Polach method shows a higher normal load. Moreover, in the beginning and end of the simulation, there are some discrepancies between both cases, as can be depicted in the magnified view in Figure 6.28. In this plot, it is possible to observe that those differences are in same order of magnitude of the ones obtained in the scenarios previously analyzed, namely with a single wheelset and bogie system. In these simulations, it becomes clearer that the discontinuities produced by the normal force model are not significant when compared with the overall contact forces.

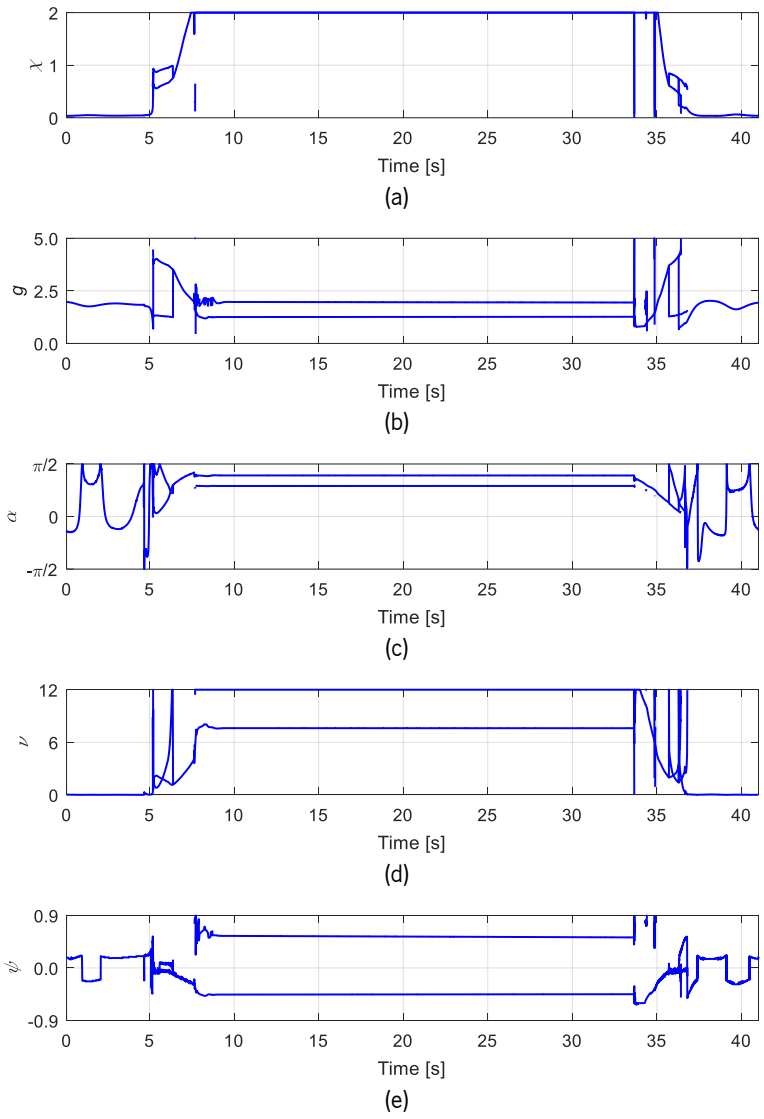

Figure 6.29 – Inputs of KBTNH in the contact of the right wheel of the leading wheelset of the front bogie for the case of a trailer vehicle running on a curved track. (a) parametrized spin creepage; (b) semi-axes ratio; (c) creepage angle; (d) parametrized creepage modulus; and (e) shape number.

The inputs of the KBTNH are analyzed again, since this case involves a more diverse range of contact scenarios. Figure 6.29 presents the values of parametrized spin creepage, semi-axes ratio, creepage angle, parametrized creepage modulus and shape number for all contact patches identified on

the right wheel of the leading wheelset of the front bogie. It must be noted that more than one value is displayed for each input variable, since several contact patches can be determined at the same instant. From the analysis of this results, it can be concluded that some of these variables reach the limits of the LuT during the curve negotiation, mainly the parametrized spin creepage and parametrized creepage modulus. The contact occurs near the wheel's flange, where the contact angle is noticeably higher than in the wheel's tread and, in this way, the longitudinal and spin creepage tend to increase. The remaining input variables seem to behave within the LuT boundaries, although the semi-axes ratio occasionally reaches its upper limit. Hence, the KBTNH needs to be extended to deal properly with flange contact.

6.5. Summary and Conclusions

The present chapter is devoted to the multibody simulations of railway vehicles, which are of paramount importance to demonstrate the effectiveness of the numerical methodologies developed in the previous chapters. In this context, the multibody model of a trailer vehicle of the Lisbon subway network is described in detail to be used as example of application. The inertia parameters, the location of the connection points and the properties of the suspension elements are properly characterized. Moreover, three different scenarios are used to verify the methodologies for contact detection and force evaluation, namely a single wheelset running on a tangent track, a single bogie running on a tangent track and a trailer vehicle running on a curved track.

The contact detection approach proposed in Chapter 3 is assessed through the comparison with the minimum distance method. For that purpose, a simplified wheel profile, in which the transition between tread and flange is removed so the surfaces become fully convex, and the real wheel profile are used in the dynamic simulations. A Hertzian contact model with damping is employed to calculate the normal forces, and the Polach method, which also considers an elliptical contact, is applied to compute the creep forces. In the simulations with a wheel simplified profile, the minimum distance method and the proposed method produce the same results, either for the bodies' kinematics and for the contact forces. This demonstrates that the proposed approach can suitably replace the minimum distance method to search for the contact between the wheel and rail. On the other hand, the use of the methodology proposed, with the real and simplified profiles, exhibits significant discrepancies, namely in what concerns to the motion of the vehicle and location of the contact points on both profiles. Although the use of the methodology proposed shows to be approximately two times slower than the minimum

distance method, and without allowing the study of local contact phenomena, the use of simplified wheel profiles leads to unacceptable results in terms of vehicle dynamics.

The calculation of both normal and creep forces is also assessed in this chapter through dynamic simulations. In this case, only the real wheel profile is considered, and the non-Hertzian approach described in Chapter 4, which assumes a curved contact area, is used. The curved contact approach combined with SZG method is selected for this analysis due to the positive performance demonstrated on the static cases. Moreover, the KBTNH strategy to compute the creep forces, detailed in Chapter 5, is also tested and compared against Polach method in the context of dynamic simulations. This LuT approach allows to regularize the contact patch into a non-Hertzian shape which provides a better agreement between the normal and tangential contact force models. From the simulations performed, the results show that the use of Polach and KBTNH methods provides significantly different dynamic response of the system. The domain of the LuT is analyzed in terms of the values employed during the simulations. Although it behaves well for the tangent track simulations, in the curve negotiation, due to flange contact, the creepage modulus and spin creepages exceed the upper boundary of the LuT. This fact clearly suggests that the KBTNH domain must be extended for both the original and for the enhanced tables proposed in this work. Furthermore, the utilization of a non-Hertzian approach to determine the contact patches, allows to identify several contact areas within the same interference region. The shapes of the contact patches obtained in different moments of the simulations show substantial differences with respect to the ones obtained with Hertzian approach, and they resemble the regularization to the SDEC region.

This page is intentionally left blank.

"*No intelligent idea can gain general acceptance unless some stupidity is mixed in with it.*"
Fernando Pessoa

7. CONCLUDING REMARKS

7.1. Conclusions

A comprehensive study on the computational modeling of the contact interaction between wheel and rail in the context of vehicle dynamics simulation has been presented in this thesis. Several aspects, such as vehicle modeling, surfaces definition, contact detection, pressure distribution or forces calculation, were discussed throughout this work, several novel methods and approaches were proposed in the process, being the main conclusions emphasized in this section.

The literature on the most relevant issues on vehicle-track dynamic interaction was revisited in Chapter 2. In this work, the dynamic analysis of railway vehicles is performed recurring to multibody dynamics formulation, using Cartesian coordinates and equations of motion based on the Newton-Euler method. This methodology produces the system's equations of motion by gathering the Newton-Euler equations with the accelerations constraint equations. Moreover, to avoid the violation of constraints at position and velocity levels arising from the integration process, the Baumgarte stabilization technique is used. Regarding the modeling of a railway vehicle, it is treated as collection of rigid bodies which are connected by kinematic constraints and force elements. Although, in some cases, it is required to develop more complex modeling strategies to mimic the real behavior of the connection components, since this work focus on the wheel-rail interaction, the nonlinearity of the connection elements is limited to the minimum when used to model the primary and secondary suspensions of the vehicle. In what concerns to the track modeling, a fully rigid track is considered, in which each rail path is defined independently. It is recognized that several methodologies have been developed to introduce flexibility into the track structure being their influence in the vehicle response demonstrated in the literature. In what concerns to the geometric definition of the contacting surfaces, the modeling strategies had evolved from simple analytical curves to complex and realistic profiles. Generally, the wheel and rail profiles can be defined as a set of points to be interpolated being their three-dimensional surfaces obtained through the sweep of

the profile of a cross-section along a prescribed path, for the rail, and through a revolution of the profile about the axis, for the wheel. A new, or unused, rail profile has always a convex shape, in turn, the wheel presents a concave zone in the transition between the tread and flange, which is sometimes neglected in the wheel-rail interaction modeling for sake of simplicity of the contact detection. Thus, the main strategies to search for the contact points were also briefly discussed in Chapter 2, namely the algebraic approaches and nodal search method, which can be used either online or with precomputed Lookup Tables, which are interpolated linearly. Then, the most relevant contact force models developed or used in the context of wheel-rail interaction were described in that Chapter. These methods usually assume that the bodies deform locally and produce a contact patch where normal pressure distribution and tangential tractions develop. The available methods were initially based on the Hertzian elastic contact theory, in which the contact area assumes an elliptical shape. Later, more advanced models allowed to find non-Hertzian contact patches and capture more accurately the contact phenomena. Finally, the usage of Lookup Tables for the acceleration of computational programs was examined, and the existing approaches in the context of railway vehicles dynamics were discussed.

A methodology to deal with the contact detection between wheel and rail parametric surfaces is presented in Chapter 3. The profiles can be described either by a set of points interpolated through splines or analytical functions, and the location of any point on each contacting surface is defined by two parameters. A point on the wheel surface is characterized by the lateral and angular coordinates, while, on the rail, it is specified through the lateral and longitudinal coordinates. The longitudinal and lateral curvatures, the longitudinal and lateral tangential vectors and the normal vector are also parametrized for both surfaces. The wheel concave zone is ignored by many authors, since this modeling strategy allows the contact search between convex surfaces which expedites this process and avoids some numerical problems. This simplification of the wheel profile description is explored and compared with the actual wheel profiles. It is shown that the minimum distance method, which is largely used to search contact between convex surfaces, does not behave well when used to find the contact points in the wheel transition zone. There is not a well-defined minimum for the contact equations. The methodology proposed here deals with this problem by searching independently the contact between each wheel lateral position, a circumference, and the rail, a convex surface. In this approach, the rail is considered locally straight to reduce the number of contact equations, and the wheel profile is projected onto the rail cross-section. In this way, multiple contact patches can be found simultaneously from the wheel and rail

interaction. In each interpenetration region, the locations of the main contact points are obtained through the resolution of an optimization problem in which the penetration between profiles is maximized.

Although the methodology proposed to find the contact points requires the solution of the contact conditions for each wheel strip separately to find the strip with highest penetration, instead of solving directly the contact between the two surfaces, it allows the use of actual wheel profiles which enhances significantly the accuracy of the results obtained in more demanding conditions. This computational approach was verified in the context of railway dynamics simulations, and the results are displayed in chapter 6. A single wheelset running on a tangent track, a bogie system running on tangent track and trailer vehicle running on curved track are used as application examples. In these simulations, the S1002 and UIC50 are used as wheel and rail profiles, respectively, and a 1:20 rail cant is considered. Both the minimum distance method and the proposed approach present equivalent results using the wheel simplified profile, which proves that the proposed approach can be used without any concern for the contact detection between wheel and rail surfaces. The simulations with the simplified wheel profile are compared against those with the actual profile, and the results demonstrate significant discrepancies. The use of real wheel profiles produces a higher oscillation frequency for the hunting motion of the wheelset and bogie simulations. Furthermore, analyzing the leading wheel external to the curve in the vehicle simulation, it is clear that, during the curve negotiation, the contact occurs in the wheel transition zone which is not modeled in the simplified profile. Therefore, the location and shape of contact patches is completely different for both cases, which demonstrates that, although the use of simplified wheel profiles reduces the simulation time, it produces inaccurate results when the contact occurs in the transition zone.

The contact interaction between two different bodies consists in a complex phenomenon which in the case of the wheel and rail, since the bodies are made of steel, can be treated as contact between rigid bodies. However, their contact leads to highly concentrated normal pressures which forces the bodies to deform locally. Based on this concept, it is possible to use the elastic approach to determine the shape of the contact area and the normal pressure distribution. In Chapter 4, several methodologies to compute the geometry of the contact patch and normal force are discussed and a curved contact patch approach is proposed. The Hertzian approach assumes an elliptical planar contact patch being its size calculated solely based on the characteristics of the main contact points, namely on their curvatures. In order to determine more accurately the shape of the contact area, more advanced models can be employed. The use of semi-Hertzian methodologies, in which the contact pressure is elliptical in the

longitudinal direction and has an arbitrary variation in the lateral direction, is detailed. Typically, the patch is discretized into lateral strips and the penetration is evaluated along the lateral direction to determine the length of each strip. Moreover, the contact area is assumed planar and its normal direction coincides with the normal vector on the main contact points. This is a suitable assumption when the contacting surfaces are convex, however, when negotiating narrow curves or in the presence of worn profiles, the contact might occur in concave regions and, therefore, the use of planar contact patch is not reasonable. A numerical methodology for the conformal contact modeling, in which the contact patch is contained in a curved surface is proposed here. The undeformed profiles inside the interpenetration region are divided in equally spaced points, and these points are used to determine a middle curve between both profiles in which the patch is comprehended. In this patch, the normal direction changes along this curve, and the penetration is measured through that direction. The normal pressure distribution is evaluated with KP method and SZG method. The latter does not depend on the location of the main point of contact to compute the normal load, however, it is significantly slower.

The curved contact patch strategy developed here was assessed and verified through the comparison with the planar assumption and the Hertzian approach. Several wheel-rail static contact cases were selected to compare these methodologies. The results exhibited considerable differences between the Hertzian and non-Hertzian approaches, either in terms of contact patch size and of maximum normal pressure. Regarding both planar and curved non-Hertzian models, they showed identical results when the contact is identified in the wheel tread in a single contact patch. However, when the contact takes place in the wheel running fillet, some differences are identified. These differences tend to be more relevant when the normal load increases, since the size of the contact patch also increases. Finally, the modeling approaches were investigated in the presence of two similar maxima of the penetration function. In such case, with a slight variation of the wheel-rail relative position, the main point of contact change from one maximum to the other. The results indicated that only the use of the curved contact approach combined with SZG model allows to avoid a normal force discontinuity, either the contact occurs on the wheel tread or in the running fillet. It must be emphasized that the existence of a normal force discontinuity in these situations is not reasonable.

Most of the methods available to calculate the wheel-rail creep forces assume the Hertzian simplification or require a large computation burden for a dynamic simulation. A LuT strategy which regularizes a non-Hertzian contact patch is employed here, namely the KBTNH which considers a simple double-elliptical contact region and requires five input parameters, i.e., the parametrized spin creepage,

semi-axes ratio, creepage angle, parametrized creepage modulus and shape number. The values of creep forces stored in this table are calculated recurring to CONTACT software, deemed as being the accurate evaluation of the contact characteristics, for each point of the domain. Although the LuT approach reduces comprehensively the computation time, it introduces interpolation errors due to the parameters discretization. A strategy to assess the interpolation error of a given LuT with multiple input parameters was presented in Chapter 5. Three different procedures were used to evaluate the accuracy of the LuT, namely a variation of the input parameters for a randomly selected sample of points, the interpolation error at the center of the cells and the interpolation error at the middle of the edges. Although the center of LuT cells are the farthest locations from the LuT points, they do not allow to identify the source of error since all parameters are interpolated simultaneously. In turn, the assessment of the interpolation error at the middle point of LuT edges enables to estimate which input parameter is the major source of error and, therefore, needs to be refined. Based on this error investigation, the original KBTNH demonstrated potential to be improved, since the level of interpolation error was not uniform for all the input parameters. Thus, to provide an evenly distributed error, the LuT points had to be added, removed and redistributed in some cases. Through these strategies, two enhanced LuTs were developed, one with reduced size but with similar accuracy to the original and another with an approximated size but reduced maximum and mean errors. In the first LuT, the number of points was reduced almost five times and, in the second LuT, the maximum interpolation error was reduced by half.

The methodologies developed for the evaluation of contact forces are also examined through the multibody dynamics simulations of railway systems presented in Chapter 6. The running scenarios used to verify the contact detection methodology are again adopted to examine the utilization of the curved contact patch approach and the KBTNH strategy. The normal contact model produces some discontinuity on the normal force magnitude due the discretization of the interpenetration region into strips, that is, when the number of strips increases or decreases, the location of each strip is slightly adjusted which modifies their penetration. However, it is important to refer that these discontinuities represent less than 0.1% of the normal load and, therefore, can be overlooked. This modeling approach showed contact patches significantly different to the ones obtained with the Hertzian methodology. The enhanced KBTNH with improved accuracy was employed to compute the creep forces and the results were compared with the ones obtained with Polach method. The KBTNH method exhibited higher lateral creep forces, which produces higher oscillation frequency in the hunting motion for the simulations in tangent track. Regarding the input parameters, in the bogie running scenario, all input parameters were far from the domain limits.

However, in the vehicle simulation, during flange contact, the values of creepage modulus and spin creepage exceed the limits of the LuT domain. Thus, the KBTNH domain needs to be extended so it can be properly applied in those situations.

To sum up, this work involved the development of several computational strategies for the contact detection and contact forces evaluation to be applied in the dynamic analysis of railway vehicles. These methodologies allow to predict in a more realistic manner the dynamic response of the vehicle under actual running conditions and were implemented and tested in an in-house MATLAB program for dynamic analysis of multibody systems called MUBODYNA (MUltiBOdy DYNAmics). Also, some dedicated codes were developed for the analysis of static cases of wheel-rail interaction and the evaluation of the accuracy of a given LuT.

7.2. Future Developments

In this work, some aspects regarding the contact modeling between wheel and rail have been investigated, namely in what concerns the surfaces' definition, search for contact points, modeling of conformal contact and Lookup Tables enhancement. Although the methodologies developed constitute advances in the state-of-the-art, further developments are appreciated in order to tackle some of their limitations and extend their applicability. In that sense, some suggestions of future research activities in this field are presented in this section.

The analysis of the contact modeling methodologies proposed in this work can be extended to other simulation cases. For instance, the track structural flexibility and track irregularities can be taken into consideration to examine the robustness of the computational methods. Moreover, different wheel and rail profiles might be utilized, namely wheel worn profiles in which the conformal contact is more prominent.

The methodology proposed to deal with conformal contact assumes that the contact patch is contained in a curved surface and it is symmetrical in the longitudinal direction. Thus, the effect of the yaw angle is not taken into consideration for the identification of the contact patch shape and, consequently, of the normal pressure distribution. A procedure to eliminate the slight discontinuities existent on the normal force magnitude would be welcome and a strategy to improve its numerical efficiency is also desirable since it might be of paramount importance in long-time simulations.

In what concerns the evaluation of the creep forces and tangential tractions, it becomes necessary to develop a contact methodology that agrees with the conformal contact model for normal direction and also considers a curved contact patch. This involves taking into account a variable spin creepage along the contact patch due to the variation of contact angle. Moreover, the tangential model may assume the same strip discretization of the normal contact model.

One of the major motivations to develop more advanced contact model concerns the investigation of wheel damaging phenomena. The use of the contact methodologies developed here to predict wear evolution on wheels or rolling contact fatigue is quite relevant.

The railway turnouts consist of 20% of the global cost of a railway track and, although the vehicles reduce their velocity in those zones, the interruption of wheel guidance leads to significantly higher forces. This tends to reduce the life expectancy of those components and increase their maintenance costs. To study the train behavior properly when passing through switches and crossings, it is necessary to consider a variable rail cross-section and include those characteristics into the contact search algorithm, which, at this moment, assumes a locally straight rail.

Regarding the study of LuT accuracy, a methodology to assess the interpolation error was presented, and two enhanced LuT were proposed based on a trial and error procedure to uniformize the interpolation error. Therefore, the automatic generation of optimal LuT with a pre-defined accuracy and evenly distributed error would improve numerical performance.

This page is intentionally left blank.

"*The more I read, the more I acquire, the more certain I am that I know nothing.*"
Voltaire

REFERENCES

Aceituno, J.F., Urda, P., Briales, E., Escalona, J.L. (2020) Analysis of the two-point wheel-rail contact scenario using the knife-edge-equivalent contact constraint method. *Mechanism and Machine Theory*, 148, 103803.

Aggestam, E., Nielsen, J.C.O., Bolmsvik, R (2018) Simulation of vertical dynamic vehicle–track interaction using a two-dimensional slab track model, *Vehicle System Dynamics*, 56(11), pp. 1633-1657.

Allotta, B., Pugi, L., Malvezzi, M., Bartolini, F., Cangioli, F. (2010). A scaled roller test rig for high-speed vehicles. *Vehicle System Dynamics*, 48(S1), pp. 3-18.

Allotta, B., Meli, E., Ridolfi, A., Rindi, A. (2014). Development of an innovative wheel–rail contact model for the analysis of degraded adhesion in railway systems. *Tribology International*, 69, pp. 128-140.

Alonso, A., Giménez, J.G. (2005). A new method for the solution of the normal contact problem in the dynamic simulation of railway vehicles. *Vehicle System Dynamics*, 43(2), pp. 149-160.

Alonso, A., Giménez, J.G. (2007). Tangential problem solution for nonelliptical contact areas with the FastSim algorithm. *Vehicle System Dynamics*, 45(4), pp. 341-357.

Alves, J., Peixinho, N., Da Silva, M.T., Flores, P., Lankarani, H.M. (2015) A comparative study of the viscoelastic constitutive models for frictionless contact interfaces in solids. *Mechanism and Machine Theory*, 85, pp. 172-188.

Ambrósio, J., Antunes, P., Pombo, J. (2015). On the requirements of interpolating polynomials for path motion constraints. In: Kecskeméthy A., Geu Flores F. (eds) *Interdisciplinary Applications of Kinematics. Mechanisms and Machine Science*, 26, pp. 179-197.

Ambrósio, J., Antunes, M., Santos, G. (2017). Multibody modelling and dynamic analysis of tapered roller bearings. In: Ambrósio, J., et al. (eds.) *EUROMECH Colloquium 578 Rolling Contact Mechanics for Multibody System Dynamics*, Funchal, Madeira, Portugal, pp. 1-29.

Ambrósio, J., Pombo, J. (2018). A unified formulation for mechanical joints with and without clearances/bushings and/or stops in the framework of multibody systems. *Multibody System Dynamics*, 42, pp. 317-345.

Andani, M.T., Peterson, A., Munoz, J., Ahmadian, M. (2016). Railway track irregularity and curvature estimation using doppler LIDAR fiber optics. Proceedings of the Institution of Mechanical Engineers, Part F: Journal of Rail and Rapid Transit, 232(1), pp. 63-72.

Antunes, P., Magalhães, H., Ambrósio, J., Pombo, J., Costa, J. (2019). A co-simulation approach to the wheel–rail contact with flexible railway track. *Multibody System Dynamics*, 45, pp. 245-272.

Antunes, P., Ambrósio, J., Pombo, J., Facchinetti, A. (2020). A new methodology to study the pantograph–catenary dynamics in curved railway tracks. *Vehicle System Dynamics*, 58(3), pp. 425-452.

Ayasse, J.B., Chollet, H. (2005). Determination of the wheel rail contact patch in semi-Hertzian conditions. *Vehicle System Dynamics*, 43(3), pp. 161-172.

Aus, H.M., Korn, G.A. (1969). Table-Lookup/Interpolation Function Generation for Fixed-Point Digital Computations. *IEEE Transactions on Computers*, C-18(8), pp. 745-749.

Bauchau, O.A., Laulusa, A. (2008). Review of contemporary approaches for constraint enforcement in multibody systems. *Journal of Computational and Nonlinear Dynamics*, 3(1), pp. 1-8.

Baumgarte, J. (1972). Stabilization of constraints and integrals of motion in dynamical systems. *Computer Methods in Applied Mechanics and Engineering*, 1(1), pp. 1-16.

Bayo, E., Garcia De Jalon, J., Serna, M.A. (1988). A modified lagrangian formulation for the dynamic analysis of constrained mechanical systems. *Computer Methods in Applied Mechanics and Engineering*, 71(2), pp. 183-195.

Berzeri, M., Sany, J.R., Shabana, A.A. (2000). Curved Track Modeling Using the Absolute Nodal Coordinate Formulation. *Technical Report*, Department of Mechanical Engineering, University of Illinois, Chicago.

Bevan, A., Molyneux-Berry, P., Eickhoff, B., Burstow, M. (2013). Development and validation of a wheel wear and rolling contact fatigue damage model. Wear, 307(1-2), pp. 100-111.

Bezin, Y., Farrington, D., Penny, C., Temple, B., Iwnicki, S. (2010). The dynamic response of slab track constructions and their benefit with respect to conventional ballasted track. *Vehicle System Dynamics*, 48(S1), pp. 175-193.

Bhaskar, A., Johnson, K.L., Wood, G.D., Woodhouse, J. (1997a). Wheel-rail dynamics with closely conformal contact Part 1: Dynamic modelling and stability analysis. *Proceedings of the Institution of Mechanical Engineers, Part F: Journal of Rail and Rapid Transit*, 211(1), pp. 11-26.

Bhaskar, A., Johnson, K.L., Woodhouse, J. (1997b). Wheel-rail dynamics with closely conformal contact Part 2: Forced response, results and conclusions. *Proceedings of the Institution of Mechanical Engineers, Part F: Journal of Rail and Rapid Transit*, 211(1), pp. 27-40.

Blajer, W. (2002). Elimination of constraint violation and accuracy aspects in numerical simulation of multibody systems. *Multibody System Dynamics*, 7(3), pp. 265-284.

Blanco-Lorenzo, J., Santamaria, J., Vadillo, E.G., Correa, N. (2016). On the influence of conformity on wheel–rail rolling contact mechanics. *Tribology International*, 103, pp. 647-667.

Bogacz, R., Frischmuth, K. (2016). On dynamic effects of wheel–rail interaction in the case of Polygonalisation. *Mechanical Systems and Signal Processing*, 79, pp. 166-173.

Bosso, N., Zampieri, N. (2020). Numerical stability of co-simulation approaches to evaluate wheel profile evolution due to wear. *International Journal of Rail Transportation*, 8(2), pp. 159-179.

Bozzone, M., Pennestrì, E., Salvini, P. (2011a). Dynamic analysis of a bogie for hunting detection through a simplified wheel-rail contact model. *Multibody System Dynamics*, 25(4), pp. 429-460.

Bozzone, M., Pennestrì, E., Salvini, P. (2011b). A lookup table-based method for wheel-rail contact analysis. *Proceedings of the Institution of Mechanical Engineers, Part K: Journal of Multi-body Dynamics*, 225(2), pp. 127-138.

Braghin, F., Lewis, R., Dwyer-Joyce, R.S., Bruni, S. (2006). A mathematical model to predict railway wheel profile evolution due to wear. *Wear*, 261(11-12), pp. 1253-1264.

Braghin, F., Bruni, S., Lewis, R. (2009). *Railway wheel wear*. In: Wheel-Rail Interface Handbook, pp. 172-210.

British Standards (2011). BS EN 13674-1: 2011. Railway applications - Track - Rail - Part 1: Vignole railway rails 46 kg/m and above.

Bruni, S., Goodall, R., Mei, T.X., Tsunashima, H. (2007). Control and monitoring for railway vehicle dynamics. *Vehicle System Dynamics*, 45(7-8), pp. 743-779.

Bruni, S., Braghin, F. (2009). *Effect of damage on vehicle dynamics*. In: Wheel-Rail Interface Handbook, pp. 456-476.

Bruni, S., Vinolas, J., Berg, M., Polach, O., Stichel, S. (2011). Modelling of suspension components in a rail vehicle dynamics context. *Vehicle System Dynamics*, 49(7), pp. 1021-1072.

Bruni, S., Bucca, G., Carnevale, M., Collina, A., Facchinetti, A. (2018). Pantograph–catenary interaction: recent achievements and future research challenges. *International Journal of Rail Transportation*, 6(2), pp. 57-82.

Bruni, S., Meijaard, J.P., Rill, G., Schwab, A.L. (2020). State-of-the-art and challenges of railway and road vehicle dynamics with multibody dynamics approaches. *Multibody System Dynamics*, 49(1).

Campbell-Kelly, M., Croarken, M., Flood, R., Robson, E. (2007). *The History of Mathematical Tables: From Sumer to Spreadsheets*, Oxford University Press, New York.

Carrarini, A. (2007). Reliability based analysis of the crosswind stability of railway vehicles. *Journal of Wind Engineering and Industrial Aerodynamics*, 95(7), pp. 493-509.

Carter, F.W. (1916). The electric locomotive. *Minutes of the Proceedings of the Institution of Civil Engineers*, 201, pp. 221-252.

Carter, F.W. (1926). On the action of a locomotive driving wheel. *Proceedings of the Royal Society of London. Series A*, 112(760), pp. 151-157.

Chamorro, R., Escalona, J.L., González, M. (2011). An approach for modeling long flexible bodies with application to railroad dynamics. *Multibody System Dynamics*, 26, pp. 135-152.

Cheli, F., Corradi, R., Rocchi, D., Tomasini, G., Maestrini, E. (2010). Wind tunnel tests on train scale models to investigate the effect of infrastructure scenario. *Journal of Wind Engineering and Industrial Aerodynamics*, 98(6-7), pp. 353-362.

Cheng, Y.C., Wu, P.H. (2015). Optimisation for suspension system of a railway vehicle with a new non-linear creep model developed by uniform design. *International Journal of Heavy Vehicle Systems*, 22(2), pp. 157-191.

Cole, C., Spiryagin, M., Wu, Q., Sun, Y.Q. (2017) Modelling, simulation and applications of longitudinal train dynamics. *Vehicle System Dynamics*, 55(10), pp. 1498-1571.

Costa, J.N., Antunes, P., Magalhães, H., Pombo, J., Ambrósio, J. (2020a). A novel methodology to automatically include general track flexibility in railway vehicle dynamic analyses. *Proceedings of the Institution of Mechanical Engineers, Part F: Journal of Rail and Rapid Transit*, https://doi.org/10.1177/0954409720945420

Costa, J.N., Ambrósio, J., Frey, D., Andrade, A.R. (2020b). A multivariate statistical representation of railway track irregularities using ARMA models. *Vehicle System Dynamics*, submitted.

Deng, L., Chakrabarti, C., Pitsianis, N., Sun, X. (2009) Automated optimization of look-up table implementation for function evaluation on FPGAs. *Proceedings of SPIE - The International Society for Optical Engineering*, no. 744413.

De Boor, C. (1978). *A Practical Guide to Splines*, Springer-Verlag, New York, New York.

De Pater, A.D. (1988). The Geometrical Contact between Track and Wheelset. *Vehicle System Dynamics*, 17(3), pp. 127-140.

De Rosa, A., Alfi, S., Bruni, S. (2019). Estimation of lateral and cross alignment in a railway track based on vehicle dynamics measurements. *Mechanical Systems and Signal Processing*, 116, pp. 606-623.

Di Gialleonardo, E., Braghin, F., Bruni, S. (2012). The influence of track modelling options on the simulation of rail vehicle dynamics. *Journal of Sound and Vibration*, 331(19), pp. 4246-4258.

Eberhard, P., Schiehlen, W. (2006). Computational dynamics of multibody systems: History, formalisms, and applications. *Journal of Computational and Nonlinear Dynamics*, 1(1), pp. 3-12.

Eich-Soellner, E., Führer, C. (1998). *Numerical Methods in Multibody Dynamics*. Springer Fachmedien Wiesbaden.

Eickhoff, B.M., Evans, J.R., Minnis, A.J. (1995). Review of Modelling Methods for Railway Vehicle Suspension Components. *Vehicle System Dynamics,* 24(6-7), pp. 469-496.

Ekberg, A., Åkesson, B., Kabo, E. (2014). Wheel/rail rolling contact fatigue - Probe, predict, prevent. *Wear*, 314 (1-2), pp. 2-12.

El Beshbichi, O., Wan, C., Bruni, S., Kassa, E. (2020). Complex eigenvalue analysis and parameters analysis to investigate the formation of railhead corrugation in sharp curves. *Wear*, 450-451, 203150.

Elkins, J.A. (1992). Prediction of wheel/rail interaction: the state-of-the-art. *Vehicle System Dynamics*, 20(S1), pp. 1-27.

EN 14363. (2016). *Railway Applications—Testing and Simulation for the Acceptance of Running Characteristics of Railway Vehicles—Running Behaviour and Stationary Tests*. European Committee for Standardization, Brussels, Belgium.

Enblom, R. (2009). Deterioration mechanisms in the wheel-rail interface with focus on wear prediction: A literature review. *Vehicle System Dynamics*, 47(6), pp. 661-700.

ERA (2020). *Report - Fostering the railway sector through the European Green Deal.*

Escalona, J.L., Aceituno, J.F. (2019). Multibody simulation of railway vehicles with contact lookup tables. *International Journal of Mechanical Sciences*, 155, pp. 571-582.

Evans, J., Berg, M. (2009). Challenges in simulation of rail vehicle dynamics. *Vehicle System Dynamics*, 47(8), pp. 1023-1048.

Facchinetti, A., Mazzola, L., Alfi, S., Bruni, S. (2010). Mathematical modelling of the secondary airspring suspension in railway vehicles and its effect on safety and ride comfort. *Vehicle System Dynamics*, 48(S1), pp. 429-449.

Falomi, S., Malvezzi, M., Meli, E. (2011). Multibody modeling of railway vehicles: Innovative algorithms for the detection of wheel-rail contact points. *Wear*, 271(1-2), pp. 453-461.

Fang, W., Bruni, S. (2019). A time domain model for the study of high frequency 3D wheelset–track interaction with non-Hertzian contact. *Multibody System Dynamics*, 46, pp. 229-255.

Fisette, P., Samin, J.C. (1994). A new wheel/rail contact model for independent wheels. *Archive of Applied Mechanics*, 64, pp. 180-191.

Flores, P., Machado, M., Seabra, E., Tavares Da Silva, M. (2011). A Parametric Study on the Baumgarte Stabilization Method for Forward Dynamics of Constrained Multibody Systems. *Journal of Computational and Nonlinear Dynamics*, 6(1), art. no. 011019.

Flores, P. (2015). *Concepts and Formulations for Spatial Multibody Dynamics*. Springer, Berlin.

Flores, P., Lankarani, H.M. (2016). *Contact Force Models for Multibody Dynamics*. Springer, Dordrecht.

Fu, B., Giossi, R.L., Persson, R., Stichel, S., Bruni, S., Goodall, R. (2020). Active suspension in railway vehicles: a literature survey. *Railway Engineering Science*, 28 (1), pp. 3-35.

Goldsmith, W. (1960). *Impact, The Theory and Physical Behaviour of Colliding Solids*, Edward Arnold Ltd., London, England.

Gonçalves, A.A., Bernardino, A., Jorge, J., Lopes, D.S. (2017). A benchmark study on accuracy-controlled distance calculation between superellipsoid and superovoid contact geometries. *Mechanism and Machine Theory*, 115, pp. 77-96.

Goodall, R.M. (2011). Control for railways – active suspensions and other opportunities. *19th Mediterranean Conference on Control and Automation*, Corfu, Greece, June 20-23, 2011.

Goodall, R., Freudenthaler, G., Dixon R. (2014). Hydraulic actuation technology for full- and semi-active railway suspensions. *Vehicle System Dynamics*, 52(12), pp. 1642-1657.

Götz, G., Polach, O. (2018). Verification and validation of simulations in a rail vehicle certification context. *International Journal of Rail Transportation*, 6(2), pp. 83-100.

Grassie, S.L. (2009). Rail corrugation: Characteristics, causes, and treatments. *Proceedings of the Institution of Mechanical Engineers, Part F: Journal of Rail and Rapid Transit*, 223(6), pp. 581-596.

Halme, J., Andersson, P. (2010). Rolling contact fatigue and wear fundamentals for rolling bearing diagnostics - State of the art. *Proceedings of the Institution of Mechanical Engineers, Part J: Journal of Engineering Tribology*, 224(4), pp. 377-393.

Hedrick, J.K. (1981). Railway Vehicle Active Suspensions. *Vehicle System Dynamics*, 10(4-5), pp. 267-283.

Hertz, H. (1881). Über die Berührung fester elastischer Körper. *Journal reine und an-gewandte Mathematik*, 92, pp. 156-171.

Ignesti, M., Innocenti, A., Marini, L., Meli, E., Rindi, A. (2013). Development of a wear model for the wheel profile optimisation on railway vehicles *Vehicle System Dynamics*, 51(9), pp. 1363-1402.

Ilchmann, A., Reis, T. (2017). *Surveys in Differential-Algebraic Equations IV*. Springer, Switzerland.

Iwnick, S. (1998). Manchester Benchmarks for Rail Vehicle Simulation. *Vehicle System Dynamics*, 30(3-4), pp. 295-313.

Iwnicki, S. (2006). *Handbook of Railway Vehicle Dynamics*, Taylor and Francis, London.

Jaschinski, A., Chollet, H., Iwnicki, S., Wickens, A., Von Würzen, J. (1999). The application of roller rigs to railway vehicle dynamics. *Vehicle System Dynamics*, 31(5-6), pp. 345-392.

Jin, T., Liu, Z., Sun, S., Ren, Z., Deng, L., Ning, D., Du, H., Li, W. (2020). Theoretical and experimental investigation of a stiffness-controllable suspension for railway vehicles to avoid resonance. *International Journal of Mechanical Sciences*, 187, 105901.

Johnson, K.L. (1958a). The effect of a tangential contact force upon the rolling motion of an elastic sphere on a plane. *Journal of Applied Mechanics*, 25, pp. 339-346.

Johnson, K.L. (1958b). The effect of spin upon the rolling motion of an elastic sphere on a plane. *Journal of Applied Mechanics*, 25, pp. 332-338.

Johnson, K.L. (1985). *Contact Mechanics*, Cambridge University Press, Cambridge, United Kingdom.

Kaiser, I., Popp, K. (2006). Interaction of elastic wheelsets and elastic rails: modelling and simulation. *Vehicle System Dynamics*, 44(S1), pp. 932-939.

Kaiser, I. (2012). Refining the modelling of vehicle–track interaction. *Vehicle System Dynamics*, 50(S1), pp. 229-243.

Kalker, J.J. (1967). *On the Rolling Contact of Two Elastic Bodies in the Presence of Dry Friction*. PhD Thesis, Delft University of Technology, Netherlands.

Kalker, J.J. (1979). Survey of Wheel Rail Rolling Contact Theory. *Vehicle System Dynamics*, 8(4), pp. 317-358.

Kalker, J.J. (1982a). *Introduction to the Fortran IV Program DUVOROL and CONTACT for the Solution of 3D Elastostatic Half-Space Contact Problems with and without Friction*. Technical Report, Delft University of Technology, Netherlands.

Kalker, J.J. (1982b). A fast algorithm for the simplified theory of rolling contact. *Vehicle System Dynamics*, 11, pp. 1-13.

Kalker, J.J. (1983). A Simplified Theory for Non-Hertzian Contact. *Vehicle System Dynamics*, 12(1-3), pp. 43-45.

Kalker, J.J. (1990). *Three-dimensional elastic bodies in rolling contact*. Kluwer Academic Publishers.

Kalker, J.J. (1996). Book of tables for the Hertzian creep-force law. In: *Proceedings of the 2nd Mini Conference on Contact mechanics and Wear of Wheel/Rail Systems*, I. Zobory, ed., Budapest University of Technology and Economics, Budapest, pp. 11-20.

Kalker, J.J. (2001). *Rolling Contact Phenomena - Linear Elasticity*. Springer, New York.

Kik, W., Piotrowski, J. (1996). A fast, approximate method to calculate normal load at contact between wheel and rail and creep forces during rolling, in: I. Zabory (Ed.), Proceedings of the Second Mini Conference on Contact Mechanics and Wear of Rail/Wheel System, Budapest.

Knothe, K., Le-The, H. (1985). A method for the analysis of the tangential stresses and the wear distribution between two elastic bodies of revolution in rolling contact. *International Journal of Solids and Structures*, 21(8), pp. 889-906.

Kozek, M., Benatzky, C., Schirrer, A., Stribersky, A. (2011). Vibration damping of a flexible car body structure using piezo-stack actuators. *Control Engineering Practice*, 19(3), pp. 298-310.

Lankarani, H.M. (1988). *Canonical Equations of Motion and Estimation of Parameters in the Analysis of Impact Problems*. Ph.D. Thesis, University of Arizona, USA.

Lee, S.Y., Cheng, Y.C. (2005). Nonlinear Analysis on Hunting Stability for High-Speed Railway Vehicle Trucks on Curved Tracks. *Journal of Vibration and Acoustics*, 127(4), pp. 324-332.

Li, T., Zhang, J.-Y., Zhang, W.-H. (2013). A numerical approach to the interaction between airflow and a high-speed train subjected to crosswind. *Journal of Zhejiang University: Science A*, 14(7), pp. 482-493.

Li, H., Terao, A., Sugiyama, H. (2014). Application of tabular contact search method to multibody gear dynamics simulation with tooth surface imperfections. *Proceedings of the Institution of Mechanical Engineers, Part K: Journal of Multi-body Dynamics*, 229(3), pp. 274-290.

Lin, M.C., Gottschalk, S. (1998). Collision detection between geometric models: a survey. *Proceedings of IMA Conference on Mathematics of Surfaces*, pp. 1-20.

Ling, L., Xiao, X.B., Jin, X.S. (2014). Development of a simulation model for dynamic derailment analysis of high-speed trains. *Acta Mechanica Sinica*, 30(6), pp. 860-875.

Liu, Y., Stratman, B., Mahadevan, S. (2006). Fatigue crack initiation life prediction of railroad wheels. *International Journal of Fatigue*, 28, pp. 747-756.

Liu, B., Bruni, S., Vollebregt, E. (2016). A non-Hertzian method for solving wheel–rail normal contact problem taking into account the effect of yaw. *Vehicle System Dynamics*, 54(9), pp. 1226-1246.

Machado, M., Moreira, P., Flores, P., Lankarani, H.M. (2012). Compliant contact force models in multibody dynamics: Evolution of the Hertz contact theory. *Mechanism and Machine Theory*, 53, pp. 99-121.

Machado, M., Flores, P., Ambrósio, J. (2014). A lookup-table-based approach for spatial analysis of contact problems. *Journal of Computational and Nonlinear Dynamics*, 9(4), 41010.

Magalhães, H., Madeira, J.F.A., Ambrósio, J., Pombo, J. (2016a). Railway vehicle performance optimisation using virtual homologation. *Vehicle System Dynamics*, 54(9), pp. 1177-1207.

Magalhães, H., Ambrósio, J., Pombo, J. (2016b). Railway vehicle modelling for the vehicle–track interaction compatibility analysis. *Proceedings of the Institution of Mechanical Engineers, Part K: Journal of Multi-body Dynamics*, 230(3), pp. 251-267.

Magalhães, H., Marques, F., Liu, B., Pombo, J., Flores, P., Ambrósio, J., Bruni, S. (2018). An Optimization Approach to Generate Accurate and Efficient Lookup Tables for Engineering Applications. *6th International Conference on Engineering Optimization - EngOpt 2018*, Lisbon, Portugal, September 17-19, 12 pages.

Magalhães, H., Marques, F., Liu, B., Antunes, P., Pombo, J., Flores, P., Ambrósio, J., Piotrowski, J., Bruni, S. (2020). Implementation of a non-Hertzian contact model for railway dynamic application. *Multibody System Dynamics*, 48(1), pp. 41-78.

Malvezzi, M., Meli, E., Falomi, S., Rindi, A. (2008). Determination of wheel-rail contact points with semianalytic methods. *Multibody Systems Dynamics*, 20, pp. 327-358.

Marques, F., Souto, A.P., Flores, P. (2017). On the constraints violation in forward dynamics of multibody systems. *Multibody System Dynamics*, 39(4), pp. 385-419.

Marques, F., Magalhães, H., Ambrósio, J., Flores, P. (2019a). Approach for conformal contact detection for wheel-rail interaction. *Mechanisms and Machine Science*, 59, pp. 71-78.

Marques, F., Magalhaes, H., Liu, B., Pombo, J., Flores, P., Ambrósio, J., Piotrowski, J., Bruni, S. (2019b). On the generation of an enhanced lookup table for wheel–rail contact models. *Wear*, 434-435, 202993.

Marques, F., Magalhães, H., Pombo, J., Ambrósio, J., Flores, P. (2020). A three-dimensional approach for contact detection between realistic wheel and rail surfaces for improved railway dynamic analysis. *Mechanism and Machine Theory*, 149, 103825.

Marquis, B., Pascal, J.P. (2008). Report on a railway Benchmark simulating a single wheelset with-out friction impacting a rigid track. *Vehicle System Dynamics*, 46(1-2), pp. 93-116.

Martínez-Casas, J., Giner-Navarro, J., Baeza, L., Denia, F.D. (2017). Improved railway wheelset-track interaction model in the high-frequency domain. *Journal of Computational and Applied Mathematics*, 309, pp. 642-653.

Meacci, M., Shi, Z., Butini, E., Marini, L., Meli, E., Rindi, A. (2019). A local degraded adhesion model for creep forces evaluation: An approximate approach to the tangential contact problem. *Wear*, 440-441, 203084.

Meymand, S.Z., Keylin, A., Ahmadian, M. (2016). A survey of wheel–rail contact models for rail vehicles. *Vehicle System Dynamics*, 54(3), pp. 386-428.

Meli, E., Magheri, S., Malvezzi, M. (2011). Development and implementation of a differential elastic wheel–rail contact model for multibody applications. *Vehicle System Dynamics*, 49(6), pp. 969-1001.

Meli, E., Ridolfi, A. (2015). An innovative wheel–rail contact model for railway vehicles under degraded adhesion conditions. *Multibody System Dynamics*, 33, pp. 285-313.

Miyatake, M., Ko, M. (2010). Optimization of Train Speed Profile for Minimum Energy Consumption. IEEJ Transactions on Electrical and Electronic Engineering, 5, pp. 263-269.

Mousavi-Bideleh, S.M., Berbyuk, V. (2016). Multiobjective optimisation of bogie suspension to boost speed on curves. *Vehicle System Dynamics*, 54(1), pp. 69-96.

Myers, R.H., Montgomery, D.C., Anderson-Cook, C.M. (2016). *Response Surface Methodology: Process and Product Optimization Using Designed Experiments*. Fourth Edition, John Wiley & Sons, Inc., New York, New York.

Naeimi, M., Zakeri, J.A., Shadfar, M., Esmaeili, M. (2015). 3D dynamic model of the railway wagon to obtain the wheel-rail forces under track irregularities. *Proceedings of the Institution of Mechanical Engineers, Part K: Journal of Multi-Body Dynamics*, 229(4), pp. 357-369.

Neto, M.A., Ambrósio, J. (2003). Stabilization methods for the integration of DAE in the presence of redundant constraints. *Multibody System Dynamics*, 10(1), pp. 81-105.

Nielsen, J.C.O., Johansson, A. (2000) Out-of-round railway wheels-a literature survey. *Proceedings of the Institution of Mechanical Engineers, Part F: Journal of Rail and Rapid Transit*, 214(2), pp. 79-91.

Nikravesh, P.E., Haug, E.J. (1983). Generalized Coordinate Partitioning for Analysis of Mechanical System with Nonholonomic Constraints. *Journal of Mechanisms, Transmissions, and Automation in Design*, 105(3), pp. 379-384.

Nikravesh, P.E. (1988). *Computer-Aided Analysis of Mechanical Systems*. Prentice Hall, Englewood Cliffs, New Jersey.

Nikravesh, P.E. (2019). *Planar Multibody Dynamics: Formulation, Programming with MATLAB®, and Applications*. Second Edition, CRC Press, Boca Raton.

Nokhbatolfoghahai, A., Noorian, M.A., Haddadpour, H. (2018) Dynamic response of tank trains to random track irregularities. *Meccanica*, 53, pp. 2687-2703.

Olivier, B., Verlinden, O., Kouroussis, G. (2020). A vehicle/track/soil model using co-simulation between multibody dynamics and finite element analysis. *International Journal of Rail Transportation*, 8(2), pp. 135-158.

Oprea, R.A., Cruceanu, C., Spiroiu, M.A. (2013). Alternative friction models for braking train dynamics. *Vehicle System Dynamics*, 51(3), pp. 460-480.

Paixão, A., Varandas, J.N., Fortunato, E., Calçada, R. (2016). Non-Linear Behaviour of Geomaterials in Railway Tracks under Different Loading Conditions. *Procedia Engineering*, 143, pp. 1128-1135.

Palermo, A., Mundo, D., Hadjit, R., Desmet, W. (2013). Multibody element for spur and helical gear meshing based on detailed three-dimensional contact calculations. *Mechanism and Machine Theory*, 62, pp. 13-30.

Pappalardo, C.M., Guida, D. (2018). On the computational methods for solving the differential-algebraic equations of motion of multibody systems. *Machines*, 6(2), art. no. 20.

Pappalardo, C.M., Lettieri, A., Guida, D. (2020). Stability analysis of rigid multibody mechanical systems with holonomic and nonholonomic constraints. *Archive of Applied Mechanics*, 90(9), pp. 1961-2005.

Park, K.C., Chiou, J.C. (1988). Stabilization of computational procedures for constrained dynamical systems. *Journal of Guidance, Control, and Dynamics*, 11(4), pp. 365-370.

Pascal, J.P., Sauvage, G. (1992). New method for reducing the multicontact wheel/rail problem to one equivalent contact patch. *Vehicle System Dynamics*, 20(S1), pp. 475-489.

Pascal, J.P. (1993). About Multi-Hertzian-Contact Hypothesis and Equivalent Conicity in the Case of S1002 and UIC60 Analytical Wheel/Rail Profiles. *Vehicle System Dynamics*, 22(2), pp. 57-78.

Pascal, J.P., Sauvage, G. (1993). The Available Methods to Calculate the Wheel/Rail Forces in Non Hertzian Contact Patches and Rail Damaging. *Vehicle System Dynamics*, 22(3-4), pp. 263-275.

Pascal, J.P., Soua, B. (2016). Solving conformal contacts using multi-Hertzian techniques. *Vehicle System Dynamics*, 54(6), pp. 784-813.

Pascal, J.P., Sany, J.R. (2019). Dynamics of an isolated railway wheelset with conformal wheel–rail interactions. *Vehicle System Dynamics*, 57(12), pp. 1947-1969.

Paul, B., Hashemi, J. (1981). Contact Pressures on Closely Conforming Elastic Bodies. *Journal of Applied Mechanics*, 48, pp. 543-548.

Perez, J., Mauer, L., Busturia, J.M. (2003). Design of active steering systems for bogie-based railway vehicles with independently rotating wheels. *Vehicle System Dynamics*, 37(S1), pp. 209-220.

Persson, I., Iwnicki, S.D. (2004). Optimization of railway wheel profiles using a genetic algorithm. *Vehicle System Dynamics*, 41, pp. 517-527.

Persson, R., Goodall, R.M., Sasaki, K. (2009) Carbody Tilting - technologies and benefits. *Vehicle System Dynamics*, 47(8), pp. 949-981.

Piotrowski, J. (1982). A Theory of Wheelset Forces for Two Point Contact Between Wheel and Rail, *Vehicle System Dynamics*, 11(2), pp. 69-87

Piotrowski, J., Kalker, J.J. (1988). The Elastic Cross-Influence between Two Quasi-Hertzian Contact Zones. *Vehicle System Dynamics*, 17(6), pp. 337-355.

Piotrowski, J., Chollet, H. (2005). Wheel–rail contact models for vehicle system dynamics including multi-point contact. *Vehicle System Dynamics*, 43(6-7), pp. 455-483.

Piotrowski, J., Kik, W. (2008). A simplified model of wheel/rail contact mechanics for non-Hertzian problems and its application in rail vehicle dynamic simulations. *Vehicle System Dynamics*, 46(1-2), pp. 27-48.

Piotrowski, J. (2010). Kalker's algorithm Fastsim solves tangential contact problems with slip-dependent friction and friction anisotropy. *Vehicle System Dynamics*, 48(7), pp. 869-889.

Piotrowski, J., Liu, B., Bruni, S. (2017). The Kalker book of tables for non-Hertzian contact of wheel and rail. *Vehicle System Dynamics*, 55(6), pp. 875-901.

Piotrowski, J., Bruni, S., Liu B., Di Gialleonardo, E. (2019). A fast method for determination of creep forces in non-Hertzian contact of wheel and rail based on a book of tables. *Multibody System Dynamics*, 45(2), pp. 169-184.

PNI2030 (2019) *Plano Nacional de Investimentos 2030: Relatório*.

Polach, O. (1999). A Fast Wheel-Rail Forces Calculation Computer Code. *Vehicle System Dynamics*, Sup. 33, pp. 728-739.

Polach, O., Evans, J. (2013). Simulations of Running Dynamics for Vehicle Acceptance: Application and Validation. *International Journal of Railway Technology*, 2(4), pp. 59-84.

Polach, O., Böttcher, A. (2014). A new approach to define criteria for rail vehicle model validation. *Vehicle System Dynamics*, 52(S1), pp. 125-141.

Polach, O., Böttcher, A., Vannucci, D., Sima, J., Schelle, H., Chollet, H., Götz, G., Garcia Prada, M., Nicklisch, D., Mazzola, L., Berg, M., Osman, M. (2015). Validation of simulation models in the context of railway vehicle acceptance. *Proceedings of the Institution of Mechanical Engineers, Part F: Journal of Rail and Rapid Transit*, 229(6), pp. 729-754.

Pombo, J., Ambrósio J. (2003). General Spatial Curve Joint for Rail Guided Vehicles: Kinematics and Dynamics. *Multibody System Dynamics*, 9, pp. 237-264.

Pombo, J. (2004). *A Multibody Methodology for Railway Dynamics Applications*. PhD Thesis, Instituto Superior Técnico, Portugal.

Pombo, J., Ambrósio, J. (2005). Dynamic analysis of a railway vehicle in real operation conditions using a new wheel-rail contact detection model. *International Journal of Vehicle Systems Modelling and Testing*, 1(1-3), pp. 79-105.

Pombo, J., Ambrósio, J., Silva, M. (2007). A new wheel-rail contact model for railway dynamics. *Vehicle System Dynamics*, 45, pp. 165-189.

Pombo, J., Ambrósio, J. (2012). An alternative method to include track irregularities in railway vehicle dynamic analyses. *Nonlinear Dynamics*, 68, pp. 161-176.

Pombo, J., Almeida, T., Magalhães, H., Antunes, P., Ambrósio, J. (2013). Finite Element Methodology for Flexible Track Models in Railway Dynamics Applications. *International Journal of Vehicle Structures & Systems*, 5(2), pp. 43-52.

Premoli, A., Rocchi, D., Schito, P., Somaschini, C., Tomasini, G. (2015). Ballast flight under high-speed trains: Wind tunnel full-scale experimental tests. *Journal of Wind Engineering and Industrial Aerodynamics*, 145, pp. 351-361.

Quost, X., Sebès, M., Eddhahak, A., Ayasse, J.B., Chollet, H., Gautier, P.E., Thouverez, F. (2006). Assessment of a semi-Hertzian method for determination of wheel–rail contact patch. *Vehicle System Dynamics*, 44(10), pp. 789-814.

Raghunathan, R.S., Kim, H.-D., Setoguchi, T. (2002). Aerodynamics of high-speed railway train. *Progress in Aerospace Sciences*, 38(6-7), pp. 469-514.

Recuero, A.M., Shabana, A.A. (2014). A Simple Procedure for the Solution of Three-Dimensional Wheel/Rail Conformal Contact Problem. *Journal of Computational and Nonlinear Dynamics*, 9(3), 034501.

Rose, K. (1984). *Kalker Table for Wheel/rail Force Prediction*, Internal Memorandum IM VTI 4, British Rail Research, Derby, UK.

Sadeghi, J., Rabiee, S., Khajehdezfuly, A. (2019) Effect of Rail Irregularities on Ride Comfort of Train Moving Over Ballast-Less Tracks. International Journal of Structural Stability and Dynamics, 19(6), 1950060.

Schiehlen, W. (1997). Multibody System Dynamics: Roots and Perspectives. *Multibody System Dynamics*, 1(2), pp. 149-188.

Schwab, K. (2018) *The Global Competitiveness Report 2016–2017*. World Economic Forum.

Sebès, M., Chollet, H., Ayasse, J.-B., Chevalier, L. (2014). A multi-Hertzian contact model considering plasticity. *Wear*, 314, pp. 118-124.

Shabana, A.A., Berzeri, M., Sany, J.R. (2001). Numerical Procedure for the Simulation of Wheel/Rail Contact Dynamics. *Journal of Dynamic Systems, Measurement, and Control*, 123(2), pp. 168-178.

Shabana, A.A., Sany, J.R. (2001). Augmented formulation for mechanical systems with non-generalized coordinates: Application to rigid body contact problems. *Nonlinear Dynamics*, 24(2), pp. 183-204.

Shabana, A.A., Zaazaa, K.E., Escalona, J.L., Sany, J.R. (2004). Development of elastic force model for wheel/rail contact problems. *Journal of Sound and Vibration*, 269, pp. 295-325.

Shabana, A.A., Tobaa, M., Sugiyama, H., Zaazaa, K.E. (2005). On the Computer Formulations of the Wheel/Rail Contact Problem. *Nonlinear Dynamics*, 40(2), pp. 169-193.

Shackleton, P., Iwnicki, S. (2008). Comparison of wheel–rail contact codes for railway vehicle simulation: an introduction to the Manchester Contact Benchmark and initial results*. Vehicle System Dynamics*, 46(1-2), pp. 129-149.

Shebani, A., Iwnicki, S. (2018). Prediction of wheel and rail wear under different contact conditions using artificial neural networks. *Wear*, 406-407, pp. 173-184.

Shen, Z.Y., Hedrick, J.K., Elkins, J.A. (1983). A Comparison of Alternative Creep Force Models for Rail Vehicle Dynamic Analysis. *Vehicle System Dynamics*, 12(1-3), pp. 79-83.

Shift2Rail (2018). *Multi-Annual Action Plan - Executive View: Part A*.

Shu, X., Wilson, N., Sasaoka, C., Elkins, J. (2006). Development of a real-time wheel/rail contact model in NUCARS® 1 and application to diamond crossing and turnout design simulations. *Vehicle System Dynamics*, 44(S1), pp. 251-260.

Sichani, M.S., Enblom, R., Berg, M. (2014a). Comparison of non-elliptic contact models: Towards fast and accurate modelling of wheel-rail contact. *Wear*, 314, pp. 111-117.

Sichani, M.S., Enblom, R., Berg, M. (2014b). A novel method to model wheel–rail normal contact in vehicle dynamics simulation. *Vehicle System Dynamics*, 52(12), pp. 1752-1764.

Sichani, M.S., Enblom, R., Berg, M. (2016). An alternative to FASTSIM for tangential solution of the wheel–rail contact. *Vehicle System Dynamics*, 54(6), pp. 748-764.

Sugiyama, H., Araki, K., Suda, Y. (2009). On-line and off-line wheel/rail contact algorithm in the analysis of multibody railroad vehicle systems. *Journal of Mechanical Science and Technology*, 23, pp. 991-996.

Sugiyama, H., Suda, Y. (2009). On the Contact Search Algorithms for Wheel/Rail Contact Problems. *Journal of Computational and Nonlinear Dynamics*, 4(4), 041001.

Sugiyama, H., Sekiguchi, T., Matsumura, R., Yamashita, S., Suda, Y. (2012) Wheel/rail contact dynamics in turnout negotiations with combined nodal and non-conformal contact approach. *Multibody System Dynamics*, 27(1), pp. 55-74.

Sun, W., Zhou, J., Gong, D., You, T. (2016). Analysis of modal frequency optimization of railway vehicle car body. *Advances in Mechanical Engineering*, 8(4), pp. 1-12.

Sun, Y., Zhai, W., Guo, Y. (2018). A robust non-Hertzian contact method for wheel–rail normal contact analysis. *Vehicle System Dynamics*, 56 (12), pp. 1899-1921.

Sun, Y., Zhai, W., Ye, Y., Zhu, L., Guo, Y. (2020). A simplified model for solving wheel-rail non-Hertzian normal contact problem under the influence of yaw angle. *International Journal of Mechanical Sciences*, 174, 105554.

Tao, G., Wen, Z., Zhao, X., Jin, X. (2016). Effects of wheel–rail contact modelling on wheel wear simulation. *Wear*, 366-367, pp. 146-156.

Telliskivi, T., Olofsson, U. (2001). Contact mechanics analysis of measured wheel-rail profiles using the finite element method. *Proceedings of the Institution of Mechanical Engineers, Part F: Journal of Rail and Rapid Transit*, 215(2), pp. 65-72.

Tsujie, M., Miura, M., Chen, H., Terumichi, Y. (2019). A study on the initiation of head check of the low rail using multibody dynamics. *Wear*, 436-437, 202989.

Turnia, J., Sinclair, J., Perez, J. (2007). A review of wheel wear and rolling contact fatigue. *Proceedings of the Institution of Mechanical Engineers, Part F: Journal of Rail and Rapid Transit*, 221(2), pp. 271-289.

UIC - International Union of Railways (2004). UIC 510-2. Trailing Stock: Wheels and Wheelsets. Conditions Concerning the Use of Wheels of Various Diameters.

UIC (2018). *Railway Statistics 2017 - Synopsis*.

Urda, P., Aceituno, J.F., Muñoz, S., Escalona, J.L. (2020). Artificial neural networks applied to the measurement of lateral wheel-rail contact force: A comparison with a harmonic cancellation method. *Mechanism and Machine Theory*, 153, 103968.

Vermeulen, P.J., Johnson, K.L. (1964). Contact of Non Spherical Bodies Transmitting Tangential Forces. *Journal of Applied Mechanics*, 31(2), pp. 338-340.

Vollebregt, E.A.H. (2009). Refinement of Kalker's rolling contact model. In A. Bracciali, editor, *Proceedings of the 8th International Conference on Contact Mechanics and Wear in Rail/Wheel Systems*, pp. 149-156.

Vollebregt, E.A.H., Wilders, P. (2011). FASTSIM2: a second-order accurate frictional rolling contact algorithm. *Computational Mechanics*, 47(1), pp. 105-116.

Vollebregt, E.A.H., Iwnicki, S.D., Xie, G., Shackleton, P. (2012). Assessing the accuracy of different simplified frictional rolling contact algorithms. *Vehicle System Dynamics*, 50(1), pp. 1-17

Vollebregt, E.A.H., (2014). Numerical modeling of measured railway creep versus creep-force curves with CONTACT. *Wear*, 314, pp. 87-95.

Vollebregt, E., Segal, G. (2014). Solving conformal wheel–rail rolling contact problems. *Vehicle System Dynamics*, 52(S1), pp. 455-468.

Vollebregt, E.A.H. (2018). Conformal contact: corrections and new results. *Vehicle System Dynamics*, 56(10), pp. 1622-1632.

Wehage, R.A., Haug, E.J. (1982). Generalized coordinate partitioning for dimension reduction in analysis of constrained dynamic systems. *Journal of Mechanical Design, Transactions of the ASME*, 104(1), pp. 247-255.

Wellmann, C., Lillie, C., Wriggers, P. (2008). A contact detection algorithm for superellipsoids based on the common-normal concept. *Engineering Computations*, 25(5), pp. 432-442.

Weston, P.F., Ling, C.S., Roberts, C., Goodman, C.J., Li, P., Goodall, R.M. (2007a). Monitoring vertical track irregularity from in-service railway vehicles. *Proceedings of the Institution of Mechanical Engineers, Part F: Journal of Rail and Rapid Transit*, 221(1), pp. 75-88.

Weston, P.F., Ling, C.S., Goodman, C.J., Roberts, C., Li, P., Goodall, R.M. (2007b). Monitoring lateral track irregularity from in-service railway vehicles. *Proceedings of the Institution of Mechanical Engineers, Part F: Journal of Rail and Rapid Transit*, 221(1), pp. 89-100.

Wickens, A.H. (1965). The dynamic stability of railway vehicle wheelsets and bogies having profiled wheels. *International Journal of Solids and Structures*, 1(3), pp. 319-341.

Wilcox, C., Strout, M.M., Bieman, J.M. (2011). Mesa: Automatic generation of lookup table optimizations. *Proceedings - International Conference on Software Engineering*, pp. 1-8.

Wilson, N., Wu, H., Tournay, H., Urban, C. (2010). Effects of wheel/rail contact patterns and vehicle parameters on lateral stability. *Vehicle System Dynamics*, 48(S1), pp. 487-503.

Wilson, N., Fries, R., Witte, M., Haigermoser, A., Wrang, M., Evans, J., Orlova, A. (2011). Assessment of safety against derailment using simulations and vehicle acceptance tests: a worldwide comparison of state-of-the-art assessment methods. *Vehicle System Dynamics*, 49(7), pp. 1113-1157.

Wu, Q., Spiryagin, M., Cole, C. (2015). Advanced dynamic modelling for friction draft gears. *Vehicle System Dynamics*, 53(4), pp. 475-492.

Wu, Q., Spiryagin, M., Cole, C. (2016a). Longitudinal train dynamics: an overview. *Vehicle System Dynamics*, 54(12), pp. 1688-1714.

Wu, Q., Yang, X., Cole, C., Luo, S. (2016b). Modelling polymer draft gears. *Vehicle System Dynamics*, 54(9), pp. 1208-1225.

Wu, Q., Sun, Y., Spiryagin, M., Cole, C. (2018) Parallel Co-Simulation Method for Railway Vehicle-Track Dynamics. *Journal of Computational and Nonlinear Dynamics*, 13(4), 041004.

Yang, Z., Li, Z., Dollevoet, R. (2016). Modelling of non-steady-state transition from single-point to two-point rolling contact. *Tribology International*, 101, pp. 152-163.

Yang, J., Zhu, S., Zhai, W. (2020). A novel dynamics model for railway ballastless track with medium-thick slabs. *Applied Mathematical Modelling,* 78, pp. 907-931.

Ye, Y., Sun, Y., Dongfang, S., Shi, D., Hecht, M. (2020). Optimizing wheel profiles and suspensions for railway vehicles operating on specific lines to reduce wheel wear: a case study. *Multibody System Dynamics* 10.1007/s11044-020-09722-4

Zhai, W., Wang, K., Cai, C. (2009) Fundamentals of vehicle-track coupled dynamics. *Vehicle System Dynamics*, 47(11), pp. 1349-1376.

Zhai, W. (2019). *Vehicle–Track Coupled Dynamics Theory and Application*. Springer, Singapore.

Zhang, W., Chen, J., Wu, X., Jin, X. (2002). Wheel/rail adhesion and analysis by using full scale roller rig. *Wear*, 253(1-2), pp. 82-88.

Zhang, X., Redon, S., Lee, M., Kim, Y. J. (2007). Continuous collision detection for articulated models using Taylor models and temporal culling. *ACM Transactions on Graphics*, 26(3), 15.

Zhao, X.J., Guo, L.C., Guo, J., Liu, Q.Y., Butini, E., Marini, L., Meli, E., Rindi, A., Wang, W.J. (2020). Effect of spherical and ballast dents on rolling contact fatigue of rail materials. *Wear*, 450-451, 203254.

Zolotas, A.C., Goodall, R.M., Halikias, G.D. (2007) Recent results in tilt control design and assessment of high-speed railway vehicles. Proceedings of the Institution of Mechanical Engineers, Part F: Journal of Rail and Rapid Transit, 221(2), pp. 291-312.

This page is intentionally left blank.

LIST OF PUBLICATIONS

Papers in Scientific Journals

1. **Marques, F.**, Magalhães, H., Pombo, J., Ambrósio, J. and Flores, P., A three-dimensional approach for contact detection between realistic wheel and rail surfaces for improved railway dynamic analysis. *Mechanism and Machine Theory*, vol. 149, 103825, 2020.
2. Magalhães, H., **Marques, F.**, Liu, B., Antunes, P., Pombo, J., Flores, P., Ambrósio, J. and Bruni, S., Implementation of a non-Hertzian contact model for railway dynamic application. *Multibody Systems Dynamics*, vol. 48(1) pp. 41-78, 2020.
3. **Marques, F.**, Magalhães, H., Liu, B., Pombo, J., Flores, P., Ambrósio, J., Piotrowski, J. and Bruni, S., On the generation of enhanced lookup tables for wheel-rail contact models. *Wear*, vol. 434-435, 202993, 2019.
4. Isaac, F., **Marques, F.**, Dourado, N. and Flores, P., A finite element model of a 3D dry revolute joint incorporated in a multibody dynamic analysis. *Multibody Systems Dynamics*, vol. 45(3) pp. 293-313, 2019.
5. **Marques, F.**, Flores, P., Claro, J.P. and Lankarani, H.M., Modeling and analysis of friction including rolling effects in multibody dynamics: a review. *Multibody Systems Dynamics*, vol. 45(2) pp. 223-244, 2019.
6. **Marques, F.**, Isaac, F., Dourado, N., Souto, A.P., Flores, P. and Lankarani, H.M., A Study on the Dynamics of Spatial Mechanisms with Frictional Spherical Clearance Joints, *Journal of Computational and Nonlinear Dynamics*, vol. 12, 051013, 10 pages, 2017.
7. **Marques, F.**, Isaac, F., Dourado, N. and Flores, P., An enhanced formulation to model spatial revolute joints with radial and axial clearances. *Mechanism and Machine Theory*, vol. 116, pp. 123-144, 2017.
8. **Marques, F.**, Souto, A.P. and Flores, P., On the constraints violation in forward dynamics of multibody systems. *Multibody Systems Dynamics*, vol. 39(4), pp. 385-419, 2017.
9. **Marques, F.**, Flores, P., Claro, J.P. and Lankarani, H.M., A survey and comparison of several friction force models for dynamic analysis of multibody mechanical systems. *Nonlinear Dynamics*, vol. 86(3), pp. 1407-1443, 2016.

Proceedings in Scientific Conferences

1. **Marques, F.**, Magalhães, H., Pombo, J., Ambrósio, J. and Flores, P., Contact detection approach between wheel and rail surfaces, 8th European Conference on Mechanism Science - EuCoMeS 2020, 8 pages.
2. Corral, E., Gismeros, R., **Marques, F.**, Flores, P., Gómez García, M.J. and Castejon, C., Dynamic Modeling and Analysis of Pool Balls Interaction, ECCOMAS Thematic Conference Multibody Dynamics, Duisburgo, Germany, July 15-18, 2019, 8 pages.
3. **Marques, F.**, Magalhães, H., Pombo, J., Ambrósio, J. and Flores, P., Utilization of Non-Conformal Wheel Surfaces for Railway Dynamics, The 15th IFToMM World Congress, Krakow, Poland, June 30 - July 4, 2019, 10 pages.
4. **Marques, F.**, Magalhães, H., Liu, B., Pombo, J., Flores, P., Ambrósio, J., Piotrowski, J. and Bruni, S., On the generation of an enhanced lookup table for wheel-rail contact models, 11th International Conference on Contact Mechanics and Wear of Rail/Wheel Systems - CM2018, Delft, Netherlands, September 24-27, 2018, 8 pages.
5. Magalhães, H., **Marques, F.**, Liu, B., Pombo, J., Flores, P., Ambrósio, J. and Bruni, S., An Optimization Approach to Generate Accurate and Efficient Lookup Tables for Engineering Applications, 6th International Conference on Engineering Optimization - EngOpt 2018, Lisbon, Portugal, September 17-19, 2018, 12 pages.
6. **Marques, F.**, Magalhães, H., Ambrósio, J. and Flores, P., Approach for Conformal Contact Detection for Wheel-Rail Interaction, 7th European Conference on Mechanism Science - EuCoMeS 2018, Aachen, Germany, September 4-6, 2018, 8 pages.
7. Corral, E., **Marques, F.**, Gómez García, M.J., Flores, P. and García-Prada, J.C., Passive Walking Biped Model with Dissipative Contact and Friction Forces, 7th European Conference on Mechanism Science - EuCoMeS 2018, Aachen, Germany, September 4-6, 2018, 8 pages.
8. **Marques, F.**, Magalhães, H., Liu, B., Pombo, J., Flores, P., Ambrósio, J. and Bruni, S., A new simplified approach to deal with conformal contact in railway dynamics, The 5th Joint International Conference on Multibody System Dynamics – IMSD2018, Lisbon, Portugal, June 24 - 28, 2018, 14 pages.
9. Magalhães, H., **Marques, F.**, Liu, B., Pombo, J., Flores, P., Ambrósio, J. and Bruni, S., Implementation of a non-Hertzian Contact Model for Railway Dynamics, The 5th Joint International Conference on Multibody System Dynamics – IMSD2018, Lisbon, Portugal, June 24 - 28, 2018, 18 pages.
10. Corral, E., **Marques, F.**, Gómez García, M.J., García-Prada, J.C. and Flores, P., Dynamic modeling and analysis of contact interaction of a passive biped-walking robot, The 5th Joint International Conference on Multibody System Dynamics – IMSD2018, Lisbon, Portugal, June 24 - 28, 2018, 15 pages.

11. Isaac, F., **Marques, F.**, Dourado, N. and Flores, P., Modelling of Spatial Mechanical Joints with Realistic Properties: A Finite Element Analysis, EUROMECH Colloquium 578 - Rolling Contact Mechanics for Multibody System Dynamics, Madeira, Portugal, April 10-13, 2017, 20 pages.
12. **Marques, F.**, Isaac, F., Dourado, N. and Flores, P., 3D Formulation for Revolute Clearance Joints, 6th European Conference on Mechanism Science - EUCOMES, Nantes, France, September 20-23, 2016, 8 pages.
13. Isaac, F., **Marques, F.**, Dourado, N. and Flores, P., Recent Developments on Cylindrical Contact Force Models with Realistic Properties, 6th European Conference on Mechanism Science - EUCOMES, Nantes, France, September 20-23, 2016, 8 pages.
14. **Marques, F.**, Isaac, F., Dourado, N., Souto, A.P., Flores, P. and Lankarani, H.M., A Study on the Dynamics of Spatial Mechanisms with Frictional Spherical Clearance Joints, ASME 2016 International Design Engineering Technical Conferences & Computers and Information in Engineering Conference - IDETC/CIE, Charlotte, North Carolina, USA, August 21-24, 2016, 12 pages.
15. **Marques, F.**, Flores, P. and Lankarani, H.M., Study of Friction Force Model Parameters in Multibody Dynamics, The 4th Joint International Conference on Multibody System Dynamics - IMSD, Montréal, Québec, Canada, May 29 - June 2, 2016, 10 pages.
16. **Marques, F.**, Rychecký, D., Isaac, F., Hajžman, M., Polach, P. and Flores, P., Spatial Revolute Joints with Clearance and Friction for Dynamic Analysis of Multibody Mechanical Systems, The 4th Joint International Conference on Multibody System Dynamics - IMSD, Montréal, Québec, Canada, May 29 - June 2, 2016, 10 pages.

Abstracts in Scientific Conferences

1. Ambrósio, J., **Marques, F.**, Magalhães, H. and Flores, P., Development of an Enhanced Wheel-Rail Contact Model for Prediction of Rolling Contact Fatigue of Rails, 19th International Conference on New Trends in Fatigue and Fracture - NT2F19, Tucson, Arizona, USA, October 8-10, 2019.
2. Dourado, N., Radu, M.-C., **Marques, F.**, Flores, P., Lankarani, H.M. and Ambrósio, J., A Combined Multibody Finite Element Approaches for Dynamic Analysis and Material Behaviour of Mechanical Systems, 19th International Conference on New Trends in Fatigue and Fracture - NT2F19, Tucson, Arizona, USA, October 8-10, 2019.
3. **Marques, F.**, Flores, P. and Lankarani, H.M., Modeling Contact Mechanics in Multibody Dynamics, 12th HSTAM International Congress on Mechanics, Thessaloniki, Greece, September 22-25, 2019.
4. **Marques, F.**, Flores, P. and Lankarani, H.M., Modelling Contact/Impact Problems with a Modified LuGre Friction Model, ECCOMAS Thematic Conference Multibody Dynamics, Duisburgo, Germany, July 15-18, 2019.

5. **Marques, F.**, Magalhães, H., Pombo, J., Flores, P. and Ambrósio, J., Development of a new wheel-rail contact model for multibody simulations, The Fourth International Conference on Railway Technology - Railways 2018, Sitges, Barcelona, Spain, September 3-7, 2018.
6. **Marques, F.**, Flores, P., Claro, J.P. and Lankarani, H.M., Modeling and Analysis of Friction Effects in Multibody Dynamics, EUROMECH Colloquium 578 - Rolling Contact Mechanics for Multibody System Dynamics, Madeira, Portugal, April 10-13, 2017.
7. Flores, P. and **Marques, F.**, Combined Effects of Elastic Deformation and Lubrication Action in Human Knee Joints, EUROMECH Colloquium 578 - Rolling Contact Mechanics for Multibody System Dynamics, Madeira, Portugal, April 10-13, 2017.
8. **Marques, F.** and Flores, P., Numerical Aspects in Multibody Dynamics with Frictional Contacts, Congress on Numerical Methods in Engineering - CMN2017, Valencia, Spain, July 3-5, 2017.
9. **Marques, F.**, Souto, A.P. and Flores, P., A Critical Overview of Several Methods to Handle the Problem of Constraints Violation in Forward Multibody Dynamics, Congress on Numerical Methods in Engineering - CMN2017, Valencia, Spain, July 3-5, 2017.